UNIVERSITY OF CALIFORNIA
SANTA CRUZ

STRUCTURE, VIBRATIONAL PROPERTIES, AND EXCITED-STATE DYNAMICS OF METAL HALIDE MATERIALS

A dissertation submitted in partial satisfaction of the requirements for the degree of

DOCTOR OF PHILOSOPHY

in

CHEMISTRY

by

Heng Zhang

June 2026

The Dissertation of Heng Zhang is approved:

Professor Jin Z. Zhang, Chair

Professor Shaowei Chen

Professor Alexander Ayzner

Peter Biehl
Vice Provost and Dean of Graduate Studies

TABLE OF CONTENTS

LIST OF FIGURES

LIST OF TABLES

ABSTRACT

Structure, Vibrational Properties, and Excited-State Dynamics of Metal Halide Materials

Heng Zhang

Metal halide nanomaterials, including molecular clusters (MCs), nanocrystals (NCs), and low-dimensional perovskites, have attracted significant interest because of their tunable optical properties, strong excitonic effects, and potential applications in optoelectronic and spintronic devices. However, the relationships among structure, excited-state dynamics, lattice vibrations, and spin relaxation remain insufficiently understood, especially in highly confined metal halide systems. This dissertation addresses how chemical composition, structural confinement, lattice softness, and dopant incorporation influence the optical, vibrational, excitonic, and spin properties of metal halide clusters and nanocrystals.

A combination of synthesis, steady-state spectroscopy, ultrafast spectroscopy, structural characterization, and vibrational analysis was used. Amino metal halide molecular clusters were synthesized and stabilized in the solid state, and their structural and optical properties were investigated using optical spectroscopy and crystallographic analysis. Their excited-state relaxation processes were further studied by femtosecond transient absorption spectroscopy. Furthermore, low-frequency Raman spectroscopy, supported by structural analysis, was used to investigate lattice vibrations in two-dimensional lead-free metal halide double

perovskites. Finally, Ni-doped $CsPbBr_3$ nanocrystals were examined using spin-polarized transient absorption to evaluate the influence of dopant-induced defect passivation and scattering processes on spin lifetime.

The results show that amino metal halide molecular clusters can form stable, strongly quantum-confined solid-state structures around 2 nm with distinct optical properties arising from their discrete metal halide units and ligand-stabilized coordination environments. Ultrafast measurements reveal that their excited-state dynamics are governed by rapid relaxation pathways associated with strong confinement and a shallow trap state. Low-frequency Raman studies of 2D lead-free perovskites demonstrate that soft metal halide lattices exhibit characteristic vibrational modes sensitive to local structure and large octahedra distortions. In Ni-doped 3D $CsPbBr_3$ nanocrystals, moderate Ni incorporation improves spin lifetime, likely through defect passivation and reduced defect-mediated spin relaxation, whereas excessive doping shortens the lifetime due to increased disorder and scattering. Overall, this dissertation establishes a structure–dynamics–spin relationship in metal halide clusters and nanocrystals and provides insight into the design of confined metal halide materials with tunable optical and spin-dependent properties.

ACKNOWLEDGEMENTS

First, I would like to thank my supervisor, Jin Zhang, for five years of support not only in research but also in life. During the hardships, he provided care and supported me to continue my PhD studies. He guided me toward the right mindset for finishing tasks and managing programs and deadlines, a key to accomplishing the projects during my PhD.

Then I would like to thank all the lab members in the Zhang lab, including Mariam, David, Kevin, Celia, Asia, and former members Melissa, Vivien, Allison, and A'Lester. They are the people whom I stayed with the most time during my academic life in US. We worked together, helped each other, discussed data, and wrote papers together in many collaborative projects. In private, we make small talk and jokes, share personal emotions, and invite each other to events to enrich each other's lives, enabling me a positive attitude to face everything.

Thanks to Emma, my girlfriend, for her company over the past year, to keep life going. Thanks to my high school friend Shaoyang from China for encouraging me to pursue a PhD degree. Thanks to friends Kemin and Xuming from Stanford University, friends Yuxi and Yusheng from UCSC, and their families, and my roommate Yiwei and his family, for hanging out and enjoying good moments during weekends, events, and holidays. Thanks to Wences, my old landlord, for always fixing my car, offering helpful tips about US life, and sharing a tabby cat named Qiu Qiu with me. The cat greatly enriched my friends' and my spiritual worlds. Thanks to all the friends who brought joy and hope along the way, during the US life I never experienced before.

I would like to thank the graduates from our department, Dun Lin, Qiming Liu, Bingzhe Yu, Dingjie Pan, Tianchen Cui, Riley Ball, John Tressel, Sam Eisenberg, Sophia Hollow, and Jeremy Barnett's support during school days and the faculty, Tim Johnstone and Laura Sanchez, for their help with measurements. Thanks to the school staff, Betsy Desta, who passed away, but

has been so nice and supportive since I knew her; the school staff, Maddie Cairns, Myrian Lius, and Steven Mercado.

Thanks to the Postdocs, Zengqing Zhuo, Jialu Li, Yifeng Cao, and Gi-Hyeok Lee, whom I met at Berkeley National Lab. They were so nice and supported me during my stay at the Advanced Light Source (ALS). We have kept in touch since I left.

Thanks to my parents for the financial support over the years. Thanks to other family members, grandparents, uncles, and aunts who bring care and support.

I would also like to thank the beautiful view, the ocean, the breeze, the town, and the sunshine in California. Thank everyone I met during my PhD phase. Many people helped me, encouraged me, lifted me up, smiled at me, shared positive attitudes, making a PhD finish happen, although it is through a hard process. Without you, I couldn't have gone so far.

……

The text of this dissertation includes reprints of the following previously published material. The co-author listed in this publication directed and supervised the research which forms the basis for the dissertation. My contributions to this work included sample synthesis, optical, structural and electronic characterization, data analysis, and manuscript preparation.

1. **Chapter 2:**

Zhang, H.; Vickers, E. T.; Erickson, S.; Guarino-Hotz, M.; Barnett, J. L.; Ghosh, S.; Zhang, J. Z. Synthesis and Properties of Stable Amino Metal Halide Molecular Clusters in the Solid State. *J. Phys. Chem. Lett.* **2022**, *13* (45), 10543–10549. https://doi.org/10.1021/acs.jpclett.2c02977.

2. **Chapter 3:**

Zhang, H.; Zeitz, D. C.; Zhang, J. Z. Ultrafast Study of Excited State Dynamics of Amino Metal Halide Molecular Clusters. *J. Phys. Chem. Lett.* **2023**, *14* (36), 8095–8099. https://doi.org/10.1021/acs.jpclett.3c01952.

3. Because this chapter does not share the same scope as the main dissertation, it is included in the Appendix.

Zhang, H.; Oduntan, A.; Zhuo, Z.; Chuang, S. S. C.; Guo, J.; Zhang, J. Z. New Insights into Nonthermal Plasma-Assisted Poly(vinyl alcohol) Depolymerization Catalyzed by TiO_2. *J. Phys. Chem. C* **2025**, *129* (10), 4950–4963. https://doi.org/10.1021/acs.jpcc.4c07876.

4. **Chapter 4:**

Zhang, H.; Leano, R. J.; Xie, G.; Todd, C.; Liu, J.; Johnstone, T. C.; Lederman, D.; Pang, Q.; Sang, L.; Strubbe, D. A.; Zhang, J. Z. Low Frequency Vibrational Modes of Two-Dimensional Lead-Free Metal Halide Double Perovskites. *J. Phys. Chem. C* **2026**, *130* (1), 498–507. https://doi.org/10.1021/acs.jpcc.5c05803.

1 Introduction to Nanocrystals and Their Characterization Methods

1.1 Introduction to Nanomaterials

The development of quantum mechanics in the 20th century profoundly advanced our understanding of matter at small length scales, laying the foundation for semiconductor technology and nanomaterials. Nanomaterials are commonly defined as materials with at least one dimension in the range of 1–100 nm. Owing to their large surface-area-to-volume ratio and the increased fraction of surface atoms, nanomaterials often exhibit size-dependent optical, electronic, magnetic, and chemical properties that differ from their bulk counterparts.[1] In contrast, bulk materials are generally large enough that surface and quantum confinement effects are not dominant, and their properties are less dependent on size.[2,3] In such a microscopic world, material properties can change dramatically and exhibit intriguing phenomena due to quantum confinement effects. For example, when the motion of charge carriers is spatially confined, the electronic energy levels become discrete and quantized rather than continuous, as commonly observed in macroscopic bulk materials.[4,5] Based on quantum mechanics, many important technologies have emerged, including transistors, lasers, magnetic resonance imaging, and integrated circuits, which constitute core technologies of modern society.[6] In the 21st century, quantum technologies have further expanded into quantum computing, quantum communication, and quantum sensing, driven by theoretical advances and

experimental progress in controlling and exploiting quantum superposition, entanglement, and coherence.[7–9] Meanwhile, the rapid development of artificial intelligence has created increasing demand for computational resources and energy. AI is now widely regarded as one of the key enabling technologies of the Fourth Industrial Revolution, reshaping industrial production, data processing, automation, and decision-making.[10]

Although nanomaterials are commonly defined as structures with at least one dimension below 100 nm, this criterion is not derived from quantum mechanics but is largely used as a practical range.[11] Quantum confinement effects generally emerge when the structural dimension becomes comparable to the carrier de Broglie wavelength or smaller than the exciton Bohr radius, which are typically on the order of a few nanometers to several tens of nanometers, depending on the semiconductor.[12] Therefore, not all nanomaterials exhibit quantum-confined behavior, and the transition from bulk-like to quantum-confined regimes depends on intrinsic material parameters rather than a universal size threshold. The bulk-like small-sized materials don’t have the quantum confinement effect, but they show properties highly related to the surface, such as catalytic, optical, and mechanical properties.

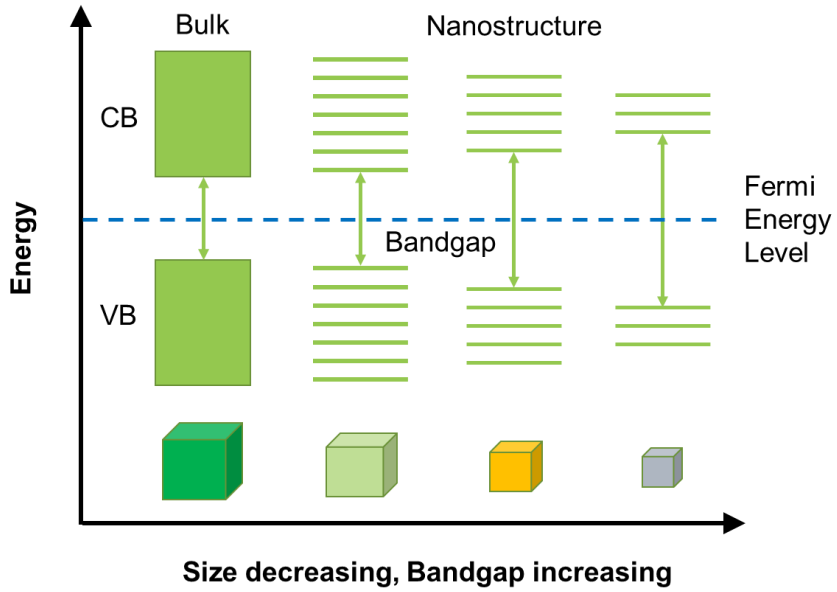

Figure 1-1 The Schematic illustration of the relationship among energy levels, bandgap, and material size. CB and VB denote the conduction band and valence band, respectively. The Fermi energy level represents the energy level with a 50% probability of electron occupation at a given temperature.

While nanomaterials generally exhibit size-dependent properties due to increased surface effects and partial quantum confinement, as you can see in Figure 1-1, quantum dots (QDs) represent a special class of zero-dimensional nanomaterials with full quantum confinement, resulting in discrete energy levels and atom-like optical behavior. Some nanocrystals with a size smaller than the exciton Bohr radius are also considered QDs that exhibit size-dependent changes in optical properties. The exciton Bohr radius is a fundamental material parameter that characterizes the average spatial separation between the electron and hole in an excitonic state. In analogy to the hydrogen atom, its value in semiconductors can be expressed as

$$a_B^* = \frac{\varepsilon_r}{\mu_r} a_0 \quad (1\text{-}1)$$

where ε_r is the relative dielectric constant, μ_r=μ/m_0 is the reduced effective mass normalized to the free electron mass, where μ is the reduced effective mass of electron-hole pairs, m_0 is the mass of free electrons, and a_0 is the Bohr radius of the hydrogen atom at 0.53 Å.[13,14]

Unlike the de Broglie wavelength, which depends dynamically on the particle momentum or kinetic energy, the exciton Bohr radius is primarily determined by intrinsic material properties, especially the dielectric screening and the effective masses of electrons and holes.[14] Therefore, it is commonly used as a characteristic length scale to evaluate the strength of quantum confinement in semiconductor nanostructures. When the crystal size becomes comparable to or smaller than the exciton Bohr radius, the motion of charge carriers is spatially restricted, leading to discrete energy levels, bandgap widening, and size-dependent optical properties.[4] This concept is particularly important in low-dimensional semiconductors and quantum dots, where excitonic effects are significantly enhanced.

Due to their low-cost solution processability, compositional diversity, and tunable size and optoelectronic properties, nanocrystals have attracted sustained research interest for applications in light-emitting diodes, photovoltaics, photodetectors, and bioimaging, and studies in this field remain a hot topic.[15–17]

1.2 Introduction to Molecular Clusters (MCs), Magic-Sized Clusters (MSCs) and Quantum Dots (QDs)

Clusters, molecular clusters (MCs), magic-sized clusters (MSCs), and quantum dots (QDs) are distinct nanocrystal types, but they are not isolated material systems. Instead, they can be viewed as a continuous developmental sequence from the molecular level to intermediate-sized stable clusters, and finally to larger quantum dots. In this dissertation, my work covers small-sized MCs and MSCs, as well as large-sized QDs. Therefore, the motivation of this dissertation is to address the remaining fundamental questions in them and manipulate their properties for modern applications. The systematic study of their size, structure, ligand chemistry, and optoelectronic properties is also included in the content.

MCs and MSCs are typically smaller than conventional QDs and often exhibit discrete compositions, narrow size distributions, sharp optical absorption features, and enhanced thermodynamic or kinetic stability.[18–20] They are therefore important model systems for understanding the nucleation, growth, and structural evolution of semiconductor nanocrystals. In contrast, QDs are larger semiconductor nanocrystals whose optical and electronic properties are mainly governed by quantum confinement, composition, and surface chemistry. The development from clusters to QDs has provided a powerful platform for studying size-dependent photophysics, ligand-controlled growth, and structure–property relationships in nanoscale semiconductors.[21,22] Based on this framework, the following sections review the development of MCs, MSCs and QDs, respectively, with an emphasis on their

structural evolution, ligand effects, and optoelectronic properties.

1.2.1 Development of Semiconductor Quantum Dots

QDs are generally defined as semiconductor nanocrystals with sizes smaller than or comparable to the exciton Bohr radius. Due to quantum confinement, their band gaps, absorption features, and photoluminescence wavelengths can be tuned by controlling their size, composition, and surface chemistry.[4,23] QDs exhibit several attractive properties that make them highly promising for optoelectronic applications. First, their band gaps and emission wavelengths can be continuously tuned by controlling particle size, composition, and surface chemistry, allowing broad spectral coverage from the visible to near-infrared region.[4,24] In addition, colloidal QDs can be synthesized and processed from solution, enabling low-cost, scalable fabrication of thin films and devices.[25] Their optical performance can be further improved through surface passivation, ligand engineering, and core–shell structures, which reduce surface traps and enhance photoluminescence efficiency and stability.[24,26] For metal halide perovskite QDs, particularly $CsPbX_3$ nanocrystals, narrow emission linewidths, high photoluminescence quantum yields, high carrier mobility and wide color-gamut emission have made them especially attractive for displays, light-emitting diodes, lasers, photodetectors, and solar cells.[27–30]

The development of QD research has generally proceeded through several stages. Early studies mainly focused on the controlled synthesis and quantum confinement properties of traditional colloidal QDs, such as CdS, CdSe, PbS, and InP, which belong to II–VI, IV–VI, and III–V semiconductor families.[23,31] Later, research

expanded to surface ligands, core–shell structures, defect passivation, and device applications.[25,26] In recent years, metal halide perovskite QDs have emerged as an important class of optoelectronic materials because of their high photoluminescence quantum yields, narrow emission bandwidths, compositional tunability, and solution processability, offering versatile functionality across a wide range of applications.[27,28,32]

While conventional QDs include diverse semiconductor systems such as II–VI, III–V, and IV–VI nanocrystals, this section focuses on metal halide perovskite QDs and their low-dimensional derivatives due to the attractive properties mentioned above. In addition to three-dimensional (3D) perovskite quantum dots, low-dimensional metal halide perovskites, including two-dimensional (2D), one-dimensional (1D), and zero-dimensional (0D) structures, have attracted significant attention due to their enhanced structural stability and unique optoelectronic properties.[33,34]

2D metal halide perovskites usually have layers structures, where inorganic metal halide sheets are separated by bulky organic spacer cations. In 1D systems, the inorganic metal halide units are connected mainly along one direction to form chain-like frameworks, while in 0D systems, isolated metal halide polyhedra or clusters are separated by organic cations. Such structural dimensionality strongly influences electronic coupling, exciton localization, charge transport, and emission behavior.[33,35] In particular, quasi-2D perovskites are important low-dimensional derivatives that combine the advantages of both 3D and strictly 2D perovskites. Compared with 3D

perovskites, quasi-2D structures usually show enhanced environmental stability and stronger quantum/dielectric confinement due to bulky organic spacer cations and reduced inorganic-layer thickness. Compared with strictly 2D perovskites with n=1, quasi-2D perovskites with larger or mixed n values retain stronger electronic coupling and more efficient charge transport while maintaining pronounced excitonic properties. Therefore, quasi-2D perovskites provide a useful platform for stable and efficient light emission.[36,37]

1D and 0D metal halides provide even stronger structural confinement than 2D systems because their inorganic frameworks are further reduced to chain-like units or isolated polyhedra or clusters. These structures often show highly localized excitons and distinctive broadband emission associated with self-trapped excitons, although their charge transport is generally more limited than that of 3D and quasi-2D perovskites.[38,39]

These low-dimensional systems share conceptual similarities with perovskite magic-sized clusters (PMSCs) and metal halide molecular clusters (MCs) because all involve strong confinement, discrete or localized electronic states, and ligand- or cation-dependent structural stabilization. However, dimensional reduction is not limited to 2D, 1D, and 0D frameworks. At even smaller length scales, perovskite-related materials can also exist as MSCs and MCs, which represent intermediate or discrete species between molecular precursors and larger QDs. Unlike low-dimensional perovskites, MSCs and MCs often possess well-defined sizes, discrete compositions, and strongly confined electronic structures. Therefore, they provide

another important perspective for understanding how precursor chemistry, structural confinement, and early-stage nucleation processes govern the formation and optical properties of perovskite QDs.[20,40]

1.2.2 Magic-Sized Clusters as Intermediates Between MCs and QDs

Early studies of semiconductor nanocrystals mainly focused on quantum confinement effects and size-dependent optical properties.[4,23] With the development of synthetic strategies and advanced characterization techniques, researchers gradually recognized that, between molecular precursors and colloidal quantum dots, there exists a class of small intermediate species with discrete compositions or unusual stability, known as magic-sized clusters (MSCs).[21,22]

MSCs usually possess narrow or even single-size distributions and exhibit sharp absorption features. During nanocrystal growth, MSCs often show discrete, stepwise growth behavior rather than continuous size evolution. Therefore, they have been regarded as key intermediates for understanding nanocrystal nucleation and growth mechanisms.[41–43] Recent reviews have further emphasized that MSCs serve as an important bridge between molecular precursors and colloidal quantum dots, providing valuable insights into QD nucleation, growth pathways, and structural evolution.[22,44]

In metal halide perovskite systems, similar highly confined species, including perovskite magic-sized clusters (PMSCs) and metal halide molecular clusters (MCs), have also attracted increasing attention.[20,40] PMSCs are generally smaller than conventional perovskite nanocrystals, possess narrower size distributions, and exhibit

sharper optical absorption features. They also show exceptional optoelectronic properties, such as near unity quantum yield, wide color tunability, high color purity and brightness.[45]

The formation and stability of PMSCs are strongly influenced by synthetic conditions, especially the identity, concentration, and binding strength of surface ligands. For example, Xu et al. reported that $CsPbBr_3$ PMSCs can be generated with ligand phenylacetic acid (PAA), not with mesitylacetic acid (MAA) or oleic acid (OA), because PMSCs require better passivation or stronger ligands than PQDs.[46] Moreover, the reversible or controllable transformation between perovskite QDs and PMSCs has become an important research topic in recent years. Such transformation relationships provide valuable insights into the structural evolution pathway from molecular precursors to highly confined clusters and, finally to quantum dots.[40] Liu et al. specifically reviewed the role of capping ligands in the synthesis and transformation between metal halide perovskite QDs and PMSCs, showing that ligands not only stabilize the surface but also regulate the formation of highly confined cluster species, highlighting that ligand identity, concentration, and binding strength can mediate the interconversion between QDs and PMSCs. For example, Zhang et al showed that combinations of different organic acid and amine ligands, such as oleic acid (OA), and amines, such as oleylamine (OLA) provided good passivation for the QDs.[47] Xu et al. found that a lower ligand concentration facilitates QD formation, whereas a higher concentration supports MSC production.[48] Related reviews have also compared the optical and structural differences among perovskite

quantum dots (PQDs), PMSCs, and metal halide MCs.[20,40]

1.2.3 From Molecular Precursors to Clusters

The formation of semiconductor nanocrystals does not necessarily proceed directly from free molecular precursors to large crystalline nanocrystals. Instead, many systems involve intermediate species such as small clusters, molecular clusters (MCs) and magic-size clusters (MSCs), which can appear during chemical conversion, coordination rearrangement, nucleation, and early-stage growth. Advances in controlled synthesis, in situ spectroscopy, mass spectrometry, and crystallographic analysis have shown that some precursor-derived clusters can be isolated, stabilized, and studied as independent material systems rather than only being regarded as transient intermediates.[21,49]

MCs represent a highly confined regime between molecular precursors and larger nanocrystals. Unlike conventional quantum dots, which usually possess size distributions and extended crystal-like lattices, MCs can have discrete compositions, atomically or molecularly defined structures, and strong ligand coordination. Therefore, MCs provide a useful platform for connecting molecular coordination chemistry with nanocrystal chemistry. Their structures are strongly affected by metal–ligand coordination, inorganic framework geometry, surface-binding motifs, and the steric or electronic effects of organic ligands.[22,49]

The importance of MCs is not limited to their structural definition. They also provide mechanistic insight into how nanocrystals form. In many semiconductor systems, nucleation and growth may occur through nonclassical pathways, where

cluster-like species assemble, transform, or fuse rather than growing only by monomer-by-monomer addition. Identifying these clusters is therefore important for understanding precursor conversion, nucleation kinetics, ligand-controlled growth, and the origin of size-dependent optical properties.[41,50]

In metal halide systems, MCs are especially attractive because soft ionic lattices and flexible coordination environments allow diverse discrete cluster structures to form. Organic cations or neutral ligands can separate and stabilize discrete metal halide units, including isolated metal halide polyhedra, dimeric or trimeric units, and larger cluster species. Unlike extended 3D perovskites with the general ABX_3 framework, MCs usually have discrete compositions and molecular-level structures, which give rise to highly confined electronic states and distinct optical features.[51,52] Studies on PMSCs and amino lead halide MCs have shown that metal halide clusters have sharp peaks with full width at half maximum (FWHM) at 10-20 nm and can interconvert or coexist with larger perovskite-like nanostructures, depending on ligand chemistry, precursor conditions, and synthetic environment.[20,40]

Similarly, the structural confinement of isolated metal halide units also gives rise to distinct photophysical behavior. For example, Zhou et al. reported a series of 0D organic–inorganic metal halide emitters based on isolated Sn-, Sb-, and Pb-halide polyhedra or cluster-like units separated by organic cations, $C_4N_2H_{14}Br^+$ and $C_9NH_{20}^+$. In these structures, the inorganic metal halide units are periodically isolated within an organic matrix, forming 0D hybrid frameworks with strong structural confinement and localized excitonic states. Such structural confinement localizes excitons within

isolated metal halide units, which can reduce nonradiative energy loss and enable efficient photoluminescence. The emission color can be further tuned by changing the metal center, halide composition, and coordination geometry. In particular, the blue-emitting lead chloride cluster assembly, $(C_9NH_{20})_7(PbCl_4)Pb_3Cl_{11}$, exhibited emission around 470 nm with a photoluminescence quantum efficiency (PLQY) of approximately 83%, while related yellow- and red-emitting 0D metal halide hybrids showed near-unity photoluminescence quantum efficiencies, demonstrating that metal halide clusters can act as efficient emitters rather than merely as precursor species.[53,54]

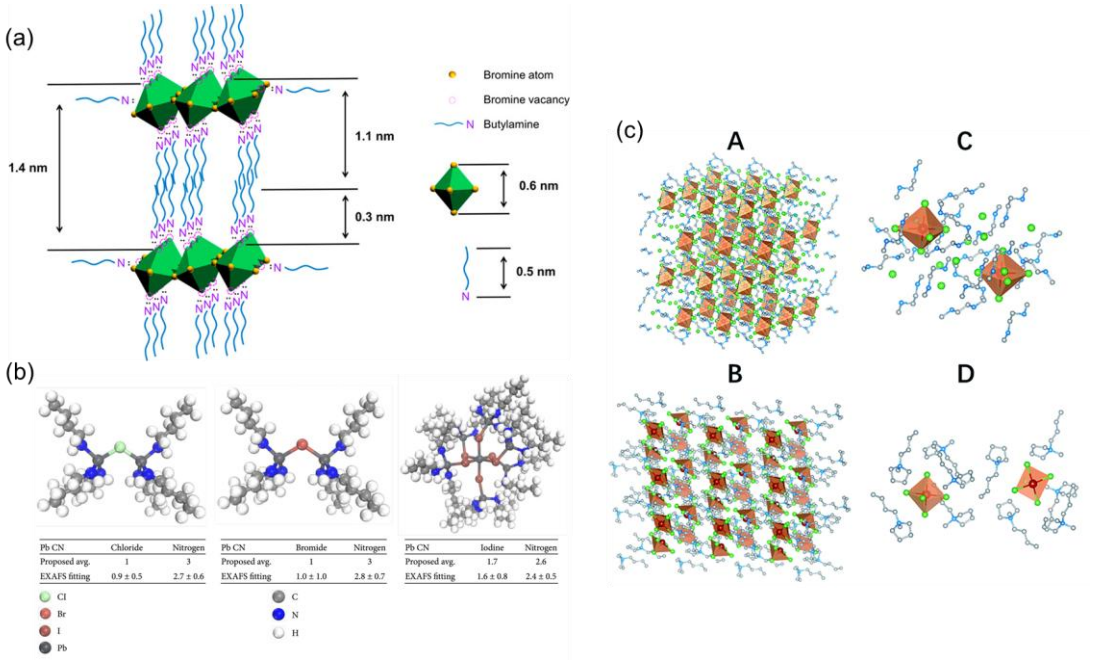

Figure 1-2 The structural comparison of MCs (left half) and 0D metal halide hybrids (right half). (a) Proposed layered structure for $PbBr_2$-BTYA MCs.[51] (b) Proposed molecular models and the Pb coordination number (CN) from the extended X-ray absorption fine structure (EXAFS) fitting results for $PbCl_2$-BTYA (left), $PbBr_2$-

BTYA (middle), and PbI_2-BTYA (right) MCs.[20] (c) Views of the crystal structures of $(C_4N_2H_{14}Br)_4SnBr_6$ (top) and $(C_9NH_{20})_2SbCl_5$ (bottom) 0D organic-inorganic metal halide hybrids.[54]

Figure 1-2 illustrates the close but nonidentical relationship between metal halide MCs and 0D organic–inorganic metal halide hybrids. In 0D hybrids, isolated metal halide polyhedra or cluster units are embedded in an organic matrix, leading to strong structural confinement and localized excitons. Some of these isolated cluster units can be described as molecular clusters when they have well-defined compositions and molecular-level structures; however, not all 0D metal halide hybrids should be classified as MCs. Therefore, 0D hybrid emitters provide useful examples of how isolated metal halide units can generate efficient photoluminescence through composition, coordination geometry, and organic–inorganic structural design.[55,56]

Representative examples of metal halide MCs include amino lead bromide molecular clusters stabilized by neutral amine ligands. For instance, Zhang et al. reported stable $PbBr_2$-based molecular clusters capped by butylamine ligands, showing that metal halide MCs can be isolated and stabilized as discrete cluster species in both solution and solid states.[51] Mn^{2+}-doped amino lead halide MCs have also been reported, demonstrating that the optical properties of MCs can be tuned through dopant incorporation.[52] Furthermore, a clear vision of MCs is the molecular structure connecting $PbBr_2$ to the ligands through coordination bonds reported from Vickers et al.[20]

Overall, MCs are no longer viewed only as temporary precursor fragments or synthetic byproducts. They are more recognized as independent material systems with defined structures, tunable optical properties, and mechanistic significance. Their study helps establish a more complete picture of the structural evolution from molecular precursors to small metal halide clusters, MCs, MSCs, and ultimately larger QDs. Therefore, investigating MCs in this dissertation provides an important foundation for understanding how precursor chemistry, ligand coordination, structural confinement, and cluster assembly govern the formation and properties of semiconductor nanomaterials.[20,21,51,57] The contribution from this dissertation to the understanding of MCs structure and charge carrier dynamics will be found in Chapters 2 and 3.

1.3 Synthesis of MCs, MSCs and QDs

Synthesis is the core of obtaining a superior-quality sample that facilitates subsequent characterization to achieve the research goal. The goals include the target bandgap tuning through composition engineering and size control, while ensuring high crystallinity, low defect density, and good colloidal stability. The main principles for achieving various colors are the quantum-size effect via A-site mixing, B-site doping, halide substitution, and ligand choice.

1.3.1 Hot Injection

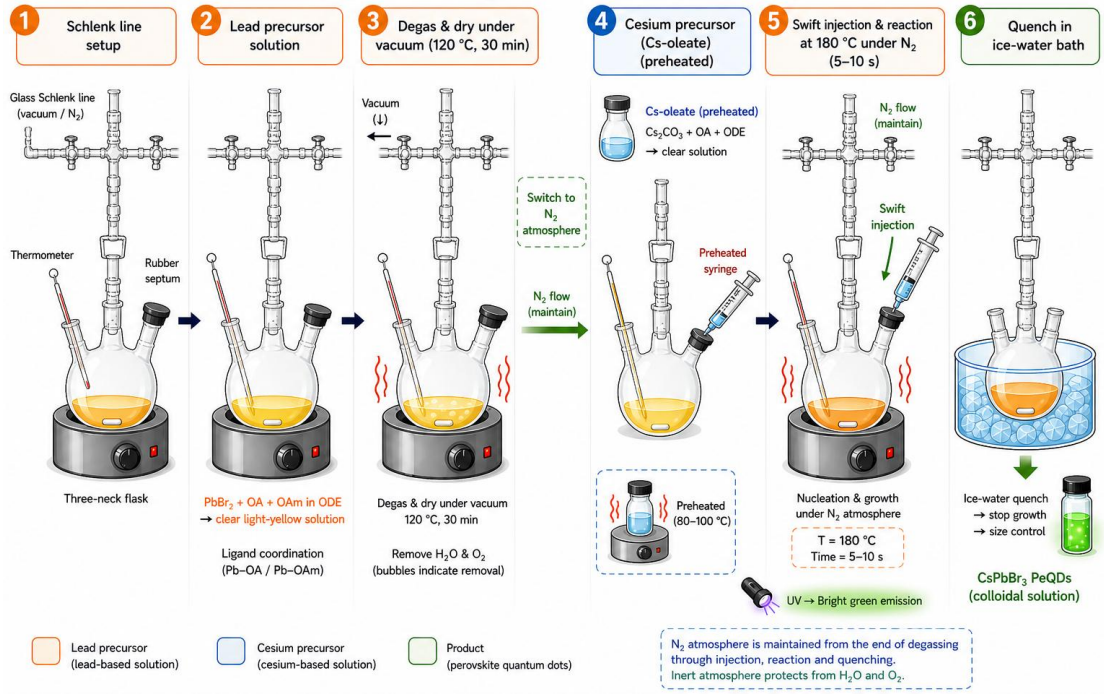

Figure 1-3 The flow chart shows the hot-injection synthesis of colloidal $CsPbBr_3$ perovskite QDs using a representative procedure. $PbBr_2$ is used in this example, while other metal sources such as SnX_2, GeX_2, BiX_3, SbX_3, or dopant metal halides such as MnX_2 and ZnX_2 can also be used, depending on the target composition. The halide component Br can be replaced to Cl, I or even mixed halides.

The hot-injection method is a classical approach to synthesizing optimal QDs with a uniform size distribution, high crystallinity, and high stability.[58,59]

As shown in Figure 1-3, usually, the hot-injection synthesis of perovskite QDs involves dissolving a lead source, such as $PbBr_2$, in a nonpolar solvent, such as 1-octadecene (ODE), along with oleic acid (OA) and oleylamine (OAm) as organic ligands. The precursor solution is then purged under vacuum at approximately 120 °C

to remove residual moisture and oxygen. After purging, the system was switched to a nitrogen (N_2) atmosphere to maintain an inert environment. The temperature was then rapidly increased to 180 °C under N_2 flow. Subsequently, a cesium precursor, typically cesium oleate, prepared by dissolving Cs_2CO_3 in ODE and OA, is rapidly injected into the hot lead precursor solution, where the rapid injection initiates nucleation and growth of $CsPbBr_3$ nanocrystals. After that, the reaction is then quickly quenched in an ice-water bath to terminate crystal growth, yielding the target perovskite QD_S. Finally, the resulting $CsPbBr_3$ PQDs were obtained as a colloidal solution for subsequent purification and characterization.

The quality and size of the obtained PQD_S strongly depend on precise control of reaction parameters, with reaction temperature being particularly critical. Lower reaction temperatures of 80–120 °C usually favor the formation of small PQD_S with sizes of approximately 3–5 nm, whereas higher temperatures of 140–200 °C typically lead to the growth of larger nanocrystals or nanostructures.[60,61] Also, long-chain ligands promote the formation of small-sized QDs.[62] However, this method also has several limitations, including the requirement for an inert-gas atmosphere and strict temperature control, which make the process relatively complicated and less suitable for large-scale applications.

1.3.2 Ligand-Assisted Reprecipitation (LARP)

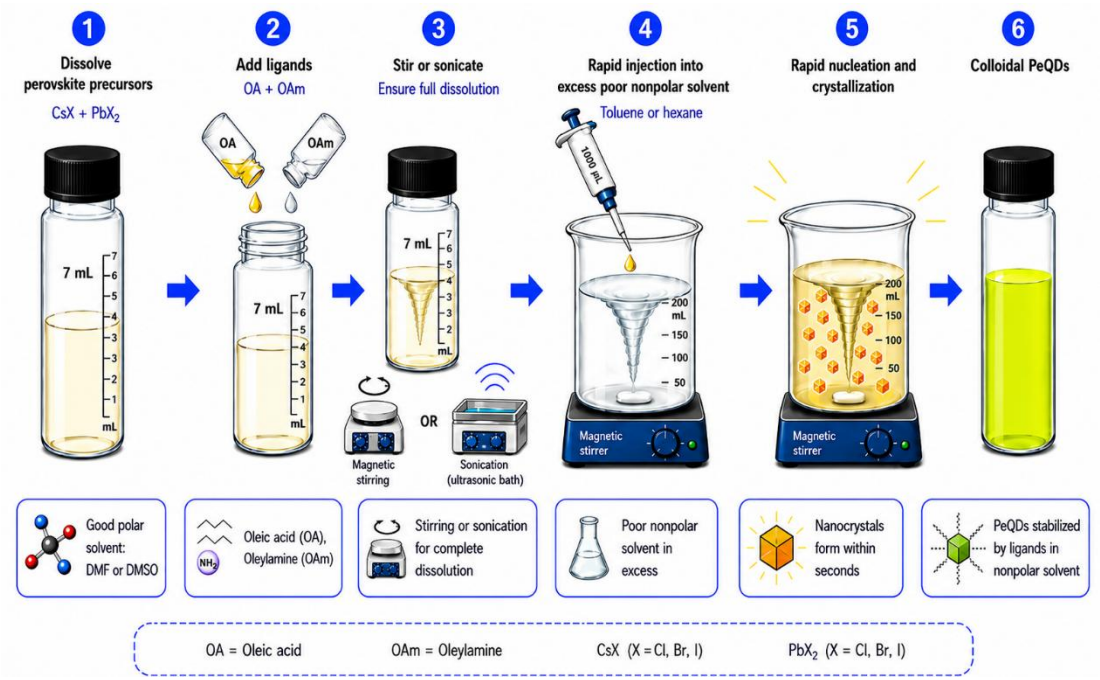

Figure 1-4 LARP synthesis of the colloidal perovskite QDs.

LARP is a simple method used to produce MSCs and MCs in our group. The LARP method isn't a long process and the key is to use a poor solvent to add to the good solvent, then precipitate the QD crystals. The whole synthesis process is low-cost, straightforward, and operates under ambient conditions at room temperature. Due to these merits, it has potential for mass production. As shown in Figure 1-4, the common LARP procedure involves dissolving perovskite precursors, such as CsX and PbX_2 (X = Cl, Br, or I), in a small borosilicate glass vial containing a good polar solvent, typically N, N-dimethylformamide (DMF) or dimethyl sulfoxide (DMSO). Surface ligands, such as oleic acid (OA) and oleylamine (OAm), are then added to stabilize the resulting nanocrystals. Stirring or sonication is usually applied to ensure complete dissolution of the precursors. The prepared precursor solution is rapidly

injected into an excess of a poor nonpolar solvent, such as toluene or hexane, under vigorous stirring. The sudden decrease in precursor solubility induces rapid supersaturation, nucleation, and crystallization, thereby yielding colloidal PQDs.

The key process parameters of LARP are the ratio of good to poor solvents and the type and concentration of ligands. Among them, the ratio between the two solvents is crucial for controlling PQD size through its direct effect on the system's supersaturation, with a typical ratio range from 1:10 to 1:50. The type and concentration of ligands are vital for achieving optimal PQD dispersibility and surface passivation. An insufficient ligand concentration can lead to PQD aggregation, whereas an excessive ligand concentration may increase the surface defect. LARP is usually conducted at room temperature, but a slight increase in temperature below 100 °C can stabilize the PQDs and lead to larger sizes.[63,64]

One major limitation of the LARP method is that the obtained PQDs often exhibit a higher density of surface defects and lower PLQY than those synthesized by the hot-injection method.[65] In this regard, post-synthetic purification or surface passivation treatments are usually required to improve their optical properties. Previous studies demonstrated that exploiting short-chain ligand modification, halide-source supplementation, and ionic-liquid passivation methods can effectively reduce the density of surface defect states, thereby enhancing the luminescence efficiency and stability of PQDs.[66–68]

1.3.3 Post-Treatment After Synthesis

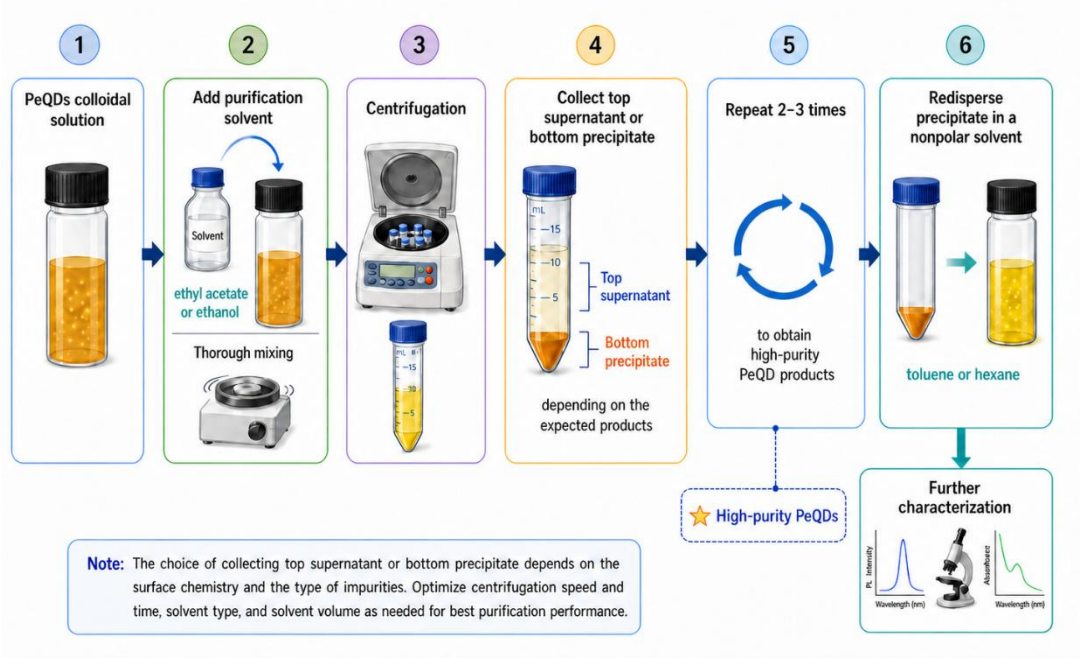

Figure 1-5 The general purification process for perovskite QDs. It is applicable to samples prepared via both hot-injection and LARP methods.

Purification is required for these synthesized PQDs to remove excess ligands, unreacted precursors, residual polar solvents, and system by-products from the synthesis process, thereby improving colloidal dispersion stability and optical properties.[69] Centrifugation is the most commonly used purification method for PQDs. A flowchart process is shown in Figure 1-5 as a typical procedure. The as-synthesized PQD colloidal solution is thoroughly mixed with a purification solvent, such as ethyl acetate or ethanol. The mixture is then centrifuged to separate components by size, mass, and colloidal stability. Depending on the target product, either the upper supernatant or the bottom precipitate can be collected. This washing and centrifugation process is usually repeated 2-3 times to obtain purified PQD

products. The collected precipitate is finally redispersed in a nonpolar solvent, such as toluene or hexane, for further characterization or device fabrication. The purification is conducive to both hot-injection and LARP methods.

The purification conditions, including the choice of washing solvent, centrifugation speed, and centrifugation time, need to be carefully optimized according to the synthesis goal. For conventional PQD purification, the bottom precipitate is often collected and redispersed. However, when the crude product contains a mixture of large and small nanocrystals and the small-sized, lightweight PQDs are the desired product, mild or medium-speed centrifugation is preferred. For example, centrifugation at approximately 2000-3000 rpm for 5 min can sediment larger aggregates or oversized particles while retaining smaller PQDs in the upper supernatant. In this case, the supernatant is collected as the final product.

1.4 Key Parameters in Studying MCs, MSCs and QDs

The properties of molecular clusters (MCs), magic-sized clusters (MSCs), and quantum dots (QDs) are strongly governed by their size, structure, composition, surface chemistry, and carrier dynamics. Therefore, a combination of optical, structural, chemical, excitonic, and spin-resolved characterization methods is required to establish the relationship between synthesis, structure, and photophysical properties. In this dissertation, these parameters are systematically investigated to understand the structure, optical properties, and electronic and spin properties.

1.4.1 Optical Properties

UV-Visible (UV-Vis) absorption and photoluminescence (PL) spectroscopy are fundamental tools for probing the electronic structure of NCs. The absorption spectrum reflects electronic transitions from the ground state to excited states, whereas the PL spectrum provides information on radiative recombination pathways following photoexcitation.

For semiconductor nanomaterials, the optical band gap can often be estimated from the absorption edge. In many cases, the Tauc relation is used:

$$(\alpha h\nu)^n = A(h\nu - E_g) \tag{1-2}$$

where α is the absorption coefficient, $h\nu$ is the photon energy, A is a constant, and E_g is the optical band gap. The exponent n depends on the type of electronic transition. For a direct allowed transition, $n = 2$, while for an indirect allowed transition, $n = 1/2$. By extrapolating the linear region of the Tauc plot to the energy axis, the optical band gap E_g can be obtained.

For QDs and small clusters, the absorption and PL peaks are strongly affected by quantum confinement. As the particle size decreases, the band gap generally increases, leading to a blue shift in both absorption and PL. This size-dependent band gap can be qualitatively described by the Brus equation:

$$E(R) = E_g^{bulk} + \frac{\hbar^2\pi^2}{2R^2}\left(\frac{1}{m_e^*} + \frac{1}{m_h^*}\right) - \frac{1.8e^2}{4\pi\varepsilon R} \tag{1-3}$$

where $E(R)$is the size-dependent band gap, $E_g^{bulk}$is the bulk band gap, $R$is the

nanocrystal radius, m_e^* and m_h^* are the effective masses of electrons and holes, respectively, and $\varepsilon$is the dielectric constant.

The Stokes shift, defined as the energy difference between the absorption and PL maxima, is another important optical parameter:

$$\Delta E_{Stokes} = E_{abs} - E_{PL} \tag{1-4}$$

A large Stokes shift may indicate structural relaxation, self-trapped exciton formation, surface-related emission, or defect-mediated recombination.

The photoluminescence quantum yield can be written as:

$$\Phi_{PL} = \frac{k_r}{k_r + k_{nr}} \tag{1-5}$$

where k_r is the radiative recombination rate and k_{nr} is the nonradiative recombination rate.

The lifetime is related to the total recombination rate:

$$\frac{1}{\tau} = k_r + k_{nr} \tag{1-6}$$

By combining Equations (1-5) and (1-6), the radiative and nonradiative recombination rate, k_r and k_{nr} can be determined.

1.4.2 Structural Information

Structural characterization is essential for distinguishing molecular clusters, magic-sized clusters, and quantum dots. These materials may show different degrees of crystallinity, atomic ordering, surface ligand coordination, and lattice distortion. Therefore, morphology, crystal structure, bonding information, and chemical

composition need to be evaluated.

1.4.2.1 Morphology

Morphology includes the size, shape, and size distribution of the particles or clusters. Transmission electron microscopy (TEM), high-resolution TEM (HRTEM), and scanning electron microscopy (SEM) are commonly used to visualize the morphology.

A narrow size distribution usually indicates better synthetic control and higher uniformity. For MSCs and MCs, direct imaging can be challenging because of their extremely small size and beam sensitivity. Therefore, microscopy results should often be combined with optical spectra, XRD, and chemical analysis.

1.4.2.2 Crystal Structure

Crystal structure determines the long-range or short-range atomic arrangement in MCs, MSCs, and QDs. Powder X-ray diffraction (pXRD) is used to identify crystalline phases, crystal systems, and lattice parameters. Single-crystal X-ray diffraction (scXRD) can provide atomically resolved structural information if high-quality single crystals are available.

For nanocrystals, the crystallite size can be estimated from peak broadening using the Scherrer equation:

$$D = \frac{K\lambda}{\beta \cos\,\theta} \tag{1-7}$$

where D is the crystallite size, K is the shape factor, λ is the X-ray wavelength, β is the full width at half maximum in radians, and θ is the Bragg angle.

High-resolution TEM (HRTEM) provides local lattice-resolved information,

including lattice fringes, interplanar spacing, crystallinity, crystal orientation, defects, and grain boundaries. The measured lattice spacing can be compared with XRD results to assign specific crystal planes and confirm the local crystal structure.

1.4.2.3 Bond Cleavage and Formation

Bond cleavage and formation are closely related to precursor conversion, cluster growth, ligand coordination, and structural transformation. Raman and FTIR spectroscopy are useful tools for probing vibrational modes and chemical bonding.

Raman spectroscopy is sensitive to changes in polarizability, while FTIR spectroscopy is sensitive to changes in dipole moment. Therefore, the two methods provide complementary information about molecular vibrations, metal–halide bonding, ligand binding, and lattice distortion.

The vibrational frequency of a chemical bond can be approximated by the harmonic oscillator model:

$$\nu = \frac{1}{2\pi c}\sqrt{\frac{k}{\mu}} \tag{1-8}$$

where ν is the vibrational wavenumber, c is the speed of light, k is the bond force constant, and μ is the reduced mass:

$$\mu = \frac{m_1 m_2}{m_1 + m_2} \tag{1-9}$$

where m_1 and m_2 are the masses of the two atoms involved in the vibration.

A stronger bond usually has a larger force constant and therefore appears at a higher vibrational frequency. In contrast, heavier atoms or weakened bonds generally lead to lower-frequency vibrational modes. In metal halide clusters and QDs, low-

frequency Raman modes are particularly useful for probing metal–halide lattice vibrations, octahedral distortion, and symmetry changes.

1.4.2.4 Chemical Composition, electronic state and chemical environment

Chemical composition, electronic state, and local chemical environment are critical for understanding the formation and properties of MCs, MSCs, and QDs. X-ray Photoelectron Spectroscopy (XPS), X-ray Absorption Spectroscopy (XAS), and Energy-Dispersive X-ray Spectroscopy (EDS) are commonly used for this purpose. XPS is mainly used to confirm elemental composition and chemical states, such as oxidation state and surface bonding environment. XAS provides element-specific information about electronic state, coordination geometry, local bond distance, and structural disorder. EDS is used to determine elemental composition at the surface and in depth, from hundreds of nanometers to several micrometers, especially for inorganic elements, and is commonly combined with SEM or TEM.

XPS is used to confirm elemental composition and chemical states, including oxidation states and bonding environments. Peak shifts in XPS can reflect changes in oxidation state, local coordination, charge transfer, and surface chemical environment. For example, a higher binding energy may indicate a more positively charged chemical environment.

XAS provides information about electronic state and local structure. X-ray absorption near-edge structure (XANES) is sensitive to oxidation state and coordination symmetry, while extended X-ray absorption fine structure (EXAFS) provides information about bond distances, coordination numbers, and local disorder.

EDS is used to determine elemental composition, especially for heavier

elements in inorganic nanomaterials. It is often coupled with SEM or TEM. However, for nanoscale materials, EDS results should be interpreted carefully because the measured signal can include contributions from the substrate, ligands, or surrounding matrix.

Together, these methods provide complementary information. XPS reveals surface composition and oxidation state, XAS probes local electronic and coordination structure, and EDS confirms elemental distribution and approximate composition.

1.4.3 Exciton Dynamics

Exciton dynamics describe how photoexcited electrons and holes relax, recombine, or transfer after excitation. Time-resolved photoluminescence (TRPL) and transient absorption (TA) spectroscopy are widely used to investigate these processes.

In TRPL and TA, the PL decay is often fitted using exponential decay functions:

$$I(t) = \sum_{i=1}^{n} A_i \, e^{-t/\tau_i} \tag{1-10}$$

where $I(t)$ is the PL intensity at time t, A_i is the amplitude of the i-th decay component, and τ_i is the corresponding lifetime.

Another commonly used average lifetime is the intensity-weighted lifetime:

$$\tau_{avg} = \frac{\sum_i A_i \, \tau_i^2}{\sum_i A_i \, \tau_i} \tag{1-11}$$

Different lifetime components can be associated with different recombination

pathways, such as vibrational relaxation, band-edge radiative recombination, surface trapping, defect-assisted recombination, or energy transfer.

TA spectroscopy measures the change in optical density after photoexcitation. The signals usually contain contributions from ground-state bleaching (GSB), stimulated emission (SE), and excited-state absorption (ESA). GSB and SE usually give negative signals, while ESA usually gives positive signals. TA provides ultrafast information on carrier cooling, exciton formation, charge separation, trapping, recombination, and energy transfer processes.

1.4.4 Spin Dynamics

In semiconductor nanomaterials, spin relaxation may be influenced by spin–orbit coupling, electron–phonon scattering, structural distortion, surface defects, and electron–hole exchange interaction. For low-dimensional and nanoscale systems, quantum confinement and surface chemistry can also modify spin relaxation pathways. Spin dynamics describe the generation, relaxation, and recombination of spin-polarized carriers or excitons. In this dissertation, spin dynamics are investigated using spin-polarized transient absorption with selective circularly polarized light excitation.

Circularly polarized light can selectively excite spin-polarized electronic transitions according to optical selection rules. The spin polarization degree can be defined as:

$$P = \frac{I_{\sigma^+} - I_{\sigma^-}}{I_{\sigma^+} + I_{\sigma^-}} \tag{1-12}$$

where I_{σ^+} and I_{σ^-} are the signals measured under right- and left-circularly polarized light configurations.

The decay of spin polarization can often be described by:

$$P(t) = P_0 e^{-t/\tau_s} \tag{1-13}$$

where P_0 is the initial spin polarization and τ_s is the spin relaxation lifetime.

The spin decay can be fitted using exponential decay functions same as TA and TRPL.

1.5 Common Characterization Methods

In this dissertation, a combination of optical spectroscopy, structural characterization, chemical analysis, and time-resolved spectroscopy was used to investigate ultra-small clusters, molecular clusters (MCs), magic-sized clusters (MSCs), and quantum dots (QDs). Each characterization method provides different but complementary information. In the following sections, each technique is introduced from three aspects: its purpose, its working principle, and the basic instrument configuration and optical path. Notes are also provided for practical measurements.

1.5.1 Ultraviolet-Visible (UV-Vis) Absorption

Purpose

Ultraviolet–visible (UV-Vis) absorption spectroscopy is used to investigate the

optical absorption properties and electronic transitions of NCs. It provides information about absorption edges, excitonic absorption peaks, optical band gaps, and size-dependent quantum confinement effects.

For QDs, the absorption edge and excitonic peak positions are strongly related to particle size. A blue shift of the absorption feature usually indicates a smaller particle size or stronger quantum confinement. For MSCs, sharp and discrete absorption peaks often indicate a highly uniform cluster size and well-defined electronic structure.

Principle

UV–Vis absorption measures how much incident light is absorbed by a sample as a function of wavelength or photon energy. When incident light passes through the sample, part of the light is absorbed due to electronic transitions, and the transmitted light is collected by the detector.

The transmittance is defined as:

$$T = \frac{I_t}{I_0} \tag{1-14}$$

where I_0 is the incident light intensity and I_t is the transmitted light intensity.

The absorbance–transmittance relationship, the Beer–Lambert law, and the Tauc relation have been introduced in Section 1.4 (Key Parameters) and will not be discussed further here.

Instrument Structure and Optical Path

A typical UV–Vis absorption spectrometer consists of a light source,

monochromator, sample holder, reference path or reference measurement, detector, and data acquisition system.

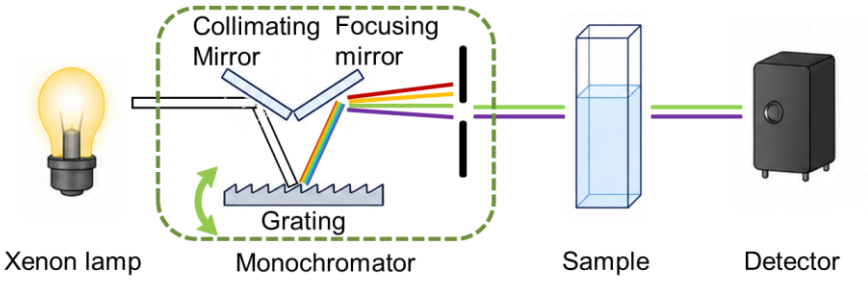

Figure 1-6 The schematic diagram of the UV-Vis absorption spectrometer optical path.

In the instrument structure diagram shown in Figure 1-6, the light first comes from a broadband light source, such as a deuterium lamp for the UV region and a tungsten-halogen lamp for the visible region. The light then enters the monochromator, where a prism or diffraction grating separates the light into different wavelengths. A selected wavelength passes through the exit slit and reaches the sample.

After passing through the sample, the transmitted light is collected by the detector. The spectrometer compares the transmitted intensity with the incident or reference intensity and converts the signal into absorbance. Therefore, the optical path can be described as:

Light source → monochromator → slit → sample → detector → computer.

The monochromator and slit are important because they control the selected wavelength and spectral resolution. The sample holder keeps the cuvette or film in a fixed position, ensuring stable optical alignment during measurement.

Notes

- Sample absorbance should not be too high; generally $A < 1$ is preferred to avoid saturation and scattering artifacts.
- Use the same solvent as the blank/background reference.
- Avoid bubbles, dust, fingerprints, or precipitation in the cuvette.
- The cuvette should be placed in the same orientation for sample and reference measurements.
- For QDs and clusters, sample concentration should be carefully controlled to avoid reabsorption or aggregation.

1.5.2 Photoluminescence (PL) and Time-Resolved Photoluminescence (TRPL) Spectroscopy

Purpose

Photoluminescence spectroscopy is used to study radiative recombination processes in materials. It provides information about emission wavelength, emission intensity, Stokes shift, trap-state emission, self-trapped exciton emission, and photoluminescence quantum efficiency.

TRPL is used to study the emission lifetime and recombination dynamics. It can help distinguish different decay pathways, such as band-edge recombination, trap-assisted recombination, surface-related emission, and nonradiative relaxation.

Principle

After photoexcitation, electrons transition from the ground state to the excited state. Since the electron and hole form a bound state, a high-energy electron is not

stable. The energized electrons will relax to the ground state again on the nanosecond (ns) or picosecond (ps) timescale. During the relaxation process, the energy is released as a photon and collected by the detector, showing as PL spectra. In PL measurements, the sample is excited by a light source with energy higher than the optical band gap. Electrons are promoted from the ground state or valence band to excited states or the conduction band. After energy relaxation, electrons recombine with holes and emit photons.

TRPL is used to investigate the temporal decay of emission. Using a time-correlated single-photon counting technique (TCSPC), the photon counts are recorded in a period of decay time. By fitting the photon decay curve, the lifetime can be extracted using single-, double-, triple-, or higher-order exponential functions, depending on the relaxation pathways in the materials.

The Stokes shift, photoluminescence quantum yield, exponential decay fitting functions, average lifetime, and radiative/nonradiative recombination rate have been introduced in Section 1.4 (Key Parameters) and will not be discussed further here.

Instrument Structure and Optical Path

A typical PL spectrometer consists of an excitation light source, wavelength selector or laser, sample holder, collection optics, monochromator, detector, and computer.

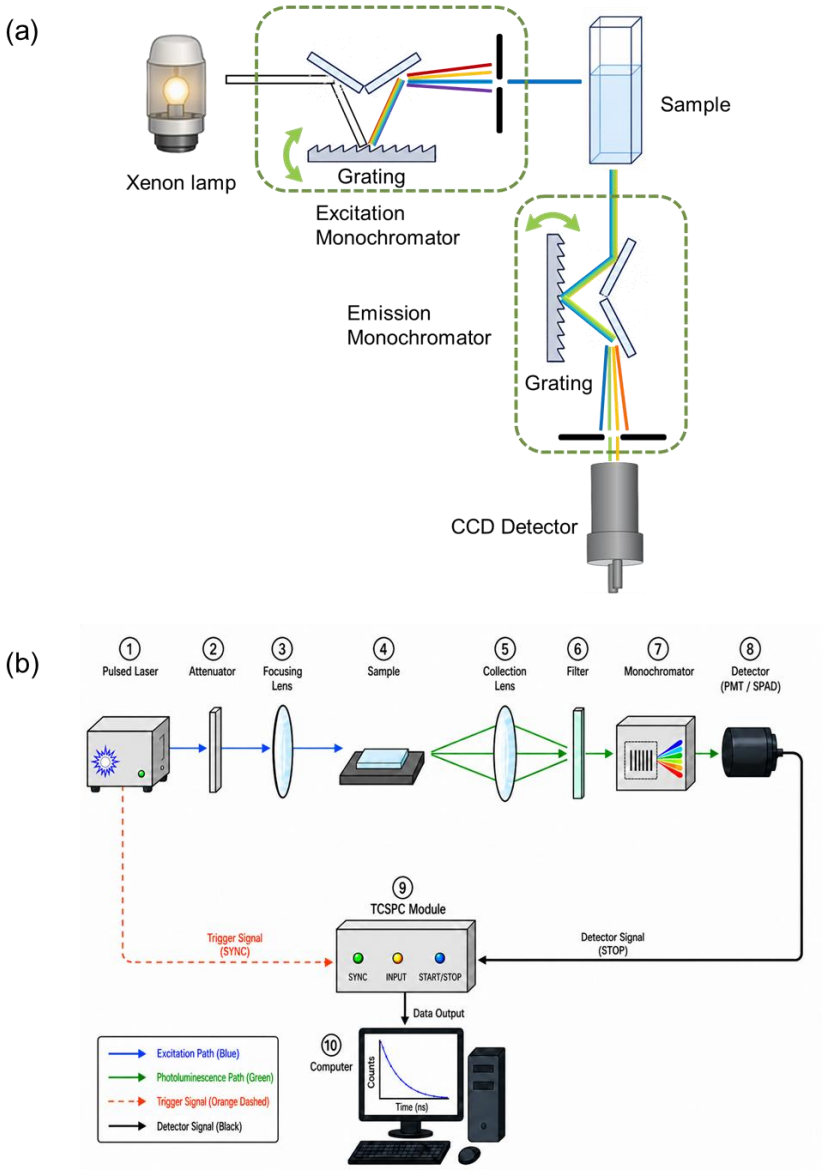

Figure 1-7 The schematic diagrams of the (a) PL and (b) TRPL spectrometer structure.

As illustrated in Figure 1-7, the excitation light first reaches the sample in the PL optical path. The sample absorbs the excitation light and emits photoluminescence. The emitted light is usually collected at a 90° angle relative to the excitation beam to reduce the influence of scattered excitation light. The emission then enters a

monochromator or spectrograph, where different emission wavelengths are separated and finally collected by a detector.

The general PL optical path is:

Excitation source → excitation monochromator/filter → sample → collection lens → emission monochromator/spectrograph → detector → computer.

For TRPL, a pulsed laser is used as the excitation source. The emitted photons are collected by the detector and analyzed by time-correlated single-photon counting. The instrument records the arrival time of emitted photons relative to the excitation pulse, generating a decay curve.

The TRPL optical path can be described as:

Pulsed laser → attenuator → focusing lens → sample → collection lens → filter → monochromator → detector → TCSPC → computer.

Important components include the pulsed excitation source, detector response time, timing electronics, and filters used to remove scattered excitation light.

Notes

- The excitation wavelength should be properly selected to excite the sample without causing strong scattering or degradation.
- Laser or lamp intensity should be controlled to avoid photobleaching, heating, or nonlinear effects.
- Use suitable filters to remove scattered excitation light.

- For PL, avoid overly concentrated samples because reabsorption and inner-filter effects can distort the emission spectrum.
- For TRPL, the instrument response function should be considered, especially for fast decay components.
- The fitting model should be chosen carefully; multiple exponential components should have physical meanings.

1.5.3 Powder X-Ray Diffraction (pXRD) and Single Crystal X-Ray Diffraction (scXRD)

Purpose

Powder X-ray diffraction (pXRD) is used to identify crystal phase, crystallinity, lattice structure, and crystallite size. For QDs and MSCs, pXRD can confirm whether the sample has a perovskite-related phase, a low-dimensional phase, or an impurity phase.

Single-crystal X-ray diffraction (scXRD) and powder X-ray diffraction (pXRD) share the same fundamental diffraction principle, both relying on Bragg's law. However, scXRD measures diffraction from an individual crystal with a well-defined orientation, generating three-dimensional crystallographic information of unit cell, space group, atomic positions, bond lengths, and bond angles.

Principle

XRD is based on constructive interference between X-rays scattered by periodic atomic planes in a crystal. The diffraction condition is described by Bragg's law:

$$n\lambda = 2d\sin\ \theta \tag{1-15}$$

where n is the diffraction order, λ is the X-ray wavelength, d is the interplanar spacing, and θ is the diffraction angle.

Instrument Structure and X-Ray Path

A typical XRD instrument consists of an X-ray source, incident slit, sample stage, receiving slit, monochromator or filter, detector, and goniometer.

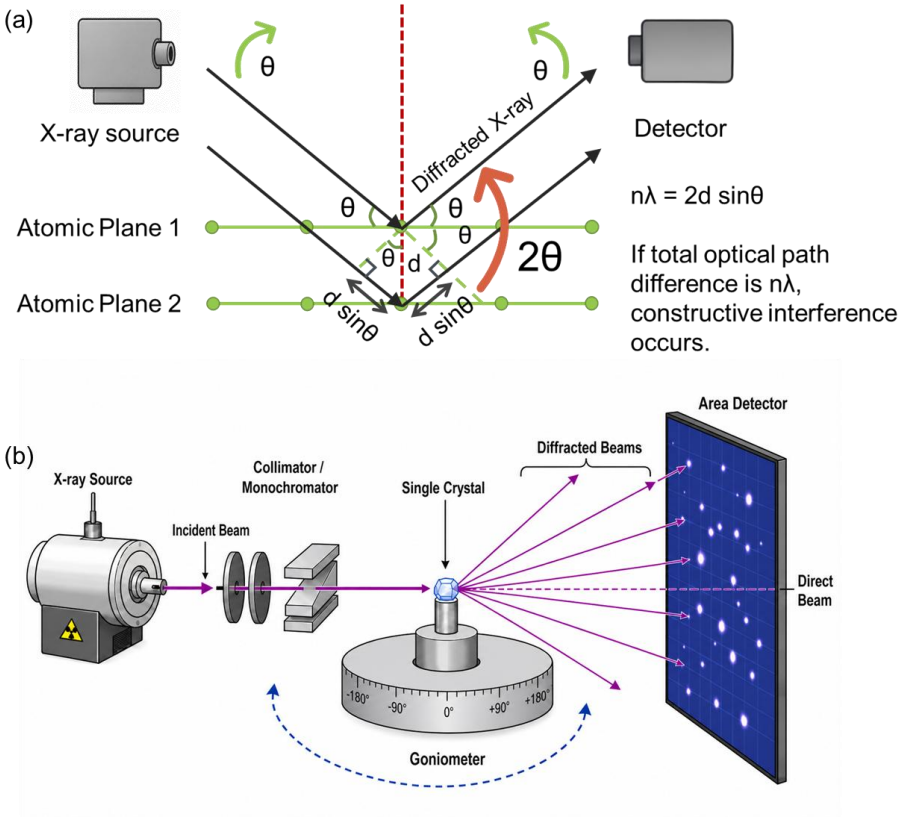

Figure 1-8 Schematic diagrams of (a) powder XRD based on Bragg's law and (b) single-crystal XRD setup.

The X-ray source generates X-rays, commonly using a Cu target. As shown in

Figure 1-8, the X-ray beam is collimated by slits and directed onto the sample. When the X-rays interact with crystalline planes, diffracted beams are generated at specific angles. The detector moves around the sample to collect the diffracted intensity as a function of 2θ.

The general XRD path is:

X-ray tube → incident slit/collimator → sample → diffracted beam → receiving slit → detector → computer.

The goniometer controls the angle between the incident beam, sample, and detector. The slits control beam divergence and resolution. The detector records diffraction intensity, and the resulting pattern is used for phase identification and structural analysis.

For single-crystal XRD, the sample is a single crystal mounted on a goniometer. The crystal is rotated during measurement so that diffraction data from many orientations can be collected and used to solve the three-dimensional crystal structure.

Notes

- The sample should be uniform, dry, and well distributed on the holder.
- Preferred orientation should be minimized, especially for plate-like or needle-like crystals.
- Air- or moisture-sensitive samples should be protected during loading and measurement.
- For nanocrystals, broad peaks are expected and should not be immediately interpreted as poor crystallinity.

- For scXRD, high-quality single crystals without cracks, twinning, or multiple domains are required.
- Beam damage should be considered for soft, organic-rich, or halide-containing materials.

1.5.4 Scanning Electron Microscopy (SEM) and Energy Dispersive Spectroscopy (EDS)

Purpose

SEM is used to observe surface morphology, particle aggregation, film morphology, and micro-scale structural features. For QDs and cluster-derived materials, SEM can reveal particle packing, film uniformity, surface roughness, and larger-scale morphology.

EDS is used to analyze the elemental composition of selected regions and confirm the presence and relative ratios of inorganic elements such as metals and halides. The signal comes from characteristic X-rays generated within the electron-beam interaction volume, which may extend from hundreds of nanometers (nm) to several micrometers (μm), depending on the measurement conditions, accelerating voltage, material density, atomic number, and sample geometry.

Principle

In SEM, electrons are accelerated by a high voltage and focused into a fine electron beam. The accelerating voltage determines the kinetic energy of the incident electrons:

$$E_k = eV \tag{1-16}$$

where E_k is the kinetic energy of the electron, e is the elementary charge, and V is the accelerating voltage.

The electron wavelength is related to the accelerating voltage. Without relativistic correction, the de Broglie wavelength of an accelerated electron can be approximated by:

$$\lambda = \frac{h}{\sqrt{2m_e eV}} \tag{1-17}$$

where λ is the electron wavelength, h is Planck's constant, m_e is the electron mass, e is the elementary charge, and V is the accelerating voltage.

A higher accelerating voltage gives a shorter electron wavelength, which is beneficial for high-resolution imaging. However, in SEM, the practical resolution also depends strongly on beam size, lens aberration, sample charging, electron scattering, and detector configuration.

Instrument Structure and Electron/X-Ray Path

A typical SEM consists of an electron gun, condenser lenses, objective lens, scanning coils, sample chamber, detectors, and vacuum system.

(a)

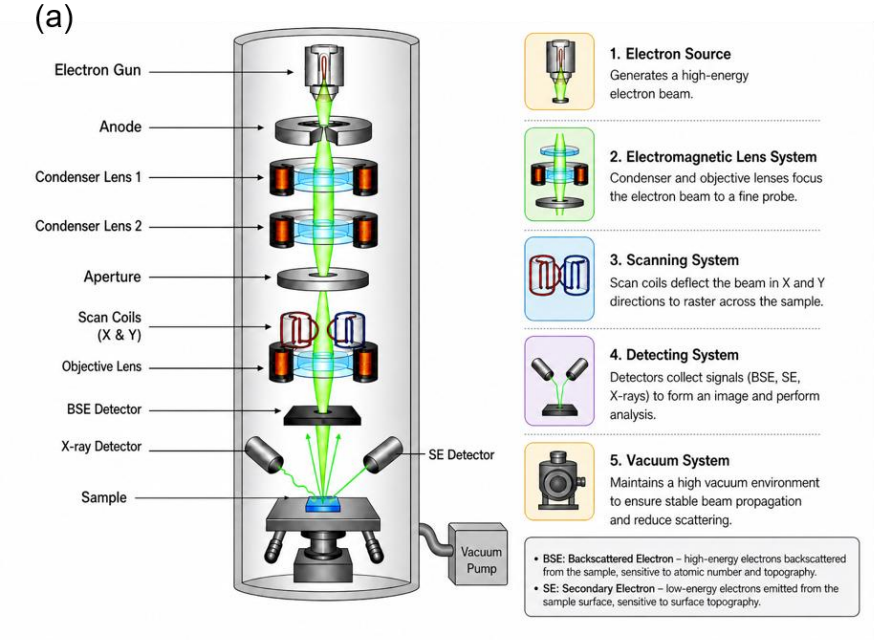
Electron Gun
Anode
Condenser Lens 1
Condenser Lens 2
Aperture
Scan Coils (X & Y)
Objective Lens
BSE Detector
X-ray Detector
Sample
SE Detector
Vacuum Pump
1. Electron Source
Generates a high-energy electron beam.
2. Electromagnetic Lens System
Condenser and objective lenses focus the electron beam to a fine probe.
3. Scanning System
Scan coils deflect the beam in X and Y directions to raster across the sample.
4. Detecting System
Detectors collect signals (BSE, SE, X-rays) to form an image and perform analysis.
5. Vacuum System
Maintains a high vacuum environment to ensure stable beam propagation and reduce scattering.
• BSE: Backscattered Electron – high-energy electrons backscattered from the sample, sensitive to atomic number and topography.
• SE: Secondary Electron – low-energy electrons emitted from the sample surface, sensitive to surface topography.

(b)

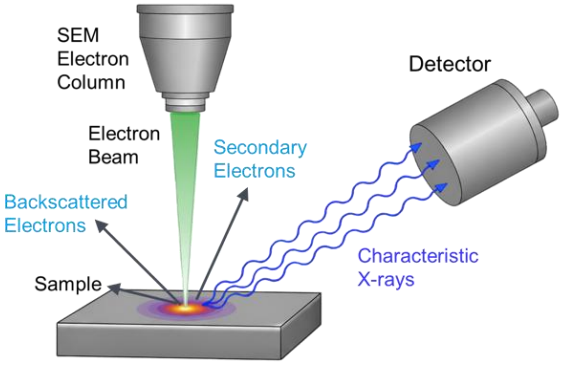
SEM Electron Column
Detector
Electron Beam
Secondary Electrons
Backscattered Electrons
Characteristic X-rays
Sample

(c)

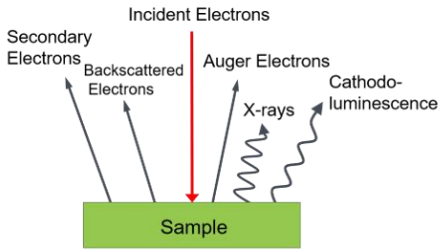
Incident Electrons
Secondary Electrons
Backscattered Electrons
Auger Electrons
Cathodo-luminescence
X-rays
Sample

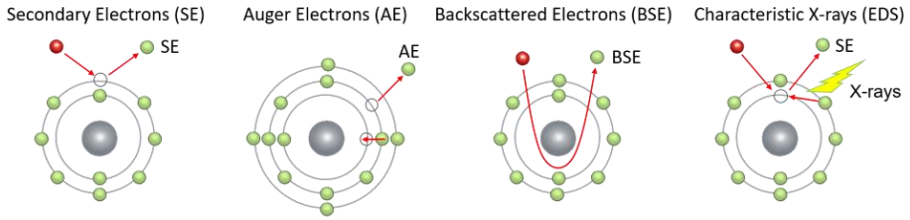
Secondary Electrons (SE)
SE
Auger Electrons (AE)
AE
Backscattered Electrons (BSE)
BSE
Characteristic X-rays (EDS)
SE
X-rays

Figure 1-9 The schematic diagram of the (a) SEM, (b) EDS spectroscopy and the illustration of electrons and sample interaction. EDS.

As illustrated in Figure 1-9 (a), the electron beam is generated by the electron gun and accelerated toward the sample. The condenser and objective lenses focus the beam into a small spot. Scanning coils move the beam across the sample surface point by point. The generated secondary electrons or backscattered electrons are collected by corresponding detectors to form images.

The SEM electron path is:

Electron gun → condenser lens → scanning coils → objective lens → sample → electron detector → image.

For EDS, the characteristic X-rays emitted from the sample are collected by an EDS detector positioned near the sample.

The EDS signal path is:

Electron beam → sample → characteristic X-rays → EDS detector → elemental spectrum/map.

In the SEM, a focused electron beam scans across the sample surface. The interaction between the electron beam and sample produces several signals, including secondary electrons, backscattered electrons, and characteristic X-rays.

Secondary electrons are mainly used for surface morphology imaging. Backscattered electrons provide contrast based on atomic number, with heavier elements usually appearing brighter.

EDS is based on characteristic X-ray emission. When the incident electron beam

removes an inner-shell electron from an atom, an outer-shell electron fills the vacancy and releases energy as an X-ray photon. The energy of this X-ray photon is characteristic of the element.

Notes

- The sample must be stable under vacuum and electron-beam irradiation.
- Nonconductive samples may require conductive coating or low-voltage imaging to reduce charging.
- The accelerating voltage should be selected carefully because it affects resolution, penetration depth, and EDS interaction volume.
- Avoid contamination from the substrate, carbon tape, or sample holder during elemental analysis.
- Beam-sensitive samples should be measured with low dose and short acquisition time.

1.5.5 Transmission Electron Microscopy (TEM) and High-Resolution Transmission Electron Microscopy (HRTEM)

Purpose

TEM is used to directly observe the size, shape, dispersion, and aggregation state of nanomaterials. It is especially important for QDs because individual particles can be imaged directly.

HRTEM provides lattice-resolved information, including lattice fringes, interplanar spacing, crystallinity, crystal orientation, defects, grain boundaries, and local structural disorder. It can help confirm the local crystal structure of QDs and

crystalline clusters.

Principle

In the TEM, a high-energy electron beam passes through a thin sample. The transmitted electrons are used to form an image. The contrast arises from electron scattering, which depends on sample thickness, density, atomic number, and crystallinity. Because TEM uses high accelerating voltages, relativistic correction is often needed. The relativistically corrected electron wavelength can be expressed as:

$$\lambda = \frac{h}{\sqrt{2m_e eV\left(1+\frac{eV}{2m_e c^2}\right)}} \tag{1-18}$$

Where λ is the electron wavelength, h is Planck's constant, m_e is the electron mass, e is the elementary charge, V is the accelerating voltage and c is the speed of light.

A higher accelerating voltage gives electrons a shorter wavelength and stronger penetration ability. This is important for TEM and HRTEM because the electron beam must pass through the sample. Shorter electron wavelength also contributes to higher theoretical spatial resolution.

However, higher voltage may also cause beam damage, especially for soft, organic-rich, or halide-containing materials. Therefore, the accelerating voltage should be selected carefully according to the sample stability.

FFT analysis of HRTEM images can provide reciprocal-space information. Ordered spots usually indicate a single-crystalline domain, while ring-like patterns

may indicate polycrystallinity or randomly oriented nanocrystals.

Instrument Structure and Electron Path

A typical TEM consists of an electron gun, condenser lens system, sample holder, objective lens, intermediate lens, projector lens, fluorescent screen or camera, and vacuum system.

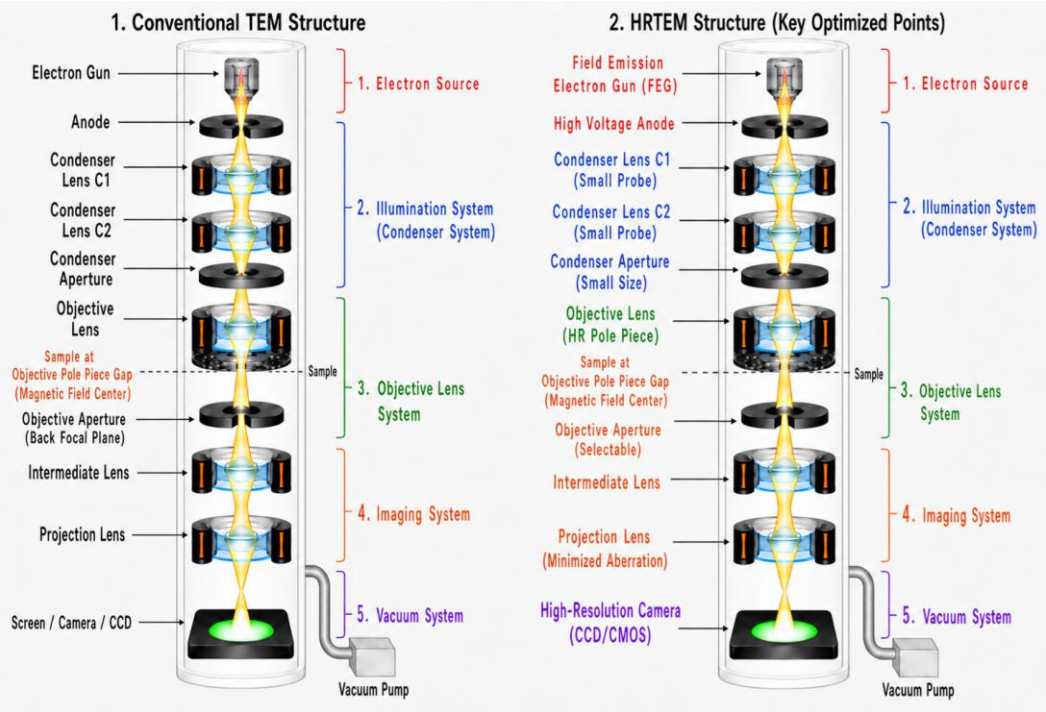

Figure 1-10 Schematic diagrams comparing (1) a conventional TEM column and (2) an HRTEM column, highlighting the difference in electron source, illumination system, objective lens system, imaging system, and vacuum system.

As shown in Figure 1-10, the electron beam is generated at the top of the column and accelerated through the microscope. The condenser lenses focus the beam onto a thin sample. Electrons transmitted through the sample are collected and magnified by the objective, intermediate, and projector lenses. The final image is

recorded by a camera.

The TEM electron path is:

Electron gun → condenser lenses → thin sample → objective lens → intermediate/projector lenses → camera.

For HRTEM, high spatial resolution and stable electron optics are required. The sample must be thin enough for electron transmission. For MCs and MSCs, electron-beam damage can be significant, so low-dose imaging and careful interpretation are often necessary.

For TEM analysis, the specimen should generally be electron-transparent, with a typical thickness below 100 nm. For HRTEM imaging, a thinner region is required, usually in 10–30 nm, to reduce multiple scattering and obtain clear lattice fringes.

Conventional TEM and HRTEM share similar column structures, including the electron source, condenser system, objective lens, imaging lenses, camera/screen, and vacuum system. HRTEM differs mainly by using optimized components, such as a field-emission gun, smaller probe/aperture, high-resolution objective pole piece, better aberration control, and high-resolution camera, which improve beam coherence and spatial resolution. Switching from TEM to HRTEM only involves adjusting operating conditions, not replacing major components, since the high-resolution parts are integrated inside. TEM contrast is mainly amplitude-based from electron scattering, whereas HRTEM relies more on phase contrast from interference of transmitted electron waves.

Notes

- The sample should be thin and well dispersed on the TEM grid.
- Aggregation should be minimized to allow accurate size and morphology analysis, thus sonication may be needed.
- Beam damage is a major concern for MCs, MSCs, and halide QDs.
- Low-dose imaging is recommended for sensitive samples.
- HRTEM lattice fringes should be interpreted carefully and compared with XRD or FFT results.
- The absence of clear lattice fringes does not necessarily mean the material is amorphous, especially for very small or beam-sensitive clusters.

1.5.6 Fourier Transform Infrared (FTIR) Spectroscopy

Purpose

FTIR spectroscopy is used to identify functional groups, ligand molecules, surface coordination, and bond formation or cleavage. For MCs, MSCs, and QDs, FTIR is especially useful for studying organic ligands and their interaction with the inorganic core or cluster surface.

The FTIR spectrum is commonly divided into the functional-group region and the fingerprint region. The functional-group region, typically >1500 cm^{-1}, contains characteristic vibrations such as O-H, N-H, C-H, and C=O stretching. The fingerprint region, usually in 1500-500 cm^{-1}, contains complex stretching, bending, and skeletal vibrations.

Principle

IR absorption occurs when molecular vibrations are accompanied by a change in

dipole moment. Therefore, FTIR is particularly sensitive to polar bonds and functional groups and metal–halide-related vibrations in asymmetric coordination environments. A vibration is IR active when:

$$\left(\frac{\partial \mu}{\partial Q}\right) \neq 0 \tag{1-19}$$

where μ is the dipole moment and Q is the vibrational normal coordinate.

Instrument Structure and Optical Path

A typical FTIR spectrometer consists of an IR source, interferometer, beam splitter, fixed mirror, moving mirror, sample holder, detector, and computer.

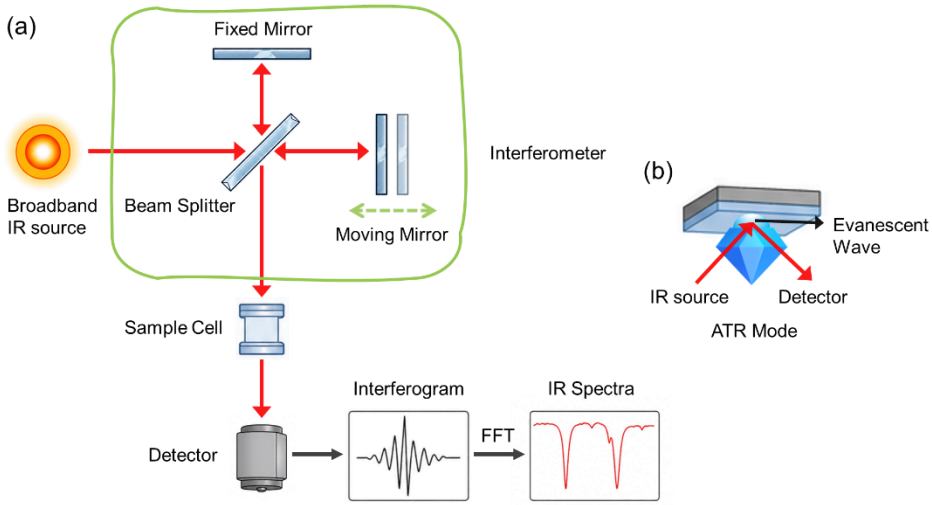

Figure 1-11 The schematic diagrams of the (a) transmission mode and (b) attenuated total reflectance (ATR) mode in the FTIR spectrometer.

As exhibited in Figure 1-11, the IR source emits broadband infrared light. The beam enters a Michelson interferometer, where it is split into two beams by a beam splitter. One beam travels to a fixed mirror, and the other travels to a moving mirror. The two beams recombine and generate an interferogram. The recombined beam then

passes through the sample and reaches the detector.

The FTIR optical path is:

IR source → beam splitter → fixed mirror/moving mirror → recombined beam → sample → detector → Fourier transform → IR spectrum.

The interferometer is the key component of FTIR. Instead of measuring one wavelength at a time, FTIR records an interferogram containing all infrared frequencies and converts it into a spectrum using Fourier transform.

Notes

- The background spectrum should be collected under the same conditions as the sample.
- Samples should be dry because water strongly absorbs in the IR region.
- For ATR-FTIR, good contact between the sample and ATR crystal is important.
- Peak assignments should consider contributions from ligands, solvent residues, and impurities.
- For ligand-capped QDs or clusters, weak inorganic vibrations may be hidden by strong organic ligand peaks.

1.5.7 Raman Spectroscopy

Purpose

Raman spectroscopy is used to study vibrational modes, lattice vibrations, metal–halide bonding, structural distortion, phase changes, and symmetry changes. For inorganic clusters and QDs, low-frequency Raman modes can provide information about metal–halide framework vibrations, octahedral distortion, and

phonon behavior.

Raman is complementary to FTIR. Some vibrations that are weak or inactive in IR may be strong in Raman, depending on molecular symmetry and selection rules.

Principle

Raman scattering occurs when incident photons interact with molecular vibrations or lattice phonons and are inelastically scattered. Most scattered photons have the same energy as the incident light, which is called Rayleigh scattering. A small fraction of photons exchange energy with vibrational modes, producing Raman scattering.

Raman activity requires a change in polarizability during molecular or lattice vibrations. Thus, Raman spectroscopy is sensitive to non-polar and symmetric vibrational units with highly deformable electron clouds, including C=C, C≡C, S-S, M-M bonds, and C-O-C units. It is also sensitive to metal–halide bonds, such as Pb-I, Pb-Br, Ag-I, Bi-I, and Cu-I, because heavy atoms and soft ionic lattices generally exhibit large polarizability. Changes in the peak number, position, intensity, and linewidth often reflect lattice distortion, reduced symmetry, phase transitions, and electron–phonon coupling. A vibration is Raman active when:

$$\left(\frac{\partial \alpha}{\partial Q}\right) \neq 0 \tag{1-20}$$

where α is the polarizability and Q is the vibrational normal coordinate.

The Raman shift is defined as:

$$\Delta\nu = \frac{1}{\lambda_0} - \frac{1}{\lambda_s} \tag{1-21}$$

where λ_0 is the incident laser wavelength and λ_s is the scattered wavelength. The unit for wavelength here is centimeters (cm).

Instrument Structure and Optical Path

A typical Raman spectrometer consists of a laser source, laser filter, beam splitter or dichroic mirror, objective lens, sample stage, Rayleigh rejection filter, spectrograph, grating, CCD detector, and computer.

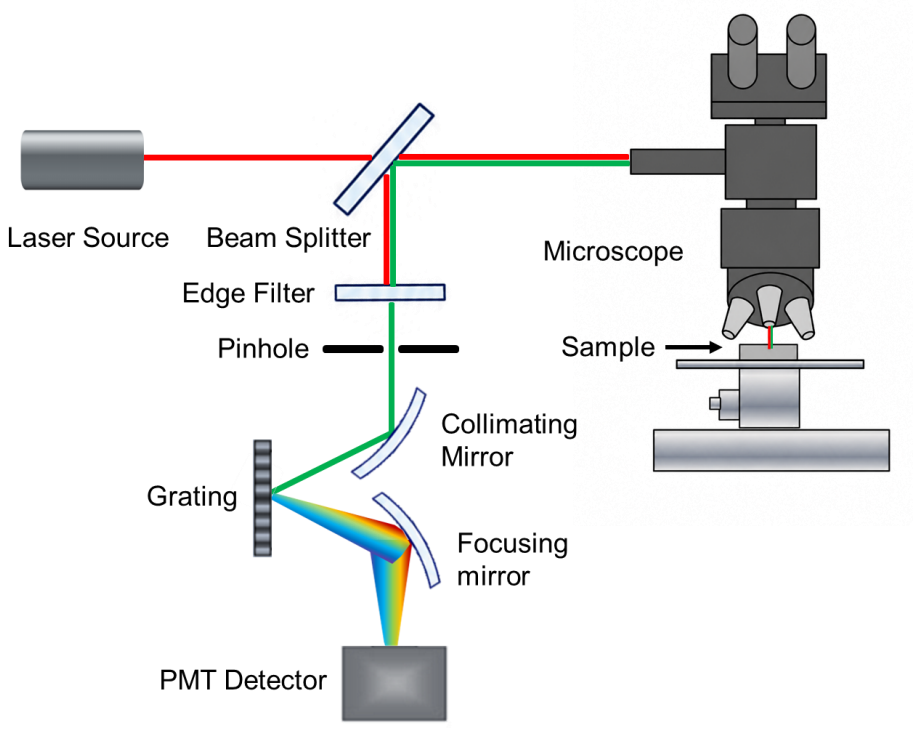

Figure 1-12 The schematic diagram of the Raman spectrometer equipped with a 785 nm laser source.

In Figure 1-12, the laser is focused onto the sample through the microscope's objective lens. The sample scatters the incident light. The scattered light is collected

by the same or another objective and directed into the spectrograph. Since Rayleigh scattering is much stronger than Raman scattering, edge or notch filters are used to remove the Rayleigh signal. The remaining Raman-scattered light is dispersed by a grating and collected by a CCD detector.

The Raman optical path is:

Laser → filter → objective lens → sample → collected scattered light → Rayleigh rejection filter → spectrograph/grating → CCD detector → Raman spectrum.

Important components include the laser source, objective lens, notch or edge filter, grating, and CCD detector. The laser wavelength and power must be chosen carefully because some nanomaterials, especially halide perovskites, can be sensitive to laser-induced heating or degradation.

Notes

- Laser power should be kept low enough to avoid heating, degradation, or phase transformation.
- The excitation wavelength should be selected carefully to reduce fluorescence background.
- Beam-sensitive halide materials require short exposure time and low laser power.
- Cosmic rays and fluorescence background should be checked during data processing.
- Low-frequency Raman measurements require appropriate filters and careful calibration.

- Peak shifts and linewidth changes should be interpreted together with structural and optical data.

1.5.8 Transient Absorption (TA)

Purpose

Transient absorption spectroscopy is used to study excited-state dynamics on ultrafast to long timescales. It provides information about carrier cooling, exciton formation, trapping, charge transfer, recombination, and energy transfer.

For MCs, MSCs, and QDs, TA is especially useful for studying how photoexcited carriers relax after excitation. It can distinguish ground-state bleaching, stimulated emission, and excited-state absorption.

Principle

TA is a pump–probe technique. A pump pulse first excites the sample, creating excited-state populations. A delayed probe pulse then measures the absorption change at different delay times.

The transient absorption signal is defined as:

$$\Delta A(\lambda, t) = A_{excited}(\lambda, t) - A_{ground}(\lambda) \tag{1-22}$$

The TA signal can be considered as a combination of different contributions:

$$\Delta A = \Delta A_{GSB} + \Delta A_{SE} + \Delta A_{ESA} \tag{1-23}$$

where GSB is ground-state bleaching, SE is stimulated emission, and ESA is excited-state absorption.

The decay kinetics fitting is the same as TRPL, but represents different relaxation or recombination processes.

Instrument Structure and Optical Path

A typical TA setup consists of an ultrafast laser source, beam splitter, pump path, probe path, delay stage, optical parametric amplifier or white-light generation system, sample holder, detector, and data acquisition system. In our lab, the fundamental beam is generated by the ytterbium-doped potassium gadolinium tungstate (Yb:KGW) lasing medium (PHAROS, Light Conversion), outputting horizontally linearly polarized light, with a frequency of 1030 nm at a power of 10 W, a repetition rate of 20 kHz and a pulse width of 159 fs.

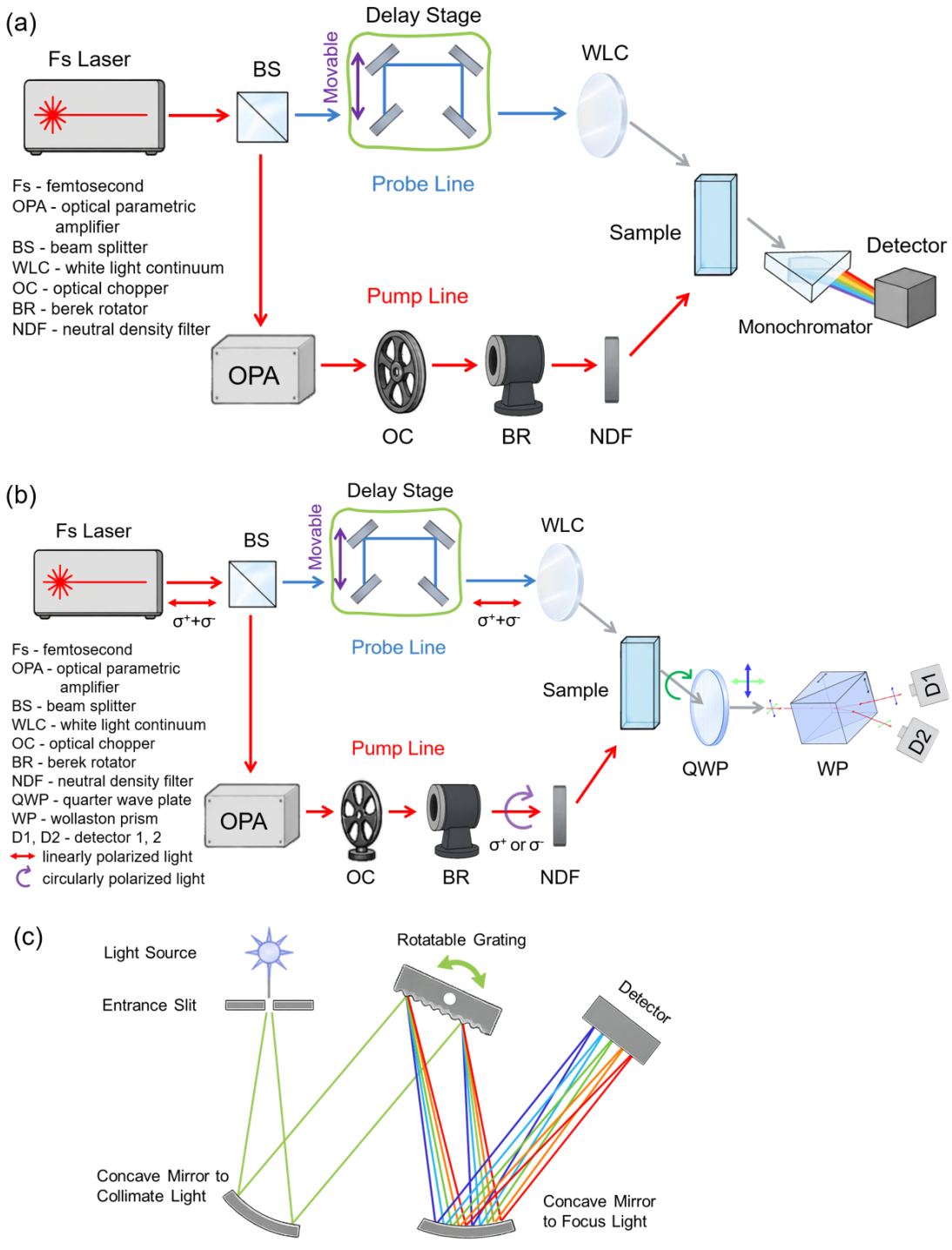

Figure 1-13 The schematic diagram of the (a) transient absorption (TA) and (b) spin polarization TA with a selective right circularly polarized (RCP) or left circularly

polarized (LCP) pump. (c) The layout and optical path in the monochromator in the femtosecond laser system. Figures need to change.

As displayed in Figure 1-13, the laser output is split into two beams. One beam is used as the pump to excite the sample. The other beam is used as the probe to monitor absorption changes. A mechanical delay stage changes the optical path length of the probe beam, controlling the delay time between pump and probe pulses. The target pump excitation wavelength is generated from the signal or idler output of the optical parametric amplifier (OPA) and subsequently frequency-doubled using a second harmonic generation (SHG) crystal. Either the signal or the idler output of the OPA can be selected by the wavelength selector for further use in the optical setup. An optical chopper is used to periodically block the pump beam, allowing the measurement of pump-induced absorption changes by comparing probe signals with and without excitation. In the normal TA measurements, the pump polarization was maintained at the target pump polarization at 0° using a wavelength-dependent Berek rotator. For each pump wavelength, the HARPIA software automatically adjusted the tilt and rotation angles of the Berek rotator to keep a consistent pump polarization condition. The Glan-Tyler prism, a linear polarizer, may be used to check the generated pure linear light. Neutral density filters were used to adjust the pump fluence.

For spin-polarized TA measurements, the Berek rotator was manually adjusted by tuning the tilt and rotation angles to generate circularly polarized pump light, which is also wavelength dependent. The polarization state was optimized until the

polarization visualization became as circular as possible, corresponding to left- or right-circularly polarized excitation (LCP/RCP). A Glan-Taylor prism is used to verify the generation of circularly polarized light. For an ideal circularly polarized beam, the transmitted intensity remains nearly unchanged as the prism is rotated. For the probe path, the angle of the quarter-wave plate is carefully adjusted to convert the linearly polarized probe beam into circularly polarized light, while the polarization state is monitored in real time using a motorized Glan-Taylor prism and the associated software to observe shape changes. The optimized quarter-wave plate is then positioned in the probe path after the sample for subsequent spin-resolved measurements.

Several optical components in the setup employ different crystalline materials according to their optical properties. The half-wave and quarter-wave plate are fabricated from birefringent quartz, which exhibits a relatively small birefringence ($\Delta n \approx 0.009$) and provides well-defined phase retardation for precise polarization control. In contrast, the Berek rotator is usually made of calcite, a crystal with significantly stronger birefringence ($\Delta n \approx 0.17$), nearly 20 times larger than that of quartz. This large birefringence enables continuously tunable retardance through adjustment of the crystal tilt and rotation angles, making the Berek rotator particularly suitable for wavelength-dependent polarization control in ultrafast spectroscopy experiments.

The white-light continuum (WLC) probe is generated by focusing femtosecond laser pulses into a sapphire crystal. Unlike quartz and calcite, which are primarily

used for birefringent polarization manipulation, sapphire serves as a nonlinear optical medium for broadband supercontinuum generation. Under intense femtosecond laser excitation, the refractive index of sapphire becomes intensity-dependent, $n = n_0 + n_2 I$. Since the laser pulse intensity varies with time, the refractive index also changes temporally, producing self-phase modulation (SPM). This time-dependent phase modulation broadens the spectrum of the incident pulse and generates a broadband white-light continuum. Additional nonlinear effects, such as self-focusing and four-wave mixing, can also contribute to spectral broadening. Sapphire is particularly well suited for this application because of its high optical damage threshold, excellent thermal stability, and wide transparency range.

The general TA optical path is:

Ultrafast laser → beam splitter → pump beam (90%) and probe beam (10%).

For the pump path:

Pump beam → wavelength conversion/OPA if needed → chopper → focusing optics → sample.

For the probe path:

Probe beam → delay stage → white-light generation or probe optics → sample → spectrograph/detector.

After the pump and probe overlap at the sample, the transmitted probe light is collected by the detector. By comparing the probe intensity with and without the pump, the transient absorption signal is obtained.

Notes

- Pump fluence should be optimized to avoid multi-exciton effects, sample degradation, or nonlinear artifacts.
- Pump and probe beams must be spatially and temporally overlapped.
- The sample should be stirred, flowed, or translated if it is sensitive to photodegradation.
- Solvent, substrate, and scattered pump signals should be checked using control measurements.
- White-light probe stability is important for good signal-to-noise ratio.
- Kinetic fitting should consider overlapping processes such as carrier cooling, trapping, recombination, and energy transfer.

1.5.9 X-ray Photoelectron Spectroscopy (XPS)

Purpose

XPS is used to analyze elemental composition, chemical states, oxidation states, and surface chemical environments. It is a surface-sensitive technique and usually probes the top few nanometers of the sample.

For MCs, MSCs, and QDs, XPS can confirm the presence of metal and halide elements, determine oxidation states, and reveal surface ligand coordination or surface oxidation. XPS typically has a probing depth of about 2–10 nm, while UV photoelectron spectroscopy (UPS) is shallower and more surface-sensitive, with a probing depth of approximately 1–5 nm due to the different photon energies used for excitation.

Principle

In XPS, incident X-rays eject core-level electrons from atoms in the sample. The kinetic energy of the emitted photoelectrons is measured by an electron energy analyzer. The binding energy is calculated using:

$$E_B = hv - E_K - \phi \tag{1-24}$$

where E_B is the binding energy, $hv$is the incident X-ray photon energy, E_K is the kinetic energy of the emitted photoelectron, and ϕ is the spectrometer work function.

Different elements have characteristic core-level binding energies. Chemical shifts in binding energy provide information about oxidation state and local chemical environment.

Instrument Structure and Electron Path

A typical XPS instrument consists of an X-ray source, sample stage, electron lens system, hemispherical analyzer, detector, and ultra-high-vacuum chamber.

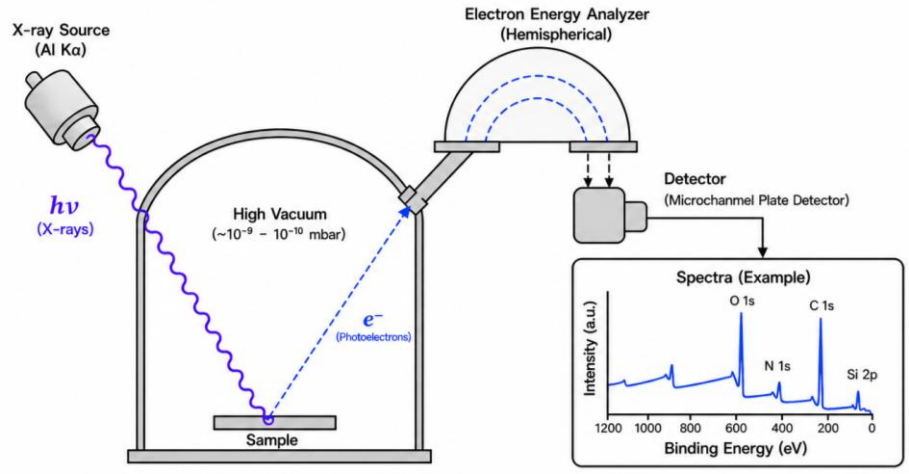

Figure 1-14 The schematic diagram of the XPS spectrometer layout.

In Figure 1-14, the X-ray source irradiates the sample surface. Photoelectrons are emitted from the top few nanometers of the sample. The emitted electrons are collected and focused by electron lenses, then enter the hemispherical analyzer. The analyzer separates electrons according to kinetic energy, and the detector records the electron intensity.

The XPS signal path is:

X-ray source → sample surface → emitted photoelectrons → electron lens → hemispherical analyzer → detector → XPS spectrum.

The ultra-high-vacuum environment is important because photoelectrons have low kinetic energy and can be easily scattered by gas molecules. Charge compensation may be required for insulating samples.

Notes

- The sample surface should be clean and free from excessive contamination.
- Air exposure should be minimized for oxidation- or moisture-sensitive samples.
- Charging effects should be corrected, often using charge compensation or reference peaks.
- Peak fitting should use reasonable constraints, including spin–orbit splitting, area ratios, and background selection.
- XPS is surface-sensitive, so the measured composition may differ from the bulk composition.
- Sputtering should be used carefully because it may damage soft materials or change oxidation states.

1.5.10 X-ray Absorption Spectroscopy (XAS)

Purpose

XAS is used to study the electronic state and local coordination environment of selected elements. It is especially useful for MCs, MSCs, and QDs because these materials may have weak long-range crystallinity but still possess important local structural order.

XAS can provide information about oxidation state, coordination number, bond distance, local symmetry, and structural disorder. It is complementary to XRD and XPS.

Principle

XAS measures the absorption of X-rays as a function of photon energy. When the incident X-ray energy matches the energy required to excite a core electron to an unoccupied state or continuum state, a sharp absorption edge appears.

XAS is usually divided into two regions:

XANES: X-ray absorption near edge structure. It is sensitive to oxidation state, electronic structure, and coordination geometry.

EXAFS: extended X-ray absorption fine structure. The spectrum provides information on local bond distance, coordination number, and disorder.

Instrument Structure and X-Ray Path

A typical XAS setup at a synchrotron beamline consists of a synchrotron X-ray source, monochromator, slits, sample holder, ion chamber or fluorescence detector, and data acquisition system.

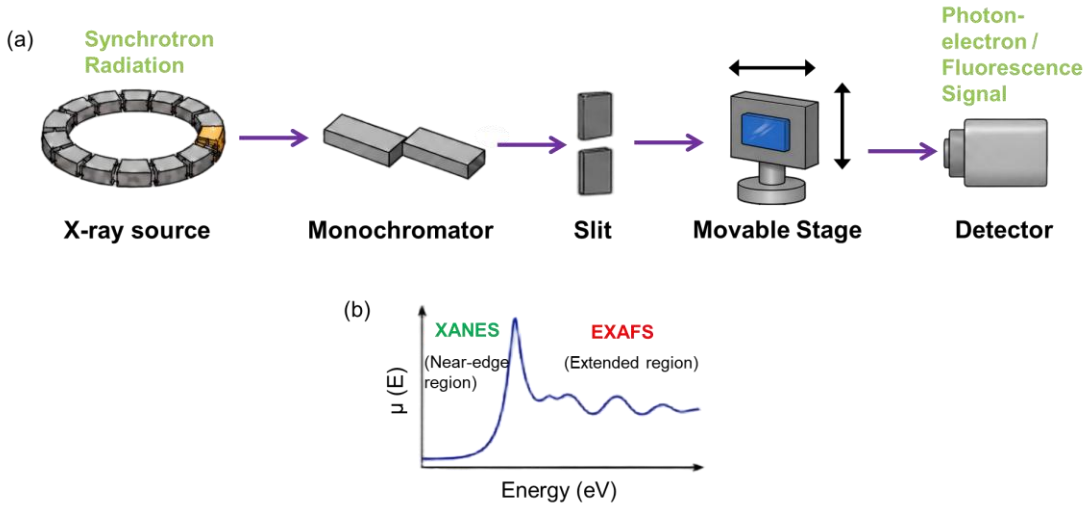

Figure 1-15 Schematic diagrams illustrating (a) the optical path of an X-ray absorption spectroscopy (XAS) beamline and (b) the XANES and EXAFS regions in a typical XAS spectrum.

In Figure 1-15, the broadband synchrotron X-ray beam first passes through a monochromator, which selects the desired photon energy. The monochromatic X-ray beam then passes through or interacts with the sample. Depending on the measurement mode, the absorption signal can be collected in transmission mode, fluorescence mode, or total electron yield mode.

The general XAS path is:

Synchrotron X-ray source → monochromator → slit/focusing optics → sample → detector → XAS spectrum.

In transmission mode, ion chambers measure the incident and transmitted X-ray intensities. In fluorescence mode, fluorescence photons emitted from the sample are collected by a fluorescence detector. Fluorescence mode is especially useful for dilute samples or thin films.

Notes

- The correct absorption edge and energy range should be selected for the target element.
- Reference compounds should be measured or used for oxidation-state comparison.
- Sample thickness should be optimized to avoid over-absorption in transmission mode.
- Fluorescence mode is preferred for dilute samples or thin films.
- Radiation damage should be monitored, especially for halide and organic-containing materials.
- EXAFS fitting should use physically reasonable coordination numbers, bond distances, and disorder parameters.

1.6 References

(1) Joudeh, N.; Linke, D. Nanoparticle Classification, Physicochemical Properties, Characterization, and Applications: A Comprehensive Review for Biologists. *J. Nanobiotechnol.* **2022**, *20*, 262. https://doi.org/10.1186/s12951-022-01477-8.

(2) Baig, N.; Kammakakam, I.; Falath, W. Nanomaterials: A Review of Synthesis Methods, Properties, Recent Progress, and Challenges. *Mater. Adv.* **2021**, *2* (6), 1821–1871. https://doi.org/10.1039/D0MA00807A.

(3) Mekuye, B.; Abera, B. Nanomaterials: An Overview of Synthesis, Classification, Characterization, and Applications. *Nano Sel.* **2023**, *4* (8), 486–501. https://doi.org/10.1002/nano.202300038.

(4) Alivisatos, A. P. Semiconductor Clusters, Nanocrystals, and Quantum Dots. *Science* **1996**, *271* (5251), 933–937. https://doi.org/10.1126/science.271.5251.933.

(5) Li, Q.; Wu, K.; Zhu, H.; Yang, Y.; He, S.; Lian, T. Charge Transfer from Quantum-Confined 0D, 1D, and 2D Nanocrystals. *Chem. Rev.* **2024**, *124* (9), 5695–5763. https://doi.org/10.1021/acs.chemrev.3c00742.

(6) Heatley, K. *The Next Quantum Revolution*. MIT Physics. https://physics.mit.edu/news/the-next-quantum-revolution/ (accessed 2026-05-02).

(7) Dowling, J. P.; Milburn, G. J. Quantum Technology: The Second Quantum Revolution. *Philos. Trans. R. Soc. Lond. Ser. Math. Phys. Eng. Sci.* **2003**, *361* (1809), 1655–1674. https://doi.org/10.1098/rsta.2003.1227.

(8) Harrington, P. M.; Mueller, E. J.; Murch, K. W. Engineered Dissipation for Quantum Information Science. *Nat. Rev. Phys.* **2022**, *4* (10), 660–671. https://doi.org/10.1038/s42254-022-00494-8.

(9) *Quantum Technologies | Stanford Emerging Technology Review*. https://setr.stanford.edu/technology/quantum-technologies/2026 (accessed 2026-05-02).

(10) *The Fourth Industrial Revolution: what it means and how to respond*. World Economic Forum. https://www.weforum.org/stories/2016/01/the-fourth-industrial-revolution-what-it-means-and-how-to-respond/ (accessed 2026-05-02).

(11) Boverhof, D. R.; Bramante, C. M.; Butala, J. H.; Clancy, S. F.; Lafranconi, M.; West, J.; Gordon, S. C. Comparative Assessment of Nanomaterial Definitions and Safety Evaluation Considerations. *Regul. Toxicol. Pharmacol.* **2015**, *73* (1), 137–150. https://doi.org/10.1016/j.yrtph.2015.06.001.

(12) Baalousha, M.; How, W.; Valsami-Jones, E.; Lead, J. R. Overview of Environmental Nanoscience. In *Frontiers of Nanoscience*; Lead, J. R., Valsami-Jones, E., Eds.; Elsevier, 2014; Vol. 7, pp 1–54. https://doi.org/10.1016/B978-0-08-099408-6.00001-3.

(13) Yu, P.; Cardona, M. *Fundamentals of Semiconductors: Physics and Materials Properties*; Springer, 1997; Vol. 1. https://doi.org/10.1007/b137661.

(14) Kittel, C. *Introduction to Solid State Physics*, 8th ed.; Wiley: Hoboken, NJ, 2005.

(15) Alivisatos, A. P. Perspectives on the Physical Chemistry of Semiconductor Nanocrystals. *J. Phys. Chem.* **1996**, *100* (31), 13226–13239. https://doi.org/10.1021/jp9535506.

(16) Panthani, M. G.; Korgel, B. A. Nanocrystals for Electronics. *Annu. Rev. Chem. Biomol. Eng.* **2012**, *3*, 287–311. https://doi.org/10.1146/annurev-chembioeng-062011-081040.

(17) Torimoto, T.; Kameyama, T.; Uematsu, T.; Kuwabata, S. Controlling Optical Properties and Electronic Energy Structure of I–III–VI Semiconductor Quantum Dots for Improving Their Photofunctions. *J. Photochem. Photobiol. C Photochem. Rev.* **2023**, *54*, 100569.

https://doi.org/10.1016/j.jphotochemrev.2022.100569.

(18) Kwon, Y.; Kim, S. Indium Phosphide Magic-Sized Clusters: Chemistry and Applications. *NPG Asia Mater.* **2021**, *13* (1), 37. https://doi.org/10.1038/s41427-021-00300-4.

(19) Xu, K.; Vickers, E. T.; Luo, B.; Allen, A. C.; Chen, E.; Roseman, G.; Wang, Q.; Kliger, D. S.; Millhauser, G. L.; Yang, W.; et al. First Synthesis of Mn-Doped Cesium Lead Bromide Perovskite Magic Sized Clusters at Room Temperature. *J. Phys. Chem. Lett.* **2020**, *11* (3), 1162–1169. https://doi.org/10.1021/acs.jpclett.9b03700.

(20) Vickers, E. T.; Chen, Z.; Cherrette, V.; Smart, T.; Zhang, P.; Ping, Y.; Zhang, J. Z. Interplay between Perovskite Magic-Sized Clusters and Amino Lead Halide Molecular Clusters. *Research* **2021**, *2021*, 6047971. https://doi.org/10.34133/2021/6047971.

(21) Busatto, S.; de Mello Donega, C. Magic-Size Semiconductor Nanostructures: Where Does the Magic Come From? *ACS Mater. Au* **2022**, *2* (3), 237–249. https://doi.org/10.1021/acsmaterialsau.1c00075.

(22) Shin, J.; Choi, M.; Kim, M.; Jeong, S. Semiconductor Clusters: Synthetic Precursors for Colloidal Quantum Dots. *Front. Nanotechnol.* **2022**, *4*, 1069178. https://doi.org/10.3389/fnano.2022.1069178.

(23) Brus, L. E. Electron–Electron and Electron-hole Interactions in Small Semiconductor Crystallites: The Size Dependence of the Lowest Excited Electronic State. *J. Chem. Phys.* **1984**, *80* (9), 4403–4409.

https://doi.org/10.1063/1.447218.

(24) García de Arquer, F. P.; Talapin, D. V.; Klimov, V. I.; Arakawa, Y.; Bayer, M.; Sargent, E. H. Semiconductor Quantum Dots: Technological Progress and Future Challenges. *Science* **2021**, *373* (6555), eaaz8541. https://doi.org/10.1126/science.aaz8541.

(25) Kagan, C. R.; Lifshitz, E.; Sargent, E. H.; Talapin, D. V. Building Devices from Colloidal Quantum Dots. *Science* **2016**, *353* (6302), aac5523. https://doi.org/10.1126/science.aac5523.

(26) Talapin, D. V.; Lee, J.-S.; Kovalenko, M. V.; Shevchenko, E. V. Prospects of Colloidal Nanocrystals for Electronic and Optoelectronic Applications. *Chem. Rev.* **2010**, *110* (1), 389–458. https://doi.org/10.1021/cr900137k.

(27) Protesescu, L.; Yakunin, S.; Bodnarchuk, M. I.; Krieg, F.; Caputo, R.; Hendon, C. H.; Yang, R. X.; Walsh, A.; Kovalenko, M. V. Nanocrystals of Cesium Lead Halide Perovskites ($CsPbX_3$, X = Cl, Br, and I): Novel Optoelectronic Materials Showing Bright Emission with Wide Color Gamut. *Nano Lett.* **2015**, *15* (6), 3692–3696. https://doi.org/10.1021/nl5048779.

(28) Dey, A.; Ye, J.; De, A.; Debroye, E.; Ha, S. K.; Bladt, E.; Kshirsagar, A. S.; Wang, Z.; Yin, J.; Wang, Y.; et al. State of the Art and Prospects for Halide Perovskite Nanocrystals. *ACS Nano* **2021**, *15* (7), 10775–10981. https://doi.org/10.1021/acsnano.0c08903.

(29) Wang, H.; Kim, D. H. Perovskite-Based Photodetectors: Materials and Devices. *Chem. Soc. Rev.* **2017**, *46* (17), 5204–5236.

https://doi.org/10.1039/C6CS00896H.

(30) Shellaiah, M.; Sun, K. W. Review on Sensing Applications of Perovskite Nanomaterials. *Chemosensors* **2020**, *8* (3), 55. https://doi.org/10.3390/chemosensors8030055.

(31) Murray, C. B.; Norris, D. J.; Bawendi, M. G. Synthesis and Characterization of Nearly Monodisperse CdE (E = Sulfur, Selenium, Tellurium) Semiconductor Nanocrystallites. *J. Am. Chem. Soc.* **1993**, *115* (19), 8706–8715. https://doi.org/10.1021/ja00072a025.

(32) Akkerman, Q. A.; Rainò, G.; Kovalenko, M. V.; Manna, L. Genesis, Challenges and Opportunities for Colloidal Lead Halide Perovskite Nanocrystals. *Nat. Mater.* **2018**, *17* (5), 394–405. https://doi.org/10.1038/s41563-018-0018-4.

(33) Saparov, B.; Mitzi, D. B. Organic–Inorganic Perovskites: Structural Versatility for Functional Materials Design. *Chem. Rev.* **2016**, *116* (7), 4558–4596. https://doi.org/10.1021/acs.chemrev.5b00715.

(34) Han, Y.; Yue, S.; Cui, B.-B. Low-Dimensional Metal Halide Perovskite Crystal Materials: Structure Strategies and Luminescence Applications. *Adv. Sci.* **2021**, *8* (15), 2004805. https://doi.org/10.1002/advs.202004805.

(35) Smith, M. D.; Connor, B. A.; Karunadasa, H. I. Tuning the Luminescence of Layered Halide Perovskites. *Chem. Rev.* **2019**, *119* (5), 3104–3139. https://doi.org/10.1021/acs.chemrev.8b00477.

(36) Leung, T. L.; Ahmad, I.; Syed, A. A.; Ng, A. M. C.; Popović, J.; Djurišić, A. B.

Stability of 2D and Quasi-2D Perovskite Materials and Devices. *Commun. Mater.* **2022**, *3* (1), 63. https://doi.org/10.1038/s43246-022-00285-9.

(37) Blancon, J.-C.; Stier, A. V.; Tsai, H.; Nie, W.; Stoumpos, C. C.; Traoré, B.; Pedesseau, L.; Kepenekian, M.; Katsutani, F.; Noe, G. T.; et al. Scaling Law for Excitons in 2D Perovskite Quantum Wells. *Nat. Commun.* **2018**, *9* (1), 2254. https://doi.org/10.1038/s41467-018-04659-x.

(38) Han, Y.; Cheng, X.; Cui, B.-B. Factors Influencing Self-Trapped Exciton Emission of Low-Dimensional Metal Halides. *Mater. Adv.* **2023**, *4* (2), 355–373. https://doi.org/10.1039/D2MA00676F.

(39) He, Y.; Liu, S.; Yao, Z.; Zhao, Q.; Chabera, P.; Zheng, K.; Yang, B.; Pullerits, T.; Chen, J. Nature of Self-Trapped Exciton Emission in Zero-Dimensional Cs_2ZrCl_6 Perovskite Nanocrystals. *J. Phys. Chem. Lett.* **2023**, *14* (34), 7665–7671. https://doi.org/10.1021/acs.jpclett.3c01878.

(40) Liu, L.; Pan, K.; Xu, K.; Zhang, J. Z. Impact of Molecular Ligands in the Synthesis and Transformation between Metal Halide Perovskite Quantum Dots and Magic Sized Clusters. *ACS Phys. Chem. Au* **2022**, *2* (3), 156–170. https://doi.org/10.1021/acsphyschemau.1c00047.

(41) Mule, A. S.; Mazzotti, S.; Rossinelli, A. A.; Aellen, M.; Prins, P. T.; van der Bok, J. C.; Solari, S. F.; Glauser, Y. M.; Kumar, P. V.; Riedinger, A.; et al. Unraveling the Growth Mechanism of Magic-Sized Semiconductor Nanocrystals. *J. Am. Chem. Soc.* **2021**, *143* (4), 2037–2048. https://doi.org/10.1021/jacs.0c12185.

(42) Harrell, S. M.; McBride, J. R.; Rosenthal, S. J. Synthesis of Ultrasmall and Magic-Sized CdSe Nanocrystals. *Chem. Mater.* **2013**, *25* (8), 1199–1210. https://doi.org/10.1021/cm303318f.

(43) Peng, L.; Dutta, A.; Xie, R.; Yang, W.; Pradhan, N. Dot–Wire–Platelet–Cube: Step Growth and Structural Transformations in $CsPbBr_3$ Perovskite Nanocrystals. *ACS Energy Lett.* **2018**, *3* (8), 2014–2020. https://doi.org/10.1021/acsenergylett.8b01037.

(44) Singh, V.; Priyanka; More, P. V.; Hemmer, E.; Mishra, Y. K.; Khanna, P. K. Magic-Sized CdSe Nanoclusters: A Review on Synthesis, Properties and White Light Potential. *Mater. Adv.* **2021**, *2* (4), 1204–1228. https://doi.org/10.1039/D0MA00921K.

(45) Peng, L.; Geng, J.; Ai, L.; Zhang, Y.; Xie, R.; Yang, W. Room Temperature Synthesis of Ultra-Small, near-Unity Single-Sized Lead Halide Perovskite Quantum Dots with Wide Color Emission Tunability, High Color Purity and High Brightness. *Nanotechnology* **2016**, *27* (33), 335604. https://doi.org/10.1088/0957-4484/27/33/335604.

(46) Xu, K.; Vickers, E. T.; Luo, B.; Wang, Q.; Allen, A. C.; Wang, H.; Cherrette, V.; Li, X.; Zhang, J. Z. Room Temperature Synthesis of Cesium Lead Bromide Perovskite Magic Sized Clusters with Controlled Ratio of Carboxylic Acid and Benzylamine Capping Ligands. *Sol. Energy Mater. Sol. Cells* **2020**, *208*, 110341. https://doi.org/10.1016/j.solmat.2019.110341.

(47) Zhang, J. Z. A “Cocktail” Approach to Effective Surface Passivation of

Multiple Surface Defects of Metal Halide Perovskites Using a Combination of Ligands. *J. Phys. Chem. Lett.* **2019**, *10* (17), 5055–5063. https://doi.org/10.1021/acs.jpclett.9b01166.

(48) Liu, L.; Xu, K.; Vickers, E. T.; Allen, A.; Li, X.; Peng, L.; Zhang, J. Z. Varying the Concentration of Organic Acid and Amine Ligands Allows Tuning between Quantum Dots and Magic-Sized Clusters of $CH_3NH_3PbBr_3$ Perovskite: Implications for Photonics and Energy Conversion. *ACS Appl. Nano Mater.* **2020**, *3* (12), 12379–12387. https://doi.org/10.1021/acsanm.0c02894.

(49) Friedfeld, M. R.; Stein, J. L.; Cossairt, B. M. Main-Group-Semiconductor Cluster Molecules as Synthetic Intermediates to Nanostructures. *Inorg. Chem.* **2017**, *56* (15), 8689–8697. https://doi.org/10.1021/acs.inorgchem.7b00291.

(50) Kwon, Y.; Oh, J.; Lee, E.; Lee, S. H.; Agnes, A.; Bang, G.; Kim, J.; Kim, D.; Kim, S. Evolution from Unimolecular to Colloidal-Quantum-Dot-like Character in Chlorine or Zinc Incorporated InP Magic Size Clusters. *Nat. Commun.* **2020**, *11* (1), 3127. https://doi.org/10.1038/s41467-020-16855-9.

(51) Zhang, H.; Vickers, E. T.; Erickson, S.; Guarino-Hotz, M.; Barnett, J. L.; Ghosh, S.; Zhang, J. Z. Synthesis and Properties of Stable Amino Metal Halide Molecular Clusters in the Solid State. *J. Phys. Chem. Lett.* **2022**, *13* (45), 10543–10549. https://doi.org/10.1021/acs.jpclett.2c02977.

(52) Liu, L.; Pan, K.; Xu, K.; Peng, X.; Zhang, J. Z. Synthesis and Optical Properties of Mn^{2+}-Doped Amino Lead Halide Molecular Clusters Assisted by Chloride Ion. *J. Phys. Chem. Lett.* **2021**, *12* (31), 7497–7503.

https://doi.org/10.1021/acs.jpclett.1c02243.

(53) Zhou, C.; Lin, H.; Worku, M.; Neu, J.; Zhou, Y.; Tian, Y.; Lee, S.; Djurovich, P.; Siegrist, T.; Ma, B. Blue Emitting Single Crystalline Assembly of Metal Halide Clusters. *J. Am. Chem. Soc.* **2018**, *140* (41), 13181–13184. https://doi.org/10.1021/jacs.8b07731.

(54) Zhou, C.; Lin, H.; Tian, Y.; Yuan, Z.; Clark, R.; Chen, B.; Burgt, L. J. van de; Wang, J. C.; Zhou, Y.; Hanson, K.; et al. Luminescent Zero-Dimensional Organic Metal Halide Hybrids with near-Unity Quantum Efficiency. *Chem. Sci.* **2018**, *9* (3), 586–593. https://doi.org/10.1039/C7SC04539E.

(55) Lin, H.; Zhou, C.; Chaaban, M.; Xu, L.-J.; Zhou, Y.; Neu, J.; Worku, M.; Berkwits, E.; He, Q.; Lee, S.; et al. Bulk Assembly of Zero-Dimensional Organic Lead Bromide Hybrid with Efficient Blue Emission. *ACS Mater. Lett.* **2019**, *1* (6), 594–598. https://doi.org/10.1021/acsmaterialslett.9b00333.

(56) Zhou, C.; Xu, L.-J.; Lee, S.; Lin, H.; Ma, B. Recent Advances in Luminescent Zero-Dimensional Organic Metal Halide Hybrids. *Adv. Opt. Mater.* **2021**, *9* (18), 2001766. https://doi.org/10.1002/adom.202001766.

(57) Zeitz, D. C.; Win, A. A.; Zhang, J. Z. Distinguishing Metal Halide Molecular Clusters from Perovskite Magic Sized Clusters in the Synthesis of Metal Halide Perovskite Nanostructures. *J. Chin. Chem. Soc.* **2023**, *70* (8), 1609–1617. https://doi.org/10.1002/jccs.202300195.

(58) Cherrette, V. L.; Babbe, F.; Cooper, J. K.; Zhang, J. Z. Octahedral Distortions Generate a Thermally Activated Phonon-Assisted Radiative Recombination

Pathway in Cubic $CsPbBr_3$ Perovskite Quantum Dots. *J. Phys. Chem. Lett.* **2023**, *14* (39), 8717–8725. https://doi.org/10.1021/acs.jpclett.3c02568.

(59) Khvichia, M.; Chou, K.-C.; Lee, S.; Zeitz, D. C.; Zou, S.; Li, Y.; Zhang, J. Z. Ultrafast Photoinduced Charge Carrier Dynamics of L-Cysteine and Oleylamine Stabilized $CsPbBr_3$ Perovskite Quantum Dots Coupled with Gold Nanoparticles. *J. Chem. Phys.* **2024**, *161* (11), 114704. https://doi.org/10.1063/5.0222815.

(60) Shi, W.; Zhang, X.; Xie, C.; Chen, H. S.; Yang, P. Blue Emitting $CsPbBr_3$: High Quantum Confinement Effect and Well-Adjusted Shapes (Nanorods, Nanoplates, and Cubes) toward White Light Emitting Diodes. *Adv. Opt. Mater.* **2024**, *12* (7), 2302129. https://doi.org/10.1002/adom.202302129.

(61) Liu, Y.; Ma, Z.; Zhang, J.; He, Y.; Dai, J.; Li, X.; Shi, Z.; Manna, L. Light-Emitting Diodes Based on Metal Halide Perovskite and Perovskite Related Nanocrystals. *Adv. Mater.* **2025**, *37* (25), 2415606. https://doi.org/10.1002/adma.202415606.

(62) Deng, C.; Huang, Q.; Fu, Z.; Lu, Y. Ligand Engineering of Inorganic Lead Halide Perovskite Quantum Dots toward High and Stable Photoluminescence. *Nanomaterials* **2024**, *14* (14), 1201. https://doi.org/10.3390/nano14141201.

(63) Guarino-Hotz, M.; Barnett, J. L.; Pham, L. B.; Win, A. A.; Cherrette, V. L.; Zhang, J. Z. Tuning between Methylammonium Lead Bromide Perovskite Magic-Sized Clusters and Quantum Dots through Ligand Assisted Reprecipitation at Elevated Temperatures. *J. Phys. Chem. C* **2022**, *126* (32),

13854–13862. https://doi.org/10.1021/acs.jpcc.2c04384.

(64) Zeitz, D. C.; Cherrette, V. L.; Creech, S. A.; Li, Y.; Ping, Y.; Zhang, J. Z. Ultrafast Spin Relaxation of Charge Carriers in Strongly Quantum Confined Methylammonium Lead Bromide Perovskite Magic-Sized Clusters. *ACS Phys. Chem. Au* **2024**, *4* (6), 610–614. https://doi.org/10.1021/acsphyschemau.4c00051.

(65) Shi, Y.; Yang, J.; Lu, Z. Perovskite Quantum Dots-Based Blue Light-Emitting Diodes: Advantages, Strategies, and Prospects. *Photonics* **2026**, *13* (2), 151. https://doi.org/10.3390/photonics13020151.

(66) Chu, P.-L.; Huang, W.-L.; Chu, S.-Y. Passivation of Surface Defects by X-Type Short-Chain Ligands for High Quantum Yield and Stable $CsPbX_3$ Quantum Dots Synthesis and Application in WLEDs. *ACS Appl. Opt. Mater.* **2023**, *1* (1), 513–522. https://doi.org/10.1021/acsaom.2c00151.

(67) Shi, J.; Cohen-Kleinstein, B.; Zhang, X.; Zhao, C.; Zhang, Y.; Ling, X.; Guo, J.; Ko, D.-H.; Xu, B.; Yuan, J.; et al. In Situ Iodide Passivation Toward Efficient $CsPbI_3$ Perovskite Quantum Dot Solar Cells. *Nano-Micro Lett.* **2023**, *15* (1), 163. https://doi.org/10.1007/s40820-023-01134-1.

(68) Zhu, N.; Xu, K.; Xing, J.; Zhang, J.; Dai, J. Ionic Liquid Passivation Eliminates Low-n Quantum Well Domains in Blue Quasi-2D Perovskite Films. *ACS Appl. Mater. Interfaces* **2021**, *13* (48), 57540–57547. https://doi.org/10.1021/acsami.1c15879.

(69) Cherrette, V. L.; Zeitz, D.; Khvichia, M.; Cooper, J. K.; Ping, Y.; Zhang, J. Z.

Enhancing the Photoexcited Carrier Spin Relaxation Lifetime in $CsPbBr_3$ Perovskite Quantum Dots by ^{208}Pb Isotope Enrichment. *J. Phys. Chem. Lett.* **2025**, *16* (13), 3336–3342. https://doi.org/10.1021/acs.jpclett.5c00123.

2 Synthesis and Properties of Stable Amino Metal Halide Molecular Clusters in Solid State

2.1 Abstract

Nano-sized molecular clusters (MCs) composed of $PbBr_2$ and neutral ligand butylamine (BTYA) with unique optical properties in solution and solid state have been synthesized using ligand-assisted reprecipitation and spin-coating, separately.

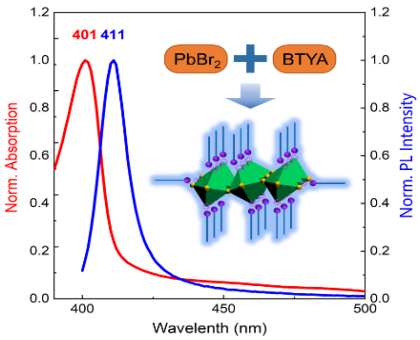

The optical properties studies from ultraviolet−visible (UV-vis) absorption and photoluminescence (PL) show the first electronic absorption and PL band of the MCs at 401 nm and 411 nm, respectively, for both the solution and solid state samples that exhibit good stability in ambient conditions. Low temperature PL spectra below 30 K show vibronic peaks indicative of single size or very narrow size distribution of the MCs. Based on Raman, XRD and TEM measurements, a layered structural model is proposed for the MCs with BTYA ligand capping on the surface of corner shared tilted $[PbBr_6]^{4-}$ octahedra framework. The stable and retained structure of MCs in solid form is promising for photonics applications.

2.2 Introduction

Molecular clusters (MCs) are small particles with single size or very narrow size distribution.[1-3] They have attracted considerable interest due to their unique

properties, including tunable size and shape at the molecular scale, and the possibility of serving as building blocks for larger structures such as nanocrystals (NCs) or bulk crystals. Recently, MCs based on metal halides and capping ligands have been reported. For example, Zhou *et al.* synthesized $(C_9NH_{20})_7(PbCl_4)Pb_3Cl_{11}$ metal halide clusters exhibiting blue emission peaked at 470 nm with cationic ligand $C_9NH_{20}^+$, showing photoluminescence quantum efficiency (PLQE) of 83 ± 1%.[1] Vickers *et al*. has found PbX_2-BTYA (X = Cl^-, Br^- or I^-) MCs with PbX_2 framework capped with neutral ligand butylamine (BTYA), which lack the A component in conventional metal halide perovskites (MHP) ABX_3 (A = Cs^+ or MA^+, B = Pb^{2+} or Sn^{2+}, X = Cl^-, Br^- or I^-) formula.[2] They exhibit bluer absorption and emission bands compared with MHP nanocrystals (NCs)[4,5] or quantum dots (QDs)[6-8] or magic sized clusters (MSCs)[9-11] due to smaller size, ranging in 335-515 nm for absorption peaks and 344-519 nm for PL peaks depending on the halides. Their ultrasmall size, sharp absorption and emission bands, with full width at half maximum (FWHM) around 10 nm, are attractive for potential photonic applications such as blue single photon emitters.[2,3,12]

Earlier attempts have been made to determine the structure of the PbX_2-BTYA MCs using the extended X-ray absorption fine structure (EXAFS) technique, and then several tentative structural models were proposed.[2] However, it has been challenging to determine their structure directly using techniques such as XRD and TEM because the MCs tend to grow into larger structure or aggregate upon drying

into solid form.[2,3,13,14] To produce isolated MCs in solid state is essential for their structural determination as well as for device applications.

In this work, we report the first successful synthesis and characterization of isolated MCs based on $PbBr_2$ and neutral capping ligands BTYA in solid state that have identical optical properties as MCs in solution state. Structural studies based on Raman, XRD and TEM led to the proposal of a structural model based on layered structure with corner shared tilted $[PbBr_6]^{4-}$ octahedra and BTYA capping ligands on the surface. Vibronic features in low temperature PL data provide evidence of exciton-phonon coupling and single size or very narrow size distribution of the MCs. Good stability is observed under ambient conditions, which is attributed to the strong ligand coordination effect on the $[PbBr_6]^{4-}$ octahedra surface.

2.3 Results and Discussion

Figure 2-1 shows the absorption and PL spectra of $PbBr_2$-BTYA MCs in solution and solid state. For MCs in solution, as shown in Figure 2-1 (a), the first absorption and PL emission peaks are at 401 nm and 411 nm, respectively, and PL band has an FWHM of 10 nm, which is in good agreement with previous reports in our group and indicates a single or narrow size distribution of MCs.[2,3] The PL Stokes shift is only 10 nm, indicating a low density of defects within the bandgap due to strong passivation of the surface with BTYA ligand.[3,15] More interestingly, when we transfer the sample from solution to solid state using spin-coating, the absorption and the emission peaks do not shift at all, as shown in Figure 2-1 (b). This is significant since it indicates that the MCs in solid state retain their properties as in solution,

which is crucial for device applications since solid state is the form that is usually required. As reported previously, clusters tend to grow into larger structure or aggregate upon drying into solid form from solution.[2,3,13,14,16,17]

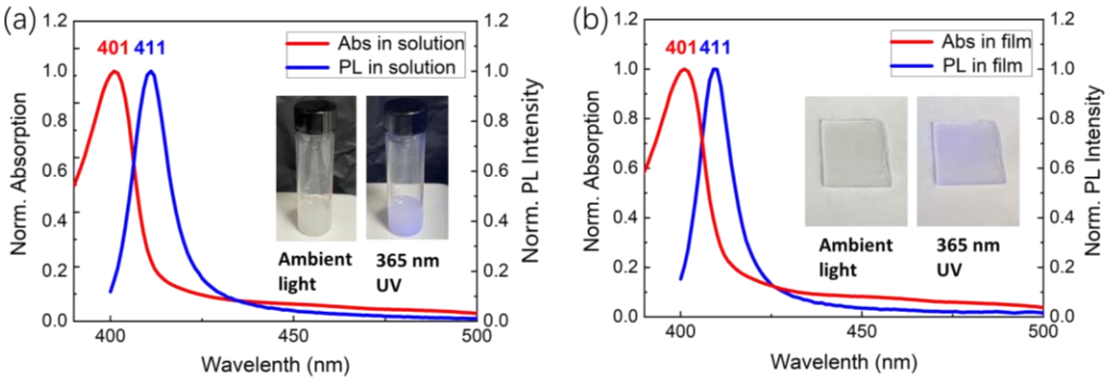

Figure 2-1 Optical properties of $PbBr_2$-BTYA MCs in solution and solid state. (a) UV-vis absorption spectra and PL spectra of $PbBr_2$-BTYA MCs in solution state. Inset: images of MCs in solution state under ambient light and 365 nm UV light. (b) UV-vis absorption spectra and PL spectra of $PbBr_2$-BTYA MCs in solid state. Inset: images of MCs in solid state under ambient light and 365 nm UV light.

To confirm that the formation of MCs involves both $PbBr_2$ and BTYA, a series of control experiments were conducted. First, the UV-vis absorption and PL spectra of solution of toluene, DMF, BTYA and MC precursors were characterized. As seen in Figures 2-2 (a) and (b), there are no peaks observed in both absorption and PL spectra for pure solution of toluene, DMF or BTYA in the spectral range of 300-800 nm. For the MC precursor solution, there are broad absorption and emission bands observed, indicating the interaction between $PbBr_2$ and BTYA in solution in the form of different kinds of lead bromide complexes assisted with BTYA, for example,

$PbBr_3^-$, $PbBr_4^{2-}$.[18] However, there are no sharp spectral features observed indicative of the formation of nanocrystals or nanoclusters with regularly arranged microscopic structures.[17] Moreover, Figures 2-2 (c) and (d) show a comparison of the UV-vis and PL spectra of $PbBr_2$ and $PbBr_2$-BTYA MCs in solution and solid state. Only the $PbBr_2$-BTYA MCs solution and film sample exhibit characteristic peaks, which clearly indicates that the spectral features of MCs around 400 nm originates from a combination of $PbBr_2$ and BTYA, not $PbBr_2$ alone.

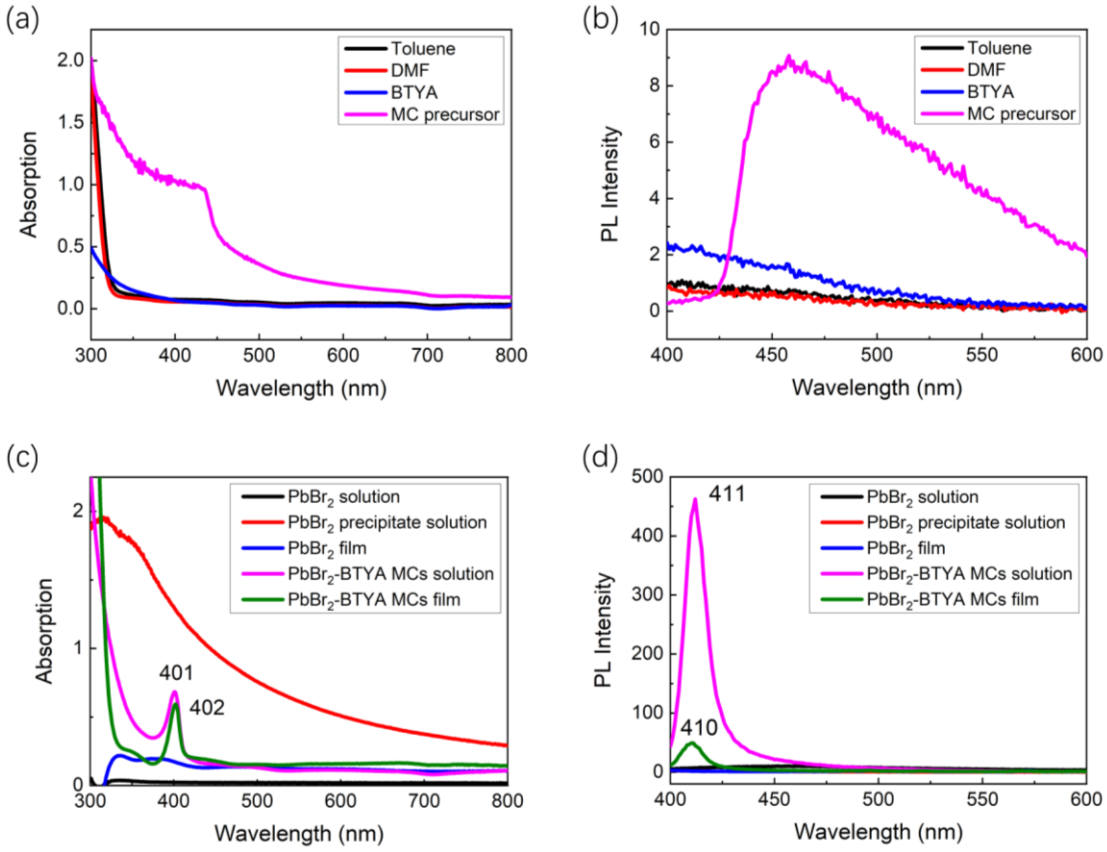

Figure 2-2 (a) UV-vis absorption spectra and (b) PL spectra of solution of toluene, DMF, BTYA and MC precursor. (c) UV-vis absorption spectra and (d) PL spectra of $PbBr_2$ solution, $PbBr_2$ precipitate in solution, $PbBr_2$ film, $PbBr_2$-BTYA MCs

precipitate in solution and $PbBr_2$-BTYA MCs in film.

Figure 2-3 shows low temperature dependent PL spectra from 20 K to 290 K. In Figure 2-3 (a), at T = 290 K, a single emission peak is observed at 416 nm (indicated by a solid blue arrow), which we identify as arising from band edge recombination. The slight red shift of the 416 nm peak compared with 411 nm is possibly due to different PL instruments use that may not be calibrated identically. As T < 240 K, a second low energy (long wavelength) peak can be seen centered at 440 nm (hollow blue arrow), which persists down to T = 20 K. This could be attributed to shallow surface-defect related trap states[9,19] or self-trapped excitons (STEs) states[20,21], which are ~ 160 meV below the conduction band according to the energy difference between the 416 nm peak and red-shifted 440 nm peak. Figure 2-3 (b) focuses on PL in the range 20-100 K to highlight the change in the band edge emission intensity as temperature is decreased.

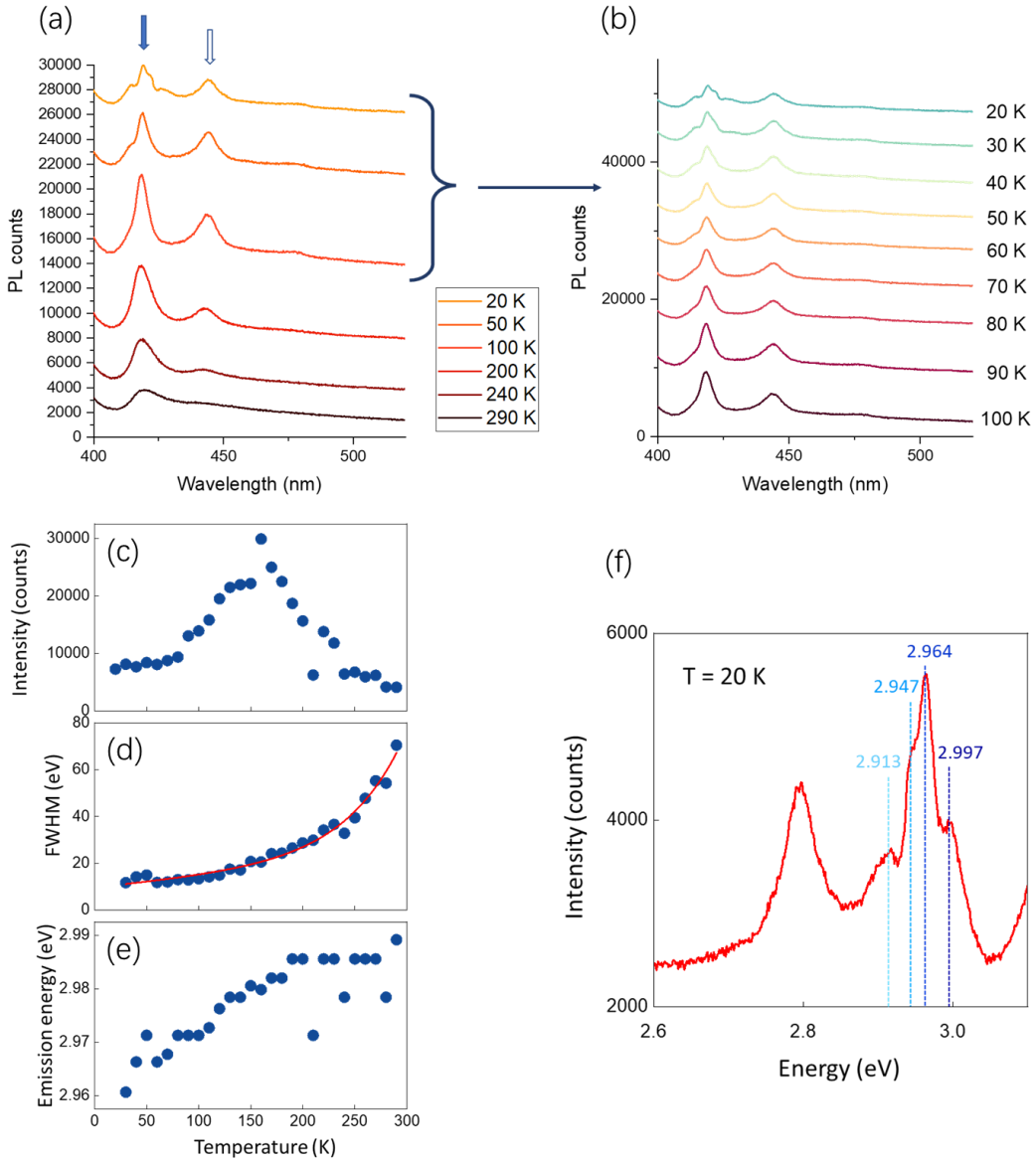

Figure 2-3 Low temperature dependent PL spectra of $PbBr_2$-BTYA MCs film. (a) PL spectra dependent on different temperature from 20 K to 290 K and the two main peaks around 416 nm and 440 nm redshift gradually as the temperature goes down. (b) PL spectra focused on temperature from 20 K to 100 K, among which the interval is 10 K. (c) PL intensity, (d) FWHM and (e) emission energy based on different temperature from 20 K to 290 K. (f) PL spectra focused on the 444 nm (left main

peak) and 418 nm (right main peak) bands with several shoulder peaks around 418 nm band at 20 K.

Figures 2-3 (c), (d), and (e) show the spectral analysis of the PL data at low temperature. The emission intensity, spectral FWHM, and peak emission energy are plotted varying with temperature *T* in Figures 2-3 (c), (d), and (e), respectively. The minor blue-shift of emission energy with increasing *T* could be due to thermally-induced excitonic emission.[22] And the spectral broadening indicated by the FWHM increasing with *T* is expected with increased inhomogeneous broadening. However, while peak energy and FWHM monotonically change with *T*, the emission intensity shows a clear maximum around *T* = 160 K.

The FWHM is fitted to[22]:

$$\Gamma(T) = \Gamma_0 + \sigma T + \frac{\Gamma_{op}}{\left(e^{\frac{E_p}{k_B T}} - 1\right)} \tag{2-1}$$

where $\Gamma(T)$ is the FWHM, Γ_O is the inhomogeneous contribution, σ and Γ_{op} the excitonic coupling constants for acoustic and optical phonons, respectively, and E_p is the optical phonon energy. The fitting reveals σ to be insignificant, implying the optical phonon contributions dominate. The phonon energy is approximately 64 meV.

Figure 2-3 (f) zooms in on the band edge PL at *T* = 20 K and reveals a series of closely-spaced emission peaks. From the lowest energy peak at 2.913 eV, the spacings are roughly 34 meV (274 cm^{-1}), 17 meV (137 cm^{-1}) and 33 meV (266 cm^{-1}), all close to phonon frequencies to be discussed later. These vibronic peaks indicate strong exciton-phonon coupling and that the MCs are single sized or have

very narrow size distribution, since such features would be unexpected if there is a broad size distribution.

The stability of the MCs in solution and solid state was studied by monitoring their absorption and PL spectra over time under different conditions involving light, oxygen and moisture factors.[23-25] First, the stability of $PbBr_2$-BTYA MCs in their native environment was studied, in which MCs are precipitates and in solution state. All the samples were kept under ambient environment (room temperature and one atmosphere) and characterized without further protection. Figures 2-4 (a) and (b) show the UV-vis and PL spectra of $PbBr_2$-BTYA MCs within 30 days. There is a small variation in peak position in both absorption or PL spectra, which is attributed to subtle size changes during storage.[2,15] The intensity of both absorption and PL decreases over time. On the 30^{th} day, the intensity is only at 20% of its initial intensity, suggesting the degradation of the emissive MCs in solution under ambient environment. Interestingly, the MCs did not seem to grow larger or aggregate in solution since the spectral position does not change over time, with the peaks only shifting 2-3 nm within 30 days, reflecting the structural stability of isolated MCs due to strong ligand passivation.[2,3,17]

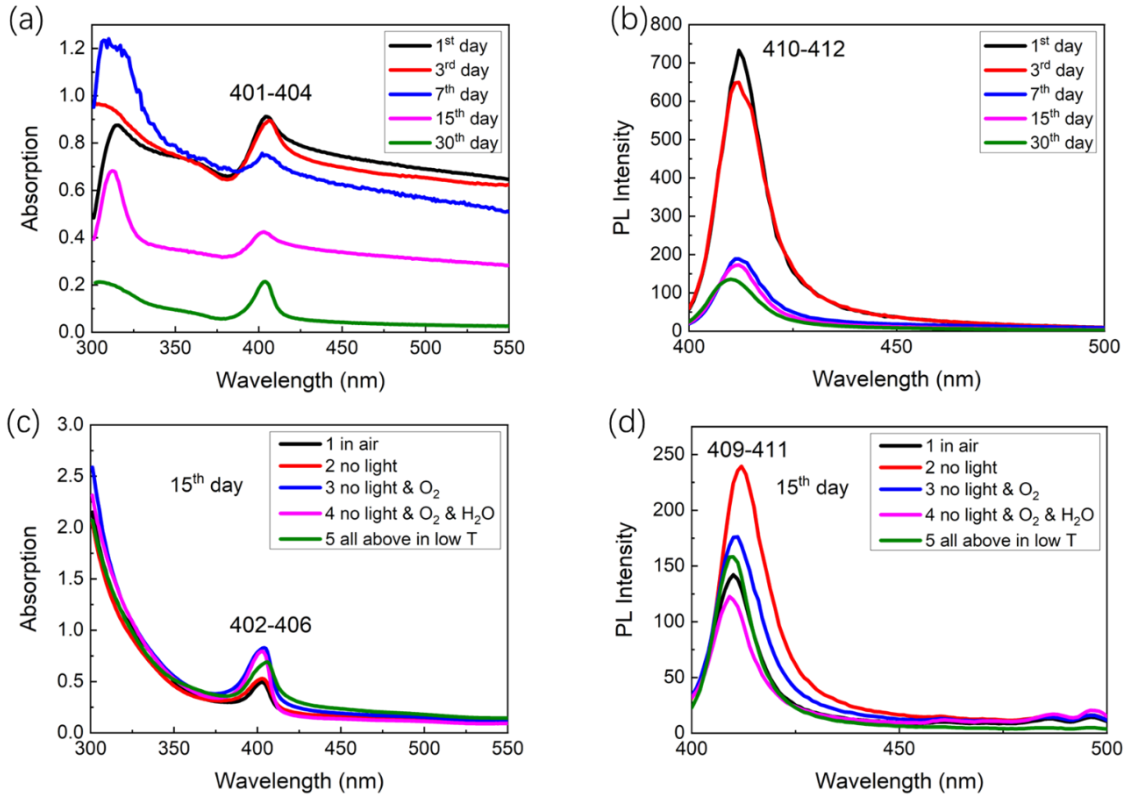

Figure 2-4 $PbBr_2$-BTYA MCs stability test in solution and solid state. (a) UV-vis absorption spectra and (b) PL spectra of $PbBr_2$-BTYA MCs in solution state. (c) UV-vis absorption spectra and (d) PL spectra of $PbBr_2$-BTYA MCs in solid state stored for 15 days in five different ambient conditions including in air (1), without light (2), without light and oxygen (3), without light, oxygen and moisture (4), and without light, oxygen, moisture at low temperature (0 °C) (5).

To study the stability of MCs in solid state, a series of experiments under different conditions were conducted up to 45 days, including film samples stored in air (1), without light (2), without light & oxygen (3), without light, oxygen and moisture (4), and without light, oxygen and moisture at low temperature (0 °C) (5). Figures 2-4 (c) and (d) show the absorption and PL spectra of all the $PbBr_2$-BTYA

MCs on the 15th day. The absorption and emission peaks fluctuate within a narrow range (absorption peaks at 4 nm, while PL peaks at 2 nm) for all five samples, which was attributed to subtle size differences when synthesizing. Surprisingly, the individual sample does not experience any peak change over 15 days, which indicates the MCs are stable and the original structure is retained even under ambient environment. This stability is attributed to the strong coordination of N atom in BTYA ligand to Pb^{2+}, which also provides exceptional passivation for the metal halide surface defects.[26] According to the absorption and PL spectra in Figures 2-5 and 2-6 separately, the intensity decreases gradually as the storage time increases. The solid control samples in air show no optical properties for absorption and emission on the 30th day due to the degradation. However, by excluding light irradiation alone, it is possible to elongate the emissive properties to 45 days. Therefore, light plays a key role in long-term stability of $PbBr_2$-BTYA MCs. Other variables such as oxygen, moisture and low temperature deteriorate less on the stability compared with light within 45 days test.

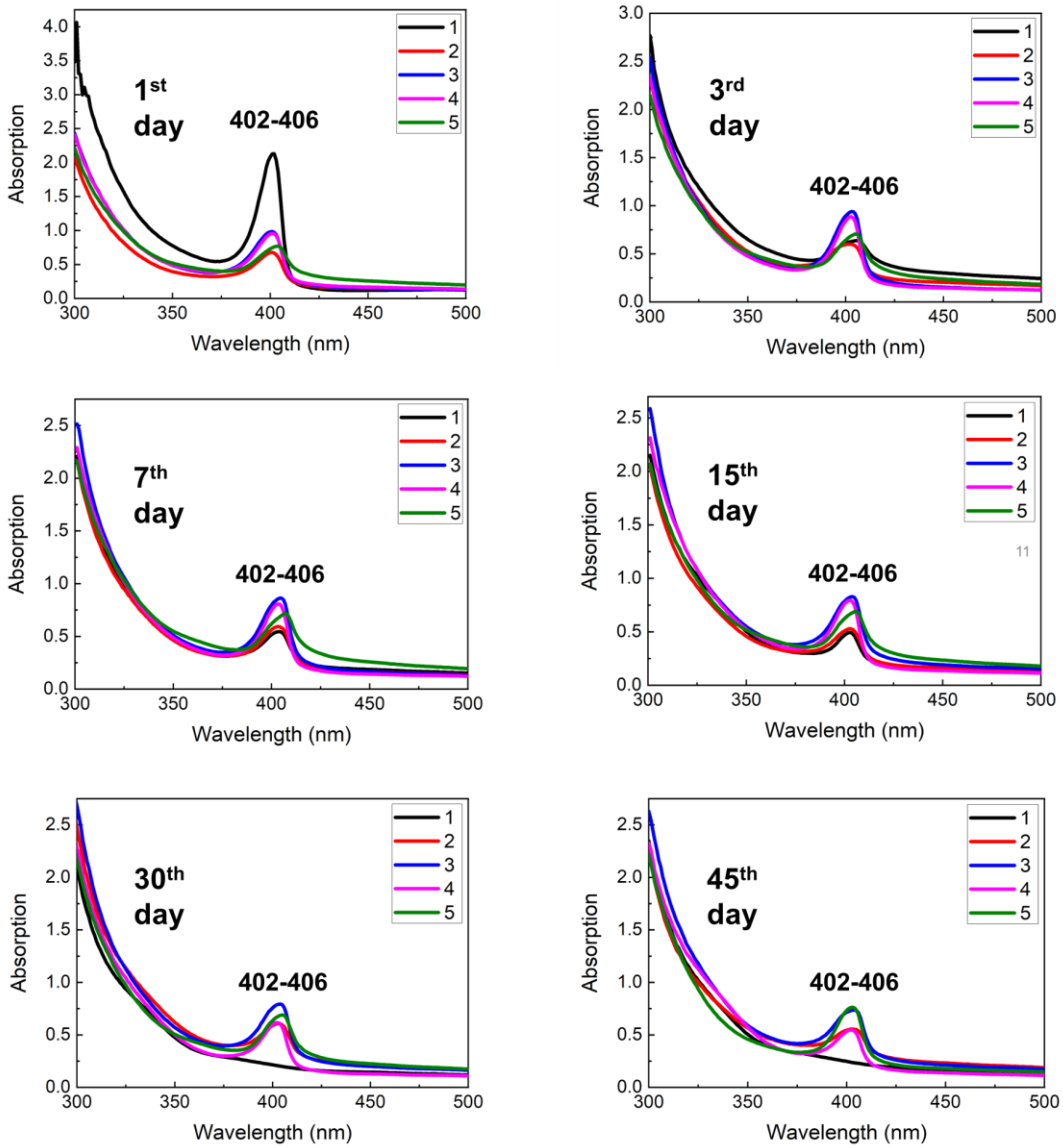

Figure 2-5 Stability tests based on UV-vis absorption spectra of $PbBr_2$-BTYA MCs film samples in five different conditions, including in air (1), without light (2), without light and oxygen (3), without light, oxygen and moisture (4), and without light, oxygen, moisture at low temperature (0 °C) (5) within 45 days.

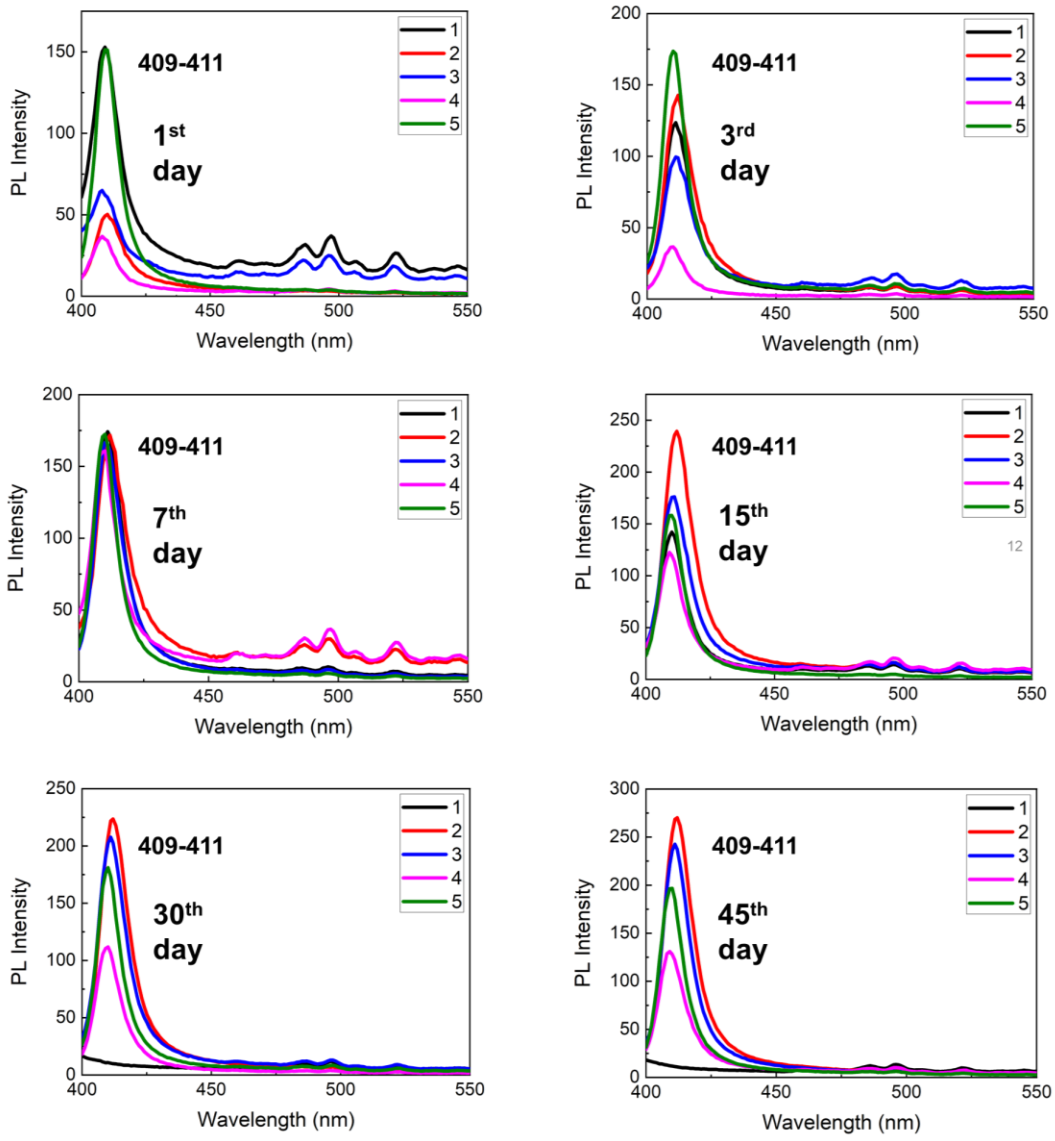

Figure 2-6 Stability tests based on PL spectra of $PbBr_2$-BTYA MCs film samples in five different conditions, including in air (1), without light (2), without light and oxygen (3), without light, oxygen and moisture (4), and without light, oxygen, moisture at low temperature (0 °C) (5) within 45 days. The random shapes of tails were caused by the glass substrate scattering due to lack of a film sample holder for PL spectrometer.

Raman spectroscopy and XRD were utilized to provide structural information on the MCs. First, $PbBr_2$-BTYA MCs were characterized in solution at high Raman vibrational frequency region to understand the interaction between ligand and $PbBr_2$. Figure 2-7 (a) shows the Raman spectra of the solvent DMF, ligand BTYA, the mixture of $PbBr_2$ powder and BTYA solution, and the $PbBr_2$-BTYA MCs solution ($PbBr_2$ powder and BTYA solution were dissolved in DMF solvent first and then precipitated in toluene). Comparing DMF and $PbBr_2$-BTYA MCs solution, the spectra are dominated by peaks from DMF, which is likely due to the dominance of DMF in the solution. Comparing BTYA solution with $PbBr_2$/BTYA mixture solution, the peaks of BTYA solution in 398 cm^{-1}, 797 cm^{-1}, 1299 cm^{-1} and 1441 cm^{-1} shift to higher vibrational frequency in the $PbBr_2$/BTYA mixture solution. These peaks are ascribed to C-N torsion, NH_2 torsion, C-H_2 twist and C-H_2 bending, respectively.[27,28] This shift in the $PbBr_2$/BTYA solution suggests the interaction between the BTYA ligand and $PbBr_2$, likely through the amine group.[29]

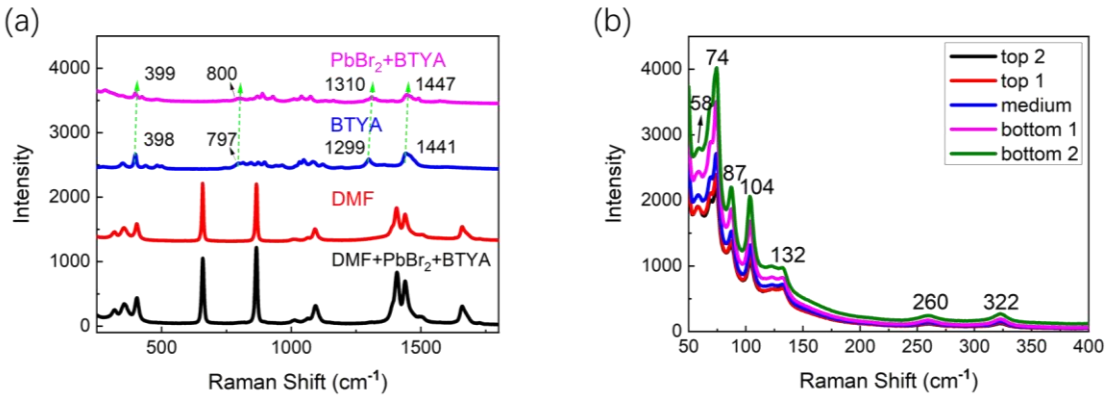

Figure 2-7 Raman spectra of $PbBr_2$-BTYA MCs at high and low vibrational frequency to show ligand interactions and MCs phonon vibrational frequencies,

respectively. (a) Raman spectra of components of $PbBr_2$-BTYA MCs in solution state. (Solvent DMF, ligand BTYA, mixture of $PbBr_2$ powder and BTYA solution, and $PbBr_2$-BTYA MCs in solution). (b) Raman spectra of $PbBr_2$-BTYA MCs in solid state at different Z axis heights.

The $PbBr_2$-BTYA MCs were characterized in solid state in the low Raman vibrational frequency region to determine the vibrational phonon modes of MCs. Figure 2-7 (b) shows several vibration peaks at low frequencies on different thicknesses of solid films. The peak assignments are summarized in Table 2-1. The peaks retain the same position on different film thicknesses, indicating the same MCs structure on different thicknesses of films and confirming the interaction between ligand and octahedra. Based on the assignments, an initial structure is proposed with corner shared tilted $[PbBr_6]^{4-}$ octahedra as framework and BTYA ligand interacting with Pb^{2+} on the surface.

Table 2-1 Assignments for Raman peaks of solid $PbBr_2$-BTYA MCs.

Raman Shift (cm^{-1})	**Assignment**
58	Octahedra distortion
74	Butylamine lurching
87	Butylamine lurching
104	Butylamine lurching
132	Butylamine lurching
260	C-N torsion

322	C-N torsion

XRD was used to determine the crystal structure of $PbBr_2$-BTYA MCs. The $PbBr_2$-BTYA MCs diffraction pattern in Figure 2-8 exhibits peaks at 6.4 °, 12.8 °, 19.3 °, 21.4 °, 25.8 °, 32.4 °, 35.8 ° and 39.1 °, which is different from conventional diffraction peaks of perovskite $CsPbBr_3$ crystals or $MAPbBr_3$ crystals at 15.3 °, 21.7 °, 30.7 °.[30,31] This demonstrates that MCs formed crystalline structure that is different from the cubic structure of conventional ABX_3 perovskite.[30] In addition, the contrast with pure $PbBr_2$ crystal illustrates that $PbBr_2$-BTYA MCs are no longer remaining $PbBr_2$ orthorhombic structure, which confirms interaction between the ligand BTYA and $PbBr_2$ (the pure $PbBr_2$ XRD data were compared to the JCPDS PDF no. 31-0679). Interestingly, the XRD peaks show regular degree intervals at 6.4 °, which corresponds to 1.4 nm distance according to Bragg's law. This XRD result matches the reported layered Ruddlesden-Popper $(BA)_2PbBr_4$ (BA = butylammonium) perovskite crystals when the number of metal halide octahedral layers is one.[32-34] It is also similar to other reported layered structures that show the close XRD peak positions and regular XRD peaks degree interval.[35] All the reports not only show comparable XRD results, but also analogous optical absorption and emission properties. This led us to propose that the $PbBr_2$-BTYA MCs have a similar layered structure as depicted later in Figure 2-10.[32-36]

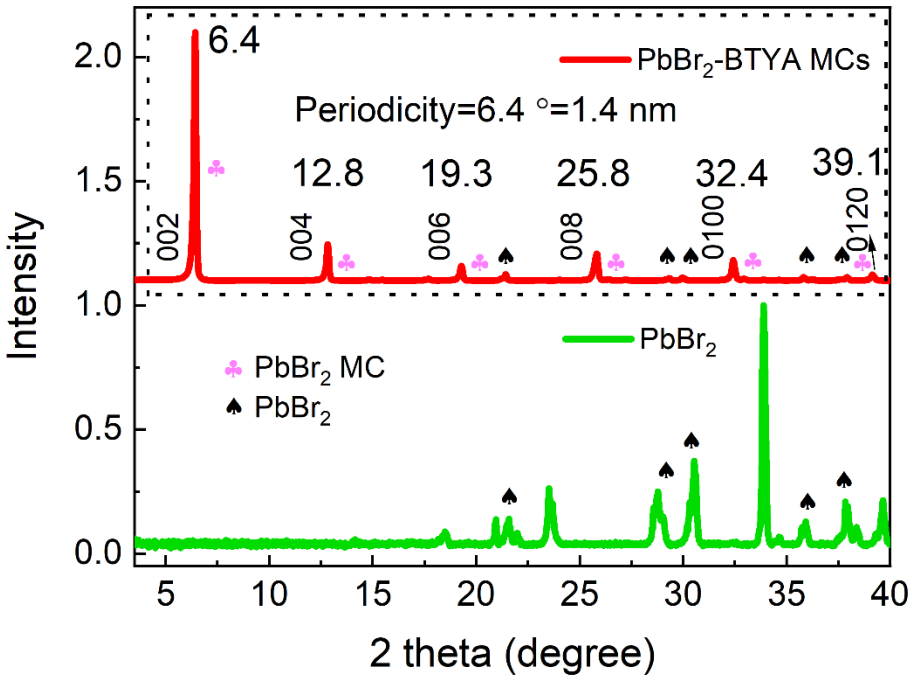

Figure 2-8 X-ray diffraction pattern of $PbBr_2$-BTYA MCs film and $PbBr_2$ film. The club sign stands for $PbBr_2$-BTYA MCs phase and spade sign stands for $PbBr_2$ phase.

Figure 2-9 shows TEM images of $PbBr_2$-BTYA MCs. Based on images of 40 MCs in Figure 2-9 (a), an average size of 2.0 ± 0.4 nm is calculated. Figure 2-9 (b) shows the high-resolution TEM (HRTEM) image of the MCs that reveal clear lattice fringes indicating good crystallinity of the $PbBr_2$-BTYA MCs. The interplanar spacing is measured to be 0.259 nm, which corresponds to (010) crystal plane and proves that octahedra are tilted between two adjacent (010) planes since one Pb-Br bond is about 0.3 nm in the Br shared Pb-Br-Pb bond between two octahedra.[33] The TEM results confirm the crystal size and crystalline nature of $PbBr_2$-BTYA MCs,

rather than disordered or amorphous as one may expect based on their expected molecular nature.

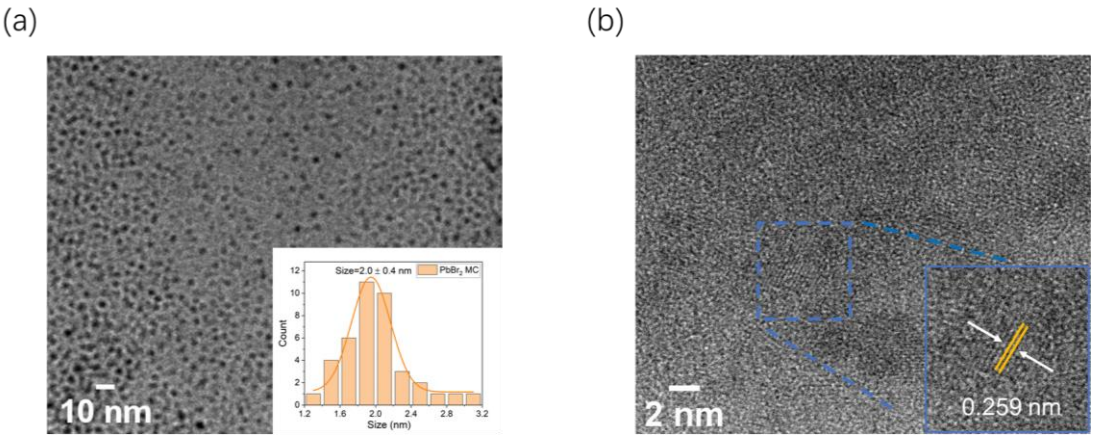

Figure 2-9 TEM images of $PbBr_2$-BTYA MCs. (a) TEM images of $PbBr_2$-BTYA MCs films. Inset: size distribution of MCs. (b) High-resolution TEM (HRTEM) images of $PbBr_2$-BTYA MCs films showing crystal lattice. Inset: enlarged HRTEM images showing interplanar spacing along (010) planes.

Based on the above structural characterizations, we propose a structure for the MCs based on corner shared tilted octahedra as the framework and BTYA ligand for coordination and passivation on the surface, as illustrated in Figure 2-10. The $[PbBr_6]^{4-}$ octahedra are tilted based on the Raman vibrational frequencies and interplanar spacing from HRTEM. The lone pair electrons in N atom in the amine group of the BTYA ligand likely coordinate with Pb^{2+} to form a stable complex.[26] BTYA also serves as a capping ligand for cationic defects on the surface like Br^- vacancy. Van der Waals' interaction between hydrocarbon tails of BTYA likely leads to the formation of stable layered structures.[34,37]

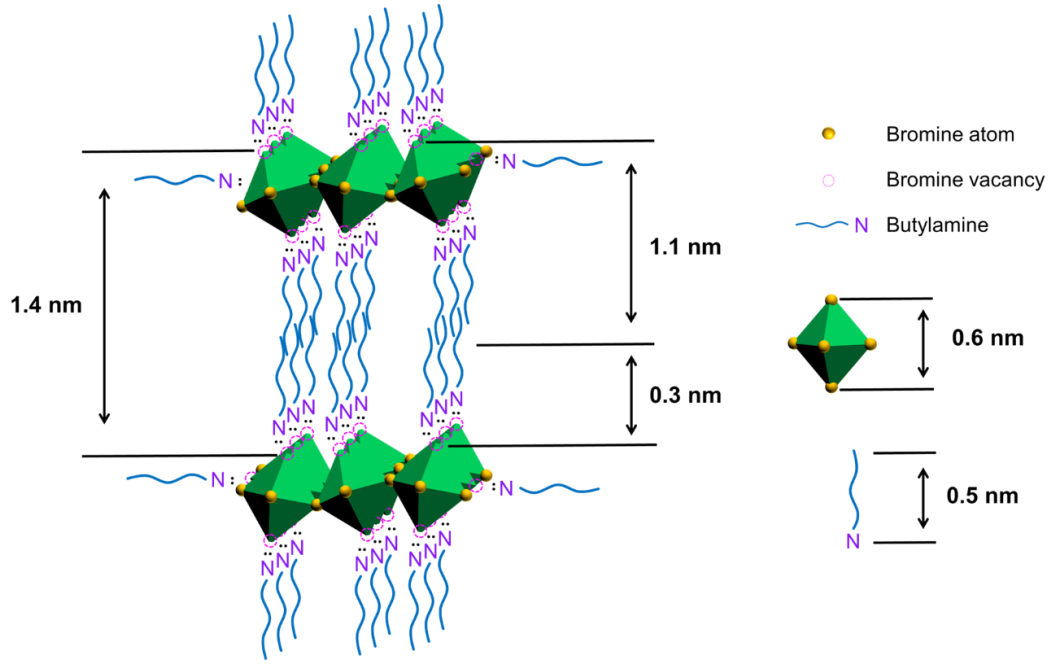

Figure 2-10 Proposed layered structure for $PbBr_2$-BTYA MCs capped with BTYA ligand. The Br atoms on the surface are replaced by N atoms in BTYA mostly on the top and bottom sides of $[PbBr_6]^{4-}$ octahedra framework through N to Pb coordination bond. Some lateral sides of the Br atom can also be replaced by N atoms due to the

electroneutrality principle.

2.4 Conclusion

In summary, stable nano sized $PbBr_2$-BTYA MCs have been synthesized in solid state as well as in solution state that show identical absorption and emission properties. The results indicate that the MCs have the same structure in solid and solution, unlike other small sized clusters synthesized in solution, which often tend to grow into larger structure or aggregate upon drying to solid, making them challenging for applications. MCs have narrow electronic absorption and emission bands with a small Stokes shift, suggesting the low density of defects due to strong surface passivation. Low temperature PL spectra show interesting vibrionic features that indicate exciton-phonon coupling and single size or narrow size distribution of the MCs. Furthermore, the MCs show good stability in solid and solution under ambient environment. Structural studies based on Raman, XRD and TEM led to the proposal of a layered structure of the MCs with corner shared tilted octahedra framework and BTYA ligand coordinating to Pb^{2+} on the surface. This study demonstrates that the facile process made amino metal halide MCs can retain their properties as isolated structures in solid form, making them promising for device applications in the future.

2.5 Experimental Methods

Materials

N,N-Dimethylformamide (DMF) 99.5% was purchased in Fisher Scientific. Butylamine (BTYA) 99.5%, toluene 99.9% and lead bromide ($PbBr_2$) 98% were purchased in Sigma-Aldrich.

Synthesis of $PbBr_2$-BTYA MCs in solution

First, 0.20 mmol $PbBr_2$ was dissolved in 500 μL DMF. Then, 2.00 mmol BTYA was added and dissolved with the help of sonication. Next, 100 μL of the precursor solution was injected quickly into 5.00 mL toluene stirring at 1300 rpm. Then, about 20 μL of colloidal sample was transferred into a 700 μL cuvette with 2 mm path length filled with toluene as anti-solution (680 μL) for UV-vis absorption and PL measurements.

Synthesis of $PbBr_2$-BTYA MCs in solid film

The glass substrates were pre-cleaned with soap, sonicated with deionized water for 20 minutes, and sonicated with acetone for 20 mins. After the cleaning, the substrates were left in the oven to dry.

The solid films were prepared with spin-coater set at the speed of ramp at 500 rpm for 10 s, followed by 3000 rpm for 30 s. About 70 μL of the MC precursor solution was used for spin-coating.

An alternative procedure of preparing a film was the drop-casting method by dropping several droplets of precursor solution on the center of glass substrate until filling the whole surface and waiting to be dried naturally in the ambient environment, which was mainly prepared for thick films towards XRD and Raman measurements.

Spectroscopic measurements

UV-vis absorption spectra were measured with an Agilent Technologies Cary 60 UV-Vis spectrophotometer. Fluorescence spectra were measured using a HORIBA Jobin Yvon Fluoromax-3 spectrofluorometer and all samples were excited at 365 nm. For low temperature PL measurements, $PbBr_2$-BTYA MCs sample was loaded into an Advanced Research Systems DMX-20 cryostat and excited at 365 nm with a UV lamp. The emitted PL was collected and dispersed onto a charged-coupled device (CCD) using a Princeton Instruments Acton 2300 Spectrometer (resolution ~ 0.18 nm). At a vacuum of 90 μTorr, PL was recorded every 10 K between 20 and 290 K.

Raman analysis was performed using a Thermo Fisher DRX3 Raman Micro Spectrometer. The laser excitation source was a diode laser (λ_{ex} = 785 nm). Spectra were recorded under the following conditions: stainless steel substrate, 50x objective, collect exposure time 30s for eight accumulations, laser power 1.5 mW (in focus) and aperture 50 μm slit. Raman spectra were recorded from ~5 different sample spots, depending on the homogeneity of the sample.

XRD measurement

X-ray diffraction (XRD) patterns were collected on a Bruker D8 Discover Diffractometer using Cu Ka radiation (40 kV and 40 mA) with degrees per step and time/step parameters of 0.02 degrees per step and 0.5 s/step, respectively, at 2θ angle from 1.5 to 40 °. X-ray diffraction patterns were plotted in Origin and the XRD diffraction pattern of pure $PbBr_2$ was compared to JCPDS PDF no. 31-0679.

TEM measurement

After preparing the colloidal sample with the precipitation method assisted by the antisolvent toluene, the solution was under sonication for 15 mins before dropping onto a hexagonal, 400 mesh copper grid with carbon support film of standard 3-4 nm thickness (Electron Microscopy Sciences, CF400H-Cu-UL) and allowed to dry in ambient environment.

HRTEM was performed at the National Center for Electron Microscopy (NCEM) at the Lawrence Berkeley National Laboratory Molecular Foundry on an FEI UT Tecnai microscope operated at 200 kV acceleration voltage. The images were analyzed with ImageJ and Gatan Digital Microscope software.

2.6 References

(1) Zhou, C.; Lin, H.; Worku, M.; Neu, J.; Zhou, Y.; Tian, Y.; Lee, S.; Djurovich, P.; Siegrist, T.; Ma, B. Blue Emitting Single Crystalline Assembly of Metal Halide Clusters. *J. Am. Chem. Soc.* **2018**, *140* (41), 13181–13184.

(2) Vickers, E. T.; Chen, Z.; Cherrette, V.; Smart, T.; Zhang, P.; Ping, Y.; Zhang, J. Z. Interplay between Perovskite Magic-Sized Clusters and Amino Lead Halide Molecular Clusters. *Research* **2021**, *2021*, 1-7.

(3) Liu, L.; Pan, K.; Xu, K.; Peng, X.; Zhang, J. Z. Synthesis and Optical Properties of Mn^{2+}-Doped Amino Lead Halide Molecular Clusters Assisted by Chloride Ion. *J. Phys. Chem. Lett.* **2021**, *12* (31), 7497–7503.

(4) Protesescu, L.; Yakunin, S.; Bodnarchuk, M. I.; Krieg, F.; Caputo, R.; Hendon, C. H.; Yang, R. X.; Walsh, A.; Kovalenko, M. V. Nanocrystals of Cesium Lead Halide Perovskites ($CsPbX_3$, X = Cl, Br, and I): Novel Optoelectronic Materials

Showing Bright Emission with Wide Color Gamut. *Nano Lett.* **2015**, *15* (6), 3692–3696.

(5) Pathak, S.; Sakai, N.; Wisnivesky Rocca Rivarola, F.; Stranks, S. D.; Liu, J.; Eperon, G. E.; Ducati, C.; Wojciechowski, K.; Griffiths, J. T.; Haghighirad, A. A.; et al. Perovskite Crystals for Tunable White Light Emission. *Chem. Mater.* **2015**, *27* (23), 8066–8075.

(6) Song, J.; Li, J.; Li, X.; Xu, L.; Dong, Y.; Zeng, H. Quantum Dot Light-Emitting Diodes Based on Inorganic Perovskite Cesium Lead Halides ($CsPbX_3$). *Adv. Mater.* **2015**, *27* (44), 7162–7167.

(7) Zhang, F.; Zhong, H.; Chen, C.; Wu, X.; Hu, X.; Huang, H.; Han, J.; Zou, B.; Dong, Y. Brightly Luminescent and Color-Tunable Colloidal $CH_3NH_3PbX_3$ (X = Br, I, Cl) Quantum Dots: Potential Alternatives for Display Technology. *ACS Nano* **2015**, *9* (4), 4533–4542.

(8) Hao, F.; Stoumpos, C. C.; Cao, D. H.; Chang, R. P. H.; Kanatzidis, M. G. Lead-Free Solid-State Organic–Inorganic Halide Perovskite Solar Cells. *Nat. Photonics* **2014**, *8* (6), 489–494.

(9) Liu, L.; Xu, K.; Vickers, E. T.; Allen, A.; Li, X.; Peng, L.; Zhang, J. Z. Varying the Concentration of Organic Acid and Amine Ligands Allows Tuning between Quantum Dots and Magic-Sized Clusters of $CH_3NH_3PbBr_3$ Perovskite: Implications for Photonics and Energy Conversion. *Acs Appl. Nano Mater.* **2020**, *3* (12), 12379–12387.

(10) Ning, J.; Banin, U. Magic Size InP and InAs Clusters: Synthesis,

Characterization and Shell Growth. *Chem. Commun.* **2017**, *53* (17), 2626–2629.

(11) Mule, A. S.; Mazzotti, S.; Rossinelli, A. A.; Aellen, M.; Prins, P. T.; van der Bok, J. C.; Solari, S. F.; Glauser, Y. M.; Kumar, P. V.; Riedinger, A.; et al. Unraveling the Growth Mechanism of Magic-Sized Semiconductor Nanocrystals. *J. Am. Chem. Soc.* **2021**, *143* (4), 2037–2048.

(12) Aharonovich, I.; Englund, D.; Toth, M. Solid-State Single-Photon Emitters. *Nat. Photonics* **2016**, *10* (10), 631–641.

(13) Xu, K.; Vickers, E. T.; Luo, B.; Wang, Q.; Allen, A. C.; Wang, H.; Cherrette, V.; Li, X.; Zhang, J. Z. Room Temperature Synthesis of Cesium Lead Bromide Perovskite Magic Sized Clusters with Controlled Ratio of Carboxylic Acid and Benzylamine Capping Ligands. *Sol. Energ. Mat. Sol. C.* **2020**, *208*, 110341.

(14) Xu, K.; Allen, A. C.; Luo, B.; Vickers, E. T.; Wang, Q.; Hollingsworth, W. R.; Ayzner, A. L.; Li, X.; Zhang, J. Z. Tuning from Quantum Dots to Magic Sized Clusters of $CsPbBr_3$ Using Novel Planar Ligands Based on the Trivalent Nitrate Coordination Complex. *J. Phys. Chem. Lett.* **2019**, *10* (15), 4409–4416.

(15) Guarino-Hotz, M.; Barnett, J. L.; Pham, L. B.; Win, A. A.; Cherrette, V. L.; Zhang, J. Z. Tuning between Methylammonium Lead Bromide Perovskite Magic-Sized Clusters and Quantum Dots through Ligand Assisted Reprecipitation at Elevated Temperatures. *J. Phys. Chem. C* **2022** *126* (32), 13854-13862.

(16) Li, H.; Yang, J.; Liang, C.; Zhang, W.; Zhou, M. Facile Electrochemical Synthesis of ZnO/PbSe Heterostructure Nanorod Arrays and PbSe Nanotube

Arrays. *Appl. Surf. Sci.* **2012**, *258* (22), 8959–8964.

(17) Vickers, E. T.; Xu, K.; Dreskin, B. W.; Graham, T. A.; Li, X.; Zhang, J. Z. Ligand Dependent Growth and Optical Properties of Hybrid Organo-Metal Halide Perovskite Magic Sized Clusters. *J. Phys. Chem. C* **2019**, *123* (30), 18746–18752.

(18) Stamplecoskie, K. G.; Manser, J. S.; Kamat, P. V. Dual Nature of the Excited State in Organic–Inorganic Lead Halide Perovskites. *Energ. Environ. Sci.* **2015**, *8* (1), 208–215.

(19) Naghadeh, S. B.; Sarang, S.; Brewer, A.; Allen, A.; Chiu, Y.-H.; Hsu, Y.-J.; Wu, J.-Y.; Ghosh, S.; Zhang, J. Z. Size and Temperature Dependence of Photoluminescence of Hybrid Perovskite Nanocrystals. *J. Chem. Phys.* **2019**, *151* (15), 154705.

(20) Smith, M. D.; Jaffe, A.; Dohner, E. R.; Lindenberg, A. M.; Karunadasa, H. I. Structural Origins of Broadband Emission from Layered Pb–Br Hybrid Perovskites. *Chem. Sci.* **2017**, *8* (6), 4497–4504.

(21) Dohner, E. R.; Jaffe, A.; Bradshaw, L. R.; Karunadasa, H. I. Intrinsic White-Light Emission from Layered Hybrid Perovskites. *J. Am. Chem. Soc.* **2014**, *136* (38), 13154–13157.

(22) Huang, S.; Yang, S.; Wang, Q.; Wu, R.; Han, Q.; Wu, W. $Cs_4PbBr_6/CsPbBr_3$ Perovskite Composites for WLEDs: Pure White, High Luminous Efficiency and Tunable Color Temperature. *RSC Adv.* **2019**, *9* (72), 42430–42437.

(23) Bryant, D.; Aristidou, N.; Pont, S.; Sanchez-Molina, I.; Chotchuangchutchaval, T.; Wheeler, S.; Durrant, J. R.; Haque, S. A. Correction: Light and Oxygen Induced Degradation Limits the Operational Stability of Methylammonium Lead Triiodide Perovskite Solar Cells. *Energ. Environ. Sci.* **2016**, *9* (5), 1850–1850.

(24) Anaya, M.; Galisteo-López, J. F.; Calvo, M. E.; Espinós, J. P.; Míguez, H. Origin of Light-Induced Photophysical Effects in Organic Metal Halide Perovskites in the Presence of Oxygen. *J. Phys. Chem. Lett.* **2018**, *9* (14), 3891–3896.

(25) Wozny, S.; Yang, M.; Nardes, A. M.; Mercado, C. C.; Ferrere, S.; Reese, M. O.; Zhou, W.; Zhu, K. Controlled Humidity Study on the Formation of Higher Efficiency Formamidinium Lead Triiodide-Based Solar Cells. *Chem. Mater.* **2015**, *27* (13), 4814–4820.

(26) Zhu, Z.; Wu, Y.; Shen, Y.; Tan, J.; Shen, D.; Lo, M.-F.; Li, M.; Yuan, Y.; Tang, J.-X.; Zhang, W.; et al. Highly Efficient Sky-Blue Perovskite Light-Emitting Diode via Suppressing Nonradiative Energy Loss. *Chem. Mater.* **2021**, *33* (11), 4154–4162.

(27) Leguy, A. M. A.; Goñi, A. R.; Frost, J. M.; Skelton, J.; Brivio, F.; Rodríguez-Martínez, X.; Weber, O. J.; Pallipurath, A.; Alonso, M. I.; Campoy-Quiles, M.; et al. Dynamic Disorder, Phonon Lifetimes, and the Assignment of Modes to the Vibrational Spectra of Methylammonium Lead Halide Perovskites. *Phys. Chem. Chem. Phys.* **2016**, *18* (39), 27051–27066.

(28) Hu, Z.; Wang, X.; Wang, W.; Zhang, Z.; Gao, H.; Mao, Y. Raman Spectroscopy for Detecting Supported Planar Lipid Bilayers Composed of Ganglioside-GM1/Sphingomyelin/Cholesterol in the Presence of Amyloid-β. *Phys. Chem. Chem. Phys.* **2015**, *17* (35), 22711–22720.

(29) Jia, Q.-Q.; Tong, L.; Lun, M.-M.; Fu, D.-W.; Zhang, T.; Lu, H.-F. Two-Dimensional Organic–Inorganic Hybrid Materials with Dielectric Switching and Photoluminescence Properties. *Cryst. Growth Des.* **2022**, *22* (5), 2799–2805.

(30) Xu, L.-J.; Worku, M.; He, Q.; Lin, H.; Zhou, C.; Chen, B.; Lin, X.; Xin, Y.; Ma, B. Ligand-Mediated Release of Halides for Color Tuning of Perovskite Nanocrystals with Enhanced Stability. *J. Phys. Chem. Lett.* **2019**, *10* (19), 5836–5840.

(31) Wang, H.; Zhao, X.; Zhang, B.; Xie, Z. Blue Perovskite Light-Emitting Diodes Based on RbX-Doped Polycrystalline $CsPbBr_3$ Perovskite Films. *J. Mater. Chem. C* **2019**, *7* (19), 5596–5603.

(32) Weidman, M. C.; Seitz, M.; Stranks, S. D.; Tisdale, W. A. Highly Tunable Colloidal Perovskite Nanoplatelets through Variable Cation, Metal, and Halide Composition. *ACS Nano* **2016**, *10* (8), 7830–7839.

(33) Chang, Y.-H.; Lin, J.-C.; Chen, Y.-C.; Kuo, T.-R.; Wang, D.-Y. Facile Synthesis of Two-Dimensional Ruddlesden–Popper Perovskite Quantum Dots with Fine-Tunable Optical Properties. *Nanoscale Res. Lett.* **2018**, *13* (1).

(34) Dou, L. Emerging Two-Dimensional Halide Perovskite Nanomaterials. *J. Mater. Chem. C* **2017**, *5* (43), 11165–11173.

(35) Era, M.; Kobayashi, T.; Noto, M. PbBr-Based Layered Perovskite Organic–Inorganic Superlattice Having Hole-Transporting Carbazole Chromophore in Organic Layer. *Curr. Appl. Phys.* **2005**, *5* (1), 67–70.

(36) Sengupta, A.; Mandal, K. C.; Zhang, J. Z. Ultrafast Electronic Relaxation Dynamics in Layered Iodide Semiconductors: A Comparative Study of Colloidal BiI_3 and PbI_2 Nanoparticles. *J. Phys. Chem. B* **2000**, *104* (40), 9396–9403.

(37) Tian, Y.; Zhou, C.; Worku, M.; Wang, X.; Ling, Y.; Gao, H.; Zhou, Y.; Miao, Y.; Guan, J.; Ma, B. Light-Emitting Diodes: Highly Efficient Spectrally Stable Red Perovskite Light-Emitting Diodes. *Adv. Mater.* **2018**, *30* (20), 1870142.

3 Ultrafast Study of Excited State Dynamics of Amino Metal Halide Molecular Clusters

3.1 Abstract

The excited state dynamics of ligand-passivated $PbBr_2$ molecular clusters (MCs) in solution have been investigated for the first time using femtosecond (fs) transient absorption spectroscopy. The results uncover a transient bleach (TB) feature peaked around 404 nm, matching the ground state electronic absorption band peaked at 404 nm. The TB recovery signal can be fitted with a triple exponential with fast (10 ps), medium (350 ps), and long (1.8 ns) time constants. The medium and long time constants are very similar to those observed in the TRPL decay monitored at 412 nm. The TB fast component is attributed to vibrational relaxation in the excited electronic state while the medium component with dominant amplitude is attributed to recombination between the relaxed electron and hole. The small amplitude long component is assigned to electrons in a relatively long-lived excited electronic state, *e.g.*, triplet state or shallow trap state due to defects. This study provides new insights into the excited state dynamics of metal halide MCs.

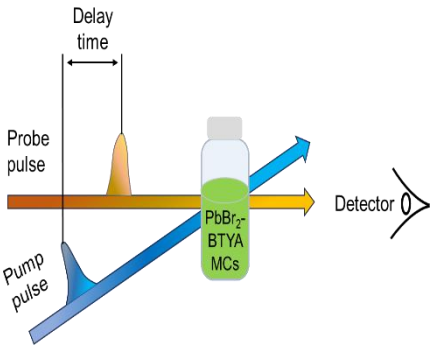

3.2 Introduction

Recently, metal halide molecular clusters (MCs) have been subject to increasing

interest due to their unique characteristics such as much smaller size and larger surface-to-volume (S/V) ratio compared to typical metal halide perovskite quantum dots (PQDs).[1-3] Their extremely small size results in stronger quantum-confined and bluer optical absorption and emission than PQDs.[4-10] In addition, they are potential intermediates to larger perovskite structures including PQDs and can be used to study the growth mechanisms of larger structures.[2,3,11]

Ligand-passivated $PbBr_2$ MCs exhibit first excitonic absorption and emission band peaked around 402 and 410 nm, respectively, which are bluer than both corresponding PQDs and perovskite magic-sized clusters (PMSCs).[2,3,8] Unlike their larger perovskite counterparts, the key difference among them is that metal halide MCs lack the A component that is present in PQDs and PMSCs with ABX_3 composition, as demonstrated by past work from our lab.[2] Also, further study showed that metal halide MCs can be generated alongside PQDs and PMSCs even when the A component is present.[12] More recent structural study incorporating Raman, XRD, and TEM suggests that $PbBr_2$-BTYA MCs consist of a possible layered structure where the layers are composed of tilted, corner-sharing $[PbBr_6]^{4-}$ octahedra with a particle size of 2.0 ± 0.4 nm.[8] Although past work has shed insights into metal halide MCs' optical and structural properties, the excited state dynamics of the ligand-passivated $PbBr_2$ MCs that are relevant to many potential optoelectronic applications have not been studied yet.

In this work, fs laser transient absorption spectroscopy was used to probe the excited state dynamics of ligand-passivated $PbBr_2$ MCs in a transient absorption

configuration. The results reveal a relatively short overall excited state lifetime on the order of 350 ps, which is consistent with the relatively low photoluminescence quantum yield (PLQY) of 4%. The radiative and nonradiative lifetimes extracted from the observed lifetime and PLQY indicate that exciton decay is dominated by a nonradiative pathway.

3.3 Results and Discussion

To acquire a transient absorption (TA) signal, an ideal sample is clear or nearly transparent. Stable MCs can be synthesized only with amine ligands, but they tend to be opaque. To achieve this, the $PbBr_2$-BTYA MCs precursor was modified by adding an acidic ligand, namely valeric acid, which results in a clear MC solution.[12]

Figure 3-1 shows the absorption and PL spectra of clear $PbBr_2$-BTYA MCs in solution, where the first electronic absorption and emission bands appear at 404 nm and 412 nm, respectively. The addition of valeric acid results in a nominal peak position difference of 3 nm for the absorption and 1 nm for the PL when compared with the $PbBr_2$-BTYA MCs reported previously, attributed to a minor difference in particle size.[2,7] The change in precursor composition for the synthesis of clear $PbBr_2$-BTYA MCs allows us to generate a sample that is sufficiently transparent for the fs TA study, as shown in the Figure 3-1 inset. In addition, the PL spectrum shows a full width at half maximum (FWHM) of 10 nm, indicative of the narrow size distribution of this MC species.[2,6,7,12,13] Moreover, the Stokes shift observed between absorption and PL emission is only 8 nm and there is no PL from trap states observed.

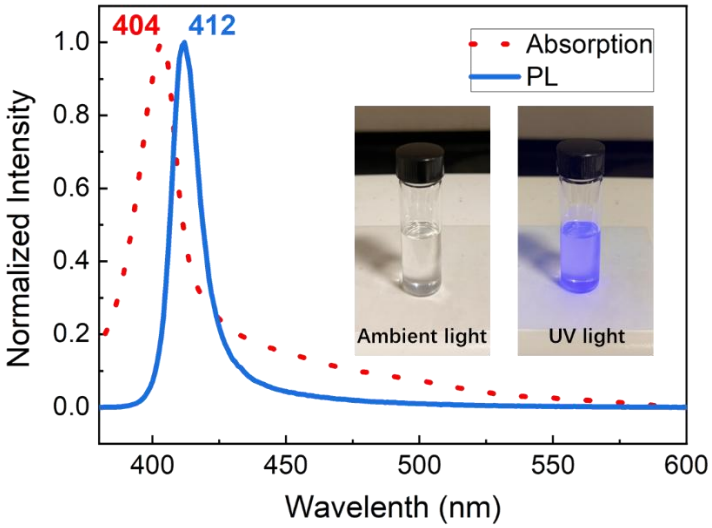

Figure 3-1 Optical properties of clear $PbBr_2$-BTYA MCs in solution. UV-vis absorption spectrum (red) and PL spectrum (blue) of clear $PbBr_2$-BTYA MCs in solution state. Inset: images of clear MCs in solution state under ambient light and 365 nm UV light.

To determine the exciton dynamics of $PbBr_2$-BTYA MCs, fs TA of colloidal $PbBr_2$-BTYA was measured in a pump–probe laser configuration (layout can be found at Chapter 1, 1.5 Instrument Section). The TB spectra were collected with a pump wavelength of 370 nm, at a low pump power of 0.1 μJ/pulse and probed by white light in the 350-550 nm region.

The control experiments for TB signal of $PbBr_2$-BTYA MCs were conducted to rule out the solvent toluene influence. Figure 3-2 shows the transient absorption spectra of the solvent toluene probed at 404 nm under 0.1, 0.3 and 0.5 μJ/pulse. From the spectra, an outstanding spike can be easily seen near t_0 due to coherent interference between the pump and probe light. More importantly, there is no

transient bleach signal shown from toluene under any pump powers, which rules out the TB signal of solvent for the $PbBr_2$-BTYA MCs.

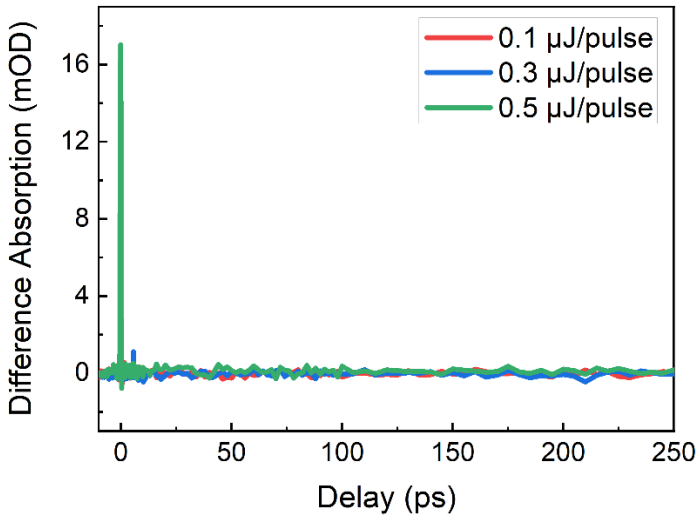

Figure 3-2 Transient absorption spectra of the solvent toluene probed at 404 nm and excited at 370 nm under 0.1, 0.3 and 0.5 μJ/pulse pump powers.

Figure 3-3 shows TB spectra across the probe wavelength region of 390-440 nm from -1 to 100 ps (Figure 3-3a), from -1 to 4000 ps (Figure 3-3b), and a kinetic trace extracted from the peak TB signal at 404 nm from -1 to 4000 ps (Figure 3-3c). Both the spectra in Figure 3-3 (a) and the kinetic trace in Figure 3-3 (c) have been modified to remove a strong positive feature immediately preceding t_0. This feature is attributed to coherent interference artifact induced between the pump and probe pulse.[14-19] Importantly, the spike was also seen in the toluene blank where no sample was present, confirming the removed feature near t_0 does not have a contribution from the sample itself. In Figure 3-3 (a), the TB signal first decreases to a minimum, limited by the laser pulse width, and then gradually recovers to zero. The TB band

shows a maximum signal around 404 nm, which matches the first electronic absorption band peak at 404 nm.

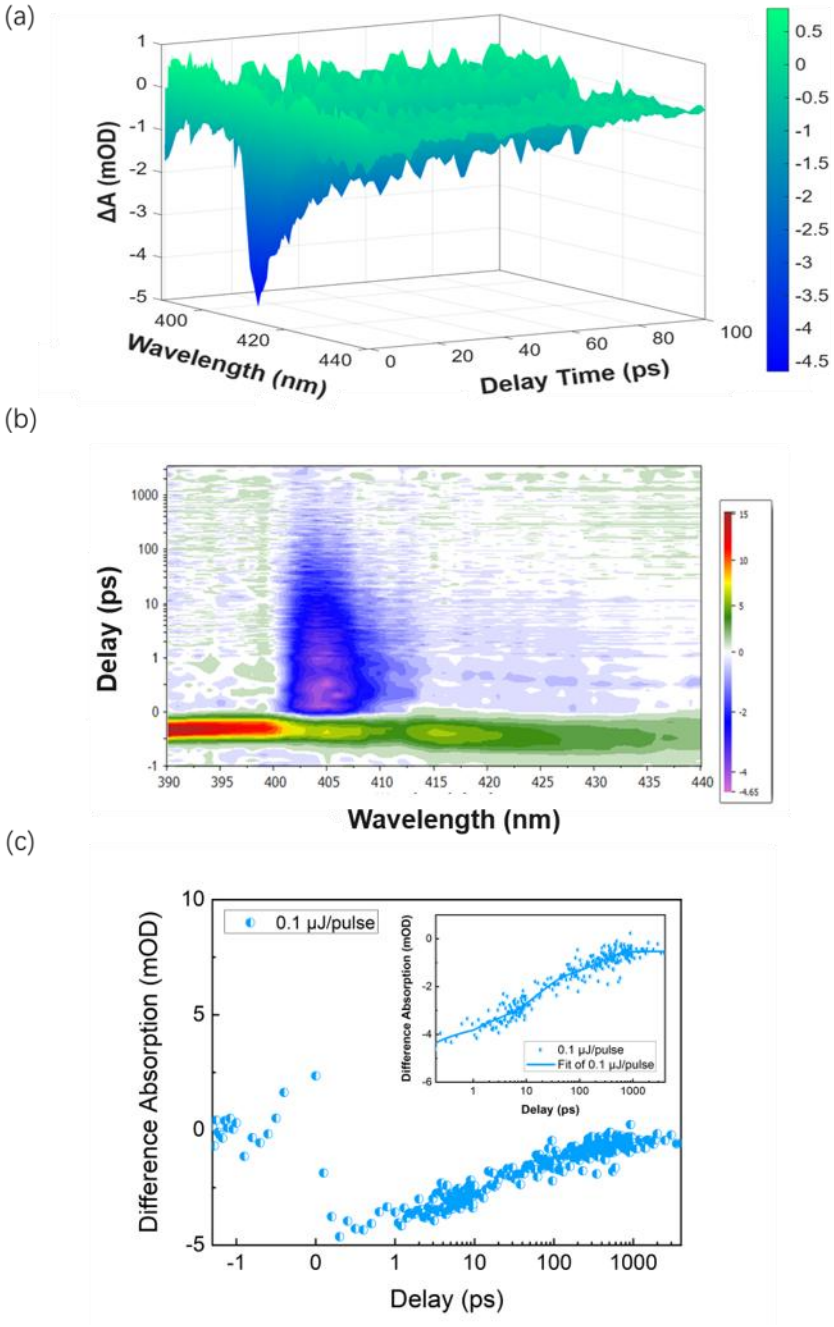

Figure 3-3 Transient bleach spectra of $PbBr_2$-BTYA MCs with excitation (pump) wavelength at 370 nm and probe wavelength in 390-440 nm region and pump power

at 0.1 μJ/pulse (plotted in (a) 3D on the -1-100 ps time scale, (b) 2D over -1-4000 ps time scale and (c) TB profile and associated fitting for TB profile at 404 nm in -1-4000 ps).

In Figure 3-3 (b), the contour plot shows the 2D evolution of the TB signal in terms of both delay time and wavelength. Consistent with Figure 3-3 (a), the strongest TB signal appears around 404 nm and recovery to baseline persists over the probe range. The aforementioned coherent pump–probe interference is also shown here as a positive feature (red and green region) just before t_0 across the range of probed wavelength.[20,21]

Figure 3-3 (c) is a TB decay profile at 404 nm plotted from -1-4000 ps with the associated fitting from 0-4000 ps shown in the inset. The TB recovery for pump power of 0.1 μJ/pulse is well fitted with a triple exponential function with time constants of 10 ps, 350 ps, and 1.8 ns. Similar TB profiles were measured with other excitation wavelengths of 360 nm and 380 nm, indicating that the dynamics are not dependent on excitation (pump) wavelength.[20]

Figure 3-4 shows the TA kinetics and spectra of $PbBr_2$-BTYA MCs under 0.1 μJ/pulse pump power. From Figure 3-4 (a), the maximum TB intensity is increasing but the maximum TA intensity is decaying with time evolving. The TA signal decayed completely after about 0.2 ps, showing the lifetime of TA is short. However, this is close to the time resolution of the laser system, which is around 0.159 ps. Figure 3-4 (b) shows the TA/TB kinetics probed at 404 nm and 416 nm. The coherent interference artifact shows up in both kinetics profiles near t=0. The TB signal decays

and recovers to 0 difference absorption in the whole probing time scale from 0- 4000 ps, while the TA signal rises and decays to 0 difference absorption in less than 1 ps and is mixed with the coherent artifact.

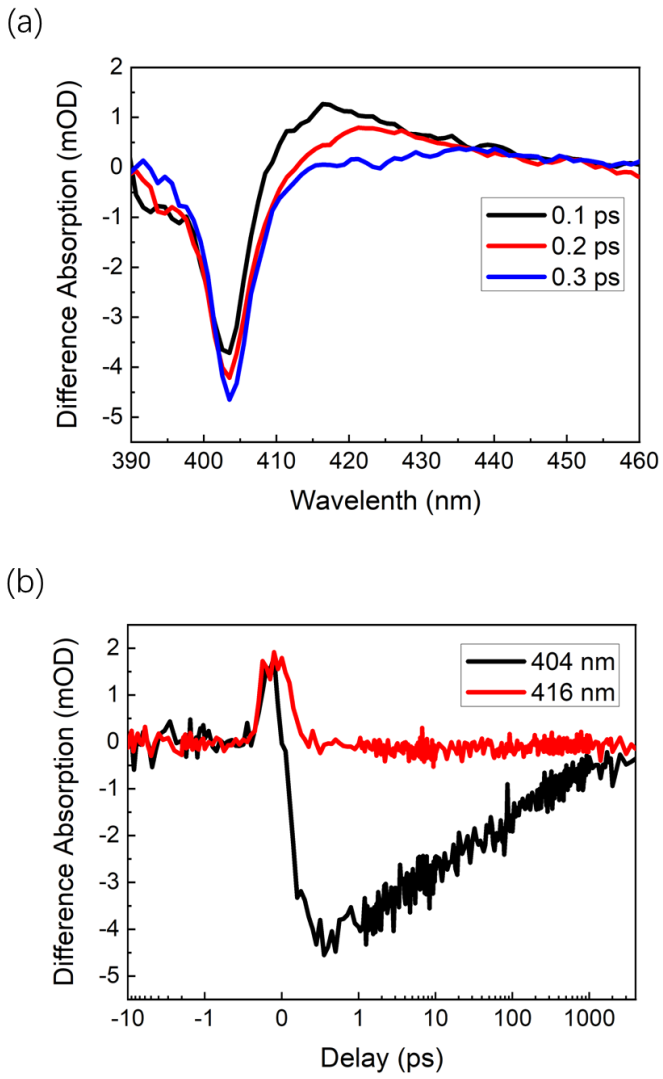

Figure 3-4 TA/TB spectra and kinetics of $PbBr_2$-BTYA MCs probed with 370 nm pump under 0.1 μJ/pulse pump power. (a) TA/TB spectra at 0.1, 0.2 and 0.3 ps delay time. (b) TA/TB kinetics probed at 404 nm and 416 nm.

To determine the possible power dependence of the excited state dynamics, TB results were measured with different pump powers. Figure 3-5 shows the TB profiles of $PbBr_2$-BTYA MCs probed at 404 nm under a range of pump powers. The artifact spike near t_0 not reflecting a true decay feature has been removed for ease of visualization of the data. The TB profiles show that the peak amplitude near t_0 increases with increasing pump powers. The amplitude of the fast component increases linearly in the low power region (0.1-0.3 μJ/pulse) but more than linearly with power under higher pump powers (0.4-0.5 μJ/pulse). However, since the amplitude becomes very small at lower power, it is not determined if the fast time constant has a real pump power dependence, although based on both the time constants and amplitudes, there appears to be a transition to the non-linear regime under higher pump power. Usually, a shorter lifetime is expected for higher power when nonlinear effects, such as exciton-exciton annihilation or Auger recombination, are involved.[20-24] The fitting parameters, including amplitudes and time constants under five pump powers corresponding to Figure 3-5, are summarized in Tables 3-1 and 3-2. The parameters A_1, A_2, and A_3 denote amplitude and τ_1 , τ_2 and τ_3 denote time constant at fast, medium and slow components, respectively. In Table 3-1, the short, medium, and long time constants are fixed, while in Table 3-2, the medium and long time constants are fixed, and the short time constants are not fixed.

To better assess the linear and nonlinear regions, the fast component time constants were held constant at 10 ps as shown in Table 3-1. In this way, it was determined that the amplitudes transition from a linear to more than linear increase at

high pump powers. In Table 3-2, this distinction is supported by allowing the fast component to vary during fitting, the result of which shows a decreasing trend in the fast component time constants and a corresponding increase in amplitude transitioning from linear at low pump powers to more than linearly at high pump powers. Both the 350 ps and 1800 ps decay time constants for medium and slow components were also held constant for all the fits based on the fitting result from TRPL due to the greatly improved signal-to-noise ratio and will be discussed later. To avoid possible nonlinear effects, we focus our discussion on the lower pump powers data that are in the linear regime as determined by the fast component amplitude and time constants.

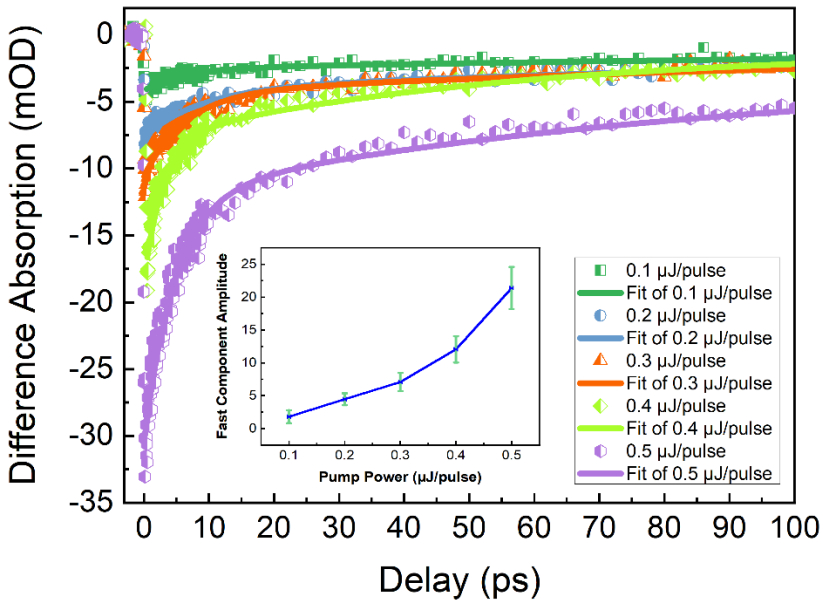

Figure 3-5 Transient bleach profile of $PbBr_2$-BTYA MCs under the pump powers at 0.1, 0.2, 0.3, 0.4 and 0.5 μJ/pulse, respectively, probed at 404 nm and excited at 370

nm. Inset: the power dependence of the fast component amplitude shows a linear process under low pump powers and a nonlinear process under high pump powers.

Table 3-1 Summary of parameters used to fit the transient bleach spectra at different pump powers with fixed tau1s.

Components	**0.1 μJ/pulse**	**0.2 μJ/pulse**	**0.3 μJ/pulse**	**0.4 μJ/pulse**	**0.5 μJ/pulse**
A_1	-2±1 (49%)	-4.5±0.9 (58%)	-7±1 (70%)	-12±2 (81%)	-21±3 (77%)
τ_1 (ps)	10±6	10±2	10±2	10±2	10±2
A_2	-1.5±0.4 (37%)	-2.6±0.3 (33%)	-2.2±0.4 (22%)	-2.1±0.4 (14%)	-3.2±0.8 (12%)
τ_2 (ps)	350±90	350±40	350±70	350±70	350±90
A_3	-0.6±0.3 (14%)	-0.7±0.2 (9%)	-0.8±0.4 (8%)	-0.8±0.4 (5%)	-3±2 (11%)
τ_3 (ps)	1800±900	1800±500	1800±900	1800±900	1800±900

Table 3-2 Summary of parameters used to fit the transient bleach spectra at different pump powers with varied tau1s.

Components	**0.1 μJ/pulse**	**0.2 μJ/pulse**	**0.3 μJ/pulse**	**0.4 μJ/pulse**	**0.5 μJ/pulse**
A_1	-2±1 (49%)	-4.5±0.9 (60%)	-7±1 (69%)	-13±2 (78%)	-22±3 (76%)
τ_1 (ps)	10±6	14±3	9±2	7±1	7±1
A_2	-1.5±0.4	-2.1±0.2	-2.5±0.5	-3.4±0.7	-5±1

	(37%)	(28%)	(25%)	(20%)	(17%)
τ_2 (ps)	350±90	350±40	350±70	350±70	350±90
A_3	-0.6±0.3 (14%)	-0.9±0.3 (12%)	-0.7±0.4 (6%)	-0.3±0.2 (2%)	-2±1 (7%)
τ_3 (ps)	1800±900	1800±500	1800±900	1800±900	1800±900

Figure 3-6 shows the TRPL profile of the $PbBr_2$-BTYA MCs measured at 412 nm following excitation at 370 nm. The selection of excitation bluer than the absorption peak at 404 nm is to allow better separation of the PL emission from the excitation light that can interfere with the TRPL measurement. The TRPL profile can be fitted with two time constants of 350 ps and 1.8 ns in an error of less than 0.2%, which are used for the medium and long time constants of the TB results. The details of the TRPL double-exponential fitting parameters can be found in Table 3-3, where A denotes the amplitude, τ denotes the time constant, and subscripts 1 and 2 denote the fast and slow components.

Therefore, we suggest that the 350 ps component in TRPL and the 350 ps component in TB correspond to the same dynamic process while, similarly, the 1.8 ns component observed in both TRPL and TB are due to the same dynamic process.

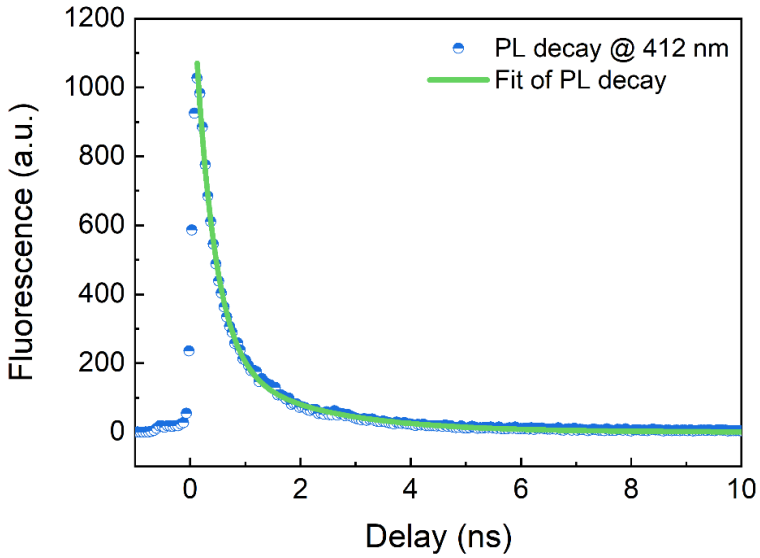

Figure 3-6 TRPL profile of $PbBr_2$-BTYA MCs monitored at 412 nm following excitation at 370 nm based on time-correlated single photon counting (TCSPC) measurements.

Table 3-3 Summary of parameters of the TRPL fitting results.

Components	**412 nm**
A_1	1219±6
τ_1 (ps)	350±10
A_2	231±6
τ_2 (ns)	1.80±0.02

To help gain deeper insight into exciton decay dynamics, the PLQY was

measured using quinine sulfate as a reference and used along with the TB results to extract the radiative and nonradiative lifetimes. Figure 3-7 shows the fitted slopes collected from both quinine sulfate and $PbBr_2$-BTYA MCs. The absorption of both samples was measured in the range of 0.02-0.1 optical density (OD) to facilitate a linear relationship between integrated PL intensity and absorption. The PLQY of $PbBr_2$-BTYA MCs was calculated as 4%, and after combining the PLQY result with the lifetime of the dominant component of 350 ps, which we consider as the observed excited state lifetime τ_{obs}, the radiative and nonradiative lifetimes were calculated based on Equations (3-1) and (3-2). The radiative lifetime is calculated as ~9 ns, 24 times longer than the nonradiative lifetime of ~365 ps, indicating that the dynamics are dominated by nonradiative decays.[25,26]

$$\frac{1}{\tau_{obs}} = \frac{1}{\tau_r} + \frac{1}{\tau_{nr}} \tag{3-1}$$

$$\phi_{PL} = \frac{\tau_{obs}}{\tau_\gamma} \tag{3-2}$$

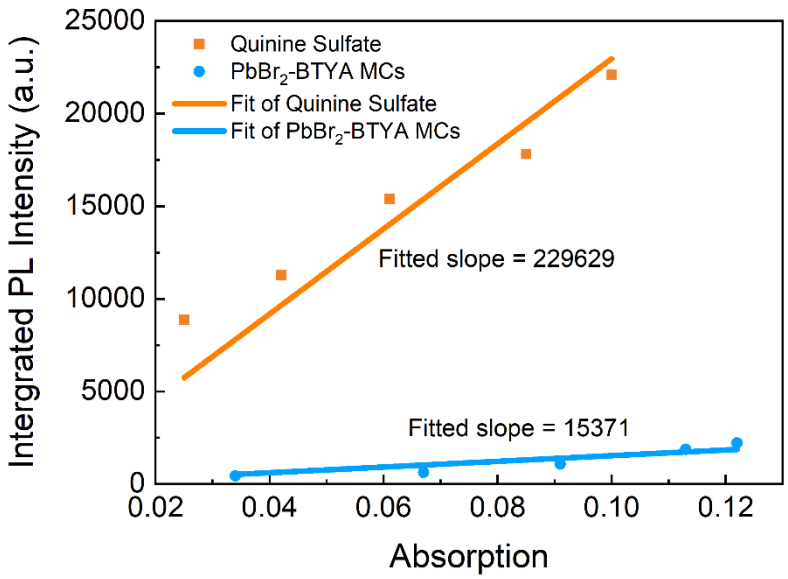

Figure 3-7 The linear correlation between integrated PL intensity versus absorption of quinine sulfate and $PbBr_2$-BTYA MCs.

Figure 3-8 illustrates the key dynamic processes in photoexcited $PbBr_2$-BTYA MCs that we propose based on the spectroscopy and dynamics results. This model only illustrates the exciton dynamics under low pump powers, where there are no nonlinear dynamic processes that tend to occur under high pump powers, such as two-photon decays, exciton-exciton annihilation, and Auger recombination, which often complicate data analysis. Under low pump powers, upon photoexcitation, an electron is generated in the excited electronic state and a hole in the ground state, forming an exciton.[27,28] If possessing excess kinetic energy, the electron will relax to the bottom of the excited electronic state through vibrational relaxation via electron–phonon coupling. The relaxed electron can recombine radiatively, resulting in PL, or nonradiatively with the hole in the ground electronic state, resulting in a medium

decay lifetime (~350 ps) in TB which corresponds to a fast component (~350 ps) in TRPL.[28] The small amplitude slow component (1.8 ns) observed in both TB and TRPL is tentatively attributed to a relatively long-lived triplet or trap state that is coupled to the first excited electronic state responsible for the primary dynamics observed (dominant 350 ps decay with large amplitude). The dynamics signal observed is always a sum of the TA signal from the excited electronic state and the TB signal from the ground electronic state. What is observed depends on the relative intensity of the TA versus TB signals at a specific probe wavelength and at a specific time during the dynamic process. At the 404 nm probe wavelength, TB is dominant and used by us to analyze the dynamics. Because the signal we measured involves both TA and TB with opposite signs, the amplitude and lifetime of the signal measured may have complex dependence on pump powers, however, the TB is dominating according to the transient absorption spectra shown in Figure 3-4. Thus, we should use both amplitude and lifetime to analyze possible power dependence, such as linear versus nonlinear effects.

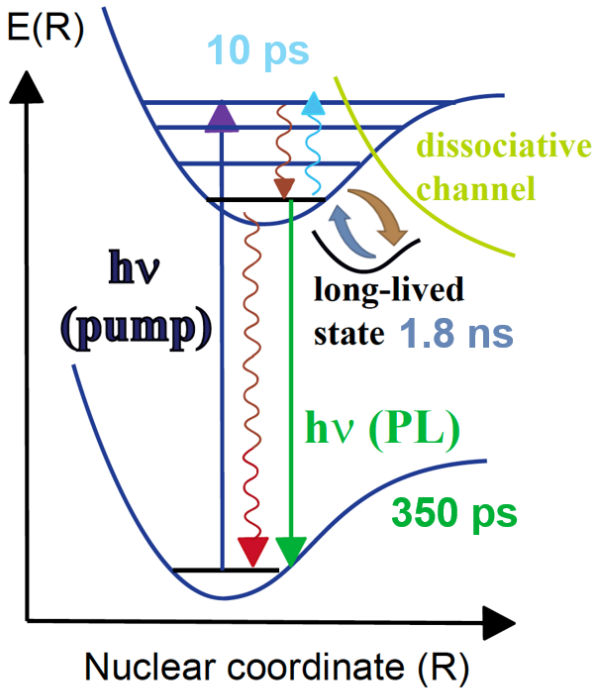

Figure 3-8 A proposed model for key dynamic processes in $PbBr_2$-BTYA MCs, including vibrational relaxation in the excited electronic state, recombination of relaxed electron and hole, a dissociative excited electronic state that leads to the overall short excited state lifetime, and a long-lived (>1 ns) triplet state or trap state that is coupled to the excited electronic state responsible for the primary dynamics observed including the PL and TRPL results.

The triple exponential decay of the TB signal indicates that the overall dynamics process is not a simple sequential or parallel process but involves energy transfer in the reverse direction, noted in Figure 3-8 as an upward curved arrow.[21,27] This back energy transfer process is usually expected to be much slower than the forward process.[27] Due to the limited dynamics data available such as all relevant time or rate constants, at present it is not possible to do meaningful kinetic modeling of the

overall dynamics of the MCs studied. Instead, based on our previous kinetic modeling of PQDs,[20,27] we suggest that a likely reverse process is a back energy transfer from vibrationally relaxed states to hot states in the excited electronic state, which could result in the multiple exponential features observed. Overall, we attribute the short decay of 10 ps to vibrational relaxation in the first excited electronic state, the medium 350 ps decay to the recombination of the relaxed electron with the hole, and the long 1.8 ns decay to a relatively long-lived electronic state, which is coupled to the first excited electronic state and mediates its dynamics. The relatively narrow absorption band and small Stokes shift between the absorption and PL bands indicate a flat potential energy surface (PES) for the excited electronic state. The dominant nonradiative decay of the first excited electronic state could be due to strong coupling to a dissociative excited electronic state. On the other hand, the moderate lifetime of the first excited electronic state observed (dominated by the 350 ps component) suggests that this state is bound and not directly dissociative in itself.

However, if the MCs are more solid-like, an explanation of the dynamics using an electronic band structure would be more appropriate.[28] In this case, the 10 ps fast decay component may be attributed to the trapping of the charge carriers (electron or hole) into shallow trap states or self-trapped excisions (STE), while the 350 ps slow component is attributed to the recombination of trapped electron and hole following trapping. The 1.8 ns slow decay would be likely due to some long-lived deep trap states that are coupled to and mediate the dynamics of the shallow trap states. Similar

to the above analysis, a reverse process is required to account for the multiple exponential decays observed, and we suggest de-trapping from the shallow trap states to the conduction band (CB) as the reverse process. If this explanation is correct, the narrow absorption band and small Stokes shift between the absorption and PL bands would suggest that the trap states are shallow or near the band edge, about 60 meV below the CB edge. Also, the relatively low PLQY of 4% indicates the trapped carriers or trapped excitons, similar to self-trapped excitons, which decay primarily nonradiatively and are usually attributed to deep trap states due to defects.[29,30]

3.4 Conclusion

In summary, the excited state dynamics of $PbBr_2$ MCs passivated with butylamine and valeric acid were studied using fs TA spectroscopy. A TB profile peaked at 404 nm shows a recovery that can be fitted with a triple exponential with a fast (10 ps), medium (350 ps) and slow (1.8 ns) component. These decay components are attributed to vibrational relaxation within the first excited electronic state, relaxed electron-hole recombination coupled to a dissociative electronic state, and another long-lived excited electronic state. A PLQY of 4% is consistent with the overall moderately long excited state lifetime of these metal halide MCs, which is revealed for the first time using ultrafast laser spectroscopy. The results are important for gaining a deeper understanding of the photophysics of metal halide clusters and related metal halide perovskite clusters.

3.5 Experimental Methods

Materials

N, N-Dimethylformamide (DMF) 99.5% was purchased from Fisher Scientific. Butylamine (BTYA) 99.5%, toluene 99.9% and lead bromide ($PbBr_2$) 98% were purchased from Sigma-Aldrich. Valeric acid (VA) 99% was purchased from Alfa Aesar. All reagents were used as received without further purification.

Synthesis of clear $PbBr_2$-BTYA MCs in solution

First, 0.20 mmol $PbBr_2$ was dissolved in 500 μL DMF. Then, 2.00 mmol VA was added and sonicated for 15 s until dissolved. Subsequently, 2.00 mmol BTYA was added and sonicated for 15 s until dissolved. Next, 100 μL of the precursor solution was injected quickly into 5.00 mL toluene under robust stirring at 1300 rpm. Finally, 20 μL of the colloidal sample was injected into a 700 μL cuvette with a 2 mm path length filled with toluene (680 μL) as anti-solution for characterization using UV-Vis absorption and PL spectroscopy. To perform ultrafast laser transient absorption (TA) measurements, the sample was further dissolved by injecting 1.00 mL of the colloidal sample into 6.00 mL of toluene for a total 1:300 dilution, and the diluted solution was transferred to a 2 mm light path cuvette.

Spectroscopic measurements

UV-vis absorption spectra were measured with an Agilent Technologies Cary 60 UV-Vis Spectrophotometer with a xenon source lamp. PL spectra were acquired using a HORIBA Jobin Yvon Fluoromax-3 spectrofluorometer.

Transient bleach (TB) measurements were taken using a Light Conversion femtosecond laser system. The pump and probe beams were generated by a ytterbium-doped potassium gadolinium tungstate (Yb:KGW) lasing medium (PHAROS, Light Conversion) with a fundamental output frequency of 1030 nm at a power of 10 W, a repetition rate of 20 kHz and pulse width of 159 fs. 90% of the fundamental beam was pathed through an optical parametric amplifier (ORPHEUS, Light Conversion) to produce tunable pump wavelengths and a nonlinear second harmonic generating unit (LYRA, Light Conversion) was employed to attain the pump wavelength of 370 nm. The generated probe beam was routed to the sample located in an ultrafast spectroscopy unit (HARPIA, Light Conversion) where the temporal alignment was controlled via an automated translating stage.

10% of the fundamental beam was routed around the OPA to the HARPIA unit, passing through a white light supercontinuum generating crystal to produce the probe light spectrum before being directed to the sample. Due to the sample absorbance falling in the UV region, a lens telescope and second harmonic generating unit were added to the probe beam path to achieve a probe region between 350 and 500 nm.

Data was collected using the corresponding Light Conversion HARPIA Service App software and using an Oxford Instruments Andor spectrometer. The transient

bleach recovery data were fitted in Origin software with a built-in triple exponential decay function $y = A_1*\exp(-x/t_1) + A_2*\exp(-x/t_2) + A_3*\exp(-x/t_3)$.

TRPL was conducted via the time-correlated single photon counting (TCSPC) measurements, using the Light Conversion equipment previously described in a similar layout to the TA measurements, but with the addition of a 400 nm long pass filter to remove the pump beam from the beam path after excitation, the probe light off, and the chopper disabled. The measurement was taken using a 370 nm excitation wavelength at minimum pump power, using a 10 s collection time, and recorded using a photomultiplier tube affixed to an Oxford Instruments Andor Kymera spectrometer and using the corresponding HARPIA service app data acquisition software. The data was processed using Origin and was fit using a built-in double exponential function $y = A_1*\exp(-x/t_1) + A_2*\exp(-x/t_2)$.

3.6 References

(1) Zhou, C.; Lin, H.; Worku, M.; Neu, J.; Zhou, Y.; Tian, Y.; Lee, S.; Djurovich, P.; Siegrist, T.; Ma, B. Blue Emitting Single Crystalline Assembly of Metal Halide Clusters. *J. Am. Chem. Soc.* **2018**, *140* (41), 13181–13184.

(2) Vickers, E. T.; Chen, Z.; Cherrette, V.; Smart, T.; Zhang, P.; Ping, Y.; Zhang, J. Z. Interplay between Perovskite Magic-Sized Clusters and Amino Lead Halide Molecular Clusters. *Research* **2021**, *2021*, 1-7.

(3) Liu, L.; Pan, K.; Xu, K.; Peng, X.; Zhang, J. Z. Synthesis and Optical Properties of Mn^{2+}-Doped Amino Lead Halide Molecular Clusters Assisted by Chloride Ion. *J. Phys. Chem. Lett.* **2021**, *12* (31), 7497–7503.

(4) Liu, L.; Xu, K.; Vickers, E. T.; Allen, A.; Li, X.; Peng, L.; Zhang, J. Z. Varying the Concentration of Organic Acid and Amine Ligands Allows Tuning between Quantum Dots and Magic-Sized Clusters of $CH_3NH_3PbBr_3$ Perovskite: Implications for Photonics and Energy Conversion. *Acs Appl. Nano Mater.* **2020**, *3* (12), 12379–12387.

(5) Guarino-Hotz, M.; Barnett, J. L.; Pham, L. B.; Win, A. A.; Cherrette, V. L.; Zhang, J. Z. Tuning between Methylammonium Lead Bromide Perovskite Magic-Sized Clusters and Quantum Dots through Ligand Assisted Reprecipitation at Elevated Temperatures. *J. Phys. Chem. C* **2022** *126* (32), 13854-13862.

(6) Xu, K.; Allen, A. C.; Luo, B.; Vickers, E. T.; Wang, Q.; Hollingsworth, W. R.; Ayzner, A. L.; Li, X.; Zhang, J. Z. Tuning from Quantum Dots to Magic Sized Clusters of $CsPbBr_3$ Using Novel Planar Ligands Based on the Trivalent Nitrate Coordination Complex. *J. Phys. Chem. Lett.* **2019**, *10* (15), 4409–4416.

(7) Zhang, H.; Vickers, E. T.; Erickson, S.; Guarino-Hotz, M.; Barnett, J. L.; Ghosh, S.; Zhang, J. Z. Synthesis and Properties of Stable Amino Metal Halide Molecular Clusters in the Solid State. *J. Phys. Chem. Lett.* **2022**, *13* (45), 10543–10549.

(8) Xu, K.; Vickers, E. T.; Luo, B.; Wang, Q.; Allen, A. C.; Wang, H.; Cherrette, V.; Li, X.; Zhang, J. Z. Room Temperature Synthesis of Cesium Lead Bromide Perovskite Magic Sized Clusters with Controlled Ratio of Carboxylic Acid and Benzylamine Capping Ligands. *Sol. Energy Mater. Sol. Cells* **2020**, *208*, 110341.

(9) Vickers, E. T.; Xu, K.; Dreskin, B. W.; Graham, T. A.; Li, X.; Zhang, J. Z. Ligand Dependent Growth and Optical Properties of Hybrid Organo-Metal Halide Perovskite Magic Sized Clusters. *J. Phys. Chem. C* **2019**, *123* (30), 18746–18752.

(10) Guarino-Hotz, M.; Barnett, J. L.; Chou, K.-C.; Win, A. A.; Zhang, H.; Song, C.; Oliver, S. R. J.; Zhang, J. Z. Structural Study of Paraffin-Stabilized Methylammonium Lead Bromide Magic-Sized Clusters. *J. Phys. Chem. C* **2023**, *127* (6), 3367–3376.

(11) Liu, L.; Pan, K.; Xu, K.; Zhang, J. Z. Impact of Molecular Ligands in the Synthesis and Transformation between Metal Halide Perovskite Quantum Dots and Magic Sized Clusters. *ACS Phys. Chem. Au* **2022**, *2* (3), 156–170.

(12) Win A.; Chou K. C.; Zeitz D. C.; Todd C.; Zhang J. Z. Origin of the near 400 nm Absorption and Emission Band in the Synthesis of Cesium Lead Bromide Nanostructures: Metal Halide Molecular Clusters Rather Than Perovskite Magic-Sized Clusters. *J. Phys. Chem. Lett.* **2023** *14* (1), 116-121.

(13) Xu, K.; Vickers, E. T.; Luo, B.; Allen, A. C.; Chen, E.; Roseman, G.; Wang, Q.; Kliger, D. S.; Millhauser, G. L.; Yang, W.; et al. First Synthesis of Mn-Doped Cesium Lead Bromide Perovskite Magic Sized Clusters at Room Temperature. *J. Phys. Chem. Lett.* **2020**, *11* (3), 1162–1169.

(14) Luo, C.-W.; Wang, Y.; Chen, F.; Shih, H. A.; Kobayashi, T. Eliminate Coherence Spike in Reflection-Type Pump-Probe Measurements. *Opt. Express* **2009**, *17* (14), 11321–11321.

(15) Borri, P.; Romstad, F.; Wolfgang Werner Langbein; Kelly, A.; Jesper Mørk; Jørn Märcher Hvam. Separation of Coherent and Incoherent Nonlinearities in a Heterodyne Pump-Probe Experiment. *Opt. Express* **2000**, *7* (3), 107–107.

(16) Vandeny Z and Tauc J. Picosecond Coherence Coupling in the Pump and Probe Technique. *Opt. Commun* **1981**, *39* (6), 396–400.

(17) Palfrey, S. L.; Heinz, T. F. Coherent Interactions in Pump–Probe Absorption Measurements: The Effect of Phase Gratings. *J. Opt. Soc. Am. B* **1985**, *2* (4), 674–674.

(18) Cundiff, S. T. Coherent Spectroscopy of Semiconductors. *Opt. Express* **2008**, *16* (7), 4639.

(19) Liu, H.; Zhang, H.; Si, J.; Yan, L.; Chen, F.; Hou, X. Elimination of the Coherent Artifact in a Pump-Probe Experiment by Directly Detecting the Background-Free Diffraction Signal. *Chinese Phys. Lett.* **2011**, *28* (8), 086602–086602.

(20) Wheeler, D. A.; Huang, J.-A.; Newhouse, R.; Zhang, W.-F.; Lee, S.-T.; Zhang, J. Z. Ultrafast Exciton Dynamics in Silicon Nanowires. *J. Phys. Chem. Lett.* **2012**, *3* (6), 766–771.

(21) Pu, Y.-C.; Kibria, M. G.; Mi, Z.; Zhang, J. Z. Ultrafast Exciton Dynamics in InGaN/GaN and Rh/Cr_2O_3 Nanoparticle-Decorated InGaN/GaN Nanowires. *J. Phys. Chem. Lett.* **2015**, *6* (13), 2649–2656.

(22) Burda, C.; Link, S.; Mona Mostafa Mohamed; El-Sayed, M. A. The Pump Power Dependence of the Femtosecond Relaxation of CdSe Nanoparticles

Observed in the Spectral Range from Visible to Infrared. *J. Chem. Phys.* **2002**, *116* (9), 3828–3833.

(23) Zheng, J.; Hoi Sing Kwok. Exciton and Biexciton Recombination in Semiconductor Nanocrystals. *Appl. Phys. Lett.* **1994**, *65* (9), 1151–1153.

(24) Xu, X.; Zhao, Y.; Sie, E. J.; Lu, Y.; Liu, B.; Ekahana, S. A.; Ju, X.; Jiang, Q.; Wang, J.; Sun, H.; et al. Dynamics of Bound Exciton Complexes in CdS Nanobelts. *ACS Nano* **2011**, *5* (5), 3660–3669.

(25) Brelle, M.; Torres-Martinez, C.; McNulty, J.; Mehra, R.; Zhang, J. Synthesis and Characterization of Cu x S Nanoparticles. Nature of the Infrared Band and Charge-Carrier Dynamics. *Pure Appl. Chem.* **2000**, *72*, 101–117.

(26) Wu, F.; Zhang, J. Z.; Kho, R.; Mehra, R. K. Radiative and Nonradiative Lifetimes of Band Edge States and Deep Trap States of CdS Nanoparticles Determined by Time-Correlated Single Photon Counting. *Chem. Phys. Lett.* **2000**, *330* (3), 237–242.

(27) Naghadeh, S. B.; Luo, B.; Pu, Y.-C.; Schwartz, Z.; Hollingsworth, W. R.; Lindley, S. A.; Brewer, A. S.; Ayzner, A. L.; Zhang, J. Z. Size Dependence of Charge Carrier Dynamics in Organometal Halide Perovskite Nanocrystals: Deciphering Radiative Versus Nonradiative Components. *J. Phys. Chem. C* **2019**, *123* (7), 4610–4619.

(28) Wheeler, D. A.; Zhang, J. Z. Exciton Dynamics in Semiconductor Nanocrystals. *Adv. Mater.* **2013**, *25* (21), 2878–2896.

(29) Meng, J.; Lan, Z.; Abdellah, M.; Yang, B.; Mossin, S.; Liang, M.; Naumova, M.;

Shi, Q.; Gutierrez Alvarez, S. L.; Liu, Y.; et al. Modulating Charge-Carrier Dynamics in Mn-Doped All-Inorganic Halide Perovskite Quantum Dots through the Doping-Induced Deep Trap States. *J. Phys. Chem. Lett.* **2020**, *11* (9), 3705–3711.

(30) Ye, J.; Byranvand, M. M.; Martínez, C. O.; Hoye, R. L. Z.; Saliba, M.; Polavarapu, L. Defect Passivation in Lead-Halide Perovskite Nanocrystals and Thin Films: Toward Efficient LEDs and Solar Cells. *Angew. Chem. Int. Ed.* **2021**, *60* (40), 21636–21660.

4 Low Frequency Vibrational Modes of Two-Dimensional Lead-Free Metal Halide Double Perovskites

4.1 Abstract

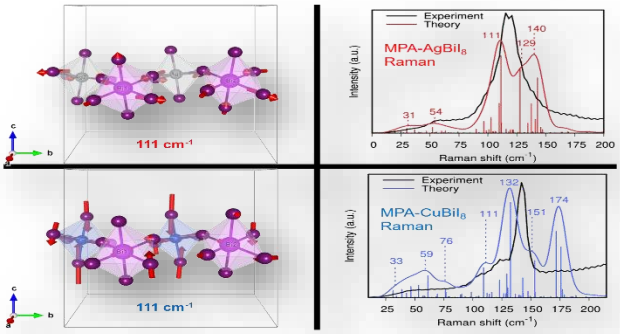

2D layered double perovskites of $(S\text{-MPA})_4AgBiI_8$ ($MPA\text{-}AgBiI_8$) and $(S\text{-MPA})_4CuBiI_8$ ($MPA\text{-}CuBiI_8$) (*S*-MPA, *S*-β-methylphenethylammonium) were synthesized with a hydrothermal method. The crystal structure of $MPA\text{-}AgBiI_8$ was determined using single-crystal X-ray diffraction (scXRD). Powder XRD (pXRD) data suggest that the crystal structure of $MPA\text{-}CuBiI_8$ is more complex than that of $MPA\text{-}AgBiI_8$. UV-Vis electronic absorption spectra of these perovskites reveal a bandgap of 2.03 eV for both. Short exciton lifetime from TRPL results and low PL intensity of the Cu-based perovskite suggest a high density of trap states within the bandgap. Low frequency Raman spectra of both materials show distinct peaks and a slightly higher frequency for the Cu-based perovskite than the Ag-based perovskite. Density functional theory (DFT) calculations were conducted to simulate the low frequency Raman spectra and help explain the different phonon modes, which are collective vibrations of metal halide bond bending and stretching within the Ag- and Cu-centered octahedra coupled with MPA libration and twisting within the inorganic

layer. The DFT theory also quantified octahedral distortions in the two perovskites. This combined experimental and computational study provides new insights into the low frequency vibrations of 2D perovskites.

4.2 Introduction

Metal halide (MH) perovskites attract increasing attention because of their exceptional optoelectronic properties, highly tunable composition, and facile synthesis.[1–3] Now, perovskites of different dimensions (i.e., 3D, 2D, 1D, and 0D) have been synthesized[4–8] and reported with defined structures and controlled properties. Intriguing properties, particularly a more substantial quantum confinement effect, were observed as dimensionality decreases.[9,10]

However, 3D perovskites suffer from undesirable attributes such as environmental instability and Pb toxicity. 2D perovskites hold superior chemical stability, as well as tunable structures and properties.[11] Large organic cations such as methylphenethylammonium (MPA) are essential for constructing 2D perovskites. The MPA cation plays dual roles in the perovskite: the -NH_2 terminal forms N-H···halogen hydrogen bonds anchoring the inorganic framework, and the bulky aromatic backbone exerts a pronounced steric effect that induces octahedral distortion, thereby enabling structural control over material properties.[12] Also, chiral MPA is potentially useful for chiral metal halides for applications such as circularly polarized luminescence (CPL) and chirality-induced spin selectivity.[13–15] In the 2D perovskites, the metal cations dominate in determining the structural and optical properties. To replace toxic Pb, Ag(I), Cu(I) and Sn(II) metal halide perovskites have

been explored and found to have exceptional optical properties, with Cu-halide clusters exhibiting more disordered structures.[16–18] Among the metals, Ag-Bi double halide perovskites remain highly promising due to their exceptional stability and optoelectronic properties, and their atomic and electronic structures have been well studied.[11,19–21] Raman spectra were utilized as a simple way to interrogate structural changes because of the characteristic changes in the vibrational modes when transitioning, for example, from 3D to 2D.[19] In the low-frequency Raman region, the metal halide bond vibrations will be prominent and were studied for Ag-Bi-based perovskite structures. The Raman signals change after replacing Ag with Cu due to the varied Bi-I and Cu-I bond lengths,[11,21] but assignment of these modes and the structural insight they could afford remain elusive.

There are many reports about the determination of the structures of low-dimensional perovskite materials by X-ray diffraction (XRD).[22–26] In contrast, studies of their structures using Raman spectroscopy are less common, especially for 2D layered double perovskites, due to the difficulty in acquiring high-quality data in the low frequency region. Such low frequency phonon modes (<200 cm^{-1}) can reveal interaction between layers and provide atomic-level information about the role of hydrogen bonding or van der Waals forces in the crystal structure. For example, the THz Raman modes for layered structures, such as MoS_2 and WSe_2, reflect shear or breathing modes between the layers.[27–30] In the high frequency "fingerprint" region (>200 cm^{-1}), Raman spectra are used for chemical bond and functional group identification.[31–33] Density functional theory (DFT) calculations can be used to

predict Raman peaks and link them to specific vibrational modes.[30,34] By combining experimental data with DFT simulations, the low frequency Raman spectra can reveal the large-scale spatial structure of the crystal, whereas the conventionally studied high-frequency Raman modes are sensitive primarily to the local structure.

Here, by using a hydrothermal method, MPA-$CuBiI_8$ and MPA-$AgBiI_8$ (MPA, methylphenethylammonium) perovskites were prepared. Single-crystal XRD demonstrates that the Ag-based perovskite exhibits a 2D layered structure, aligning with previously reported data.[13] Simulated and experimental powder XRD, Raman, and IR data for the Cu-based perovskite indicate that its structure is more complex than that of the Ag-based perovskite, with evidence of multiple phases. Nevertheless, the UV-Vis absorption and PL spectra show a similar electronic structure and the Tauc plot shows the same bandgap at 2.03 eV for both materials. From the TRPL results, a shorter exciton lifetime is extracted in the Cu-based perovskite, which we ascribe to distortion-induced trap states in the structure. In addition, first-principles DFT calculations were performed to simulate the low frequency vibrational modes and structural distortion of the two 2D layered double perovskites.

4.3 Results and Discussion

4.3.1 Optical Properties

Figure 4-1 shows the UV-Vis electronic absorption spectra and Tauc plot of the MPA-$AgBiI_8$ and MPA-$CuBiI_8$. In Figure 4-1 (a), the absorption peaks reside at 330 and 550 nm for both materials, and the Cu-based perovskite has a slightly broader

absorption spectrum shape, suggesting a more complex composition for Cu. From the Tauc plot in Figure 4-1 (b), the bandgaps of both materials were determined to be 2.03 eV, indicating no change in the bandgap between Ag- and Cu-based perovskites.

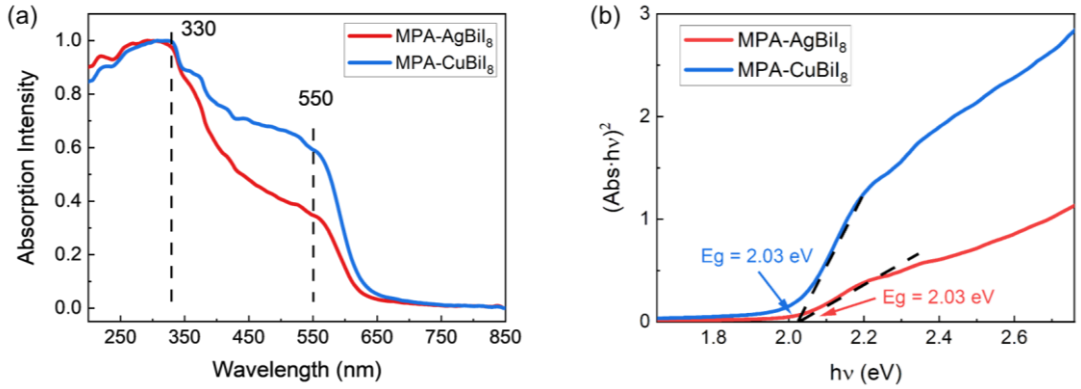

Figure 4-1 UV-Vis electronic absorption spectra (a) and Tauc plot (b) of MPA-$AgBiI_8$ and MPA-$CuBiI_8$.

Figure 4-2 shows the PL spectra and TRPL profiles of the two materials. In Figure 4-2 (a), a narrow emission peak is observed at 548 nm with a full width at half maximum (FWHM) of 50 nm for MPA-$AgBiI_8$. A 550 nm main emission peak was also observed for MPA-$CuBiI_8$, with another shoulder peak at 472 nm. The PL shape of the Cu-based perovskite is broader than that of the Ag-based perovskite, suggesting a more distorted structure.[35] The 472 nm peak is attributed to the transition associated with Cu. Meanwhile, the PL intensity of the Cu-based perovskite is one order of magnitude lower than that of the Ag-based perovskite, indicating more non-radiative recombination and a high density of trap states. The TRPL in Figure 4-2 (b) shows exciton lifetimes of the Ag and Cu-based perovskites and both materials exhibit long decay curves to 4000 ns. The TRPL curves are fitted

with a bi-exponential function, and the average lifetime (τ_{avg}) was calculated based on the following equations:[36–39]

$$\tau_{avg} = \frac{A_1\tau_1^2+A_2\tau_2^2}{A_1\tau_1+A_2\tau_2} \quad (4\text{-}1)$$

where A_1 and A_2 denote fast and slow component amplitudes, τ_1 and τ_2 denote fast and slow component time constants. The τ_{avg} resolves to be 348±40 and 326±40 ns for microcyrstalline MPA-$AgBiI_8$ and MPA-$CuBiI_8$, respectively, with the lifetime of the Cu-based perovskite being 22 ns shorter. After considering the margin of errors, no exciton lifetime difference is observed at ~550 nm between two crystalline materials, implying the same decay channels at ~550 nm, possibly due to domination by Bi metal energy levels. The slightly shorter exciton lifetime indicates more trap states in MPA-$CuBiI_8$, possibly involving oxidized Cu compounds.

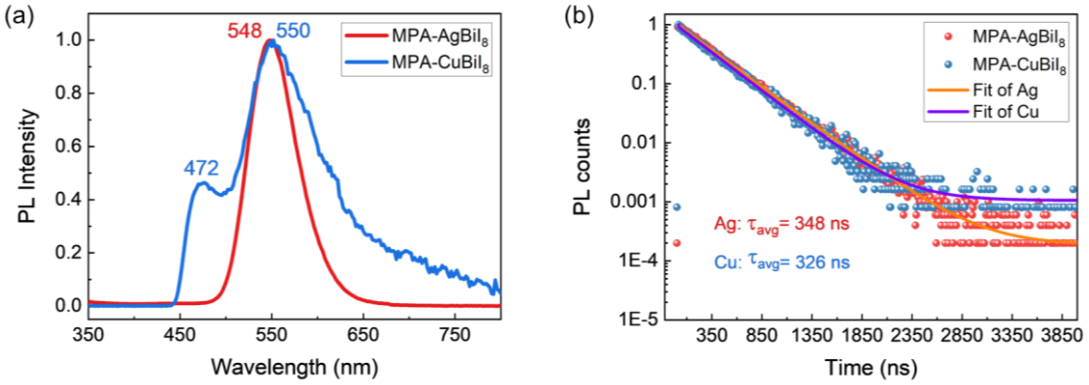

Figure 4-2 (a) PL spectra of MPA-$AgBiI_8$ and MPA-$CuBiI_8$, excited at 278 nm and 254 nm, respectively. (Excitation at 303 nm for the Ag-based perovskite shows the same PL peak at 548 nm.) (b) TRPL spectra of Ag- and Cu-based perovskites. Ag-based perovskite: excited at 278 nm and monitored at 548 nm. Cu-based perovskite: excited at 260 nm and monitored at 550 nm.

The TRPL profiles were recorded using the time-correlated single-photon counting (TCSPC) technique. Ag-based perovskite was excited at 278 nm and monitored at 548 nm, and Cu-based perovskite was excited at 260 nm and monitored at 550 nm. The profiles are fit using the function:

$$y = y_0 + A_1 e^{(-x/\tau_1)} + A_2 e^{(-x/\tau_2)} \quad (4\text{-}2)$$

where A_1 and A_2 denote fast and slow component amplitudes, τ_1 and τ_2 denote fast and slow component time constants. The detailed fitting parameters are summarized in Table 4-1.

Table 4-1 Summary of fitting parameters of the TRPL results.

Components	**Ag @ 548 nm**	**Cu @ 550 nm**
y_0	$1.9\pm0.4\times10^{-4}$	$1.1\pm0.5\times10^{-3}$
A_1	0.5±0.1	1.6±0.2
	(45%)	(62%)
τ_1 (ns)	300±40	5±2
A_2	0.6±0.1	1.0±0.2
	(55%)	(38%)
τ_2 (ns)	380±40	330±40

4.3.2 Morphology and Crystal Structures of MPA-$AgBiI_8$ and MPA-$CuBiI_8$

Figure 4-3 shows the morphology and shape of the MPA-$AgBiI_8$ and MPA-$CuBiI_8$ crystals. MPA-$AgBiI_8$ forms slabs around 100 μm in size with a roughly 20 μm distance between the cracks (Figure 4-3 (a.b), which we attribute to weak van der Waals forces between the organic layers. MPA-$CuBiI_8$ forms small rods with a length of about 10 μm (Figure 4-3 (c,d)). From the images, the crystallinity of the Cu-based perovskite is not comparable to that of the Ag-based perovskite. We were unable to grow single-crystals of MPA-$CuBiI_8$ suitable for X-ray structure determination, however, SEM confirms that microcrystals are present.

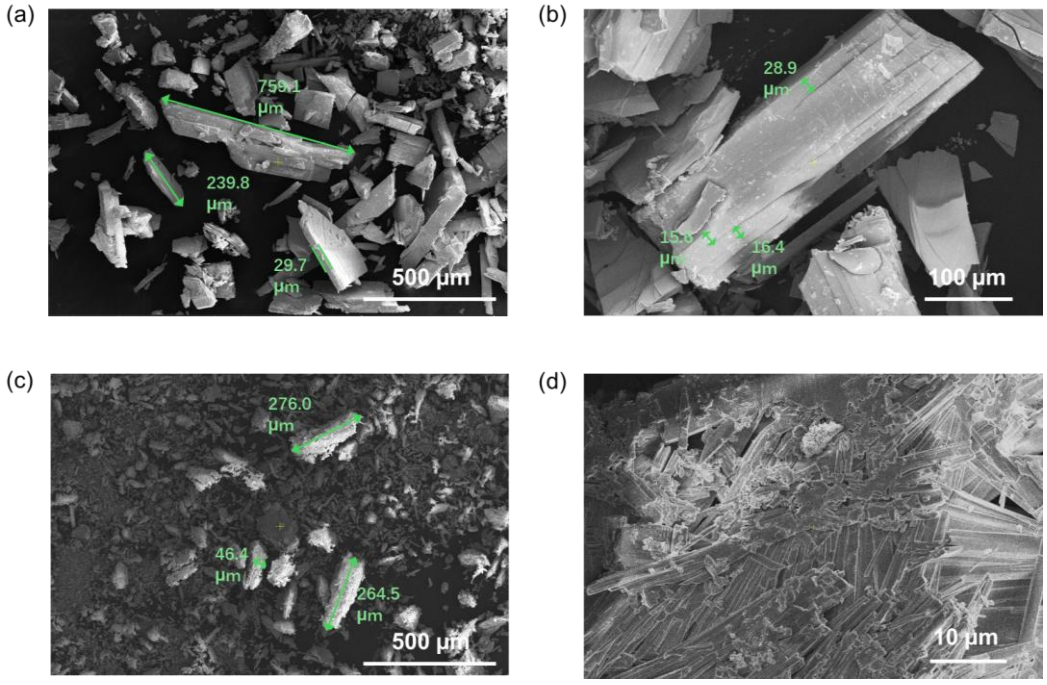

Figure 4-3 SEM images of the MPA-$AgBiI_8$ (a, b) and MPA-$CuBiI_8$ (c, d) crystals. The green labels show the size of individual crystals and the distance between the cracks along the cleavage direction.

Figure 4-4 shows the powder XRD pattern of MPA-$AgBiI_8$ and MPA-$CuBiI_8$ to confirm the 2D layered structure. In Figure 4-4 (a), the diffraction peaks for the Ag-based perovskite were observed at 10.6, 15.8, 20.5, 25.5, 27.6, 30.3, 32.6, 37.7, 41.1, and 47.0°. The 10.6, 15.8, 20.5, 27.6, 32.6, 37.7° diffraction peaks match with reported XRD data of MPA-$AgBiI_8$ films, indicating a 2D layered structure in our case.[13] For the Cu-based double perovskite, in addition to the diffraction peaks observed for the Ag-based perovskite, there are new peaks at 12.1, 22.4, 29.4, 32.5, 38.0 and 44.4°. Closer examination of the experimental XRD peaks in Figure 4-4 (b) reveals different intensities in the same diffraction peaks between two perovskites.

We were able to grow diffraction-quality single crystals of MPA-$AgBiI_8$ and solve and refine its crystal structure (*vide infra*). The Ag-I bonds that are parallel to the *c* axis are 2.665(3) and 2.683(3) Å long, and the equatorial Ag-I bond lengths range from 3.335(6) to 3.524(6) Å, indicating a distorted octahedra structure of $[AgI_6]^{5-}$. In contrast, all the Bi-I bonds fall within a narrow range from 3.023(5) to 3.112(5) Å (see Figure 4-5). As Cu^+ (0.77 Å) has a much smaller radius than Ag^+ (1.15 Å) and Bi^{3+} (1.03 Å), more distorted $[CuI_6]^{5-}$ octahedra are expected.[40] According to Jahn-Teller distortion theory, the octahedrally coordinated transition metals Cu^+, Ag^+ will split e_g orbitals to stabilize the double perovskites by elongating or shortening the metal halide bonds, leading to a crystal symmetry-breaking.[41] The XRD pattern of the Cu-based perovskite retains most of the characteristic peaks of the Ag-based counterpart but exhibits additional peaks, suggesting a similar but more complex composition, possibly due to multiple phases arising from oxidized Cu compounds or unreacted starting materials.

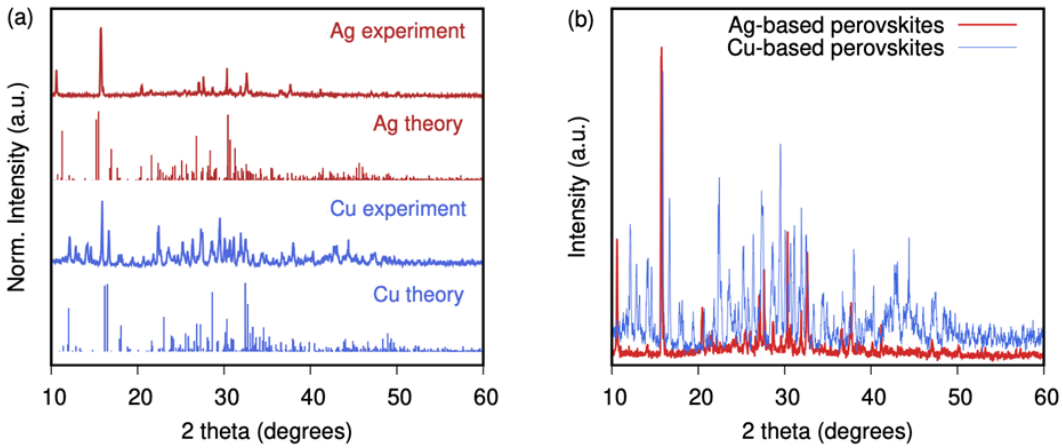

Figure 4-4 Powder XRD pattern of the MPA-$AgBiI_8$ and MPA-$CuBiI_8$. (a) The experimental and simulated XRD pattern comparison. (b) Overlaid plots of experimental XRD results of MPA-$AgBiI_8$ and MPA-$CuBiI_8$.

Figure 4-5 shows the structure of the MPA-$AgBiI_8$ double perovskite in which layers of the organic *S*-β-MPA cation alternate with inorganic $[AgBiI_8]^{4-}$. The inorganic layer features vertex-sharing $[AgI_6]^{5-}$ and $[BiI_6]^{3-}$ octahedra. Three of the I atoms were each disordered across two closely spaced positions, as was the Ag atom. The bond metrics in Table 4-2 were calculated using the centroid for each pair of disordered atoms. The Bi–I distances range from 3.023(5) to 3.112(5) Å and the I–Bi–I angles closely approach those of an octahedron. The Ag–I distances exhibit a much greater distribution. As expected, the Ag(I) center adopts a linear geometry with two tightly bound I atoms, I3 and I9, at distances of 2.665(3) and 2.683(3) Å, respectively. The remaining four I atoms are vertices shared with the $[BiI_6]^{3-}$ octahedra and the Ag–I distances are substantially longer, ranging from 3.335(6) to 3.524(6) Å. These four Ag–I interactions are paired with a short distance (3.335(6) or

3.388(4) Å) *trans* to a long distance (3.423(7) or 3.524(6) Å). The I–Ag–I angle with the tightly bound, non-bridging I atoms is nearly linear, but the remaining equatorial I atoms exhibit a greater range of angles, with one *cis* I–Ag–I angle even exceeding 105°. Although the Bi and Ag atoms are arrayed on a nearly centrosymmetric lattice, with the Ag atoms almost coincident with Bi–Bi centroids, the tilting of the octahedra (Figure 4-5) breaks the overall inversion symmetry between the layers. The structure has a 2_1 screw symmetry axis, and there are 4 unique molecular cations per unit cell. The detailed crystal and refinement data for MPA-$AgBiI_8$ perovskite can be found in Table 4-3.

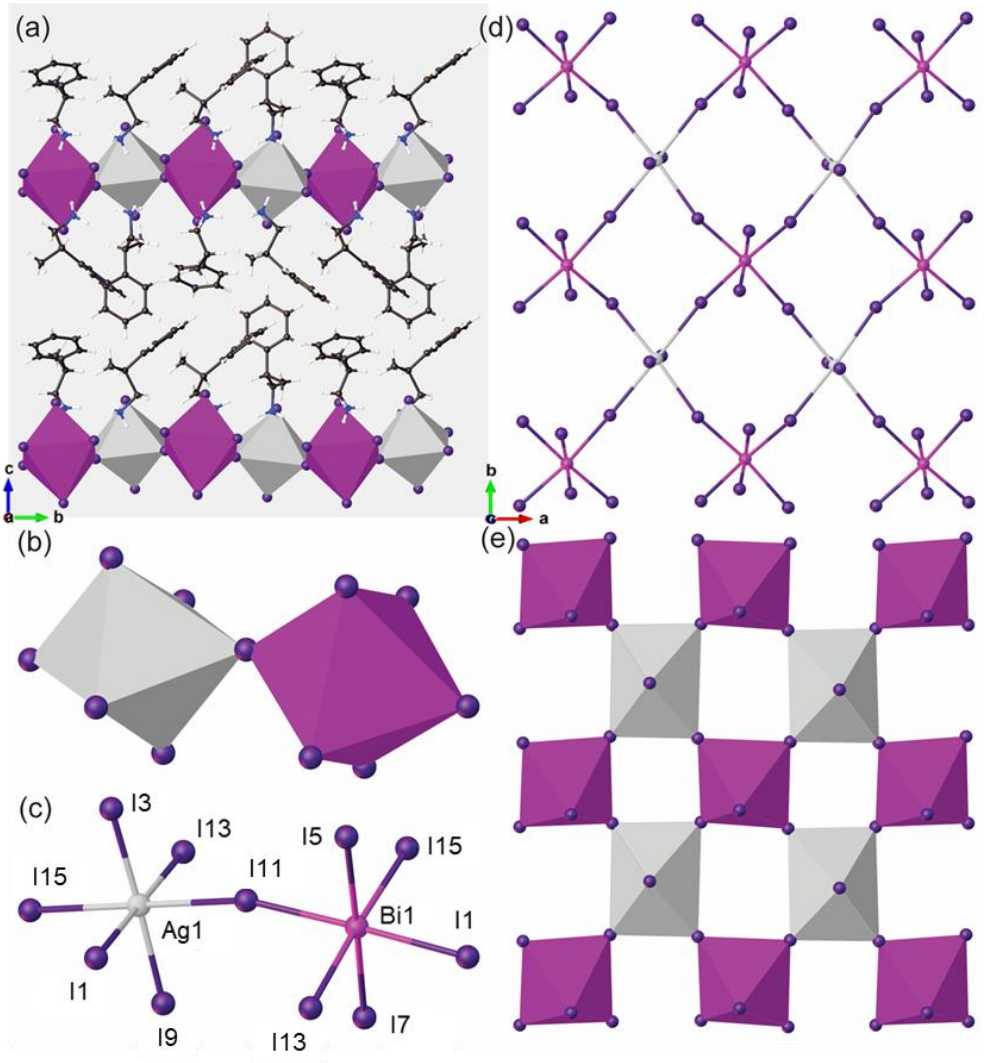

Figure 4-5 (a) View of the layered structure of MPA-$AgBiI_8$ along *a* with *S*-β-MPA cations as balls and sticks and Bi and Ag as polyhedra. (b) One vertex-bridged AgI_6/BiI_6 pair shown as polyhedra. (c) The same atoms and orientation as (b) but without polyhedral and atom labels corresponding to Table 4-2. (d) View of the inorganic layer along *c* with atoms shown as balls and sticks. (e) The same orientation as (d) but with Ag and Bi polyhedra. For all depictions, disordered Ag1, I1, I11, and I15 atoms are represented with a single sphere at the position of the

centroid of the two disordered atoms. Color code: C black, N blue, H white, Ag grey, Bi magenta, I purple.

Table 4-2 Selected bond lengths in angstrom and bond angles in degree. M is Ag or Cu. I3 and I9 are out of plane, and the rest are in plane.[a]

Bond	**Ref. Exp. Ag**[13] **(Å)**	**Exp. Ag (Å)**	**Ag PBE (Å)**	**Cu PBE (Å)**
Bi1–I1	3.0907(16)	3.112(5)	3.074	3.024
Bi1–I5	3.0896(15)	3.0816(8)	3.036	2.982
Bi1–I7	3.0762(14)	3.0721(8)	3.081	2.995
Bi1–I11	3.0512(19)	3.025(6)	3.016	2.967
Bi1-I13	3.078(2)	3.1077(9)	3.046	2.964
Bi1-I15	3.039(2)	3.023(5)	2.960	2.880
M1–I1	3.368(4)	3.388(4)	3.076	2.783
M1–I3	2.669(3)	2.665(3)	2.758	2.560
M1–I9	2.663(3)	2.683(3)	2.758	2.568
M1–I11	3.603(4)	3.423(7)	3.044	2.689
M1–I13	3.681(5)	3.524(6)	3.062	2.767
M1–I15	3.418(4)	3.335(6)	2.977	2.733

Bond	Ref. Exp. Ag (°)[13]	Exp. Ag (°)	Ag PBE (°)	Cu PBE (°)
I11–Bi1–I13	179.29(6)	177.01(13)	170.973	172.159
I15–Bi1–I1	175.55(5)	176.99(10)	173.347	98.671
I7–Bi1–I5	179.05(5)	178.65(3)	177.983	176.447
I15–Bi1–I13	87.03(6)	91.84(12)	103.554	106.188
I5–Bi1–I13	90.84(5)	89.26(5)	92.999	93.734
I5–Bi1–I15	89.04(5)	89.82(8)	88.285	85.859
I3–M1–I9	176.33(17)	177.95(16)	173.341	171.093
I15–M1–I11	176.00(10)	176.92(17)	169.376	79.631
I1–M1–I13	174.49(11)	178.07(13)	81.511	171.257
I3–M1–I11	84.71(9)	87.54(13)	82.427	84.811
I3–M1–I1	92.06(11)	91.39(11)	89.949	91.337
I1–M1–I11	105.11(9)	105.34(13)	104.313	101.782

[a] Ag1, I1, I2, and I3 were each disordered across two positions in the experimental Ag-based structure. These bond metrics were calculated using the centroid of the two disordered atom positions.

Table 4-3 Crystal and refinement data for MPA-$AgBiI_8$ perovskite.

Empirical formula	$C_{36}H_{58}AgBiI_8N_4O$

Formula Weight	1894.91
Temperature (K)	104(6)
Wavelength (Å)	1.54184
Crystal system	monoclinic
Space group	$P2_1$
Point group	C_2
***a* (Å)**	9.56840(10)
***b* (Å)**	16.7665(2)
***c* (Å)**	16.5699(2)
***β* (°)**	102.5080(10)
Volume (Å^3)	2595.19(5)
Z	2
ρ_{calc} (Mg/m^3)	2.425
Crystal size (mm^3)	0.11 × 0.04 × 0.02
θ range (°)	5.464 to 134.154
Total reflections	31574
Unique reflections	9260
Parameters	510
Completeness	100.0
R_{int}	0.0436
R_1 (I > 2σ)	0.0285
R_1 (all data)	0.0309
wR_2 (I > 2σ)	0.0689
wR_2 (all data)	0.0700
Goodness of fit, *S*	1.042

Figures 4-6 (a) and (b) show the DFT-optimized crystal structures of MPA-$AgBiI_8$ and MPA-$CuBiI_8$ along the in-plane (equatorial) and out-of-plane (axial) directions (detailed lattice parameters in Table 4-4). Both exhibit a 2D layered

structure. The structures were optimized starting from the crystal structure of MPA-$AgBiI_8$.[13] In Figures 4-6 (c) and (e), the hydrogen bond lengths are slightly longer in the Ag-based perovskite, with a range from 3.427 to 5.157 Å, than in Cu-based perovskite, which span from 3.232 to 4.775 Å, indicating a longer distance between the organic and inorganic layers. In Figures 4-6 (d) and (f), the Cu-I bonds are shown to be shorter than Ag-I bonds, and the metal halide bond lengths between Ag/Cu-I and Bi-I bonds are unmatched in the corner-connecting direction, along the equatorial plane. Specifically, the metal halide bonds in both octahedra are compressed with two axial bonds of 2.758 Å, four equatorial bonds ranging from 2.977 to 3.067 Å in the Ag-based perovskite and two axial bonds of ~2.568 Å, four equatorial bonds ranging from 2.689 to 2.783 Å in the Cu-based perovskite, indicating a Jahn-Teller distortion. The Jahn-Teller distortion allows empty metal d orbitals with low enough energy to mix with filled non-metal p orbitals, stabilizing a distorted geometry.[42,42,43] These Jahn-Teller distortions are present in the Cu and Ag-centered octahedra, but not in Bi-centered octahedra, due to Bi's fully occupied d-orbitals. These are evidenced by the relatively large distortion index (*D*) values obtained for Cu and Ag-centered octahedra compared to Bi (Table 4-8), with Bi octahedra having values near 1×10^{-2} in the theoretical structures and values of 2.97×10^{-2} in the Cu-centered octahedra and 4.26×10^{-2} in Ag-centered octahedra.

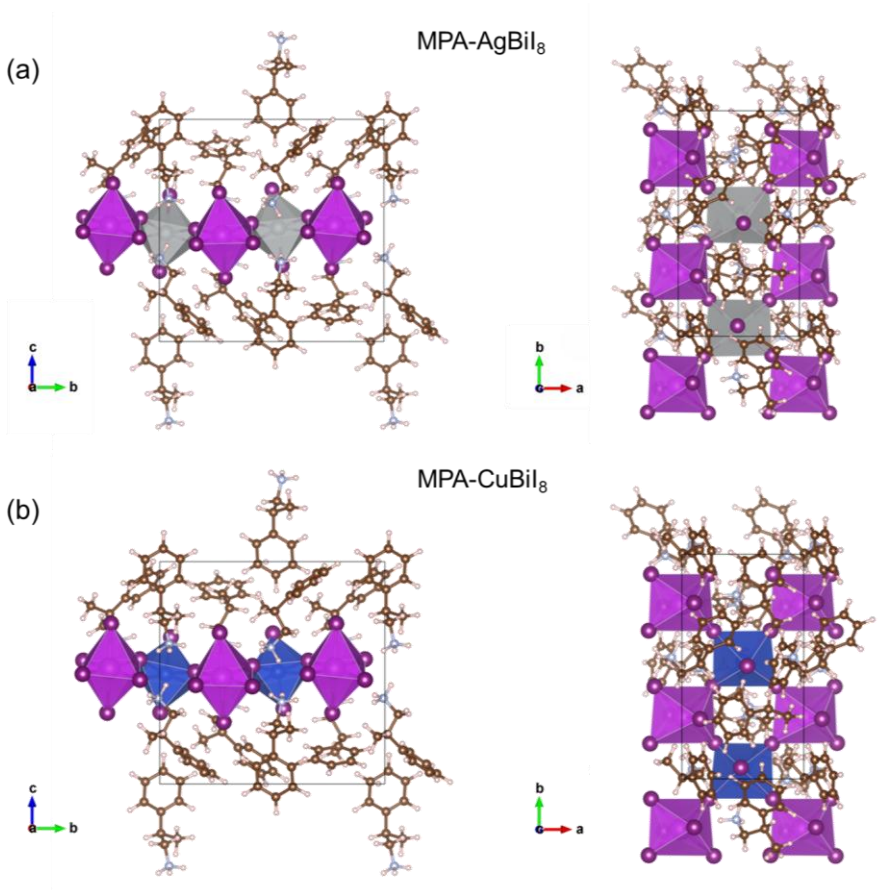
(a)
MPA-AgBiI8
c
b
b
a
(b)
MPA-CuBiI8
c
b
b
a

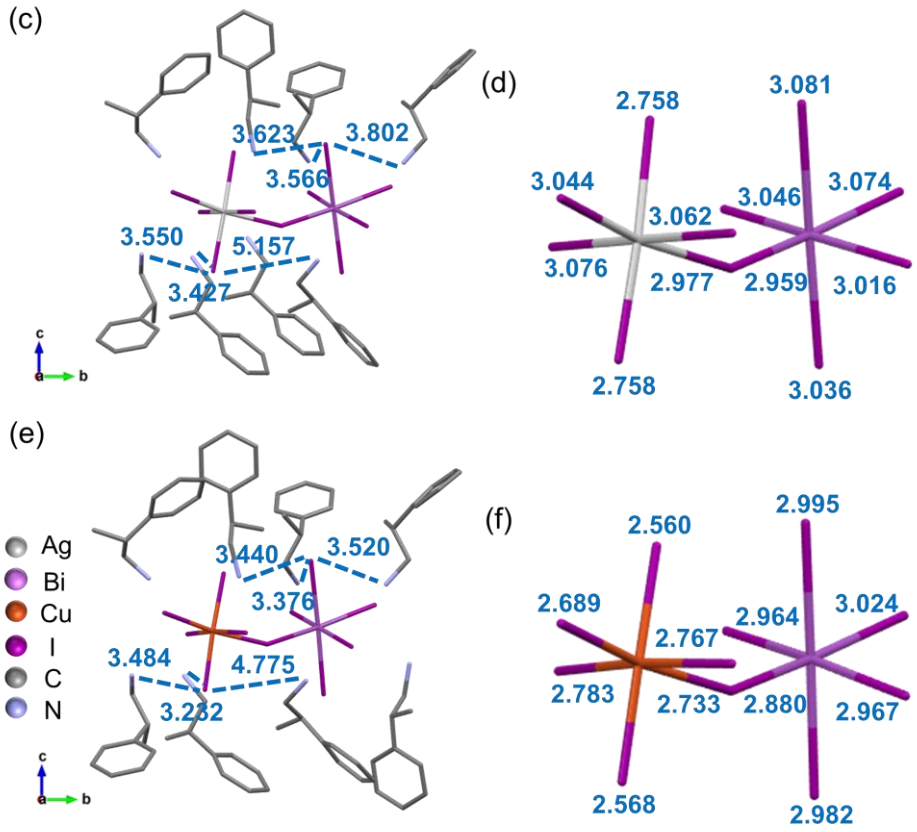

Figure 4-6 DFT-PBE-simulated crystal structure of the (a) MPA-$AgBiI_8$ and (b) MPA-$CuBiI_8$ viewed along the *a* and *c* axes. Ag, Bi, and Cu-centered octahedra are shown in silver, magenta, and blue colors. (c) The hydrogen bond lengths between N and I atoms between the organic and inorganic layers in MPA-$AgBiI_8$ and (d) Ag-I, Bi-I bond lengths inside the octahedra. (e) The hydrogen bond lengths between N and I atoms between the organic and inorganic layers in MPA-$CuBiI_8$ and (f) Cu-I and Bi-I bond lengths inside the octahedra. The hydrogen atoms are omitted for clarity in figures (c) and (e). All bond lengths are in Å.

Table 4-4 The summary of the experimental and calculated lattice parameters of MPA-$XBiI_8$ (X=Ag or Cu) single crystal.[a]

	a **(Å)**	***b*** **(Å)**	***c*** **(Å)**	β (°)	**Unit-cell Volume (bohr^3)**	**Temp (K)**
Exp. Ag structure from literature[13]	9.657	17.051	16.754	102.503	18173.7	290
Exp. Ag structure in this work	9.568	16.767	16.570	102.508	17232.1	104
Theory Ag structure (PBE)	8.728	15.891	16.047	101.651	14711.2	0
Theory Ag structure (LDA)	8.339	15.178	15.367	101.398	12866.4	0

Theory Ag structure (PBE+GD2)	8.566	15.423	15.408	101.701	13452.2	0
Theory Cu structure (PBE)	8.239	14.880	15.035	101.763	12178.0	0

[a] The α and γ angles are both 90° in monoclinic crystal system.

4.3.3 Low Frequency Raman Vibration Modes

Figure 4-7 shows the comparison between experimental and calculated Raman and IR spectra for crystalline MPA-$AgBiI_8$ and MPA-$CuBiI_8$. The experimental data were adjusted to remove temperature dependence to generate the reduced Raman spectra[44] (see treatment method in Experimental Section 4.5), and the theoretical data were treated with a 6 cm^{-1} Gaussian broadening to match the experimental result. The original Raman spectra with temperature dependence are shown in Figure 4-8 for comparison. Figures 4-7 (a) and (b) show the comparison of experimental and calculated Raman spectra in the low frequency range from 0-200 cm^{-1}. The broad low-energy Raman bands from the experiment indicate strong molecular interactions within the perovskites.[45] For both materials, the theoretical results match the experimental peaks except that theory shows a separate peak at 140 cm^{-1} for the Ag-based perovskite and 174 cm^{-1} for the Cu-based one. One reason for the mismatch

between the experimental and theoretical Raman spectra is that disorder from thermal or other causes is inevitably present in the structure, which changes interactions between neighboring unit cells and leads to shifts and broadening of vibrations, especially of low-frequency vibrations.[47] In contrast, the DFT calculations use an idealized crystal structure without disorder. In the high-frequency region from 200-1800 cm^{-1} in Figures 4-7 (c) and (d), the theoretical peak positions match the experimental Raman data, but this is not the case for the intensities. Comparison of the IR spectra in Figures 4-7 (e) and (f) shows good agreement for both the peak positions and intensities. Together with the comparison of XRD patterns, these results suggest a correspondence between the DFT-simulated crystal structures and the actual crystal structures.

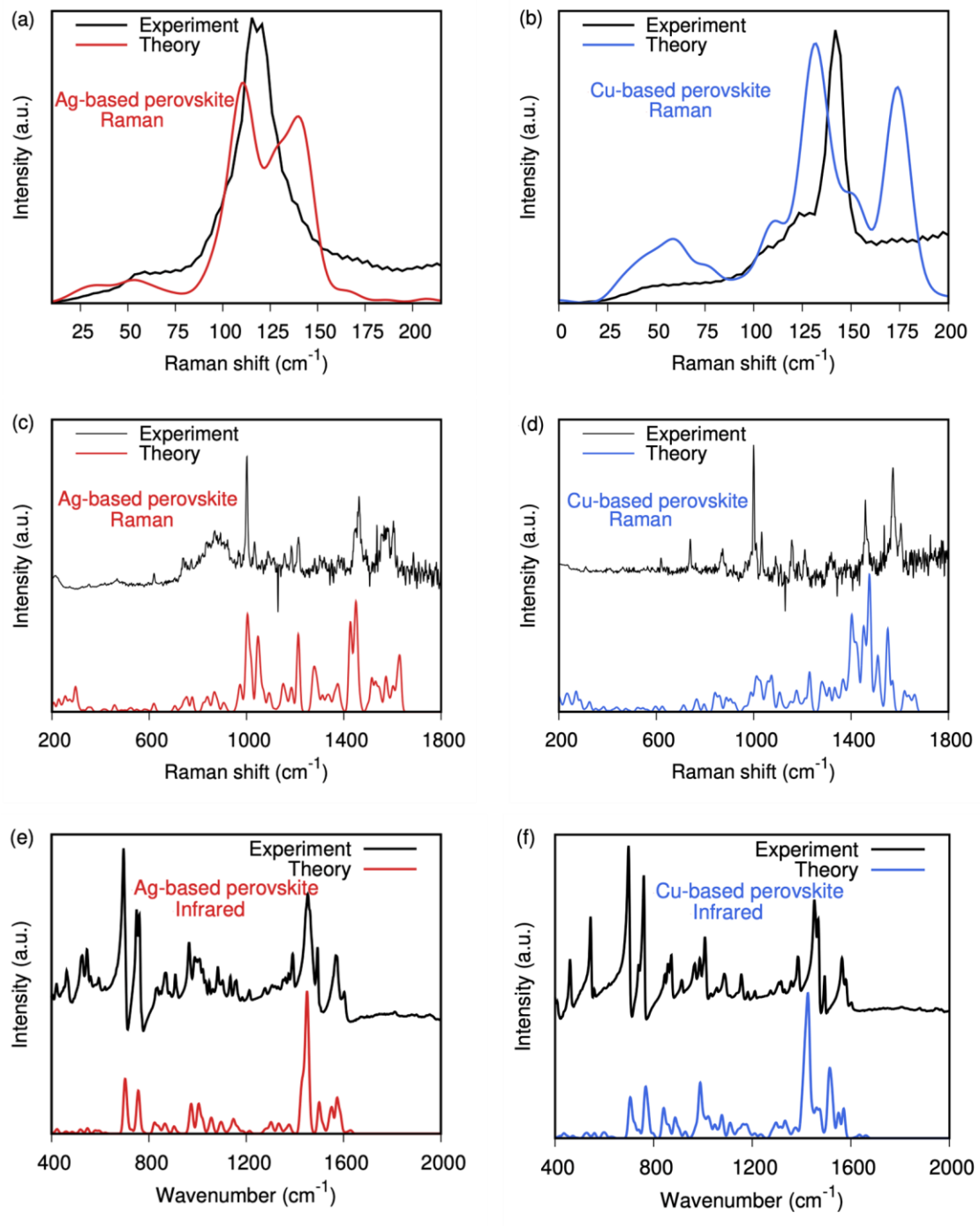

Figure 4-7 The Raman and IR spectra of MPA-$AgBiI_8$ (red legend) and MPA-$CuBiI_8$ (blue legend). (a, b) Low frequency (0-200 cm^{-1}) Raman spectra; (c, d) High frequency Raman spectra (200-1800 cm^{-1}); (e, f) IR spectra (400-2000 cm^{-1}).

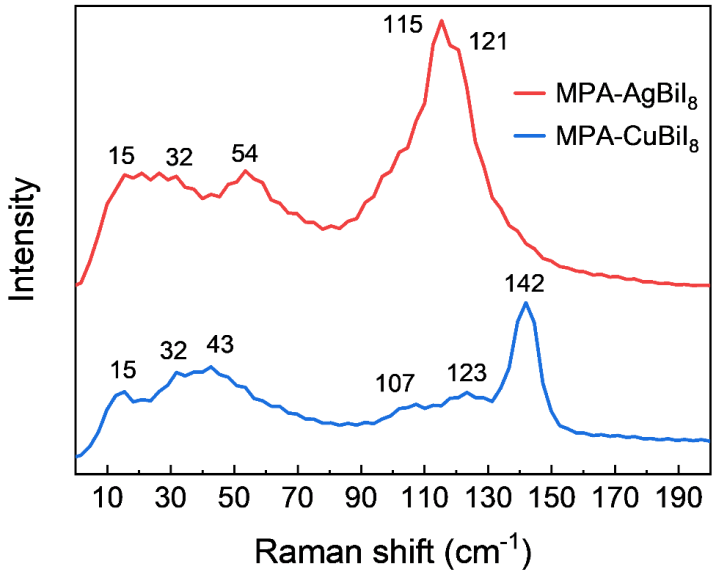

Figure 4-8 Experimental Raman spectrum in the low frequency region (0-200 cm-1) with temperature dependence.

To decipher the character of the low frequency vibrational modes, the DFT calculations were conducted and compared to the experimental results. Only the most significant contributions to each vibrational peak are shown here to match the experimentally measured ones, though 636 modes in total are obtained from the calculation, with the subset in the range 0-200 cm^{-1} shown by vertical lines at the bottom of Figures 4-9. It should be noted that the motions repeat periodically in each unit cell of the lattice. Comparing the low frequency Raman spectra between Ag- and Cu-based perovskites, more and broader peaks are generated from the Cu-based perovskite based on the DFT computation. This could be due to the stronger hydrogen bond between the organic and inorganic layer, which broadens the

vibrational peak and a more distorted lattice structure and lower symmetry, leading to more vibrational modes.[43,46] A summary of the vibrational modes interpretation is listed in Table 4-5.

Figure 4-9 shows the assignment of experimentally measured vibrational modes from Raman spectra of MPA-$AgBiI_8$ and MPA-$CuBiI_8$ aided with simulated Raman spectra below 200 cm^{-1}. We provide here only the most dominant characteristics of each mode, and where a distortion or motion is mentioned without specifying whether it is in or out of plane, the distortion has components in both directions. In the Ag spectrum, the peak at 31 cm^{-1} is ascribed to both in-plane and out-of-plane bond angle distortions of octahedra, coupled with tilting of the Ag octahedra. The mode at 54 cm^{-1} is assigned to octahedra bond angle distortions and in-plane and out-of-plane motion of Bi and Ag centers. The mode at 111 cm^{-1} arises from in-plane bond length distortions and out-of-plane Bi bond length distortions. The mode at 129 cm^{-1} consists of in-plane bond length distortions on both octahedra, bond angle distortions of Bi-centered octahedra, out-of-plane Ag bond length distortions, and in-plane motion of Bi. The peak at 140 cm^{-1} consists of in-plane bond-length distortions on both octahedra, and motion of Bi centers.

In the Cu spectrum, at 33 cm^{-1}, the dominant motions are octahedra bond angle distortions coupled with in-plane motions of the octahedral centers. The peak at 59 cm^{-1} is characterized by angle distortions of both in-plane and out-of-plane octahedra bonds, with significant contributions from motion of Cu atoms. At 76 cm^{-1}, in-plane bond angle distortions on both Cu and Bi octahedra, bond angle distortions of out-of-

plane Cu-I bonds, and tilting of Bi-centered octahedra are dominant. At 111 cm^{-1}, Cu centers move in plane, Cu octahedra exhibit in-plane bond angle distortions, and both Cu and Bi octahedra display bond length distortions. At 132 cm^{-1}, Cu atoms move in plane, Cu octahedra undergo bond angle distortion, both Bi and Cu octahedra have in-plane bond length distortions, and Bi octahedra have bond length distortions along out-of-plane Bi-I bonds. The 151 cm^{-1} mode includes in-plane bond length distortions on Bi and Cu octahedra, while Cu atoms move in plane. The peak at 174 cm^{-1} contains bond length distortions of octahedra, and significant NH_3 group rotation on MPA molecules. In both the Ag-containing and Cu-containing materials, all peaks listed in this range exhibit libration and internal twisting of MPA molecules coupled to the vibration of the inorganic layers.

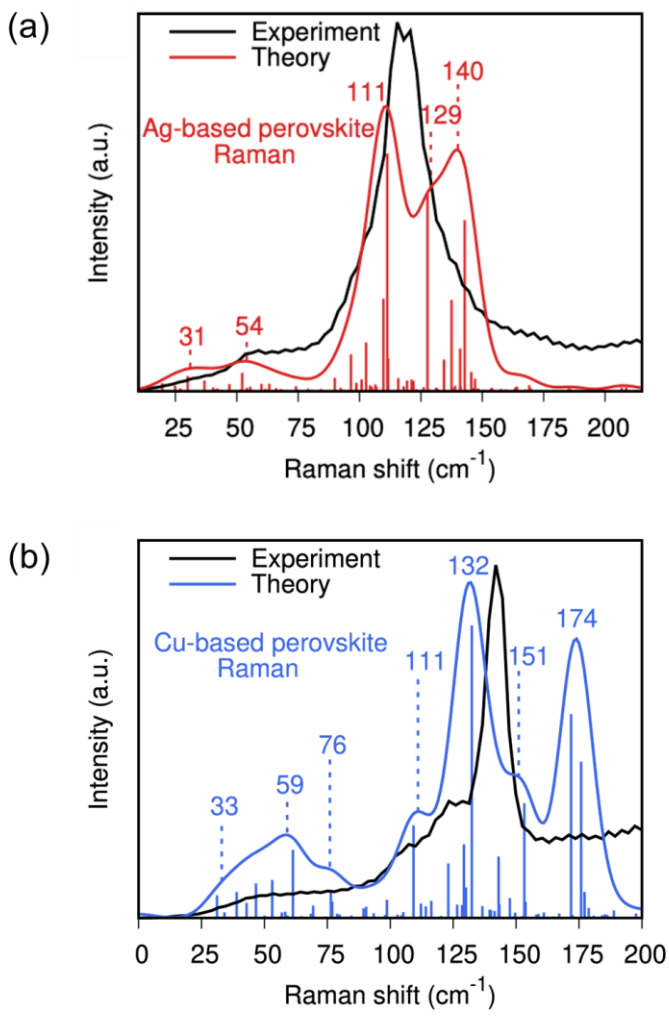

Figure 4-9 Reduced experimental and theoretical (with 6 cm^{-1} Gaussian broadening) Raman spectra of (a) MPA-$AgBiI_8$ and (b) MPA-$CuBiI_8$. Solid vertical lines show all the individual mode positions and intensities in the DFT calculation within the 0-200 cm^{-1} range.

Table 4-5 Summary of experimental and theoretical vibration modes in the low Raman frequency region (0-200 cm^{-1}) of MPA-$AgBiI_8$ and MPA-$CuBiI_8$.

MPA-$AgBiI_8$ (cm^{-1})	**MPA-$CuBiI_8$ (cm^{-1})**

Experiment	Theory	Assignment	Experiment	Theory	Assignment
31	31	Ag-I-Bi bending	32	33	Cu-I-Bi bending
53	54	Ag-I-Bi bending	43	59-76	Cu-I-Bi bending
101-116	111	I-Ag/Bi-I stretching	107	111	I-Cu-I bending/ I-Cu/Bi-I stretching
121	129	I-Ag/Bi-I stretching	123	132	I-Cu/Bi-I stretching
	140	I-Ag/Bi-I stretching	142	151	I-Cu/Bi-I stretching
				174	MPA librating I-Cu/Bi-I stretching

A. Low Frequency Raman Vibration Modes Elaboration of MPA-AgBiI$_8$ Perovskite

Density-functional perturbation theory calculations were applied to calculate and understand the vibrational modes of MPA-AgBiI$_8$ with the computational method described in the Experimental Section number 10. The mode illustrations are in Figure 4-10, and the symmetry and description of different modes are summarized in Table 4-6.

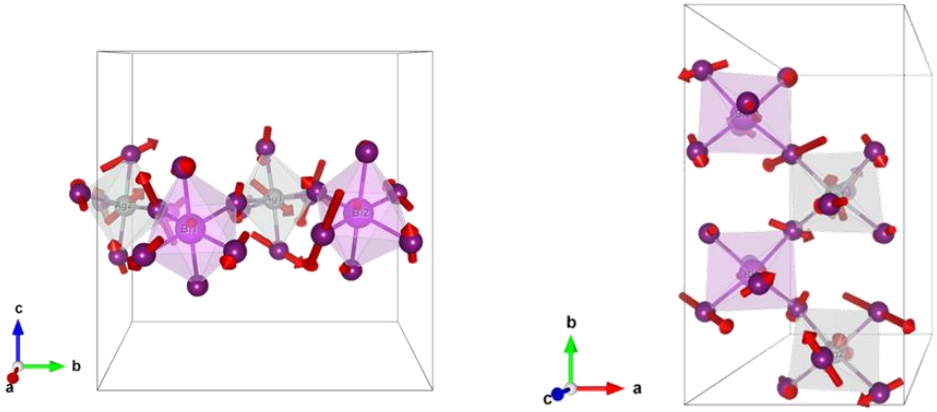

29.9 cm^{-1}

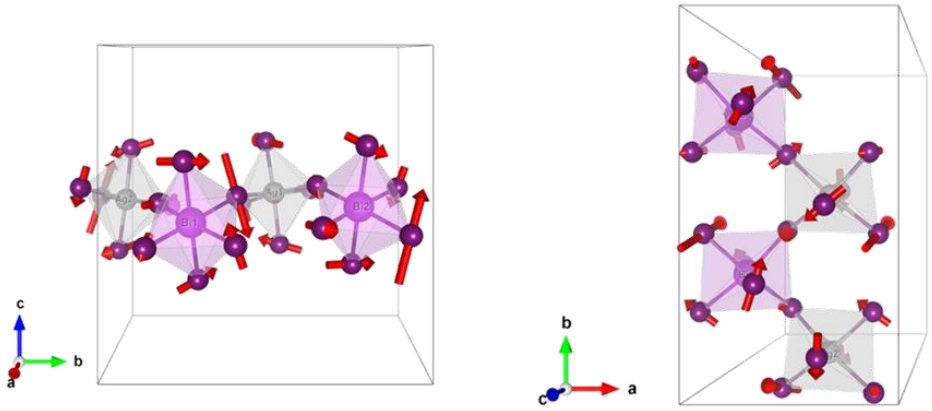

52.1 cm^{-1}

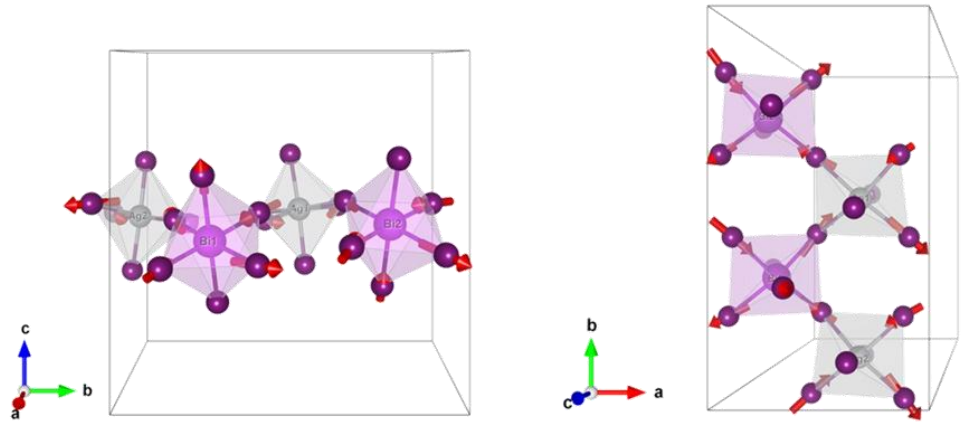

111.3 cm^{-1}

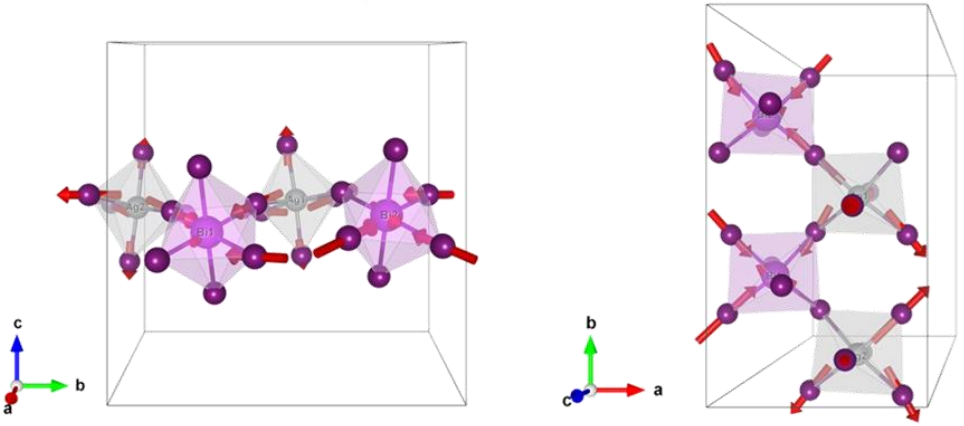

127.6 cm^{-1}

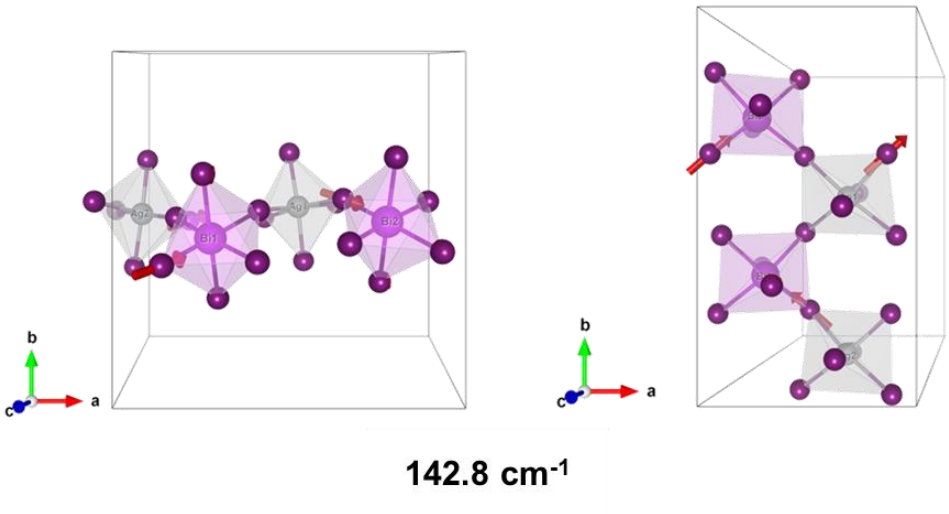

Figure 4-10 Low frequency vibration modes in the crystal structure as calculated for MPA-$AgBiI_8$ perovskite, shown from two different perspectives.

Table 4-6 Full description of the assignments of the vibration modes in the low Raman frequency region (0-200 cm^{-1}) of the Ag-based 2D double perovskite.

Peak Frequency [cm^{-1}]	**Freq. of Main Mode [cm^{-1}]**	**Symmetry**	**Description**	**Mode #**
31	29.9	A	In- and out-of-plane bond angle distortions of octahedra. Ag octahedra tilt.	9
54	52.1	A	Bond angle distortions. In-plane and out-of-plane motion of Bi and Ag centers.	31

111	111.3	B	In-plane bond length distortion on octahedra. Slight bond length distortion along out-of-plane I-Bi-I bonds.	77
129	127.6	A	In-plane bond length distortion on octahedra. Bond angle distortion on Bi-centered octahedra. Symmetric bond length distortion on out-of-plane I-Ag-I bonds. In-plane motion of Bi centers.	92
140	142.8	A	In-plane bond-length distortion of octahedra. Motion of Bi centers.	103

In all modes, molecules librate and have some degree of internal twisting. Where a distortion or motion is mentioned without specifying whether it is in or out of plane, the distortion has components in both directions. A and B are Mulliken symbols, irreducible representations for point group C_2, where A is symmetric and B is antisymmetric. The peak position after applying 6 cm^{-1} Gaussian broadening is given in the first column, and the dominant mode from DFT is given in the second column.

B. Low frequency Raman Vibration Modes Elaboration for MPA-$CuBiI_8$ Perovskite

The simulation of the Raman vibration modes is based on DFT calculations. The mode illustrations are in Figure 4-11, and the symmetry and description of different modes are in Table 4-7.

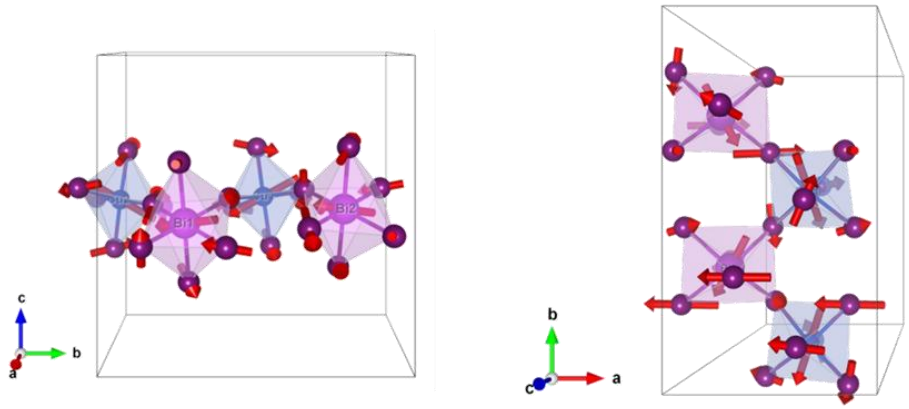

46.6 cm^{-1}

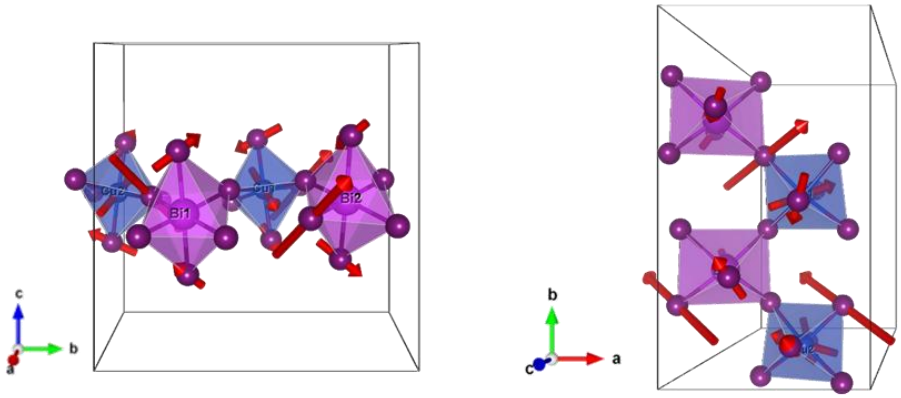

61.3 cm^{-1}

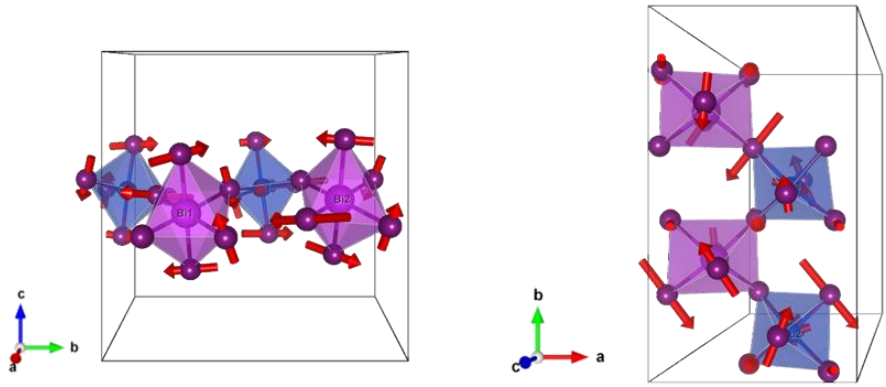

76.4 cm^{-1}

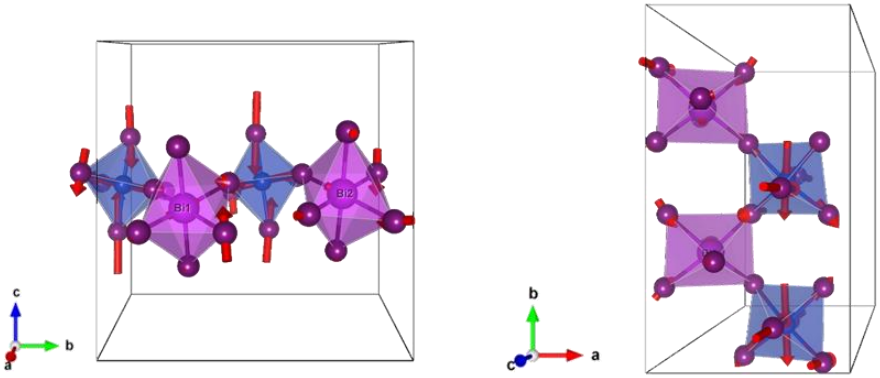

109.2 cm^{-1}

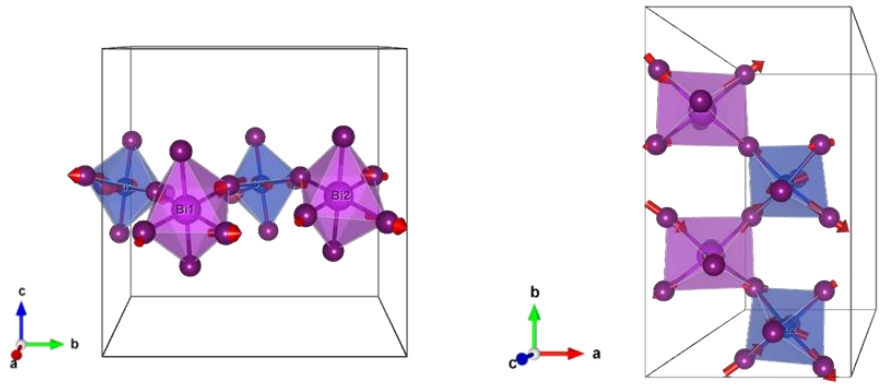

132.4 cm^{-1}

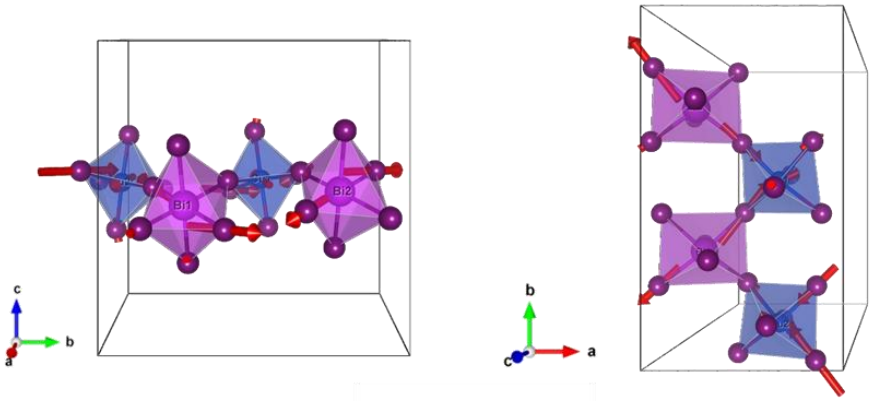

153.2 cm^{-1}

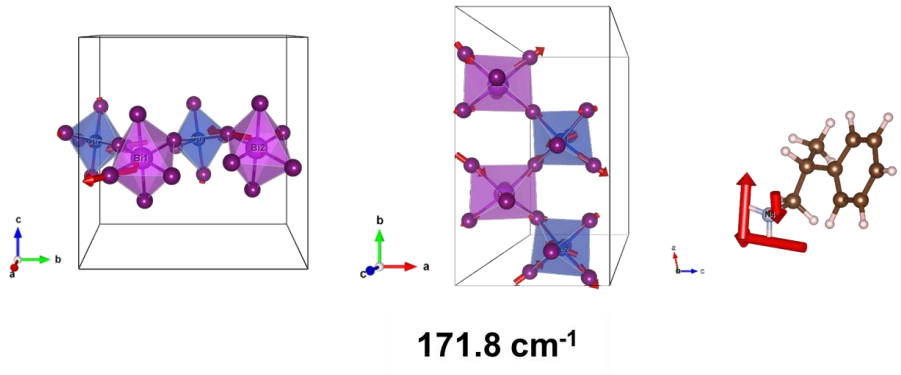

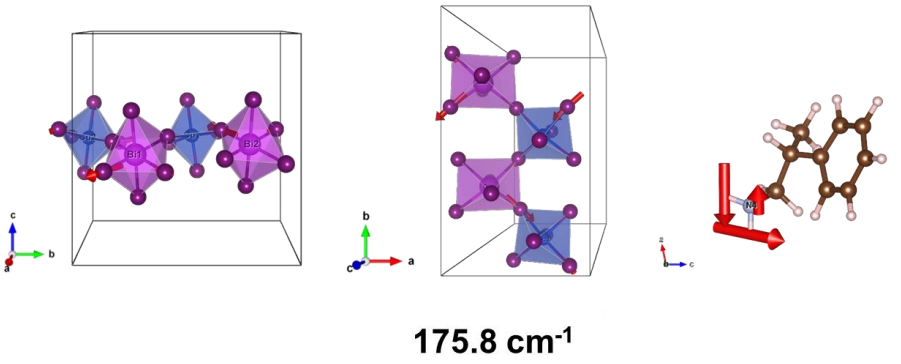

Figure 4-11 Low frequency vibration modes in the crystal structure as calculated for the MPA-$CuBiI_8$ perovskite, shown from two different perspectives.

Table 4-7 Full description of the assignments of the vibration modes in the low Raman frequency region (0-200 cm^{-1}) of the Cu-based 2D double perovskite.

Peak Frequency	Freq. of Main Mode	Symmetry	Description	Mode #

[cm^{-1}]	[cm^{-1}]			
33	46.6	A	Octahedra bond angle distortion. In-plane motion of octahedral centers.	11
59	61.3	A	Angle distortion of in-plane and out-of-plane octahedra bonds. Motion of Cu.	21
76	76.4	A	In-plane bond angle distortion of in-plane bonds. Bond angle distortion of out-of-plane Cu octahedra bonds. Tilting of Bi octahedra.	33
111	109.2	A	Cu centers move in plane. In-plane Cu octahedra bond angle distortion. Octahedra bond length distortion.	54
132	132.4	B	Bond angle distortion on Cu octahedra. In-plane bond length distortion of both Bi and Cu octahedra. Slight bond length	67

			distortion of out-of-plane Bi octahedra bonds. Cu atoms move in plane.	
151	153.2	A	In-plane bond length distortion on Bi and Cu octahedra. Cu atoms move in plane.	80
174	171.8, 175.8	A	NH_3 group rotation. Bond length distortion of octahedra.	90, 92

In all modes, molecules librate and have some degree of internal twisting. Where a distortion or motion is mentioned without specifying whether it is in or out of plane, the distortion has components in both directions. A and B are Mulliken symbols, irreducible representations for point group C_2, where A is symmetric and B is antisymmetric. The peak position after applying 6 cm^{-1} Gaussian broadening is given in the first column, and the dominant mode from DFT is given in the second column.

4.3.4 Density of States

Figure 4-12 presents the calculated partial vibrational density of states (VDOS) of MPA-$AgBiI_8$ and MPA-$CuBiI_8$ based on the DFT-optimized crystal structures. The VDOS figures describe the number of vibrational states in each unit frequency and the partial VDOS describes how individual elements contribute to the total vibrational states, which is shown over a 0-3300 cm^{-1} frequency range. In Figure 4-

12 (a), in the 0-500 cm^{-1} region, the main contributions to vibration involve C and H, while contributions from Bi, Ag, and I are at their strongest compared to the rest of the spectrum. In the 500-1500 cm^{-1} region, these contributions from Bi, Ag, and I are less present and are superseded by contributions from C, H and N atoms. In the vicinity of 3000 cm^{-1}, characteristic high frequency vibrations involving H atoms, for example, N-H or C-H stretching, are observed. After replacing Ag with lighter Cu (Figure 4-12 (c)), vibrations with higher frequency were observed.

In the enlarged low frequency regions in Figure 4-12 (b) and (d), there is a pronounced vibrational contribution from Bi element near 55 cm^{-1} in the Ag-based perovskite, but that contribution peak shifts slightly to 60 cm^{-1} and broadens in the Cu-based one. This demonstrates that Bi contributes significantly to low frequency modes, involving bond bending with Bi, and makes a greater contribution when Cu metal is involved. Ag contributes around 70 cm^{-1} and a broader peak is observed from Cu atoms in the 60-140 cm^{-1} range, indicating that Cu contributes more pronouncedly in low-frequency vibrations than Ag. This is likely due to the smaller mass of Cu and greater bond strength.[47,48] The I atom contributes to vibrations in the 80-150 cm^{-1} region for both materials, with slightly higher frequency for MPA-$CuBiI_8$. The observation that the I atoms contributed to higher frequencies in Cu than Ag highlights that I atoms couple strongly to metal (Bi, Ag, and Cu) atoms, and the shift reflects structural differences in bonding geometry and octahedral distortion, as shown in Table 4-8. C and N show broad contributions across the low frequency range in both perovskites. These mode

peaks are broad and overlap with inorganic lattice motions, showing that the MPA twisting and rocking vibrations are coupled with the inorganic layer.

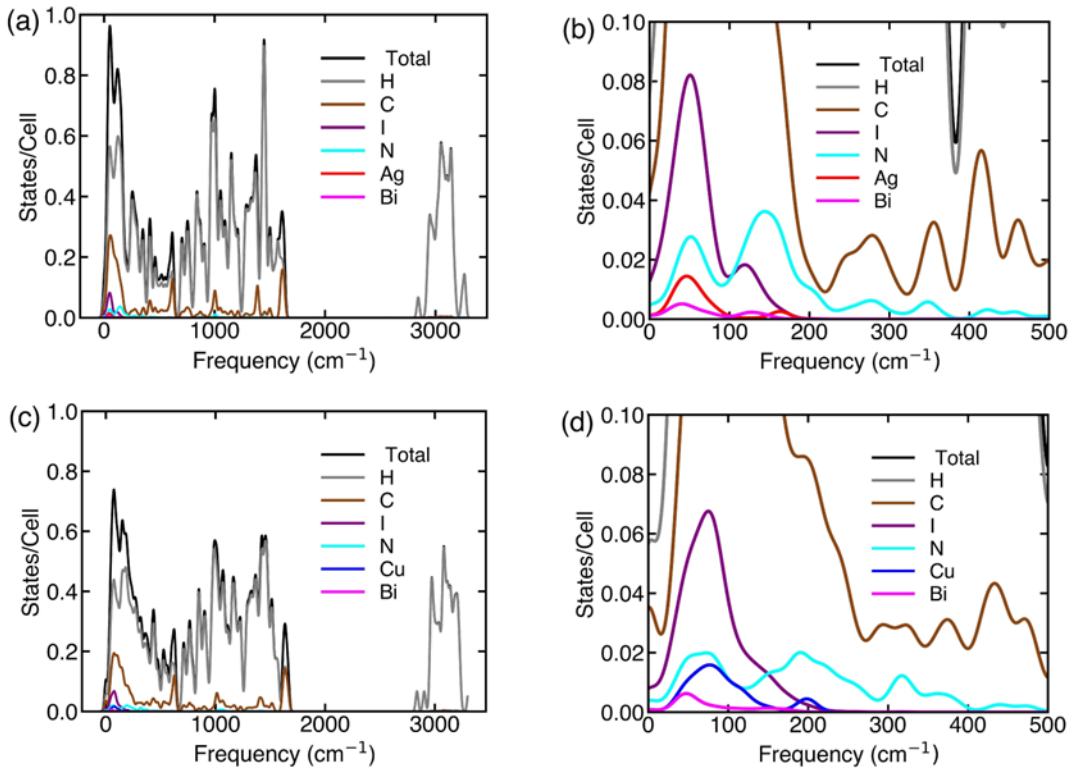

Figure 4-12 Calculated partial vibrational density of states (VDOS) of (a, b) MPA-$AgBiI_8$ and (c, d) MPA-$CuBiI_8$.

For MPA-$AgBiI_8$, the experimental Raman vibration modes reside at 31, 53, 101, 116, and 121 cm^{-1}, while for MPA-$CuBiI_8$, the vibration modes are at 32, 43, 107, 123, and 142 cm^{-1}. According to Hooke's law,

$$f = \frac{1}{2\pi}\sqrt{\frac{k}{m}} \tag{4-3}$$

where k is the force constant, m is the reduced mass, f is the frequency.[49] After treating the atoms and bonds as harmonic oscillators, k is directly proportional to

bond strength. Since the mass of Cu is smaller than the Ag and the force constant of a Cu-I bond (173 N/m) at is higher than that of an Ag-I bond (145.8 N/m),[47,48] the vibrational frequencies of Cu-based perovskite are expected to shift to higher positions as can be confirmed by experimental results with an increase from 101 to 107, 116 to 123 and 121 to 142 cm^{-1}, respectively.

Some researchers have combined experiments and DFT simulations to assign the peaks to the vibration modes in low frequency Raman. For example, Quarti *et al*. attributed the vibrational frequency at 62 cm^{-1} to Pb-I bending, 94 cm^{-1} to Pb-I stretching in inorganic layers and the libration of organic cations at 119 and 154 cm^{-1} in the $CH_3NH_3PbI_3$ 3D structure.[13] Other studies exploited single crystal XRD to help elucidate the structural distortion, such as A site libration and metal halide bond length and angle changes that account for the low frequency vibrational peaks in 2D perovskites.[26]

In terms of the optical properties of double perovskites, previous reports revealed via partial density of states (PDOS) that they are mainly dominated by the inorganic layer.[13,43] The valence band maximum (VBM) is largely contributed by I 5p states with a small contribution from Ag 4d and Bi 6s states and the conduction band minimum (CBM) is mainly contributed by the Bi 6p orbitals.[43,50] From our PDOS (Figure 4-13) and band structure (Figure 4-14) and calculations, we found that the band edges are mostly due to p-orbitals from I atoms, with small contributions from Ag d-orbitals and Cu d-orbitals in the VBM and Bi p-orbitals in the CBM. Our calculations give a bandgap of 1.6 eV for the Cu-based perovskite and 2.1 eV for the

Ag-based perovskite, showing a substantial difference between the two, unlike the bandgaps determined from the Tauc plots. While it is unsurprising that our DFT results do not quantitatively match the experimental bandgap, it is unclear why there is such a discrepancy in the difference between the two structures' bandgaps. Possible reasons are given below.

The partial electronic density of states (PDOS) was calculated using DFT with PBE to determine the atomic orbital character of the band edges. The same input parameters used for relaxation of the structure were used for the SCF and non-SCF calculations to obtain the DOS, except for a 4 × 4 × 4 unshifted k-grid with Blöchl's tetrahedron method for Brillouin-zone integrations[51] being used for the non-SCF calculation.

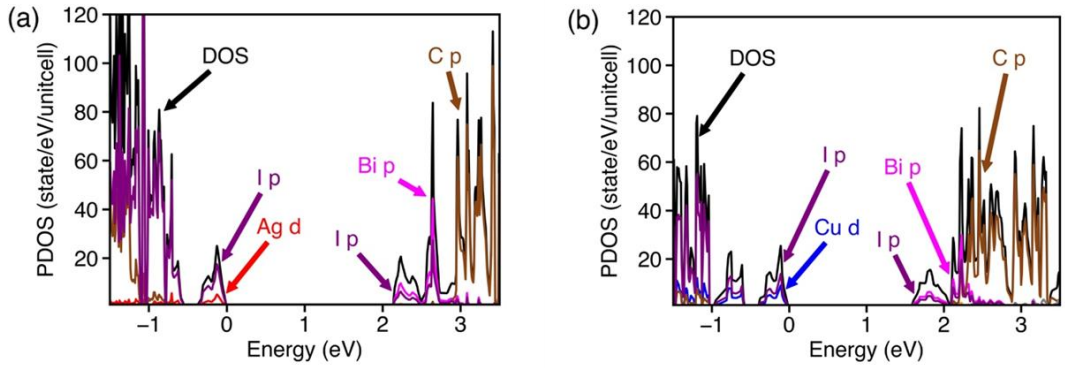

Figure 4-13 Partial electronic density of states for (a) Ag-based perovskite, and (b) Cu-based perovskite. Energies are plotted with reference to the valence band maximum (VBM).

4.3.5 Band Structure

The band structure is calculated using plane-wave DFT with the PBE functional on the relaxed theoretical structures to show the band gap of the two systems. SeeK-path was used to obtain the *k*-path.[52,53] For the bandstructure calculation on the theoretical Ag- and Cu-based perovskite structures, there are 30 points between each high-symmetry point. 340 bands for Ag-based perovskite and 320 bands for Cu-based perovskite are calculated in total, but we only depict those closest to the band edges in Figure 4-13. All inputs for the SCF are the same as used for relaxation.

Both band gap transitions are direct at the Γ and B points in the Brillouin zone. We have found that the top of the valence band is composed of I p-orbitals, with small contributions from Ag or Cu d-orbitals, and the bottom of the conduction band is composed of Bi p-orbitals and I p-orbitals. Our calculations show a band gap difference of about 0.5 eV, with the Cu-based perovskite having a theoretical bandgap of 1.6 eV, and the Ag-based perovskite having a bandgap of 2.1 eV. There are a variety of factors that can lead to discrepancy between theory and experiment, but it's not clear from our calculations why the experimental band gaps are similar. We confirmed via random-phase approximation optical absorption calculations in BerkeleyGW[54] that the lowest transition in the Cu-based perovskite is dipole-allowed. Additionally, we did not include the spin-orbit coupling (SOC) effect in our calculations, which, while typically PBE is comparable to the true bandgap, could account for some discrepancy between our theoretical results and experiment. Spin-orbit coupling may be especially relevant due to the presence of heavy elements Bi

and I in our structure.[43,55] Compared to the experimentally obtained values of the bandgaps of 2.03 eV for both Ag and Cu structures, the theoretical value for the Cu-based perovskite is smaller, and the theoretical value of the Ag-based perovskite is higher. Previous work[10] on the 1D organic metal halide hybrid $C_8H_{28}N_5Pb_3Cl_{11}$ resulted in a difference of 0.27 eV, a nearly 8% difference between DFT with PBE and experiment. Our results show a difference of 21% for the Cu-based perovskite, and a 3% difference for the Ag-based perovskite compared to experiment. It appears that in the Cu-based perovskite spin-orbit coupling, excitonic, and quasiparticle effects do not cancel closely[56] and must be directly accounted for in calculations.

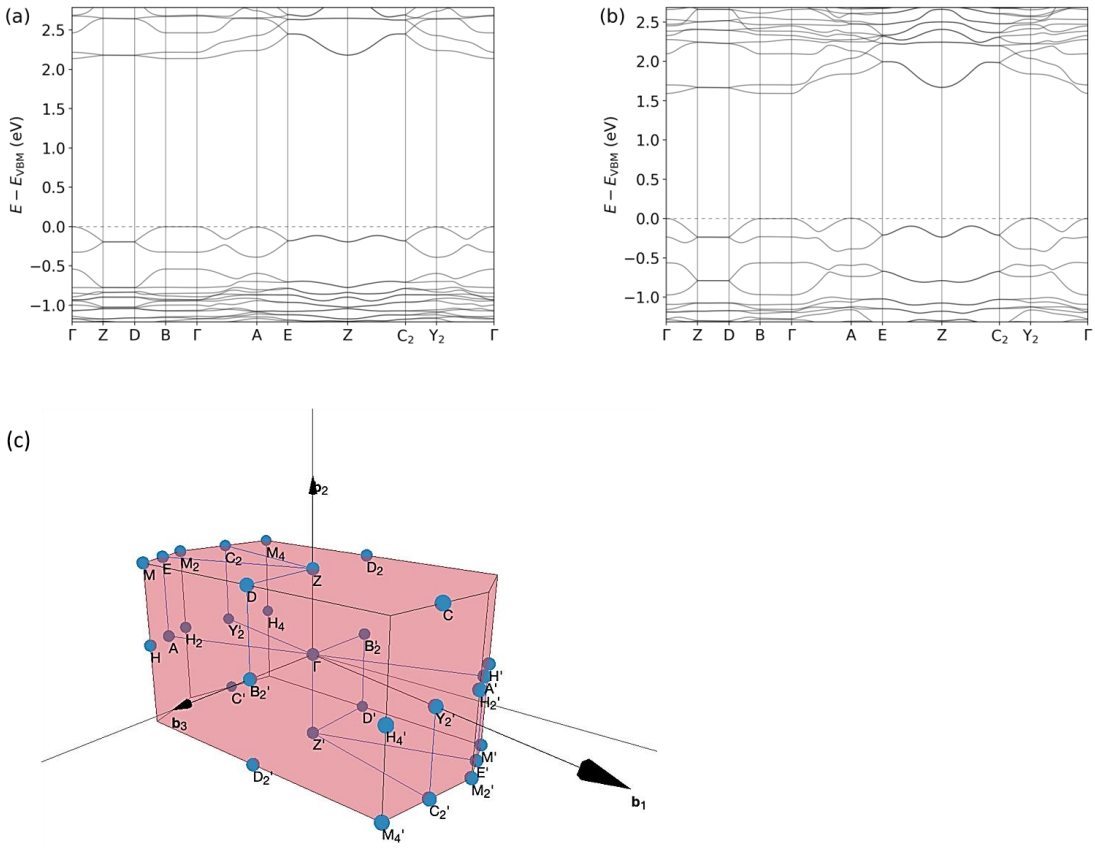

Figure 4-14 Band structure for (a) the Ag-based perovskite, and (b) the Cu-based

perovskite. Energies are plotted with reference to the valence band maximum (VBM). (c) The high-symmetry points in the Brillouin zone as used in the band structure of Ag- and Cu-based perovskites.

In other work on 1D organic metal halide hybrids, specifically $C_4N_2H_{14}PbBr_4$, the VBM was dominated by p-orbitals of Br, while the CBM was dominated by p-orbitals of Pb.[57] In a study of 2D lead bromide perovskites, VBM had strong Br p-orbital character followed by Pb s-orbitals, and the CBM had strong Pb p-orbital character.[58] Our results match with the existing trend of the VBM being dominated by metal and the CBM having significant contributions from halide (I, Cl, or Br) p-orbitals. In each case, the halide atom is a major contributor to the band edges, with the metal atoms affecting the size of the band gap, but not significantly changing the character or shape of the band edges. It is expected that the contribution from Ag and Cu would be less than the contribution from iodine in the density of states because there are more iodine atoms in the unit cell.

4.3.6 Octahedral Parameters

There are four octahedra in each unit cell, but only two of the four octahedra are unique, by symmetry. We calculated octahedral parameters, including bond-length deviations (D), tilting (D_{tilt}), in- and out-of-plane tilting defined with respect to the (0 0 1) plane[59] (D_{in} and D_{out}), and bond angle variance (σ^2) as defined in Ref.[58] Code from Ref.[58] is used to calculate the octahedral tilt distortion parameters, while D, σ^2 are calculated with VESTA.[60] We have calculated ΔD_{tilt} as the difference between the

largest and smallest D_{tilt} angles for a given structure. Each similarly labeled iodine atom in the three structures is in a similar molecular environment between the three structures due to the orientation of the organic molecules, even if bonded to different metal atoms (Ag or Cu). The centroid (midpoint here for two same atoms) of disordered atomic sites was used to calculate the octahedral parameters of experimental structures obtained from single-crystal XRD.

As shown in Figure 4-15 and Table 4-8, the arrangement of Cu octahedra in MPA-$CuBiI_8$ is more distorted than the Ag octahedra in MPA-$AgBiI_8$ based on ΔD_{tilt}, and therefore MPA-$CuBiI_8$ has the greater inversion symmetry-breaking. In Table 4-8, the bond length distortion of Bi octahedra is about the same in both theoretical Cu and Ag structures, but the bond angle variance of Bi octahedra is much higher in the Cu theoretical structure. Cu and Ag-centered octahedra have greater bond length distortion than Bi, due to Jahn-Teller effects. Ag has greater bond angle variance than Bi, but Bi has more than Cu. DFT underestimates the disparity between Ag/Cu and Bi octahedra within a structure. The level of distortion between Bi atoms in the theoretical Cu-based and Ag-based structures differs. The bond length distortion index D is nearly identical (1.07 in Cu vs 1.05 in Ag). However, the bond angle variance, σ^2, is quite different ($70.53^{\circ 2}$ in Cu and $38.63^{\circ 2}$ in Ag).

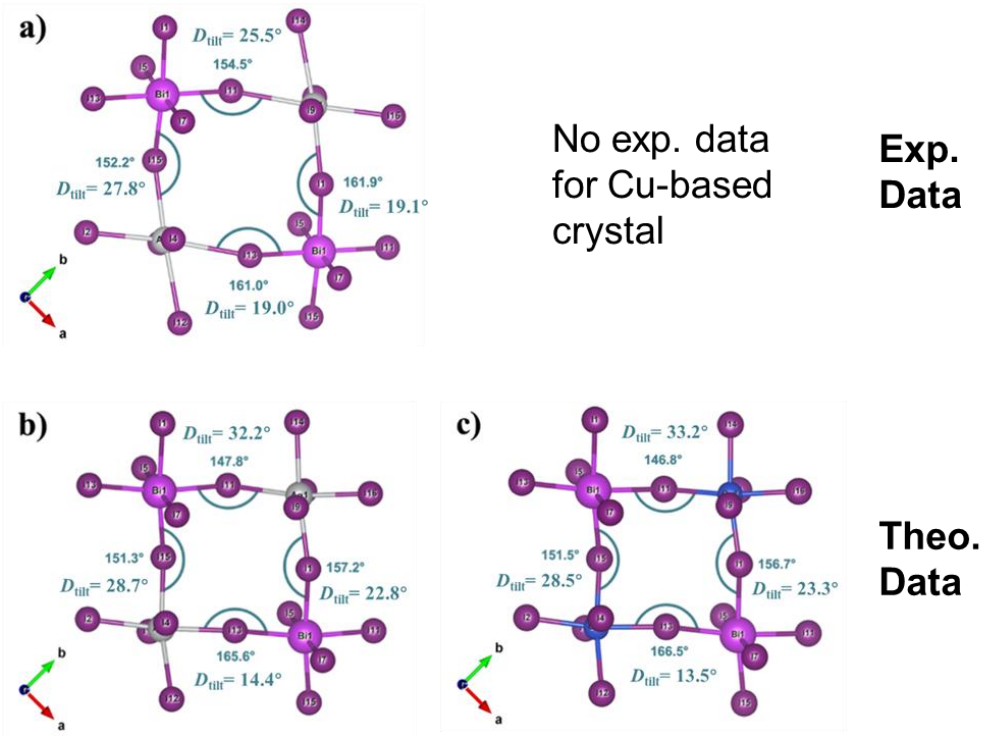

Figure 4-15 Octahedral tilt angles for (a) the experimental Ag-based perovskite structure, (b) the theoretical Ag-based perovskite structure, and (c) the theoretical Cu-based perovskite structure.

Table 4-8 Octahedral tilt angles and parameters for the Ag-based and Cu-based perovskites. Each iodine has one equivalent site within the unit cell, by symmetry. I1 is equivalent to I2, I11 is equivalent to I12, I13 is equivalent to I14, and I15 is equivalent to I16. *D* is the distortion index (bond length). σ^2 (degrees^2) is the bond angle variance.

Structure	**Vertex**	D_{tilt} (°)	D_{out} (°)	D_{in} (°)	ΔD_{tilt} (°)	D ($\times 10^{-2}$) **Bi**	D ($\times 10^{-2}$) **M=Ag,Cu**	σ^2 (°^{2}) **Bi**	σ^2 (°^{2}) **M=Ag,Cu**

Exp. Ag	I1	19.07	18.37	5.21	13.72	1.01	10.42	3.39	83.58
	I11	22.88	21.04	9.21					
	I13	14.06	12.53	6.43					
	I15	27.78	27.04	6.63					
Exp. Ag[13]	I1	18.13	17.50	4.83	9.72	0.56	11.70	2.39	106.81
	I11	25.48	23.52	10.10					
	I13	19.05	15.30	11.48					
	I15	27.85	26.07	10.15					
Theory Ag	I1	22.83	21.86	6.78	17.84	1.05	4.26	38.63	53.89
	I11	32.21	31.16	8.64					
	I13	14.38	13.58	4.76					
	I15	28.69	27.33	9.08					
Theory Cu	I1	23.26	22.54	5.89	19.71	1.07	2.97	70.53	44.65
	I11	33.18	33.16	1.10					
	I13	13.47	10.78	8.13					
	I15	28.46	26.06	11.85					

*Each similarly labeled iodine atom in the three structures is in a very similar molecular environment between the three structures due to the orientation of the organic molecules, even if bonded to different metal atoms (Ag or Cu).

One application of a highly distorted structure is to induce a larger Rashba effect to modulate the spin lifetime, because the lattice distortion could break the inversion symmetry in the crystal, which arises from the organic cation rotation and unmatched metal halide bonds.[59,61,62] The Rashba effect will split the electronic band into finer structures and affect the spin-related excited state lifetime.[63–65] To this end, we have calculated octahedral distortion parameters, in particular, ΔD_{tilt}, which is an indicator of inversion symmetry breaking and has been tied to chiral light emission. We can compare the octahedral parameters, as a measure of distortion, for the experimental Ag structure and theoretical Ag and Cu structures. These parameters have been used as predictors of experimental properties such as broadband emission, band gaps, and exciton trapping. In particular, Smith *et. al.* found that broadband emission upon near-ultraviolet excitation becomes more intense with increasing out-of-plane angle distortion.[66] Additionally, larger values of ΔD_{tilt} indicate inversion symmetry-breaking,[59,67] which enables chiral emission.[58,68] Larger octahedra tilt angles also show wider bandgaps and greater exciton trapping.[69,70] We find that DFT overestimates the level of angle distortion compared to experiment, as quantified by ΔD_{tilt}, in agreement with previous work.[58]

4.4 Conclusion

In conclusion, crystalline MPA-$AgBiI_8$ and MPA-$CuBiI_8$ were successfully synthesized using a hydrothermal method. Their structural, photophysical and Raman vibration modes have been studied. The structure of MPA-$CuBiI_8$ is more complex than that of MPA-$AgBiI_8$, as confirmed by XRD. This enhanced complexity may stem from oxidation. The optical studies show a similar electronic band structure and the same bandgap, and more trap states are inferred for the Cu-based perovskite from the TRPL measurements, implying structural distortion and strong electron–phonon coupling. The vibrational modes of the Cu-based perovskite are at higher frequencies than those of the Ag-based perovskite due to stronger metal halide bonds and smaller metal mass. Furthermore, the decreased exciton lifetime supports stronger electron–phonon coupling in the more distorted Cu-containing perovskite. The vibrational modes for both Ag- and Cu-based Pb-free double perovskites are fully investigated by first-principles DFT simulation and assigned to metal halide bond bending and stretching in the octahedra, coupled to vibrations of the organic layer of the 2D perovskites. At higher vibrational frequencies, stronger vibrational motion from the organic layers in the structure manifests for both perovskites. DFT also shows a slightly larger lattice distortion for the Cu-based perovskite compared to the Ag-based perovskite, as indicated by ΔD_{tilt} value. Induced centrosymmetry-breaking by lattice distortions may open a new avenue to achieve larger Rashba effects in double perovskites.

4.5 Experimental and Computational Methods

1. Materials

Ag_2O (99+%) was purchased from Acros, Cu_2O (97%) was purchased from Aldrich, and Bi_2O_3 (99.99%) was purchased from Thermo Scientific. (S)-(+)-b-methylphenethylamine (*S*-β-MPA) and hydroiodic acid (57 wt% in H_2O, 99.99%) were purchased from Sigma-Aldrich without any further purification.

2. Synthesis of MPA-$AgBiI_8$ and MPA-$CuBiI_8$

Ag_2O (0.232 g, 1.00 mmol) or Cu_2O (0.143 g, 1.00 mmol) and Bi_2O_3 (0.476 g, 1.00 mmol) were dissolved in 48 wt% aqueous HI solution (diluted to 48 wt% from 57 wt%) (20 mL) under heating at 120 °C, and medium-speed stirring, resulting in a red solution. Subsequent addition of *S*-β-MPA (0.540 g, 4.00 mmol) to the hot solution led to the formation of a red precipitate, which subsequently redissolved with continued stirring, ending up with a red solution. The solution was then cooled to room temperature and concentrated by evaporation to yield red crystals of the product, followed by a rinse with ethyl acetate three times.

3. SEM Measurements

Scanning electron microscopy (SEM) images were acquired with Thermo Scientific Scios 2 DualBeam, equipped with an Oxford Instruments AZtecLive Ultim Max 100 EDS detector.

4. Spectroscopy Measurements

The electronic absorption spectra of the powder were measured with a UV2600

variable slit UV-Vis spectrophotometer based on reflection mode (converted to absorption via Kubelka-Munk function) from Shanghai Tianmei Scientific Instrument. The scanning speed was set at 600 nm/min, and the slit width was set at 5.0.

The photoluminescence (PL) spectra of the samples were acquired at room temperature using an Edinburgh Instruments FLS1000 fluorescence photometer with an Xe900 excitation source and a PMT1700 detector.

Time-resolved photoluminescence (TRPL) profiles of samples were determined at room temperature using the Edinburgh μF2 light source of the FLS1000 fluorescence photometer from Edinburgh Instruments.

5. Single Crystal X-ray Diffraction (scXRD)

A single crystal of (*S*-MPA)$_4$AgBiI$_8$ was selected under a microscope, loaded onto a MiTeGen polyimide sample loop using Type NVH Cargille immersion oil, and mounted onto a Rigaku XtaLAB Synergy-S single-crystal diffractometer. The crystal was cooled to 100 K under a stream of nitrogen. Diffraction of Cu Kα radiation from a PhotonJet-S microfocus source was detected using a HyPix6000HE hybrid photon counting detector. Screening, indexing, data collection, and data processing were performed with CrysAlisPro. The structures were solved using SHELXT and refined using SHELXL following established strategies.[71–73] All non-H atoms were refined anisotropically. C-bound H atoms were placed at calculated positions and refined with a riding model and coupled isotropic displacement parameters (1.2 × U_{eq} for non-methyl C-H atoms and 1.5 × U_{eq} for methyl groups). Crystal structure visualization was performed with Mercury.[74]

6. Powder X-ray Diffraction (pXRD)

Powder XRD patterns were collected on a Bruker D8 Discover Diffractometer using Cu Kα radiation (40 kV and 40 mA) with degrees per step and time/step parameters of 0.02 degrees per step and 0.4 s/step, respectively, at 2θ angle from 10 to 60°. The simulated pXRD pattern is based on the MPA-$AgBiI_8$ scXRD data at 290 K from Li's work.[13] The theoretical pXRD patterns were simulated via VESTA.

7. Low Frequency Raman Spectroscopy (0 cm^{-1} to 200 cm^{-1})

Low frequency Raman spectra were acquired by an Olympus BX51 microscope equipped with an ONDAX THz-Raman spectroscope probe. 976 nm excitation laser was generated at the source (THz-Raman) with a power of 500 mW, and the power onto the sample is about 150 mW after decaying. The built-in amplified spontaneous emission filter and notch filter enable measurements of Raman signals down to 5 cm^{-1} and we can still attain data down to 0 cm^{-1} with uncertainties. Signal was captured by using a 10X objective lens (Olympus, NA = 0.3, FN = 26.5). The Raman scattering signal was directed into spectrograph (Andor SR-303i-B, 300 l/m, Blaze 1000) through fiber optics (Diamond USA) and eventually detected by InGaAs CCD (Andor DU90A). Each spectrum was accumulated from 90 scans (1s/scan).

8. High Frequency Raman Spectroscopy (200 cm^{-1} to 1800 cm^{-1})

High frequency Raman spectra were acquired using a Thermo Fisher DRX3 Raman microspectrometer. The laser excitation source was a diode laser (λ_{ex} = 785 nm). Spectra were recorded under the following conditions: stainless-steel substrate,

50× objective, collect exposure time 30 s for five accumulations, laser power 30 mW (in focus), and aperture 50 μm slit.

9. FTIR Spectroscopy

The FTIR spectra of the perovskites were collected using a PerkinElmer FTIR Spectrum Two series spectrometer with a universal ATR sampling accessory (UATR). This solid FTIR uses a high refractive index diamond to apply pressure on the solid samples and guide the beam up to a few microns to the samples. To make the IR signal intensities consistent, the force applied to all the samples was at 100 N.

10. DFT Calculation

We performed first-principles density-functional perturbation theory[75] calculations as implemented in Quantum ESPRESSO[76] on *R*-MPA-XBiI$_8$ (X=Ag, Cu) with the Perdew-Burke-Ernzerhof (PBE)[77] exchange-correlation functional to predict and understand its vibrational modes (Raman and IR). PBE was used for both structural relaxation and for the calculation of Raman frequencies. Another exchange-correlation functional, Local Density Approximation (LDA), was used to calculate the Raman tensor as a separate calculation, as calculation of the Raman tensor is not yet implemented for PBE in Quantum ESPRESSO version 7.2, allowing us to obtain Raman intensities. The calculation of intensities as implemented in Quantum ESPRESSO is described in Lazzeri *et al.*[78] We selected PBE as our exchange functional due to its closer agreement with the experimental lattice parameters compared to LDA and PBE with Grimme dispersion correction, version 2 (GD2)[79] (Table 4-3). Norm-conserving scalar-relativistic pseudopotentials from

ONCVPSP (Optimized Norm-Conserving Vanderbilt Pseudopotential) code version 3.3.0 with standard accuracy were used as obtained from Pseudo Dojo.[80,81] Relaxation fixed at the experimental lattice parameters resulted in imaginary phonon modes.

For the Ag-based perovskite, we ran a variable-cell relaxation calculation starting from the experimental XRD structure of (*R*-MPA)$_4$AgBiI$_8$ from Ref.[13] The *R*-version of the structure was used for simulation, and all the properties would be identical for *R* and *S* enantiomers.[58] The unit cell has 212 atoms. The planewave cutoff energy is 56 Ry. Energy convergence thresholds are 10^{-8} Ry. Our variable-cell relaxation forces thresholds are set to 10^{-5} Ry/bohr. Our self-consistency convergence thresholds for the ground state are set to 10^{-18} Ry. The BFGS geometry optimization algorithm is used for structural relaxation, with the trust radius set to 10^{-5} bohr. The components of the stress tensor were converged to a magnitude of less than 1 kbar. We use only the Γ-point for *k*-point sampling, given the large unit cell. We use 10^{-16} for the phonon convergence threshold. These strict thresholds for both structural relaxation and calculation of phonons were required to accurately obtain the lowest frequency phonon modes – at less stringent thresholds, imaginary phonon modes were obtained. We combine PBE Raman frequencies with LDA Raman intensities and apply the acoustic sum rule. Our methods for MPA-CuBiI$_8$ are the same, starting again from the experimental Ag-based structure of Ref.,[13] but substituting Cu atoms for Ag before structural relaxation.

The DFT results are a temperature-independent reduced Raman spectrum. Temperature dependence has been removed from the experimental Raman spectra, to generate a reduced Raman spectrum, by multiplying the experimental intensity by the temperature factor[44]:

$$\omega\left(1-e^{-\frac{\hbar\omega}{kT}}\right) \tag{4-4}$$

where ω is frequency in s^{-1}, $\hbar$ is the reduced Planck constant ($1.054571817\times10^{-34}$ $J\cdot s^{-1}$), k is the Boltzmann constant (1.380649×10^{-23} $J\cdot K^{-1}$), and T is the temperature in Kelvin (293 K).

4.6 References

(1) Kojima, A.; Teshima, K.; Shirai, Y.; Miyasaka, T. Organometal Halide Perovskites as Visible-Light Sensitizers for Photovoltaic Cells. *J. Am. Chem. Soc.* **2009**, *131* (17), 6050–6051. https://doi.org/10.1021/ja809598r.

(2) Suresh Kumar, N.; Chandra Babu Naidu, K. A Review on Perovskite Solar Cells (PSCs), Materials and Applications. *J. Materiomics* **2021**, *7* (5), 940–956. https://doi.org/10.1016/j.jmat.2021.04.002.

(3) Zhao, B.; Guo, B.; Xing, S.; Liu, Z.; Yuan, Y.; Ren, Z.; Tang, W.; Lian, Y.; Zhang, G.; Zou, C.; et al. Highly Stable Perovskite Light-Emitting Diodes. *Matter* **2024**, *7* (3), 772–793. https://doi.org/10.1016/j.matt.2023.11.022.

(4) Protesescu, L.; Yakunin, S.; Bodnarchuk, M. I.; Krieg, F.; Caputo, R.; Hendon, C. H.; Yang, R. X.; Walsh, A.; Kovalenko, M. V. Nanocrystals of Cesium Lead Halide Perovskites ($CsPbX_3$, X = Cl, Br, and I): Novel Optoelectronic Materials

Showing Bright Emission with Wide Color Gamut. *Nano Lett.* **2015**, *15* (6), 3692–3696. https://doi.org/10.1021/nl5048779.

(5) Ding, N.; Wang, N.; Liu, S.; Wang, Y.; Zhou, D.; Xu, W.; Song, H. Research Progress on Doped Perovskite Materials. *Laser Optoelectron. Prog.* **2021**, *58* (15), 1516011. https://doi.org/10.3788/LOP202158.1516011.

(6) Chen, Q.; Wu, J.; Ou, X.; Huang, B.; Almutlaq, J.; Zhumekenov, A. A.; Guan, X.; Han, S.; Liang, L.; Yi, Z.; et al. All-Inorganic Perovskite Nanocrystal Scintillators. *Nature* **2018**, *561* (7721), 88–93. https://doi.org/10.1038/s41586-018-0451-1.

(7) Chen, X.; Zhou, H.; Wang, H. 2D/3D Halide Perovskites for Optoelectronic Devices. *Front. Chem.* **2021**, *9*, 715157. https://doi.org/10.3389/fchem.2021.715157.

(8) Lin, H.; Zhou, C.; Tian, Y.; Siegrist, T.; Ma, B. Low-Dimensional Organometal Halide Perovskites. *ACS Energy Lett.* **2018**, *3* (1), 54–62. https://doi.org/10.1021/acsenergylett.7b00926.

(9) Zhou, C.; Lin, H.; Tian, Y.; Yuan, Z.; Clark, R.; Chen, B.; van de Burgt, L. J.; Wang, J. C.; Zhou, Y.; Hanson, K.; et al. Luminescent Zero-Dimensional Organic Metal Halide Hybrids with near-Unity Quantum Efficiency. *Chem. Sci.* **2018**, *9* (3), 586–593. https://doi.org/10.1039/C7SC04539E.

(10) Lee, S.; Karkee, R.; Ben-Akacha, A.; Luong, D.; Winfred, J. S. R. V.; Lin, X.; Strubbe, D. A.; Ma, B. One-Dimensional Organic Metal Halide Nanoribbons with Dual Emission. *Chem. Commun.* **2023**, *59* (25), 3711–3714.

https://doi.org/10.1039/D3CC00044C.

(11) Jana, M. K.; Janke, S. M.; Dirkes, D. J.; Dovletgeldi, S.; Liu, C.; Qin, X.; Gundogdu, K.; You, W.; Blum, V.; Mitzi, D. B. Direct-Bandgap 2D Silver–Bismuth Iodide Double Perovskite: The Structure-Directing Influence of an Oligothiophene Spacer Cation. *J. Am. Chem. Soc.* **2019**, *141* (19), 7955–7964. https://doi.org/10.1021/jacs.9b02909.

(12) Chakraborty, N.; Ngo, T. A.; Dominguez Montero, A.; Liyanage, T.; McCandless, G. T.; Chan, J. Y.; Nguyen, T. D.; Whittaker-Brooks, L. Decoding Chirality Transfer Strengths and Structure–Property Relationships in Bismuth-Containing Chiral Hybrid Organic–Inorganic Semiconductors. *J. Am. Chem. Soc.* **2025**, *147* (32), 29431–29443. https://doi.org/10.1021/jacs.5c09713.

(13) Li, D.; Liu, X.; Wu, W.; Peng, Y.; Zhao, S.; Li, L.; Hong, M.; Luo, J. Chiral Lead-Free Hybrid Perovskites for Self-Powered Circularly Polarized Light Detection. *Angew. Chem. Int. Ed.* **2021**, *60* (15), 8415–8418. https://doi.org/10.1002/anie.202013947.

(14) Huizi-Rayo, U.; Gutierrez, J.; Seco, J. M.; Mujica, V.; Diez-Perez, I.; Ugalde, J. M.; Tercjak, A.; Cepeda, J.; San Sebastian, E. An Ideal Spin Filter: Long-Range, High-Spin Selectivity in Chiral Helicoidal 3-Dimensional Metal Organic Frameworks. *Nano Lett.* **2020**, *20* (12), 8476–8482. https://doi.org/10.1021/acs.nanolett.0c02349.

(15) Naskar, S.; Mujica, V.; Herrmann, C. Chiral-Induced Spin Selectivity and Non-Equilibrium Spin Accumulation in Molecules and Interfaces: A First-Principles

Study. *J. Phys. Chem. Lett.* **2023**, *14* (3), 694–701. https://doi.org/10.1021/acs.jpclett.2c03747.

(16) Zhou, Y.; Chen, J.; Bakr, O. M.; Mohammed, O. F. Metal Halide Perovskites for X-Ray Imaging Scintillators and Detectors. *ACS Energy Lett.* **2021**, *6* (2), 739–768. https://doi.org/10.1021/acsenergylett.0c02430.

(17) Hu, Y.; Jin, J.; Han, K.; Xia, Z. Unveiling The Role of Cu^{+} Doping in Rb_2AgBr_3 Scintillators toward Enhanced Photoluminescence Quantum Efficiency and Light Yield. *Adv. Opt. Mater.* **2024**, *12* (9), 2302063. https://doi.org/10.1002/adom.202302063.

(18) Han, K.; Zhang, S.; Jin, J.; Sun, Y.; Wang, Y.; Xia, Z. Lattice Distortion Promoting Wavelength-Tunable Emissions in Cu(I)-Based Halides for Thermography and Anti-Counterfeiting. *Angew. Chem. Int. Ed.* **2025**, *64* (32), e202504406. https://doi.org/10.1002/anie.202504406.

(19) Martín-García, B.; Spirito, D.; Lin, M.-L.; Leng, Y.-C.; Artyukhin, S.; Tan, P.-H.; Krahne, R. Low-Frequency Phonon Modes in Layered Silver-Bismuth Double Perovskites: Symmetry, Polarity, and Relation to Phase Transitions. *Adv. Opt. Mater.* **2022**, *10* (14), 2200240. https://doi.org/10.1002/adom.202200240.

(20) Rury, A. S.; Sanni, A. M.; Konadu, D.; Danielson, T. Evidence of Defect-Induced Broadband Light Emission from 2D Ag–Bi Double Perovskites Grown at Liquid–Liquid Interfaces. *J. Chem. Phys.* **2023**, *158* (1), 011101. https://doi.org/10.1063/5.0134568.

(21) Su, C.-Y.; Yao, Y.-F.; Zhang, Z.-X.; Wang, Y.; Chen, M.; Huang, P.-Z.; Zhang, Y.;

Qiao, W.-C.; Fu, D.-W. The Construction of a Two-Dimensional Organic–Inorganic Hybrid Double Perovskite Ferroelastic with a High T_c and Narrow Band Gap. *Chem. Sci.* **2022**, *13* (17), 4794–4800. https://doi.org/10.1039/D1SC07045B.

(22) Jaffe, A.; Lin, Y.; Beavers, C. M.; Voss, J.; Mao, W. L.; Karunadasa, H. I. High-Pressure Single-Crystal Structures of 3D Lead-Halide Hybrid Perovskites and Pressure Effects on Their Electronic and Optical Properties. *ACS Cent. Sci.* **2016**, *2* (4), 201–209. https://doi.org/10.1021/acscentsci.6b00055.

(23) Mao, L.; Stoumpos, C. C.; Kanatzidis, M. G. Two-Dimensional Hybrid Halide Perovskites: Principles and Promises. *J. Am. Chem. Soc.* **2019**, *141* (3), 1171–1190. https://doi.org/10.1021/jacs.8b10851.

(24) Yuan, Z.; Zhou, C.; Tian, Y.; Shu, Y.; Messier, J.; Wang, J. C.; van de Burgt, L. J.; Kountouriotis, K.; Xin, Y.; Holt, E.; et al. One-Dimensional Organic Lead Halide Perovskites with Efficient Bluish White-Light Emission. *Nat. Commun.* **2017**, *8* (1), 14051. https://doi.org/10.1038/ncomms14051.

(25) Sun, S.; Lu, M.; Gao, X.; Shi, Z.; Bai, X.; Yu, W. W.; Zhang, Y. 0D Perovskites: Unique Properties, Synthesis, and Their Applications. *Adv. Sci.* **2021**, *8* (24), 2102689. https://doi.org/10.1002/advs.202102689.

(26) Gao, L.; Hu, P.; Liu, S. Low-Dimensional Perovskite Modified 3D Structures for Higher-Performance Solar Cells. *J. Energy Chem.* **2023**, *81*, 389–403. https://doi.org/10.1016/j.jechem.2023.01.061.

(27) Zhang, X.; Han, W. P.; Wu, J. B.; Milana, S.; Lu, Y.; Li, Q. Q.; Ferrari, A. C.;

Tan, P. H. Raman Spectroscopy of Shear and Layer Breathing Modes in Multilayer MoS_2. *Phys. Rev. B* **2013**, *87* (11), 115413. https://doi.org/10.1103/PhysRevB.87.115413.

(28) Scheuschner, N.; Gillen, R.; Staiger, M.; Maultzsch, J. Interlayer Resonant Raman Modes in Few-Layer MoS_2. *Phys. Rev. B* **2015**, *91* (23), 235409. https://doi.org/10.1103/PhysRevB.91.235409.

(29) Zhao, Y.; Luo, X.; Li, H.; Zhang, J.; Araujo, P. T.; Gan, C. K.; Wu, J.; Zhang, H.; Quek, S. Y.; Dresselhaus, M. S.; et al. Interlayer Breathing and Shear Modes in Few-Trilayer MoS_2 and WSe_2. *Nano Lett.* **2013**, *13* (3), 1007–1015. https://doi.org/10.1021/nl304169w.

(30) Guerrero, E.; Karkee, R.; Strubbe, D. A. Phase Stability and Raman/IR Signatures of Ni-Doped MoS_2 from Density Functional Theory Studies. *J. Phys. Chem. C* **2021**, *125* (24), 13401–13412. https://doi.org/10.1021/acs.jpcc.1c02974.

(31) Zhang, H.; Vickers, E. T.; Erickson, S.; Guarino-Hotz, M.; Barnett, J. L.; Ghosh, S.; Zhang, J. Z. Synthesis and Properties of Stable Amino Metal Halide Molecular Clusters in the Solid State. *J. Phys. Chem. Lett.* **2022**, *13* (45), 10543–10549. https://doi.org/10.1021/acs.jpclett.2c02977.

(32) Xue, X.; Liu, Z.; Eisenberg, S.; Ren, Q.; Lin, D.; Coester, E.; Zhang, H.; Zhang, J. Z.; Wang, X.; Li, Y. Regulated Interfacial Proton and Water Activity Enhances Mn^{2+}/MnO_2 Platform Voltage and Energy Efficiency. *ACS Energy Lett.* **2023**, *8* (11), 4658–4665. https://doi.org/10.1021/acsenergylett.3c01354.

(33) Zhang, H.; Oduntan, A.; Zhuo, Z.; Chuang, S. S. C.; Guo, J.; Zhang, J. Z. New Insights into Nonthermal Plasma-Assisted Poly(Vinyl Alcohol) Depolymerization Catalyzed by TiO_2. *J. Phys. Chem. C* **2025**, *129* (10), 4950–4963. https://doi.org/10.1021/acs.jpcc.4c07876.

(34) Pérez-Osorio, M. A.; Lin, Q.; Phillips, R. T.; Milot, R. L.; Herz, L. M.; Johnston, M. B.; Giustino, F. Raman Spectrum of the Organic–Inorganic Halide Perovskite $CH_3NH_3PbI_3$ from First Principles and High-Resolution Low-Temperature Raman Measurements. *J. Phys. Chem. C* **2018**, *122* (38), 21703–21717. https://doi.org/10.1021/acs.jpcc.8b04669.

(35) Ma, Z.; Lv, P.; He, X.; Wang, F.; Li, Y.; Xiao, G.; Zou, B. Self-Trapped Excitons or Bi^{3+} Ions for Broad Emission in a Lead-Free Double Perovskite? Hearing What Pressure Says. *Nano Lett.* **2025**, *25* (23), 9345–9352. https://doi.org/10.1021/acs.nanolett.5c01709.

(36) Vickers, E. T.; Xu, K.; Dreskin, B. W.; Graham, T. A.; Li, X.; Zhang, J. Z. Ligand Dependent Growth and Optical Properties of Hybrid Organo-Metal Halide Perovskite Magic Sized Clusters. *J. Phys. Chem. C* **2019**, *123* (30), 18746–18752. https://doi.org/10.1021/acs.jpcc.9b05521.

(37) Vickers, E. T.; Enlow, E. E.; Delmas, W. G.; DiBenedetto, A. C.; Chowdhury, A. H.; Bahrami, B.; Dreskin, B. W.; Graham, T. A.; Hernandez, I. N.; Carter, S. A.; et al. Enhancing Charge Carrier Delocalization in Perovskite Quantum Dot Solids with Energetically Aligned Conjugated Capping Ligands. *ACS Energy Lett.* **2020**, *5* (3), 817–825. https://doi.org/10.1021/acsenergylett.0c00093.

(38) Zhang, H.; Zeitz, D. C.; Zhang, J. Z. Ultrafast Study of Excited State Dynamics of Amino Metal Halide Molecular Clusters. *J. Phys. Chem. Lett.* **2023**, *14* (36), 8095–8099. https://doi.org/10.1021/acs.jpclett.3c01952.

(39) Cherrette, V. L.; Zeitz, D.; Khvichia, M.; Cooper, J. K.; Ping, Y.; Zhang, J. Z. Enhancing the Photoexcited Carrier Spin Relaxation Lifetime in $CsPbBr_3$ Perovskite Quantum Dots by ^{208}Pb Isotope Enrichment. *J. Phys. Chem. Lett.* **2025**, *16* (13), 3336–3342. https://doi.org/10.1021/acs.jpclett.5c00123.

(40) Volonakis, G.; Filip, M. R.; Haghighirad, A. A.; Sakai, N.; Wenger, B.; Snaith, H. J.; Giustino, F. Lead-Free Halide Double Perovskites via Heterovalent Substitution of Noble Metals. *J. Phys. Chem. Lett.* **2016**, *7* (7), 1254–1259. https://doi.org/10.1021/acs.jpclett.6b00376.

(41) Ji, G.; Xiao, Z. Jahn−Teller Distortion-Stabilized Halide Double Perovskites with Unusual Rock-Salt-Type Ordering of Divalent B-Site Cations. *Chem. Mater.* **2022**, *34* (18), 8207–8212. https://doi.org/10.1021/acs.chemmater.2c01496.

(42) Bhuvanesh, N. S. P.; Gopalakrishnan, J. Solid-State Chemistry of Early Transition-Metal Oxides Containing d^0 and d^1 Cations. *J. Mater. Chem.* **1997**, *7* (12), 2297–2306. https://doi.org/10.1039/a703996d.

(43) Connor, B. A.; Leppert, L.; Smith, M. D.; Neaton, J. B.; Karunadasa, H. I. Layered Halide Double Perovskites: Dimensional Reduction of $Cs_2AgBiBr_6$. *J. Am. Chem. Soc.* **2018**, *140* (15), 5235–5240. https://doi.org/10.1021/jacs.8b01543.

(44) Brooker, M. H.; Nielsen, O. F.; Praestgaard, E. Assessment of Correction Procedures for Reduction of Raman Spectra. *J. Raman Spectrosc.* **1988**, *19* (2), 71–78. https://doi.org/10.1002/jrs.1250190202.

(45) Tuschel, D. Raman Spectroscopy and Imaging of Low Energy Phonons. *Spectroscopy* **2015**, *30* (9), 18–31.

(46) Zhang, J.; Wang, C.-Z.; Zhu, Z. Z.; Dobrovitski, V. V. Vibrational Modes and Lattice Distortion of a Nitrogen-Vacancy Center in Diamond from First-Principles Calculations. *Phys. Rev. B* **2011**, *84* (3), 035211. https://doi.org/10.1103/PhysRevB.84.035211.

(47) Bowmaker, G. A.; Healy, P. C.; Kildea, J. D.; White, A. H. Far Infrared Spectroscopy of Complexes of Copper(I) Halides with Phosphine and Amine Ligands. *Spectrochim. Acta A Mol. Spectrosc.* **1988**, *44* (11), 1219–1223. https://doi.org/10.1016/0584-8539(88)80096-5.

(48) Stephens, S. L.; Tew, D. P.; Walker, N. R.; Legon, A. C. $H_3P\cdots AgI$: Generation by Laser-Ablation and Characterization by Rotational Spectroscopy and Ab Initio Calculations. *Phys. Chem. Chem. Phys.* **2016**, *18* (28), 18971–18977. https://doi.org/10.1039/c6cp03512d.

(49) Castner, E. W. Modern Spectroscopy, 4th Edition (J. Michael Hollas). *J. Chem. Educ.* **2005**, *82* (1), 43. https://doi.org/10.1021/ed082p43.1.

(50) Brandt, R. E.; Stevanović, V.; Ginley, D. S.; Buonassisi, T. Identifying Defect-Tolerant Semiconductors with High Minority-Carrier Lifetimes: Beyond Hybrid Lead Halide Perovskites. *MRS Commun.* **2015**, *5* (2), 265–275.

https://doi.org/10.1557/mrc.2015.26.

(51) Blöchl, P. E. Improved Tetrahedron Method for Brillouin-Zone Integrations. *Phys. Rev. B* **1994**, *49* (23), 16223–16233. https://doi.org/10.1103/PhysRevB.49.16223.

(52) Hinuma, Y.; Pizzi, G.; Kumagai, Y.; Oba, F.; Tanaka, I. Band Structure Diagram Paths Based on Crystallography. *Comput. Mater. Sci.* **2017**, *128*, 140–184. https://doi.org/10.1016/j.commatsci.2016.10.015.

(53) Togo, A.; Shinohara, K.; Tanaka, I. Spglib: A Software Library for Crystal Symmetry Search. *Sci. Technol. Adv. Mater. Methods* **2024**, *4* (1), 2384822. https://doi.org/10.1080/27660400.2024.2384822.

(54) Deslippe, J.; Samsonidze, G.; Strubbe, D. A.; Jain, M.; Cohen, M. L.; Louie, S. G. BerkeleyGW: A Massively Parallel Computer Package for the Calculation of the Quasiparticle and Optical Properties of Materials and Nanostructures. *Comput. Phys. Commun.* **2012**, *183* (6), 1269–1289. https://doi.org/10.1016/j.cpc.2011.12.006.

(55) Haque, M. A.; Beard, M. C. Spin Effects in Metal Halide Perovskite Semiconductors. *Nanoscale* **2025**, *17*, 9895–9906. https://doi.org/10.1039/D5NR00127G.

(56) Leppert, L. Excitons in Metal-Halide Perovskites from First-Principles Many-Body Perturbation Theory. *J. Chem. Phys.* **2024**, *160* (5), 050902. https://doi.org/10.1063/5.0187213.

(57) McClintock, L. M.; Yuan, L.; Song, Z.; Pettes, M. T.; Yarotski, D.; Karkee, R.;

Strubbe, D. A.; Tan, L. Z.; Ben-Akacha, A.; Ma, B.; et al. Surface Effects on Anisotropic Photoluminescence in One-Dimensional Organic Metal Halide Hybrids. **2023**, *4* (8), 2200378. https://doi.org/10.1002/sstr.202200378.

(58) Masud, M. M.; Viera, J.; Ben-Akacha, A.; Ma, B.; Strubbe, D. A. Computational and Experimental Investigation of Chiral and Achiral 2D Organic Lead Bromide Perovskites: Octahedral Distortions and Electronic and Optical Properties. arXiv 2025, arXiv:2509.07152. https://doi.org/10.48550/arXiv.2509.07152.

(59) Jana, M. K.; Song, R.; Xie, Y.; Zhao, R.; Sercel, P. C.; Blum, V.; Mitzi, D. B. Structural Descriptor for Enhanced Spin-Splitting in 2D Hybrid Perovskites. *Nat. Commun.* **2021**, *12* (1), 4982. https://doi.org/10.1038/s41467-021-25149-7.

(60) Momma, K.; Izumi, F. VESTA 3 for Three-Dimensional Visualization of Crystal, Volumetric and Morphology Data. *J. Appl. Crystallogr.* **2011**, *44* (6), 1272–1276. https://doi.org/10.1107/S0021889811038970.

(61) Etienne, T.; Mosconi, E.; De Angelis, F. Dynamical Origin of the Rashba Effect in Organohalide Lead Perovskites: A Key to Suppressed Carrier Recombination in Perovskite Solar Cells? *J. Phys. Chem. Lett.* **2016**, *7* (9), 1638–1645. https://doi.org/10.1021/acs.jpclett.6b00564.

(62) Park, I.-H.; Zhang, Q.; Kwon, K. C.; Zhu, Z.; Yu, W.; Leng, K.; Giovanni, D.; Choi, H. S.; Abdelwahab, I.; Xu, Q.-H.; et al. Ferroelectricity and Rashba Effect in a Two-Dimensional Dion-Jacobson Hybrid Organic–Inorganic Perovskite. *J. Am. Chem. Soc.* **2019**, *141* (40), 15972–15976.

https://doi.org/10.1021/jacs.9b07776.

(63) Kepenekian, M.; Robles, R.; Katan, C.; Sapori, D.; Pedesseau, L.; Even, J. Rashba and Dresselhaus Effects in Hybrid Organic–Inorganic Perovskites: From Basics to Devices. *ACS Nano* **2015**, *9* (12), 11557–11567. https://doi.org/10.1021/acsnano.5b04409.

(64) Kepenekian, M.; Even, J. Rashba and Dresselhaus Couplings in Halide Perovskites: Accomplishments and Opportunities for Spintronics and Spin–Orbitronics. *J. Phys. Chem. Lett.* **2017**, *8* (14), 3362–3370. https://doi.org/10.1021/acs.jpclett.7b01015.

(65) Becker, M. A.; Vaxenburg, R.; Nedelcu, G.; Sercel, P. C.; Shabaev, A.; Mehl, M. J.; Michopoulos, J. G.; Lambrakos, S. G.; Bernstein, N.; Lyons, J. L.; et al. Bright Triplet Excitons in Caesium Lead Halide Perovskites. *Nature* **2018**, *553* (7687), 189–193. https://doi.org/10.1038/nature25147.

(66) Smith, M. D.; Jaffe, A.; Dohner, E. R.; Lindenberg, A. M.; Karunadasa, H. I. Structural Origins of Broadband Emission from Layered Pb–Br Hybrid Perovskites. *Chem. Sci.* **2017**, *8* (6), 4497–4504. https://doi.org/10.1039/C7SC01590A.

(67) Liu, S.; Kepenekian, M.; Bodnar, S.; Feldmann, S.; Heindl, M. W.; Fehn, N.; Zerhoch, J.; Shcherbakov, A.; Pöthig, A.; Li, Y.; et al. Bright Circularly Polarized Photoluminescence in Chiral Layered Hybrid Lead-Halide Perovskites. *Sci. Adv.* **2023**, *9* (35), eadh5083. https://doi.org/10.1126/sciadv.adh5083.

(68) Zhao, X.-H.; Li, N.-N.; Peng, J.; Xu, J.; Luo, P.; Dong, X.-Y.; Hu, X. Circularly Polarized Luminescence Enlargement from Crystals to Oriented Films of Enantiopure 2D Hybrid Perovskites. *Chem. Commun.* **2023**, *59* (45), 6881–6884. https://doi.org/10.1039/D3CC01739G.

(69) Prasanna, R.; Gold-Parker, A.; Leijtens, T.; Conings, B.; Babayigit, A.; Boyen, H.-G.; Toney, M. F.; McGehee, M. D. Band Gap Tuning via Lattice Contraction and Octahedral Tilting in Perovskite Materials for Photovoltaics. *J. Am. Chem. Soc.* **2017**, *139* (32), 11117–11124. https://doi.org/10.1021/jacs.7b04981.

(70) Shao, Y.; Gao, W.; Yan, H.; Li, R.; Abdelwahab, I.; Chi, X.; Rogée, L.; Zhuang, L.; Fu, W.; Lau, S. P.; et al. Unlocking Surface Octahedral Tilt in Two-Dimensional Ruddlesden-Popper Perovskites. *Nat. Commun.* **2022**, *13* (1), 138. https://doi.org/10.1038/s41467-021-27747-x.

(71) Sheldrick, G. M. SHELXT – Integrated Space-Group and Crystal-Structure Determination. *Acta Crystallogr., Sect. A* **2015**, *71* (1), 3–8. https://doi.org/10.1107/S2053273314026370.

(72) Sheldrick, G. M. Crystal Structure Refinement with SHELXL. *Acta Crystallogr., Sect. C* **2015**, *71* (1), 3–8. https://doi.org/10.1107/S2053229614024218.

(73) Müller, P. Practical Suggestions for Better Crystal Structures. *Crystallogr. Rev.* **2009**, *15* (1), 57–83. https://doi.org/10.1080/08893110802547240.

(74) Macrae, C. F.; Sovago, I.; Cottrell, S. J.; Galek, P. T. A.; McCabe, P.; Pidcock, E.; Platings, M.; Shields, G. P.; Stevens, J. S.; Towler, M.; et al. Mercury 4.0: From Visualization to Analysis, Design and Prediction. *J. Appl. Crystallogr.*

2020, *53* (1), 226–235. https://doi.org/10.1107/S1600576719014092.

(75) Baroni, S. Phonons and Related Crystal Properties from Density-Functional Perturbation Theory. *Rev. Mod. Phys.* **2001**, *73* (2), 515–562. https://doi.org/10.1103/RevModPhys.73.515.

(76) Giannozzi, P.; Baroni, S.; Bonini, N.; Calandra, M.; Car, R.; Cavazzoni, C.; Ceresoli, D.; Chiarotti, G. L.; Cococcioni, M.; Dabo, I.; et al. QUANTUM ESPRESSO: A Modular and Open-Source Software Project for Quantum Simulations of Materials. *J. Phys.: Condens. Matter* **2009**, *21* (39), 395502. https://doi.org/10.1088/0953-8984/21/39/395502.

(77) Perdew, J. P. Generalized Gradient Approximation Made Simple. *Phys. Rev. Lett.* **1996**, *77* (18), 3865–3868. https://doi.org/10.1103/PhysRevLett.77.3865.

(78) Lazzeri, M.; Mauri, F. First-Principles Calculation of Vibrational Raman Spectra in Large Systems: Signature of Small Rings in Crystalline SiO_2. *Phys. Rev. Lett.* **2003**, *90* (3), 036401. https://doi.org/10.1103/PhysRevLett.90.036401.

(79) Grimme, S. Semiempirical GGA-type density functional constructed with a long-range dispersion correction. *J. Comput. Chem.* **2006**, *27* (15), 1787–1799. https://doi.org/10.1002/jcc.20495.

(80) Hamann, D. R. Optimized Norm-Conserving Vanderbilt Pseudopotentials. *Phys. Rev. B* **2013**, *88* (8), 085117. https://doi.org/10.1103/PhysRevB.88.085117.

(81) van Setten, M. J.; Giantomassi, M.; Bousquet, E.; Verstraete, M. J.; Hamann, D. R.; Gonze, X.; Rignanese, G.-M. The PseudoDojo: Training and Grading a 85 Element Optimized Norm-Conserving Pseudopotential Table. *Comput. Phys.*

Commun. **2018**, *226*, 39–54. https://doi.org/10.1016/j.cpc.2018.01.012.

5 Ni Doping Effect on the Spin Lifetime in $CsPbBr_3$ QDs

5.1 Abstract

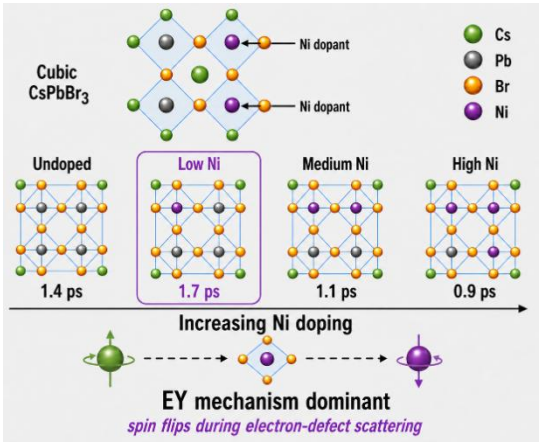

Quantum applications, such as quantum information storage, quantum computing and spintronics, rely on spin properties, especially spin lifetime. In this study, we studied the effect of Ni doping on the spin lifetime in the $CsPbBr_3$ perovskite QD system. The synthesized Ni-doped QDs exhibit several nanometers of blue-shift absorption and PL peaks compared to pristine ones. SEM shows a cubic shape and a 10-20 nm size. The XRD, Raman, and XPS measurements suggest that Ni^{2+} goes into the host $CsPbBr_3$ QDs lattice. Further, from the semi-quantitative EDS study, the Ni doping concentrations are 0.1%, 0.3%, and 0.8%, with Ni-to-Pb loading ratios of 25%, 33%, and 50%, respectively. With the ultrafast pump–probe system and the spin-selective pump, the spin dynamics of the pristine and Ni-doped $CsPbBr_3$ QDs were studied and extracted via the single exponential decay function. The extracted spin lifetime shows a rise from 1.4 to 1.7 ps and then a drop to 1.1 and 0.9 ps as the Ni doping content increases, and the spin relaxation mechanism was explained by the domination of the Elliott–Yafet (EY) mechanism. The doping concentration influences both surface passivation and defect formation within the lattice, thereby determining the dominant

spin relaxation pathway in this 3D perovskite quantum dot system.

5.2 Introduction

Owing to their facile synthesis, low cost, abundant tunability, and exceptional optoelectronic properties, metal halide (MH) perovskites have emerged as a hot class of research materials over the past decade, since the report utilizing $MAPbI_3$ as the light absorber.[1] Besides their well-known applications in photovoltaics, metal halide perovskites have also been widely explored for light-emitting diodes,[2] photodetectors,[3] lasers,[4] and other emerging optoelectronic applications.[5] Their compositional tunability, strong light–matter interaction, defect tolerance, and solution processability make them highly versatile semiconductor platforms. More recently, their strong spin–orbit coupling (SOC), together with structural inversion asymmetry, has attracted increasing interest in spin-related optoelectronics.[6,7] In non-centrosymmetric metal halide perovskites, the combination of SOC and broken inversion symmetry can induce Rashba- or Rashba–Dresselhaus-type spin splitting, enabling the generation, detection, and manipulation of spin-polarized carriers.[6,8] Therefore, metal halide perovskites are emerging as promising candidates for spintronics, spin-optoelectronics, and quantum-information-related photonic applications.

With the growing demand for energy-efficient computing and information processing, the use of spin degrees of freedom has become an important strategy for developing next-generation low-power and quantum-related technologies.[9,10] In these

applications, the spin lifetime is a key parameter because it determines how long spin information can be preserved before decoherence.[11] However, although strong SOC is beneficial for efficient spin generation and manipulation, it can also accelerate spin relaxation.[10] For example, composition-dependent studies on lead halide perovskites showed that the room-temperature spin lifetime increases as the molar mass decreases, suggesting that SOC plays a dominant role in carrier spin relaxation.[12,13] Similarly, lead-free $CsSnBr_3$ nanocrystals, which have weaker SOC than lead halide perovskites, exhibited prolonged room-temperature spin lifetime while still maintaining efficient optical orientation.[14] Therefore, partially replacing heavy-metal components or introducing dopants provides a practical route to tune spin relaxation in metal halide perovskites.

Doping can modify the local lattice structure, electronic states, defect environment, and metal–halide orbital interactions, thereby affecting both carrier dynamics and spin relaxation pathways.[15] For example, Cheng et al. reported dopant-induced slow spin relaxation in $CsPbBr_3$ perovskite nanocrystals and demonstrated that metal-ion doping can effectively prolong spin lifetime in quantum-confined perovskite NCs.[16] This suggests that dopant engineering is a promising strategy for optimizing perovskite materials for spin-based optoelectronic and quantum-related applications.

The spin relaxation in metal halide perovskites is generally discussed in terms of three major mechanisms: Elliott–Yafet (EY) scattering, D'yakonov–Perel' (DP) relaxation, and electron–hole exchange (EHE) interaction.[12,13,17–19] In the EY

mechanism, SOC mixes spin-up and spin-down states, so spin flips occur during momentum-scattering events such as electron–phonon or electron–defect scattering.[10,20] Therefore, stronger scattering generally leads to faster spin relaxation. Temperature-dependent studies on $CsPbBr_3$ and $MAPbBr_3$ perovskite quantum dots showed that the carrier spin lifetime of $CsPbBr_3$ increases significantly at lower temperature, which was mainly attributed to the EY mechanism modulated by reduced electron–phonon interaction at cryogenic temperatures.[20] In contrast, the DP mechanism usually dominates in systems with broken inversion symmetry.[17,21] In this case, spin relaxation arises from spin precession in an effective spin–orbit field between scattering events; increased momentum scattering can interrupt the spin precession process and thus prolong the spin lifetime, giving an opposite scattering dependence compared with the EY mechanism.[10,21] The EHE mechanism is an intrinsic excitonic spin relaxation pathway, where electron–hole exchange interaction drives exciton spin precession without requiring external scattering.[14,22] Such exchange-related fine-structure splitting and exciton spin dynamics have been observed in perovskite nanocrystals, highlighting the importance of excitonic effects in quantum-confined perovskites.

Ni^{2+} was selected as the dopant because of its paramagnetic $3d^8$ electronic configuration, which can introduce localized magnetic moments into $CsPbBr_3$ NC_S and potentially interact with photogenerated carriers. Such magnetic dopants may modulate spin relaxation dynamics through carrier–spin coupling, impurity scattering, localized electronic states, and local lattice perturbation.[16,23] In addition, the ionic-

size mismatch between Ni^{2+} and Pb^{2+} may induce local structural distortion or symmetry perturbation, which could influence Rashba-type spin splitting associated with SOC and broken inversion symmetry. Inspired by previous reports showing that dopant-induced carrier trapping can suppress EHE-mediated spin relaxation in $CsPbBr_3$ NC_S, where Bi doping prolonged the spin relaxation time from ~4.4 ps to ~24.6 ps, Ni^{2+} doping is expected to tune EHE-, EY-, and SOC-related spin-dephasing pathways.[16,20]

In this paper, we report the Ni doping effect on the spin lifetime in the $CsPbBr_3$ system. Absorption and PL spectra peaks showed a blue shift in the doped samples, and XRD and TEM revealed a decrease in lattice spacing, indicating incorporation of Ni into the host lattice without altering the host cubic structure. By selecting the right circularly polarized pump, the spin lifetime exhibited a non-monotonic dependence on Ni concentration, increasing at low doping levels and decreasing at higher doping levels. An optimal spin lifetime was obtained at a Ni/Pb ratio of 25%. This is explained by the domination of the EY mechanism.

5.3 Results and Discussion

Figure 5-1 shows the UV-Vis absorption and PL spectra of pristine and Ni-doped $CsPbBr_3$ QDs dispersed in toluene in solution state. The absorption spectra exhibit peaks at 508, 505, 502, and 504 nm for pristine and 25%, 33%, 50% Ni-loaded $CsPbBr_3$ QDs. Correspondingly, PL spectra show peaks at 513 and 506-508 nm for pristine and Ni-doped $CsPbBr_3$ QDs. The absorption and PL peaks blue-shifted after the introduction of Ni, with absorption peaks shifting by 3-6 nm and PL

peaks shifting by 5-7 nm, respectively, which is in accordance with the blue shift after Ni doping in such QDs reported in the literature.[25,26] The blue shift is probably due to the lattice size contraction after incorporation of the Ni ion ((Pb^{2+} ions (r = 1.19 Å) vs Ni^{2+} ions (r = 0.69 Å)) and negligible effect on the bandgap structure of host $CsPbBr_3$ because no obvious new optical features are observed.[27,28]

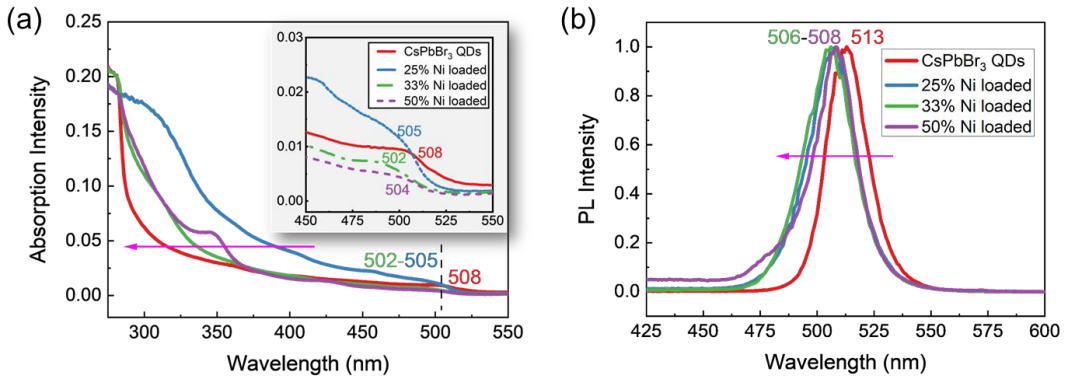

Figure 5-1 Optical properties of pristine and Ni-doped $CsPbBr_3$ QDs in solution state. (a) UV-vis absorption and (b) PL spectra of pristine and Ni-doped $CsPbBr_3$ QDs. Inset in (a) is the enlarged absorption peaks around 500 nm.

SEM images in Figure 5-2 (a) and (b) demonstrate a cubic shape and a dispersed size distribution of 10-20 nm, indicating homogeneous particle size and sufficient control over the conditions during hot-injection synthesis.[29] TEM images in Figure 5-2 (c) and (d) show a decrease in the lattice spacing of the (200) plane from 3.28 Å to 3.04 Å with the rise of Ni ion, which exhibits the shrinkage of the lattice spacing and implies the incorporation of Ni in the lattice.[30,31]

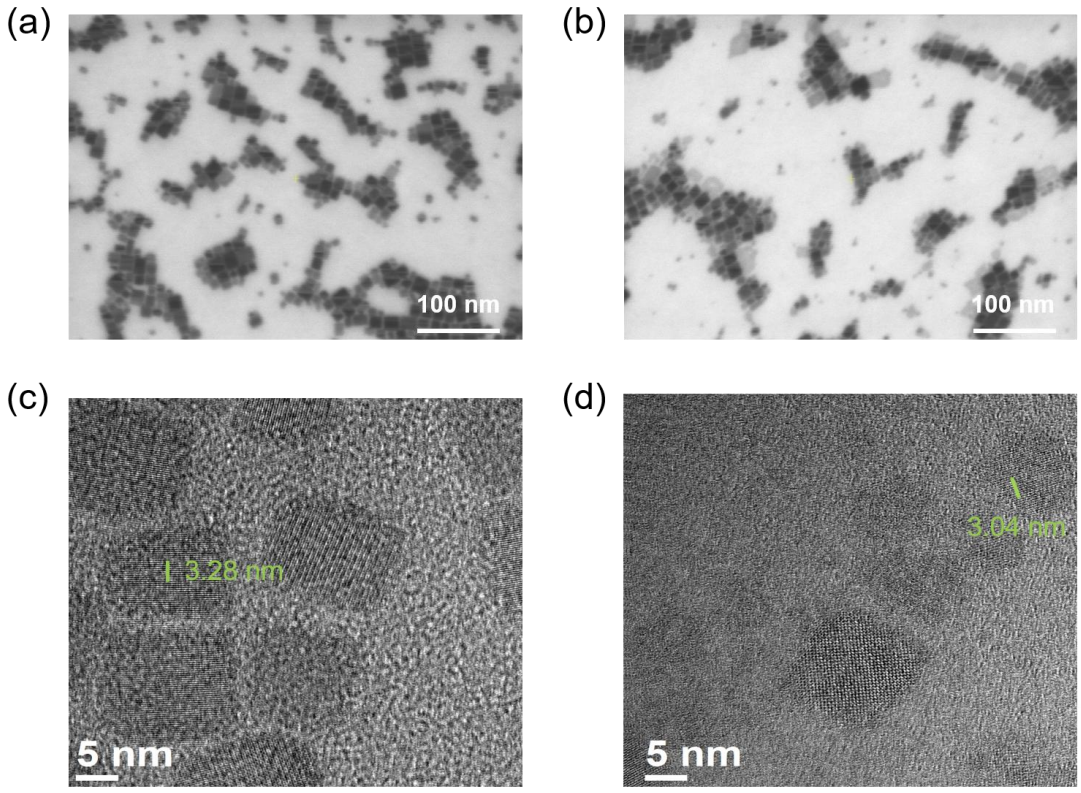

Figure 5-2 SEM images of (a) pristine and (b) 25% Ni-loaded $CsPbBr_3$ NCs under a 100 μm scale bar. High-resolution TEM (HRTEM) images of (c) pristine, (d) 25% Ni-loaded $CsPbBr_3$ NCs under a 5 nm scale bar.

To determine the change in lattice structure after the introduction of Ni^{2+} into host QDs, the powder XRD experiment was performed. Figure 5-3 (a) shows the XRD pattern of the pristine and Ni-doped samples deposited on the borosilicate glass substrate. In the pristine sample, the diffraction peaks at 15.2°, 21.4°, and 30.7° match well with the cubic phase in the standard Powder Diffraction File (PDF) card (PDF#52–0752).[30,32] As displayed in enlarged XRD pattern of Figure 5-3 (a), the incorporation of the Ni^{2+} into the $CsPbBr_3$ lattice leads to a slight broadening and a shift to a lower degree (from 30.7° to 30.66°, 30.64°, and 30.6°) compared to the

pristine sample at the (200) crystal plane. This result suggests that Ni^{2+} enters the host lattice and induces local structural disorder, thus deteriorating the crystal quality. Raman spectra in Figure 5-3 (b) show a gradual shift to higher frequencies of the transverse optical (TO) phonon modes in $CsPbBr_3$ QDs, which implies the short bond length and stronger bond strength as more small-sized Ni are in the lattice. At the same time, the Ni-Br bond vibration peaks start to emerge and grow stronger in the treated samples.[33,34] All the measurements so far agree well with the presence of Ni doping in the $CsPbBr_3$ lattice.

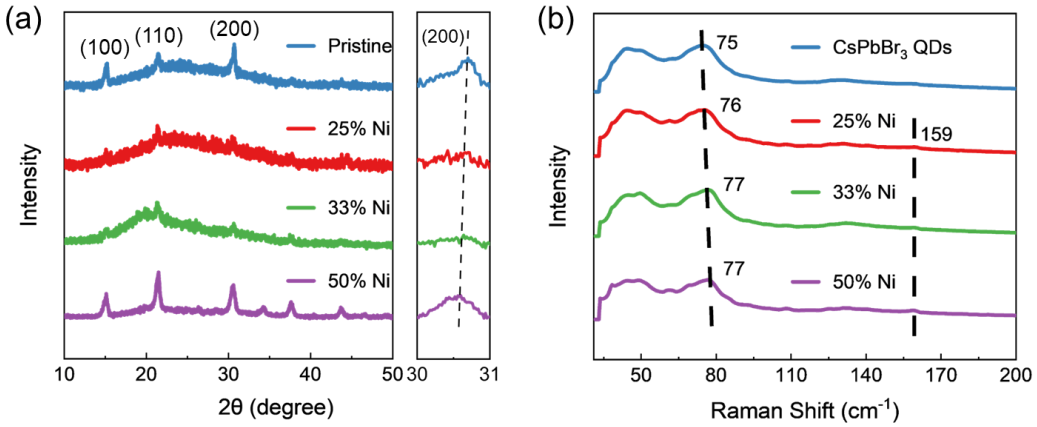

Figure 5-3 (a) XRD pattern and zoomed-in XRD pattern focusing at (200) crystal plane and (b) Raman spectra of the pristine and Ni-doped $CsPbBr_3$ QDs.

Figure 5-4 shows XPS spectra as a supplemental experiment confirming the elemental composition and Ni doping in the pristine and treated samples. Taking 25% Ni-loaded QDs as examples, the Br 3d, Cs 3d, Ni 2p, and Pb 4f signals of the interested elements were observed, indicating the successful doping of the Ni element into the host crystal. In Figure 5-5, Ni $2p_{1/2}$ and $2p_{3/2}$ states exhibit binding energies

of 869.8 eV and 854.5 eV. By comparing the Ni 2p XPS signals of the pristine and Ni-doped samples, it is further confirmed that doping occurs within the treated crystal lattice. These observations demonstrate that the synthesized samples are as designed. The corresponding Ni doping content is studied and confirmed by the EDS. As shown in Table 5-1, the Pb % content decreases while the Ni % content increases. The detailed Ni doping concentrations across the whole lattice are 0.2%, 0.3%, and 0.8% for the 25%, 33%, and 50% Ni-loaded samples, according to EDS.

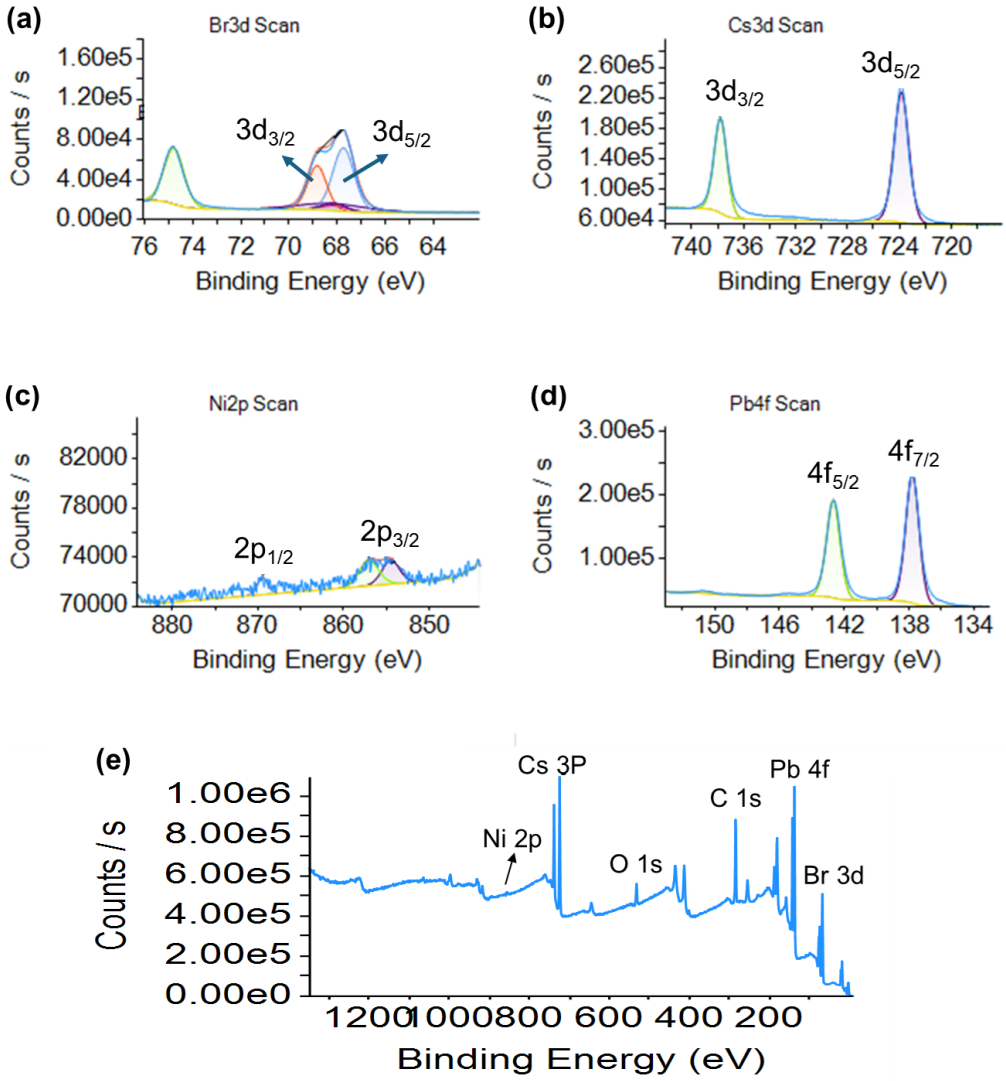

Figure 5-4 XPS images of the 25% Ni-loaded $CsPbBr_3$ NCs. The figures are binding energy of (a) Br 3d, (b) Cs 3d, (c) Ni 2p, (d) Pb 4f, and (e) survey spectra, respectively, showing Ni is present.

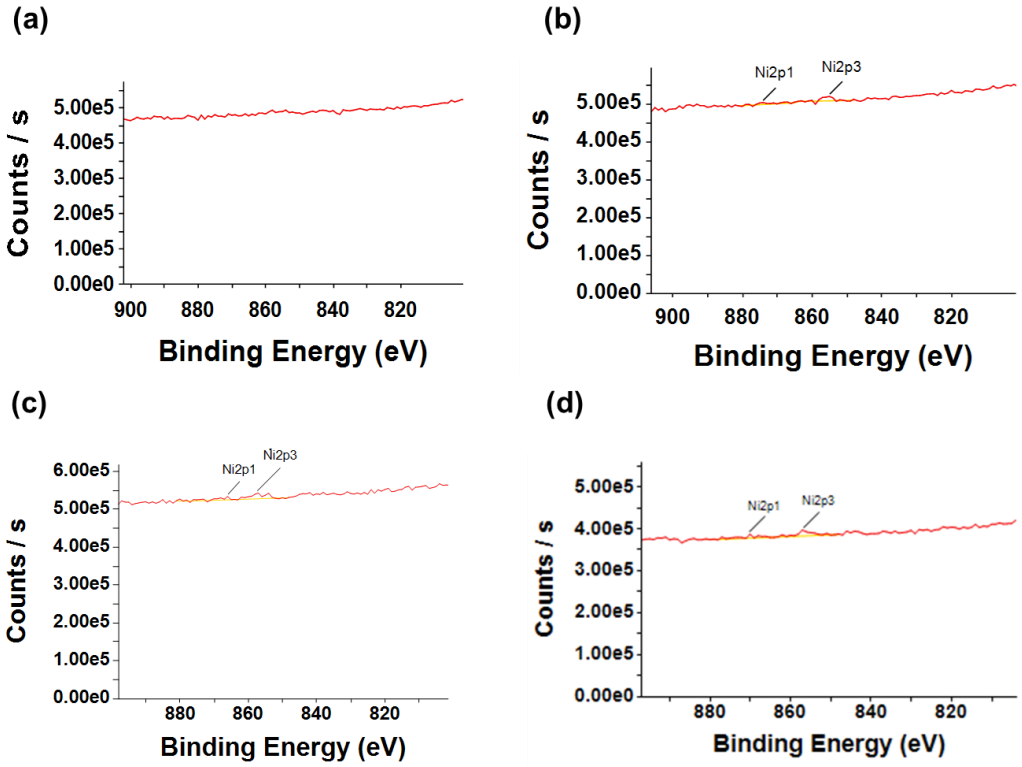

Figure 5-5 XPS spectra of the pristine and 25 %, 33 %, 50 % Ni-loaded $CsPbBr_3$ QDs, showing Ni element signal in the Ni-loaded QD samples.

Table 5-1 Elemental compositions of pristine and Ni-doped $CsPbBr_3$ QDs determined by EDS.

	Pb	Ni	Cs	Br	Total
Pristine	19.9	0	19.3	60.7	100
25%	19.1	0.2	15.3	65.5	100
33%	18.5	0.3	14.8	66.4	100
50%	15.7	0.8	14.5	69.1	100

To avoid high-exciton-density effects such as exciton–exciton annihilation and Auger recombination, the pump power was kept as low as possible in our system, namely 25 nJ per pulse.[35,36] In Figure 5-6 (a-d), the absorption peak positions blueshift by 3-6 nm for Ni-doped samples, in accordance with the UV-Vis absorption spectra. By comparing TB spectra of pristine and Ni-doped QDs, we find that incorporating Ni^{2+} alters the dynamics of ground-state bleach recovery. A feature at a longer wavelength of 513 nm shows up and decays to 0 quickly after 100 ps. This is probably due to a shallow local trap state induced by Ni, which changes the band structure.[37] Figure 5-6 (e) displays the TB average recovery time extracted from the double exponential fitting. The fitting method and average time are based on equations (1) and (2) below. The average recovery time first rises, then decays with increasing Ni doping. This means that a small amount of Ni doping can passivate lattice defects and improve the exciton lifetime; in contrast, excessive Ni doping can degrade crystal quality and induce additional local trap states, thereby decreasing the exciton lifetime.[26] This result is also supported by the TRPL fitting data shown in Figure 5-6 (f). A detailed summary of fitting parameters is provided in Tables 5-2 and 5-3.

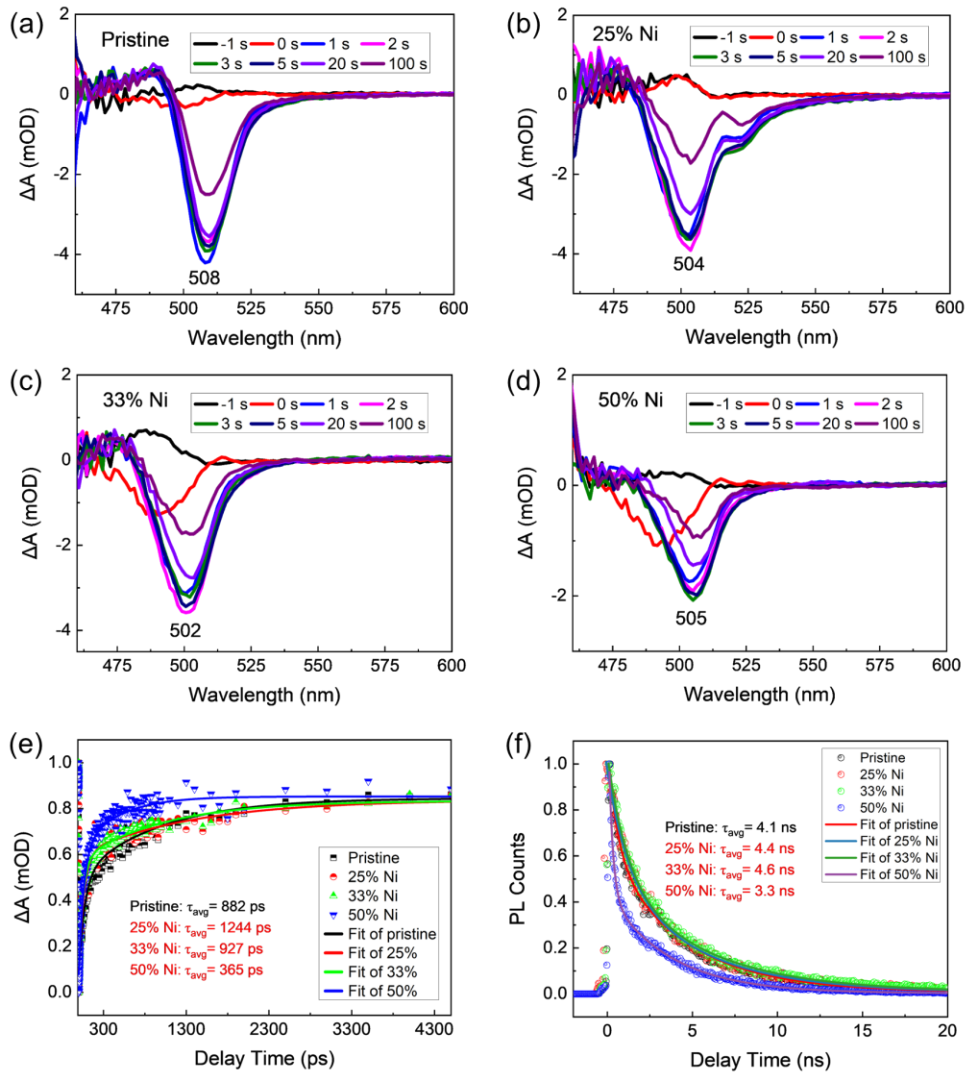

Figure 5-6 Transient bleach spectra (a-d) and fitting (straight line) of the recovery of the transient bleach feature (e) of the pristine and 25 %, 33 %, 50 % Ni-loaded $CsPbBr_3$ QDs pumped at 450 nm. (f) TRPL decay trace and the associated fitting curves.

$$y = A_1 e^{(-x/\tau_1)} + A_2 e^{(-x/\tau_2)} \tag{5-1}$$

$$\tau_{avg} = \frac{A_1\tau_1^2 + A_2\tau_2^2}{A_1\tau_1 + A_2\tau_2} \quad (5\text{-}2)$$

Table 5-2 Fitting parameters of the transient bleach recovery kinetics of pristine and Ni-doped $CsPbBr_3$ QDs under 450 nm excitation.

	Pristine	**25% Ni**	**33% Ni**	**50% Ni**
A_1	-0.5 ± 0.1	-0.5 ± 0.1	-0.5 ± 0.1	-0.6 ± 0.1
τ_1 (ps)	74 ± 6	60 ± 3	50 ± 2	58 ± 4
A_2	-0.3 ± 0.1	-0.2 ± 0.1	-0.3 ± 0.1	-0.2 ± 0.1
τ_2 (ps)	965 ± 100	1362 ± 300	1015 ± 100	456 ± 100
τ_{avg} (ps)	**882 ± 100**	**1244 ± 200**	**927 ± 100**	**365 ± 100**

Table 5-3 Fitting parameters of TRPL decay traces of pristine and Ni-doped $CsPbBr_3$ QDs, excited at 400 nm and monitored their respective peak positions.

	Pristine	**25% Ni**	**33% Ni**	**50% Ni**
A_1	0.4 ± 0.1	0.4 ± 0.1	0.5 ± 0.1	0.9 ± 0.1
τ_1 (ns)	0.6 ± 0.1	1.2 ± 0.1	1.1 ± 0.1	0.2 ± 0.1
A_2	0.6 ± 0.1	0.5 ± 0.1	0.5 ± 0.1	0.4 ± 0.1
τ_2 (ns)	4.4 ± 0.1	5.1 ± 0.1	5.4 ± 0.1	3.7 ± 0.1
τ_{avg} (ns)	**4.1 ± 0.1**	**4.4 ± 0.1**	**4.6 ± 0.1**	**3.3 ± 0.1**

In Figure 5-7 (a-d), the transient absorption traces obtained under co-circularly and counter-circularly polarized pump–probe configurations exhibit opposite recovery behaviors, consistent with previous reports from our group.[20,38] For comparison, the signals were normalized to their long-time delay values, where the transient response approaches the baseline. This normalization enables direct comparison of the spin-dependent signal amplitudes and facilitates extraction of the spin dynamics from the difference between the co- and counter-circularly polarized measurements.

In the co-circularly polarized configuration (σ^+/σ^+), the probe interrogates the same spin-selective transition that has been populated by the circularly polarized pump pulse. As a result of state filling in the conduction band, the absorption is reduced, producing a strong transient spin signal, as shown in Figure 5-7 (a)-(d).

In contrast, counter-circular probing (σ^+/σ^-) addresses transitions involving the opposite spin channel, which remains largely unoccupied immediately after excitation. Therefore, the corresponding spin signal is significantly weaker.

The difference between the co- and counter-circularly polarized signals reflects the degree of spin polarization and can be expressed as: $S(t) \propto (\sigma^+/\sigma^+) - (\sigma^+/\sigma^-)$. The temporal decay of $S(t)$ provides direct access to the spin relaxation dynamics of the system and these dynamics can be influenced by several mechanisms, such as Elliott–Yafet scattering, D'yakonov–Perel relaxation, and electron-hole exchange interactions.[10,12,21] The detailed spin relaxation fitting result is presented in Table 5-4.

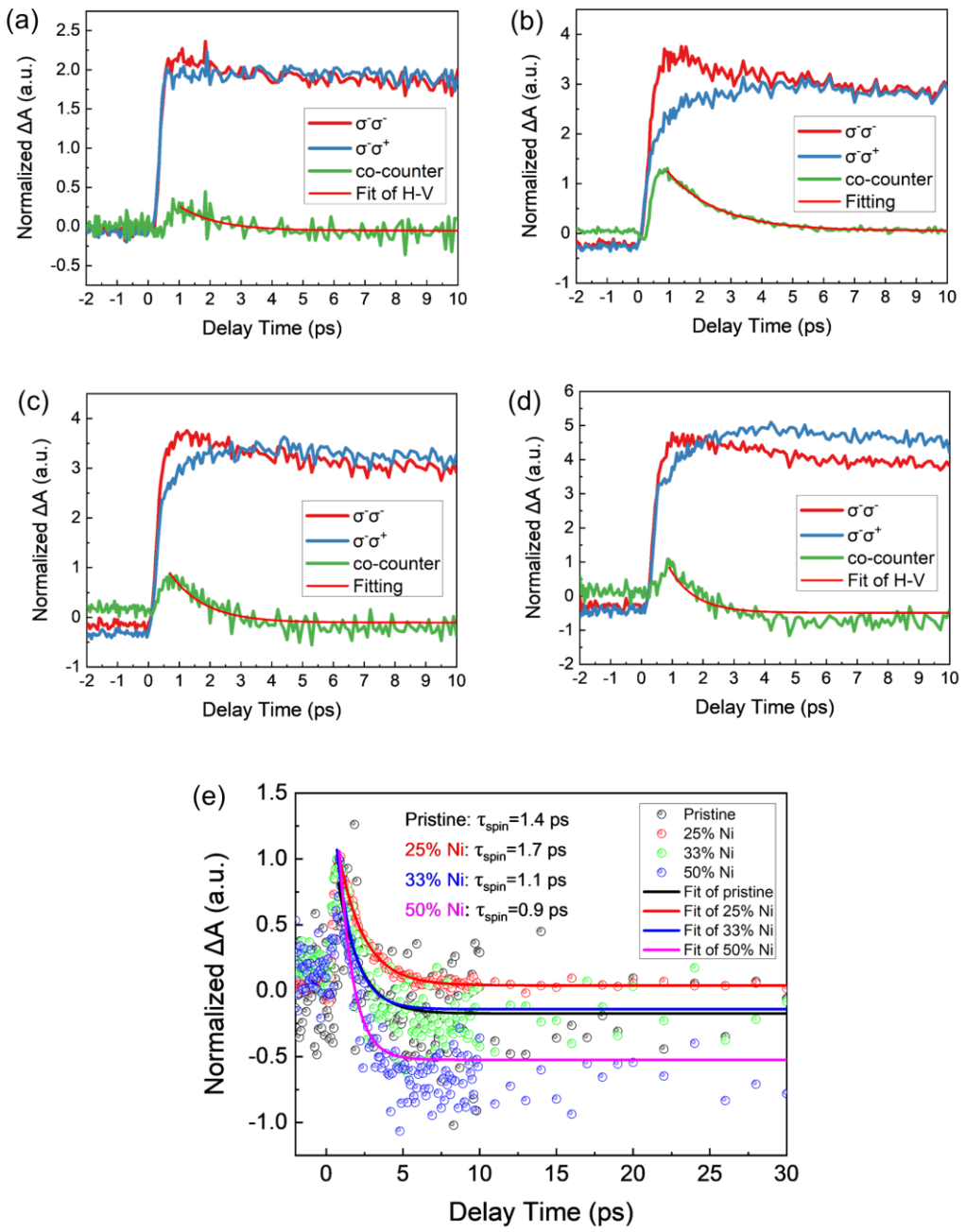

Figure 5-7 Decay trace (a-d) and fitting (smoothed curve) (e) of the spin relaxation of the pristine and 25%, 33%, 50% Ni-loaded $CsPbBr_3$ QDs probed at their absorption peak in TA spectra.

Table 5-4 Fitting parameters of spin relaxation dynamics of pristine and Ni-doped $CsPbBr_3$ QDs under RCP excitation at 450 nm.

	Pristine	**25% Ni**	**33% Ni**	**50% Ni**
A_1	1.7 ± 0.4	1.6 ± 0.1	2.2 ± 0.3	3.9 ± 0.6
τ_1 (ps)	1.4 ± 0.3	1.7 ± 0.1	1.1 ± 0.1	0.9 ± 0.1
τ_{avg} (ps)	**1.4 ± 0.3**	**1.7 ± 0.1**	**1.1 ± 0.1**	**0.9 ± 0.1**

The spin relaxation dynamics exhibit a non-monotonic dependence on Ni^{2+} doping concentration. In our previous study on the spin relaxation mechanism in $CsPbBr_3$ crystals, we suggested that spin relaxation in $CsPbBr_3$ quantum dots is primarily governed by the EY mechanism. This conclusion was supported by the absence of the strong temperature dependence typically associated with the DP mechanism.[20,38] These findings suggest that the EY mechanism is likely the dominant spin relaxation pathway in the present system. As shown in Figure 5-8, under right-circularly polarized excitation (σ^-), spin-selective optical transitions are governed by angular-momentum conservation, with $\Delta mj = \pm 1$. A σ^- pump with angular momentum -ħ preferentially excites carriers from the valence band to the conduction band with a specific angular momentum projection, e.g., m_J=+1/2, leading to the polarization in the spin state population of m_J=–1/2 over that of m_J=+1/2 in the conduction band. At low doping levels, the incorporation of Ni^{2+} effectively passivates surface defects and reduces trap-assisted scattering as evidenced by the increased photon lifetime, thereby enhancing spin lifetime. This improvement can be

attributed to the suppression of spin relaxation channels associated with defect-mediated EY mechanism, in which spin flips occur during momentum-scattering events such as electron–defect or electron–phonon scattering.[39]

However, as the Ni^{2+} concentration increases, the introduction of localized magnetic moments and impurity states becomes dominant. These local states enhance spin-defect scattering via inducing more trap states, thereby favoring spin relaxation. In addition, the increased impurity density can promote carrier localization, further contributing to spin decoherence. The competition between defect passivation at low doping levels and impurity-induced scattering at higher concentrations results in the observed non-monotonic behavior of spin lifetime.

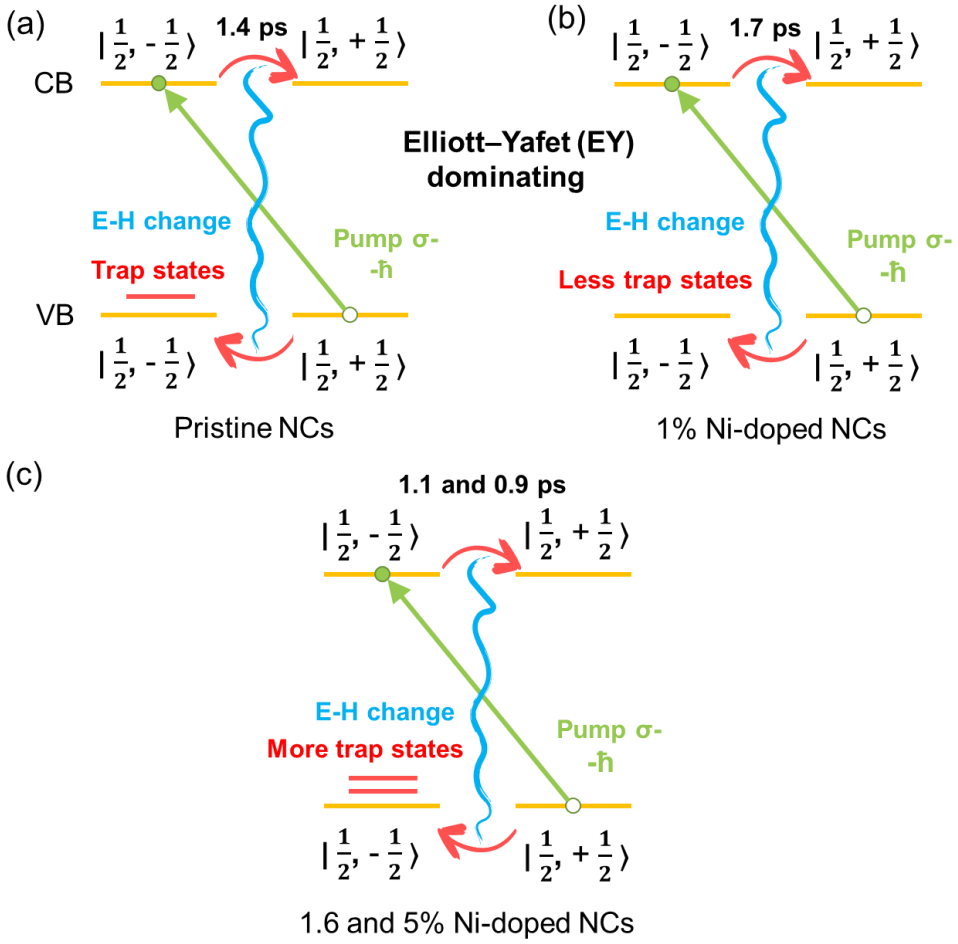

Figure 5-8 Proposed spin relaxation pathways in the pristine and 25 %, 33 %, 50 % Ni-loaded $CsPbBr_3$ QDs. Ni-to-Pb ratios are 1%, 1.6%, and 5% according to the EDS results.

5.4 Conclusion

The pristine and Ni-doped $CsPbBr_3$ QDs were synthesized via the hot injection method, and their crystal structure, electronic structure, doping concentrations, and transient absorption and spin dynamics were investigated. Ni doping doesn't dramatically change the host cubic crystal structure but introduces local lattice

distortion and symmetry breaking. The doping concentrations are revealed at 0.2%, 0.3%, and 0.8%, respectively, with increasing loading conditions, indicating a low doping level despite a high Ni-to-Pb loading ratio. The spin relaxation mechanism in Ni-doped $CsPbBr_3$ is primarily governed by the EY and EHE interactions, with lattice defects playing a critical role in determining the dominant spin relaxation pathway. Further mechanistic studies are required, such as low-temperature spin experiment, which is the key to distinguishing the EY and DP mechanisms. This study may be conducive to understanding how magnetic dopants regulate the spin lifetime in perovskite materials.

5.5 Experimental Methods

1. Materials

CsBr (99.9%) was purchased from Fisher Scientific, $PbBr_2$ (98%) was purchased from Thermo Scientific, and $NiBr_2$ (98%) was purchased from Sigma-Aldrich. All the chemicals were as received without any further purification.

2. Synthesis of $CsPbBr_3$ QDs and Ni doped $CsPbBr_3$ QDs

Undoped and Ni-doped $CsPbBr_3$ nanocrystals (NC_S) were synthesized using a hot-injection method reported previously. Cesium source, cesium oleate, was first prepared, by loading Cs_2CO_3 (0.407 g), oleic acid (OA, 1.5 mL), and 1-octadecene (ODE, 20 mL) into a 50 mL three-neck flask. The mixture was stirred under vacuum at 130 °C for 1.5 h until Cs_2CO_3 was completely dissolved. The resulting cesium oleate solution was then cooled to 100 °C and kept for later use.

For the synthesis of undoped $CsPbBr_3$ NCs, $PbBr_2$ (0.276 g), ODE (20 mL), OA (2 mL), and oleylamine (OAm, 2 mL) were added to a 100 mL three-neck flask. The mixture was dried under vacuum at 120 °C for 30 min with continuous stirring. The temperature was then rapidly increased to 180 °C, followed by swift injection of the pre-prepared cesium oleate precursor solution (1.6 mL). After 5–10 s of reaction, the flask was immediately cooled to room temperature using an ice-water bath to terminate nanocrystal growth.

The crude product was purified by centrifugation at 5000 rpm for 10 min. The collected precipitate was re-dispersed in hexane and centrifuged again at 5000 rpm for 10 min. The resulting supernatant was collected and used for further characterization and measurements.

The Ni-doped $CsPbBr_3$ NCs were synthesized using the same procedure as $CsPbBr_3$ NCs, except using a mixture of $PbBr_2$ and $NiBr_2$ as the source. The 25%, 33%, and 50% Ni loading ratios in this work correspond to 1:3, 1:2, and 1:1 molar ratios of $NiBr_2$ to $PbBr_2$, respectively.

3. Spectroscopy Measurements (Absorption, PL and Transient Absorption Spectra)

UV-vis absorption spectra were measured with an Agilent Technologies Cary 60 UV-Vis Spectrophotometer with a xenon source lamp. The photoluminescence (PL) spectra were acquired using a HORIBA Jobin Yvon Fluoromax-3 spectrofluorometer.

Transient bleach (TB) measurements were performed using a Light Conversion femtosecond transient absorption spectroscopy system. Laser pulses were generated by a ytterbium-doped potassium gadolinium tungstate (Yb) laser source (PHAROS, Light Conversion) operating at a fundamental wavelength of 1030 nm with an average power of 10 W, a repetition rate of 20 kHz, and a pulse duration of 159 fs.

Approximately 90% of the fundamental output was directed into an optical parametric amplifier (ORPHEUS, Light Conversion) to generate tunable excitation wavelengths. The pump wavelength of 450 nm was produced through frequency conversion in a second-harmonic generation module (LYRA, Light Conversion). The pump beam was then directed to the sample housed within the transient absorption spectrometer (HARPIA, Light Conversion).

The remaining 10% of the fundamental beam was routed directly to the HARPIA unit and focused into a sapphire crystal to generate a white-light supercontinuum probe through self-phase modulation and other nonlinear optical processes. The broadband probe covered the spectral range of 350–800 nm, encompassing the absorption region of the samples studied. The temporal delay between the pump and probe pulses was controlled by an automated motorized translation stage.

Transient absorption data were acquired using the Light Conversion HARPIA software in conjunction with an Oxford Instruments Andor spectrometer. The transient bleach recovery dynamics were analyzed in Origin by fitting the data with a built-in bi-exponential decay function: $y = A_1*\exp(-x/t_1) + A_2*\exp(-x/t_2)$.

Spin-polarized transient absorption measurements were performed using the femtosecond laser system described above with additional components to generate and analyze circularly polarized light. The fundamental laser output was horizontally linearly polarized and passed through a motorized Berek rotator, which was adjusted to generate either left- or right-circularly polarized pump pulses by selecting appropriate crystal tilt and rotation angles.

The probe beam, which remained horizontally linearly polarized, passed through the sample and was subsequently converted into circular polarization using a quarter-wave (λ/4) plate. The circularly polarized probe was then analyzed by a Wollaston prism, which separated the orthogonal polarization components. These signals were simultaneously detected by two visible-array detectors coupled to an Oxford Instruments spectrometer.

The circular polarization of the pump beam was verified using a Glan–Taylor polarizer, while the probe circularity was optimized and confirmed using a motorized polarizer and photodiode system. Data acquisition was performed using the Light Conversion Dual Detection software in conjunction with an Oxford Instruments Andor spectrometer. The transient bleach recovery data were fitted in Origin software using a built-in single-exponential decay function: $y = A_1*\exp(-x/t_1)$.

Time-resolved photoluminescence (TRPL) was conducted via the time-correlated single photon counting (TCSPC) measurements, using the Light Conversion equipment previously described in a similar layout to the TA measurements, but with the addition of a 420 nm long pass filter to remove the pump beam from the beam path after

excitation, the probe light off, and the chopper disabled. The measurement was taken using a 400 nm excitation wavelength at minimum pump power, using a 10 s collection time, and recorded using a photomultiplier tube affixed to an Oxford Instruments Andor Kymera spectrometer and using the corresponding HARPIA service app data acquisition software. The data were processed in Origin and fit with a built-in bi-exponential function, $y = A_1*\exp(-x/t_1) + A_2*\exp(-x/t_2)$.

4. SEM and TEM Measurements

$CsPbBr_3$ QDs and Ni-doped $CsPbBr_3$ QDs powders were redispersed in hexane and later dropped onto a hexagonal, 400 mesh copper grid coated with carbon film of standard 3-4 nm thickness (Electron Microscopy Sciences, CF400H-Cu-UL) and allowed to dry in an ambient environment. SEM images were acquired with Thermo Scientific Scios 2 DualBeam, equipped with an Oxford Instruments AZtecLive Ultim Max 100 EDS detector.

We used the same prepared samples from the SEM measurement for the TEM characterization. TEM and HRTEM (high-resolution TEM) were performed at the National Center for Electron Microscopy (NCEM) at the Lawrence Berkeley National Laboratory Molecular Foundry on an FEI UT Tecnai microscope operated at an acceleration voltage of 200 kV. The images were analyzed with Gatan Digital Microscope and ImageJ software.

5. Powder X-ray Diffraction (pXRD)

Powder XRD patterns were collected on a Bruker D8 Discover Diffractometer using Cu Kα radiation (40 kV and 40 mA) with degrees per step and time/step parameters of 0.02 degrees per step and 0.4 s/step, respectively, at 2θ angle from 10 to 60°. The simulated pXRD pattern is based on the MPA-$AgBiI_8$ scXRD data at 290 K from Li's work.[82] The theoretical pXRD patterns were simulated via VESTA.

6. Raman Spectroscopy

Raman spectra were acquired using a Thermo Fisher DRX3 Raman microspectrometer. The laser excitation source was a diode laser (λ_{ex} = 785 nm). Spectra were recorded under the following conditions: stainless-steel substrate, 50× objective, collect exposure time 30 s for five accumulations, laser power 30 mW (in focus), and aperture 50 μm slit.

7. XPS Spectroscopy

The elemental composition and chemical state were obtained on the surface and at depths of 2-10 nm in the sample by X-ray photoelectron spectroscopy (XPS) using a Thermo Fisher K-alpha system, with the binding energy calibrated against the C 1s peak of graphite.

8. EDS Spectroscopy

Several regions of interest were located using energy-dispersive X-ray spectroscopy (EDS) elemental mapping on the Thermo Fisher Scientific Apreo Field-Emission scanning electron microscope (SEM) at UCSC. The SEM is equipped with

an Oxford Instruments UltimMax energy dispersive spectrometer (EDS) that uses the AZtec software, allowing for real-time element mapping.

5.6 References

(1) Kojima, A.; Teshima, K.; Shirai, Y.; Miyasaka, T. Organometal Halide Perovskites as Visible-Light Sensitizers for Photovoltaic Cells. *J. Am. Chem. Soc.* **2009**, *131* (17), 6050–6051. https://doi.org/10.1021/ja809598r.

(2) Liu, X.-K.; Xu, W.; Bai, S.; Jin, Y.; Wang, J.; Friend, R. H.; Gao, F. Metal Halide Perovskites for Light-Emitting Diodes. *Nat. Mater.* **2021**, *20* (1), 10–21. https://doi.org/10.1038/s41563-020-0784-7.

(3) Pan, X.; Ding, L. Application of Metal Halide Perovskite Photodetectors. *J. Semicond.* **2022**, *43* (2), 020203. https://doi.org/10.1088/1674-4926/43/2/020203.

(4) Lei, L.; Dong, Q.; Gundogdu, K.; So, F. Metal Halide Perovskites for Laser Applications. *Adv. Funct. Mater.* **2021**, *31* (16), 2010144. https://doi.org/10.1002/adfm.202010144.

(5) Wu, S.; Chen, Z.; Yip, H.-L.; Jen, A. K.-Y. The Evolution and Future of Metal Halide Perovskite-Based Optoelectronic Devices. *Matter* **2021**, *4* (12), 3814–3834. https://doi.org/10.1016/j.matt.2021.10.026.

(6) Kepenekian, M.; Even, J. Rashba and Dresselhaus Couplings in Halide Perovskites: Accomplishments and Opportunities for Spintronics and Spin–Orbitronics. *J. Phys. Chem. Lett.* **2017**, *8* (14), 3362–3370. https://doi.org/10.1021/acs.jpclett.7b01015.

(7) Ping, Y.; Zhang, J. Z. Spin-Optotronic Properties of Organometal Halide Perovskites. *J. Phys. Chem. Lett.* **2018**, *9* (20), 6103–6111. https://doi.org/10.1021/acs.jpclett.8b02498.

(8) Kim, M.; Im, J.; Freeman, A. J.; Ihm, J.; Jin, H. Switchable $S = 1/2$ and $J = 1/2$ Rashba Bands in Ferroelectric Halide Perovskites. *Proc. Natl. Acad. Sci.* **2014**, *111* (19), 6900–6904. https://doi.org/10.1073/pnas.1405780111.

(9) Haque, M. A.; Beard, M. C. Spin Effects in Metal Halide Perovskite Semiconductors. *Nanoscale* **2025**, *17*, 9895–9906. https://doi.org/10.1039/D5NR00127G.

(10) Xu, J.; Li, K.; Huynh, U. N.; Fadel, M.; Huang, J.; Sundararaman, R.; Vardeny, V.; Ping, Y. How Spin Relaxes and Dephases in Bulk Halide Perovskites. *Nat. Commun.* **2024**, *15* (1), 188. https://doi.org/10.1038/s41467-023-42835-w.

(11) Tang, B.; Li, G.; Ru, X.; Gao, Y.; Li, Z.; Shen, H.; Yao, H.; Fan, F.; Du, J. Evaluating Lead Halide Perovskite Nanocrystals as a Spin Laser Gain Medium. *Nano Lett.* **2022**, *22* (2), 658–664. https://doi.org/10.1021/acs.nanolett.1c03671.

(12) Zhou, M.; Sarmiento, J. S.; Fei, C.; Zhang, X.; Wang, H. Effect of Composition on the Spin Relaxation of Lead Halide Perovskites. *J. Phys. Chem. Lett.* **2020**, *11* (4), 1502–1507. https://doi.org/10.1021/acs.jpclett.0c00004.

(13) Li, Y.; Luo, X.; Liu, Y.; Lu, X.; Wu, K. Size- and Composition-Dependent Exciton Spin Relaxation in Lead Halide Perovskite Quantum Dots. *ACS*

Energy Lett. **2020**, *5* (5), 1701–1708. https://doi.org/10.1021/acsenergylett.0c00525.

(14) Liang, W.; Li, Y.; Xiang, D.; Han, Y.; Jiang, Q.; Zhang, W.; Wu, K. Efficient Optical Orientation and Slow Spin Relaxation in Lead-Free $CsSnBr_3$ Perovskite Nanocrystals. *ACS Energy Lett.* **2021**, *6* (5), 1670–1676. https://doi.org/10.1021/acsenergylett.1c00413.

(15) Guria, A. K.; Dutta, S. K.; Adhikari, S. D.; Pradhan, N. Doping Mn^{2+} in Lead Halide Perovskite Nanocrystals: Successes and Challenges. *ACS Energy Lett.* **2017**, *2* (5), 1014–1021. https://doi.org/10.1021/acsenergylett.7b00177.

(16) Cheng, H.; Leng, J.; Sun, F.; Zhao, S.; Tang, J.; Wu, K.; Bian, J.; Jin, S. Dopant-Induced Slow Spin Relaxation in $CsPbBr_3$ Perovskite Nanocrystals. *ACS Energy Lett.* **2022**, *7* (12), 4325–4332. https://doi.org/10.1021/acsenergylett.2c01901.

(17) Lü, C.; Cheng, J. L.; Wu, M. W. Hole Spin Dephasing in p-Type Semiconductor Quantum Wells. *Phys. Rev. B* **2006**, *73* (12), 125314. https://doi.org/10.1103/PhysRevB.73.125314.

(18) Tartakovskii, A. I.; Cahill, J.; Makhonin, M. N.; Whittaker, D. M.; Wells, J.-P. R.; Fox, A. M.; Mowbray, D. J.; Skolnick, M. S.; Groom, K. M.; Steer, M. J.; et al. Dynamics of Coherent and Incoherent Spin Polarizations in Ensembles of Quantum Dots. *Phys. Rev. Lett.* **2004**, *93* (5), 057401. https://doi.org/10.1103/PhysRevLett.93.057401.

(19) Teng, L. H.; Zhang, P.; Lai, T. S.; Wu, M. W. Density Dependence of Spin

Relaxation in GaAs Quantum Well at Room Temperature. *Europhys. Lett.* **2008**, *84* (2), 27006. https://doi.org/10.1209/0295-5075/84/27006.

(20) Khvichia, M.; Zeitz, D. C.; Chou, K.-C.; Ping, Y.; Zhang, J. Z. Temperature Dependence of Photoinduced Carrier Spin Relaxation Dynamics in $CsPbBr_3$ and $MAPbBr_3$ Perovskite Quantum Dots. *J. Phys. Chem. Lett.* **2025**, *16* (23), 5681–5686. https://doi.org/10.1021/acs.jpclett.5c01192.

(21) Cai, R.; Wadgaonkar, I.; Lim, J. W. M.; Dal Forno, S.; Giovanni, D.; Feng, M.; Ye, S.; Battiato, M.; Sum, T. C. Zero-Field Quantum Beats and Spin Decoherence Mechanisms in $CsPbBr_3$ Perovskite Nanocrystals. *Nat. Commun.* **2023**, *14* (1), 2472. https://doi.org/10.1038/s41467-023-37721-4.

(22) Tamarat, P.; Hou, L.; Trebbia, J.-B.; Swarnkar, A.; Biadala, L.; Louyer, Y.; Bodnarchuk, M. I.; Kovalenko, M. V.; Even, J.; Lounis, B. The Dark Exciton Ground State Promotes Photon-Pair Emission in Individual Perovskite Nanocrystals. *Nat. Commun.* **2020**, *11* (1), 6001. https://doi.org/10.1038/s41467-020-19740-7.

(23) Thawarkar, S.; Rana, P. J. S.; Narayan, R.; Singh, S. P. Ni-Doped $CsPbBr_3$ Perovskite: Synthesis of Highly Stable Nanocubes. *Langmuir* **2019**, *35* (52), 17150–17155. https://doi.org/10.1021/acs.langmuir.9b02450.

(24) Li, D.; Liu, X.; Wu, W.; Peng, Y.; Zhao, S.; Li, L.; Hong, M.; Luo, J. Chiral Lead-Free Hybrid Perovskites for Self-Powered Circularly Polarized Light Detection. *Angew. Chem. Int. Ed.* **2021**, *60* (15), 8415–8418. https://doi.org/10.1002/anie.202013947.

(25) Salari, R.; Amjadi, M. An Efficient Chemiluminescent Probe Based on Ni-Doped $CsPbBr_3$ Perovskite Nanocrystals Embedded in Mesoporous SiO_2 for Sensitive Assay of L–Cysteine. *Sci. Rep.* **2024**, *14* (1), 20871. https://doi.org/10.1038/s41598-024-70624-y.

(26) Kim, H.; Bae, S.-R.; Lee, T. H.; Lee, H.; Kang, H.; Park, S.; Jang, H. W.; Kim, S. Y. Enhanced Optical Properties and Stability of $CsPbBr_3$ Nanocrystals Through Nickel Doping. *Adv. Funct. Mater.* **2021**, *31* (28), 2102770. https://doi.org/10.1002/adfm.202102770.

(27) Yong, Z.-J.; Guo, S.-Q.; Ma, J.-P.; Zhang, J.-Y.; Li, Z.-Y.; Chen, Y.-M.; Zhang, B.-B.; Zhou, Y.; Shu, J.; Gu, J.-L.; et al. Doping-Enhanced Short-Range Order of Perovskite Nanocrystals for Near-Unity Violet Luminescence Quantum Yield. *J. Am. Chem. Soc.* **2018**, *140* (31), 9942–9951. https://doi.org/10.1021/jacs.8b04763.

(28) Liu, M.; Jiang, N.; Huang, H.; Lin, J.; Huang, F.; Zheng, Y.; Chen, D. Ni^{2+}-Doped $CsPbI_3$ Perovskite Nanocrystals with near-Unity Photoluminescence Quantum Yield and Superior Structure Stability for Red Light-Emitting Devices. *Chem. Eng. J.* **2021**, *413*, 127547. https://doi.org/10.1016/j.cej.2020.127547.

(29) Protesescu, L.; Yakunin, S.; Bodnarchuk, M. I.; Krieg, F.; Caputo, R.; Hendon, C. H.; Yang, R. X.; Walsh, A.; Kovalenko, M. V. Nanocrystals of Cesium Lead Halide Perovskites ($CsPbX_3$, X = Cl, Br, and I): Novel Optoelectronic Materials Showing Bright Emission with Wide Color Gamut. *Nano Lett.* **2015**,

15 (6), 3692–3696. https://doi.org/10.1021/nl5048779.

(30) He, J.; Liu, S.; Gu, J.; Xu, S. Enhanced Luminescence of $CsPbBr_3$ Quantum Dot Glass through Eu^{3+}–Rb^{+} Codoping. *ACS Appl. Nano Mater.* **2025**, *8* (6), 2721–2729. https://doi.org/10.1021/acsanm.4c06144.

(31) Teku, J. A.; Lee, N.; Taylor, D. A.; Selvaraj, J.; Lee, J.-S. Highly Stable $CsPbBr_3$ Perovskite Quantum Dots with ZnS Shells from Single-Molecule Precursors for Optoelectronic Devices. *ACS Appl. Nano Mater.* **2024**, *7* (17), 20034–20045. https://doi.org/10.1021/acsanm.4c02560.

(32) Qaid, S. M. H.; Ghaithan, H. M.; Al-Asbahi, B. A.; Aldwayyan, A. S. Ultra-Stable Polycrystalline $CsPbBr_3$ Perovskite–Polymer Composite Thin Disk for Light-Emitting Applications. *Nanomaterials* **2020**, *10* (12), 2382. https://doi.org/10.3390/nano10122382.

(33) Liao, M.; Shan, B.; Li, M. In Situ Raman Spectroscopic Studies of Thermal Stability of All-Inorganic Cesium Lead Halide ($CsPbX_3$, X = Cl, Br, I) Perovskite Nanocrystals. *J. Phys. Chem. Lett.* **2019**, *10* (6), 1217–1225. https://doi.org/10.1021/acs.jpclett.9b00344.

(34) Kharlamova, M. V. Raman Spectroscopy Study of the Doping Effect of the Encapsulated Iron, Cobalt, and Nickel Bromides on Single-Walled Carbon Nanotubes. *J. Spectrosc.* **2015**, *2015* (1), 653848. https://doi.org/10.1155/2015/653848.

(35) Wei, K.; Zheng, X.; Cheng, X.; Shen, C.; Jiang, T. Observation of Ultrafast Exciton–Exciton Annihilation in $CsPbBr_3$ Quantum Dots. *Adv. Opt. Mater.*

2016, *4* (12), 1993–1997. https://doi.org/10.1002/adom.201600352.

(36) Aneesh, J.; Swarnkar, A.; Kumar Ravi, V.; Sharma, R.; Nag, A.; Adarsh, K. V. Ultrafast Exciton Dynamics in Colloidal $CsPbBr_3$ Perovskite Nanocrystals: Biexciton Effect and Auger Recombination. *J. Phys. Chem. C* **2017**, *121* (8), 4734–4739. https://doi.org/10.1021/acs.jpcc.7b00762.

(37) Chen, T.; Liu, R.; Tang, S.; Li, X.; Ye, S.; Duan, X.; Wang, R.; Shi, Y.; Yang, J.; Qiu, F.; et al. Ni^{2+} Doping Induced Structural Phase Transition and Photoluminescence Enhancement of $CsPbBr_3$. *AIP Adv.* **2021**, *11* (11), 115006. https://doi.org/10.1063/5.0067153.

(38) Zeitz, D. C.; Cherrette, V. L.; Creech, S. A.; Li, Y.; Ping, Y.; Zhang, J. Z. Ultrafast Spin Relaxation of Charge Carriers in Strongly Quantum Confined Methylammonium Lead Bromide Perovskite Magic-Sized Clusters. *ACS Phys. Chem. Au* **2024**, *4* (6), 610–614. https://doi.org/10.1021/acsphyschemau.4c00051.

(39) Zhang, H.; Zhai, Z.; Bi, Z.; Gao, H.; Ye, M.; Xu, Y.; Tan, H.; Yang, L. Spin Coherence and Spin Relaxation in Hybrid Organic–Inorganic Lead and Mixed Lead–Tin Perovskites. *Nano Lett.* **2023**, *23* (17), 7914–7920. https://doi.org/10.1021/acs.nanolett.3c01734.

Appendix

6 New Insights into Non-Thermal Plasma-Assisted Polyvinyl Alcohol Depolymerization Catalyzed by TiO_2

6.1 Abstract

In this study, we investigated the solid residual PVA and TiO_2 after non-thermal air, CO_2 and nitrogen plasma depolymerization in the absence and presence of TiO_2. Scanning electron microscopic (SEM) studies showed the absence of highly viscous tar and carbonaceous residues on the surface of PVA and TiO_2. In the absence of TiO_2, PVA particles exhibited micron-sized holes on their surfaces, whereas in the presence of TiO_2, the surface roughness of PVA particles was observed at the submicron scale. These observations suggest that TiO_2 facilitates the even distribution of non-thermal plasma at a submicron scale, leading to a more uniform depolymerization of PVA surfaces. Raman, Fourier transform infrared (FTIR) spectroscopy and X-ray absorption spectroscopy (XAS) showed that (i) the surface of residual PVA contains mainly ketone functional groups and less C-H bonds than the pristine PVA and (ii) further confirmed the absence of highly viscous tar and carbonaceous residues on both used TiO_2 and residual PVA. The nuclear magnetic

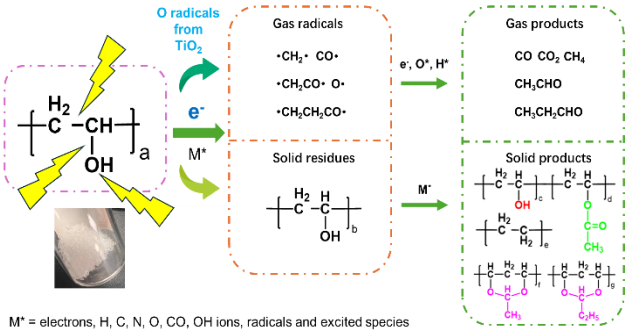

resonance (NMR) and mass spectrometry (MS) analyses suggested the PVA is growing back to poly polyvinyl acetate (PVAc) by esterification reaction, and the ethers are produced by the acetal reaction between PVA and aldehyde. The transmission electron microscopic (TEM) and X-ray diffraction (XRD) analysis indicated no major crystal structural change of the TiO_2 catalyst after the plasma reactions. This study demonstrates that non-thermal plasma-assisted depolymerization is a viable alternative to thermal depolymerization, offering the unique advantage of converting polymer wastes into gaseous small organic molecules without generating recalcitrant viscous tar and carbonaceous residues on the surfaces of the polymer and TiO_2 catalysts.

6.2 Introduction

Consumer polymers, also known as commodity polymers, have significantly benefited our society because of their low cost, lightweight nature, ease of processing, and durability. These characteristics have led to the widespread adoption of consumer polymers in numerous industries, including packaging, automotive, construction, electronics, and healthcare.[1–5] However, their durability poses substantial challenges for their disposal.[6–10] Polymer wastes enter our ecosystem, contaminating oceans and land, and infiltrating our food chain through microplastics.[11–13] Despite the seriousness of polymer waste pollution, efforts in upcycling and recycling polymer waste have been limited. For example, only about 5% of the 1 trillion plastic bags used annually in the US are recycled.[14,15]

A major obstacle to the recycling of polymer waste is downcycling, which

produces materials of lower value than the cost required for the recycling process. Thermal depolymerization methods, including pyrolysis and catalytic cracking, can be considered upcycling under specific conditions where high yields of high-value small organic molecules are generated. However, these methods require high thermal energy, i.e., high temperatures (over 300°C), to break polymer bonds, and face challenges in the disposal of carbonaceous species, coking, and tar formation.[16,17] Depolymerization at lower temperatures could alleviate these issues. Many non-thermal plasma-assisted depolymerizations have shown a wide range of gas, liquid, and solid products, depending on the type of polymer, plasma, and operating conditions.[16–20] These studies are summarized in Table 6-1. However, most plasma-treated polymers show tar or coke products, or they don't report the related information. This hinders further practical applications in the industry as the carbonaceous species, coking, and tar can cover the catalyst and container surface, mix with products, and make the container hard to clean up and catalyst and valuable products challenging to separate[21,22] In addition, the conventional thermal cracking method, which consumes huge energy, produces heavy pollution and is against the green economy and environment nowadays.

We have recently conducted low-temperature depolymerization of polyvinyl alcohol (PVA) with non-thermal air and nitrogen plasma generated by dielectric barrier discharge (DBD) in the presence and absence of TiO_2.[9] PVA was used as a model polymer because of its variety of chemical bonds: C-C, C-H, C-O, and O-H; TiO_2 was used because of its partial and total oxidation activity as well as its

stability.[23] The high energy electrons in the plasma can break down the chemical bonds and actively react with the gas reactants and generate excited species, such as, free radicals, excited atoms, ions and molecules, followed by the initial chemical reaction in the depolymerization process.[24,25] The major gaseous products were found to be acetaldehyde, propionaldehyde, methane, CO_2, and CO. The presence of oxygen and TiO_2 can further enhance the yields toward aldehyde products. A key issue remaining to be addressed is the residual polymers and catalysts. Are there byproducts such as carbonaceous species, coke, and tar present on the surface of polymers and catalysts? The presence of these species will significantly decrease the activity of non-thermal plasma in contacting the raw polymer waste for depolymerization; the presence of these species on the TiO_2 surface will impede its catalytic activity.

In this study, residual polymers with and without TiO_2 as a catalyst after non-thermal air CO_2 and N_2 plasma-assisted depolymerization were characterized using an array of techniques, including scanning electron microscopy (SEM), transmission electron microscopy (TEM), X-ray diffraction (XRD), Raman spectroscopy, Fourier transform infrared spectroscopy (FTIR), X-ray absorption spectroscopy (XAS), nuclear magnetic resonance spectroscopy (NMR), and mass spectrometry (MS). SEM images showed the absence of highly viscous tar and carbonaceous residues on the surface of PVA and TiO_2, and the presence of TiO_2 enables the surface roughness of PVA particles at the submicron scale, indicative of even distribution of non-thermal plasma and depolymerization reaction on the PVA surface. Raman, FTIR,

and XAS spectroscopy showed evidence of decreased alcohol groups and generated ketone groups in residual PVA. The NMR and MS suggested the poly polyvinyl acetate (PVAc) and the cyclic cross-linking ether structures such as PVA-PVAc-PVA-acetal (O-CH_3CH_2-O) and PVA-PVAc-PVA-propional (O-$CH_3CH_2CH_2$-O). For the catalyst TiO_2, the TEM and XRD analysis indicated no major crystal structural change of the TiO_2 catalyst after the plasma reactions.

6.3 Results and Discussion

6.3.1 Non-Thermal Plasma Effect on PVA–TiO_2 Mixture

The PVA and PVA-TiO_2 mixture were first characterized using SEM to determine the plasma effect on the surface area with and without catalyst TiO_2. As is well known, surface structure is vital in catalysis reactions and unfavorable morphology will decrease or disable the catalyst function, leading to a low efficiency in the polymer depolymerization reactions. The reason is that the catalyst surface acts as an essential diffusion pathway for all the plasma species and the active sites on the surface area are critical to promote the reaction time and efficiency in catalysis reaction.[17,19] According to the Mars-van Krevelen mechanism, the organic molecules like PVA adsorbed on metal oxides (such as TiO_2) surface are oxidized by oxygen radicals (atoms) emerging from the crystal lattice of TiO_2 and then the reduced metal oxides (such as TiO_{2-x}) are oxidized back to TiO_2 by uptake of gaseous oxygen, which is crucial for the oxidative depolymerization of PVA.[26] Also, by enhancing the dispersion of reactant aided by the catalyst, further with the non-thermal process, we expect the homogeneous reaction on the polymer surface, thus coking and tar

formation will be alleviated.

SEM images for pure PVA samples

Figure 6-1 shows the SEM images of the pure PVA crystals before and after different plasma reactions. The images show that the PVA sizes are around 0.5-1 mm and the crystals are in cuboid shape. Except for the pristine sample, erosion effects are present on the surface of all other samples, including the holes for the air plasma-treated sample, the ridges for the CO_2 plasma-treated sample, and pits for the N_2 plasma-treated sample. At 1 μm scale bar, the pristine sample shows the original defects on the surface, however, the PVA surface treated under N_2 plasma presents some viscous substance-like structures, probably related to the coalescence of scissored chain structures.[27] These images exhibit that the plasma species attack the surface and even inside of PVA, indicating the bond breaking in the microscale. More images of the reacted spots on the surface are in Figure 6-2.

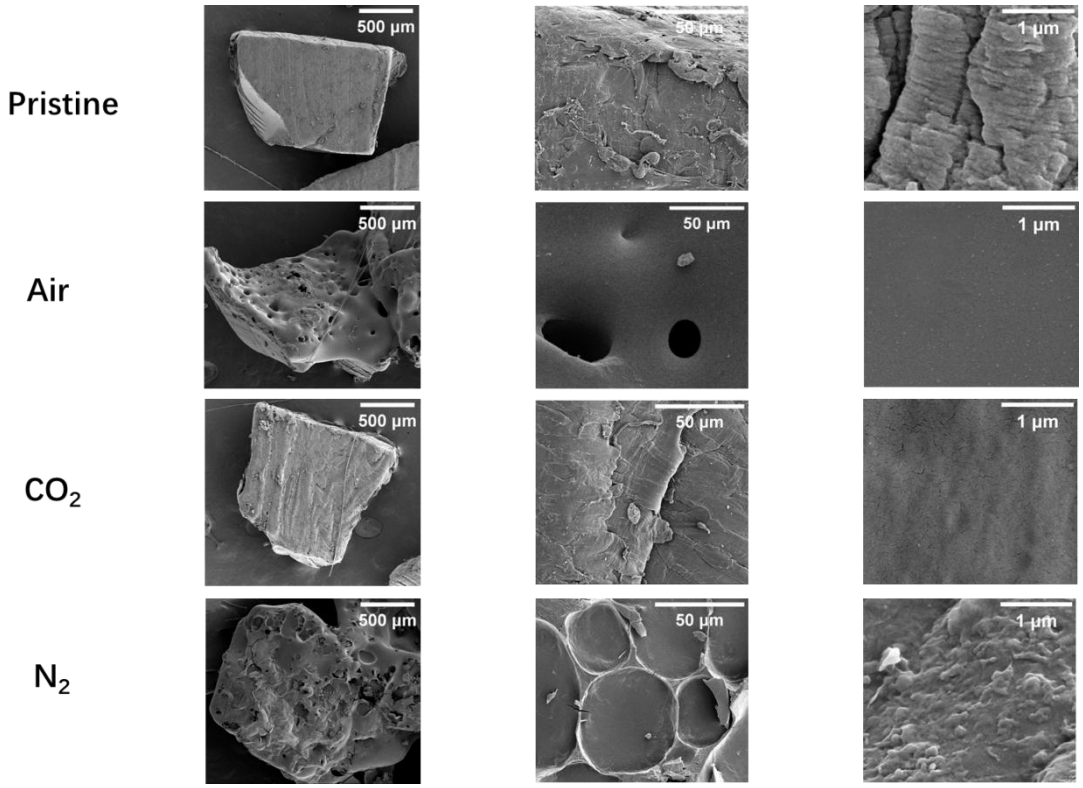

Figure 6-1 SEM images of the pure PVA crystals without catalyst addition before and after air, CO_2 and N_2 non-thermal plasma at 25 ℃.

Figure 6-2 shows the SEM images of the pure PVA samples before and after different plasma treatments at higher resolutions. The images exhibit more spots captured under the electron microscope and combined with other SEM images in the main paper, the uniformity of the non-thermal plasma is revealed due to the uneven electric field applied. This is evidenced by the reported non-thermal plasma-assisted PE depolymerization work and it indicates a better design and application of the plasma is required for polymer upcycling in the future.[18]

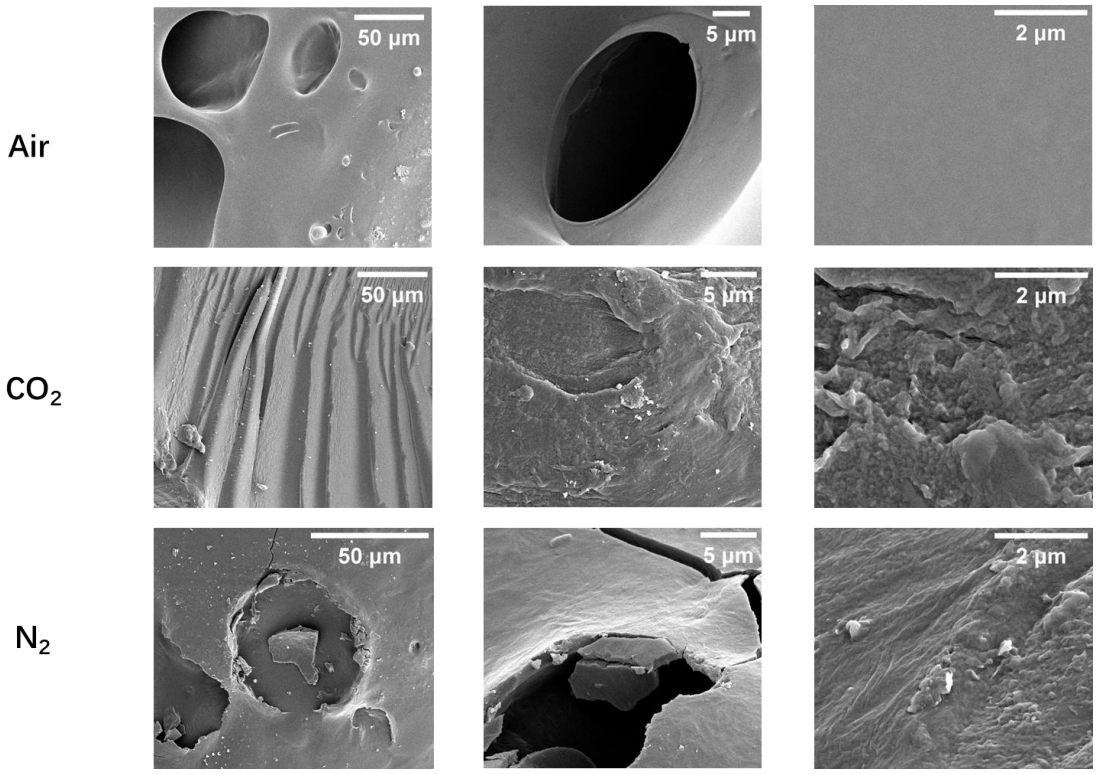

Figure 6-2 SEM images of pure PVA samples before and after air, CO_2 and N_2 non-thermal plasma treatments at 25 °C at higher resolutions.

SEM images for PVA-TiO_2 mixture (2:1 and 4:1 molar ratios)

Figure 6-3 shows the SEM images of the PVA-TiO_2 mixture (2:1 molar ratio) samples before and after different plasma reactions. The images at low magnification (500 µm) show that the PVA surface is covered by the powder clusters in different thicknesses. After enlarging the images with a 50 µm scale bar, undestroyed plain surfaces were observed without holes, ridges or pits compared to the treated pure PVA crystals in Figure 6-1 and Figure 6-2. This result is significant and demonstrates an even reaction that happened on the surface with the aid of catalyst TiO_2 powders. By looking at the morphology in high resolution (1 µm), the materials hold similar

spherical morphology, confirming they are the TiO_2 particles other than decomposed small pieces of PVA polymers on the surface. Figure 6-4 for PVA-TiO_2 4-1 mixture samples exhibits a similar effect. By comparing Figures 6-1, 6-3 and 6-4, TiO_2 helps in achieving a more homogeneous reaction on the polymer surface, which showed that deep craters with the size of 10-50 micrometers were produced in the absence of TiO_2 in non-thermal air plasma. It is interesting to observe shallow craters with the size of 30-50 microns in the absence of TiO_2 in non-thermal N_2 plasma. TiO_2 enhanced the rate of reactions and produced more uniform PVA surfaces. Notably, another key observation from the SEM results is the absence of coke or tar formation in the TiO_2-assisted non-thermal polymer depolymerization.

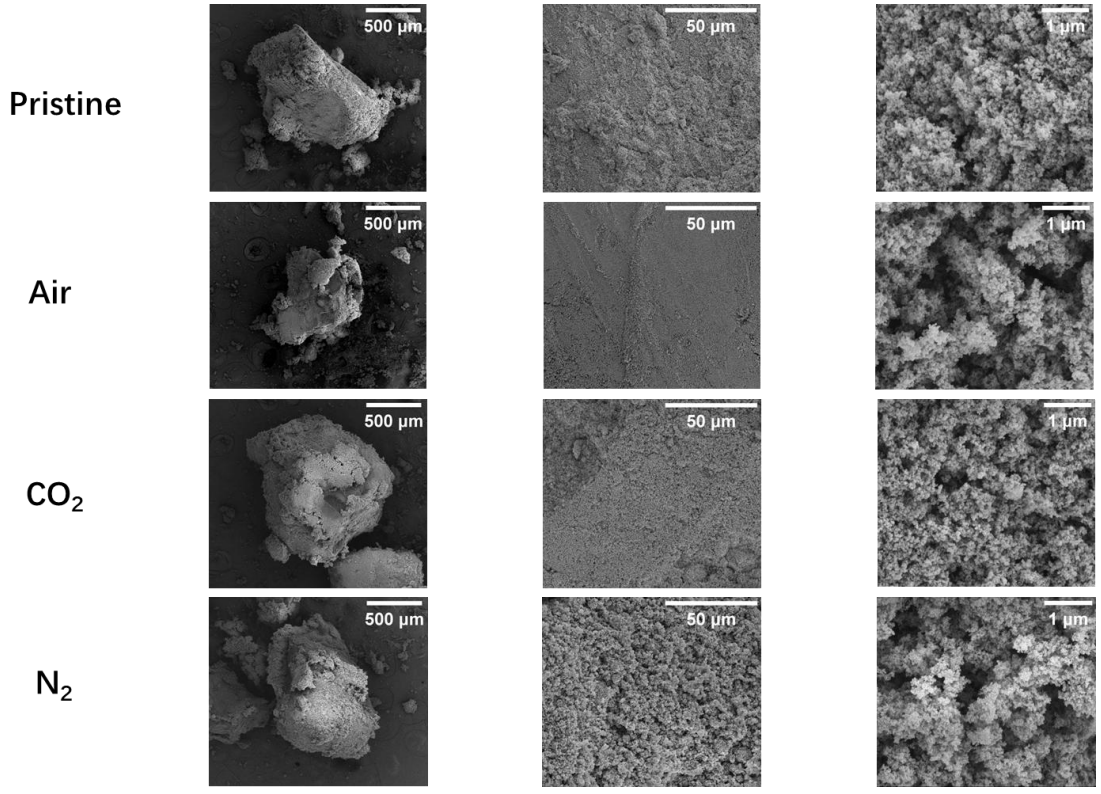

Figure 6-3 SEM images of PVA-TiO_2 mixture (2:1 molar ratio) samples before and

after air, CO_2 and N_2 non-thermal plasma reactions at 25 ℃.

Figure 6-4 shows the SEM images of the PVA-TiO_2 mixture samples (4:1 molar ratio) before and after different plasma treatments. The images show that the PVA covered by the TiO_2 on the surface is mostly in cuboid shape with 1-2 mm size. The images at low magnification (500 μm) show that the PVA surface is covered by the powder clusters in different thicknesses. With a higher resolution at a 50 μm scale bar, a uniformed treated surface was observed without holes, ridges or pits compared to the treated pure PVA crystals. This result is significant and demonstrates an even reaction that happened on the surface with the aid of catalyst TiO_2 powders. When focusing on the morphology in high resolution (1 μm), the materials exhibit similar spherical morphology and size, confirming they are the TiO_2 particles on the surface. All in all, PVA-TiO_2 4:1 mixture samples exhibit a similar morphology as PVA-TiO_2 2:1 mixture samples.

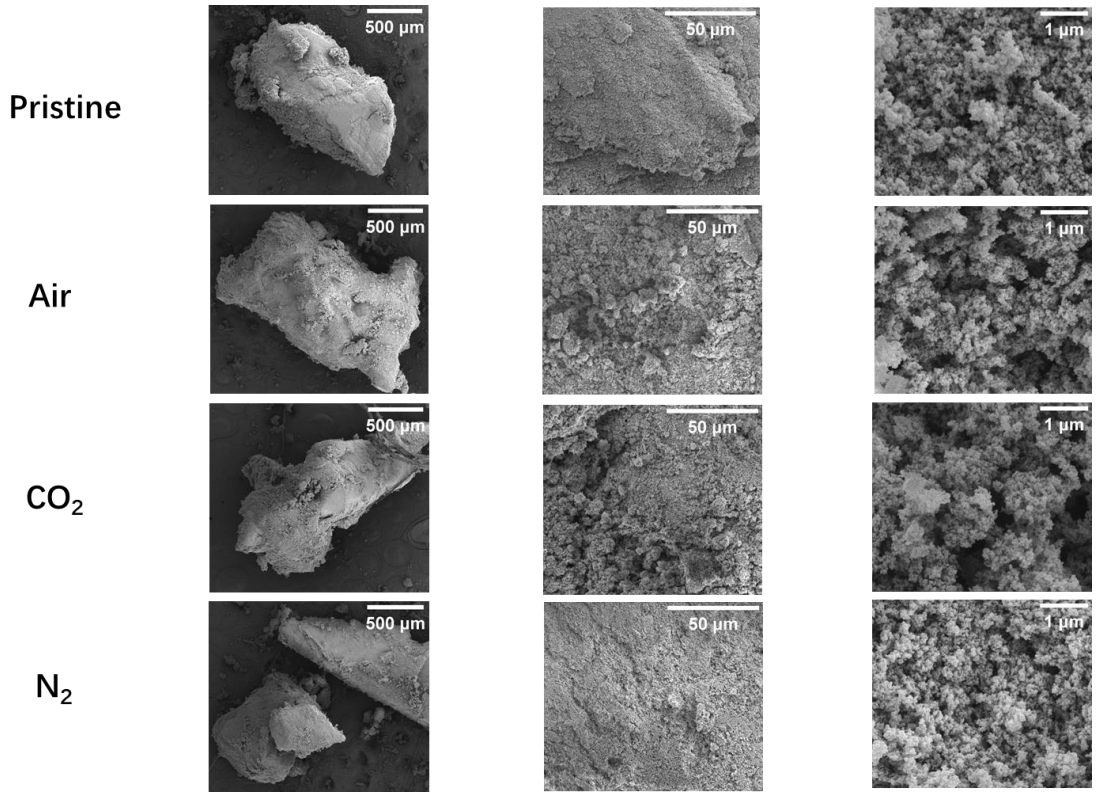

Figure 6-4 SEM images of PVA-TiO_2 mixture (4:1 molar ratio) samples before and after air, CO_2 and N_2 non-thermal plasma treatments at 25 ℃.

6.3.2 Non-Thermal Plasma Effect on TiO_2 Catalyst

SEM images for TiO_2 powders from PVA-TiO_2 2:1 and 4:1 molar ratios

Figure 6-5 shows the morphology of TiO_2 powders separated from PVA-TiO_2 mixture (2:1 molar ratio) before and after the air, CO_2 and N_2 gas plasma reactions. When focusing on a low resolution (1 μm scale bar), we can see that the clusters of the powders are in different shapes. After zooming in to a higher resolution (100 nm scale bar), the individual TiO_2 powder particles can be observed, and their size is around 10-20 nm. By comparing the powders in different reaction conditions, the pristine ones have more homogenous spherical shapes, while the powders treated in

other conditions (air, CO_2 and N_2 plasma) show smaller sizes and links between the powders. However, there are no major morphology or shape changes observed for the individual particles after the reactions. A similar morphology of the TiO_2 powers was also observed in the PVA-TiO_2 4:1 ratio in Figure 6-6. Through more refined morphology and structural study via TEM (see Figure 6-7, 6-8), the results of no significant morphology or shape changes are consistent with our SEM findings.

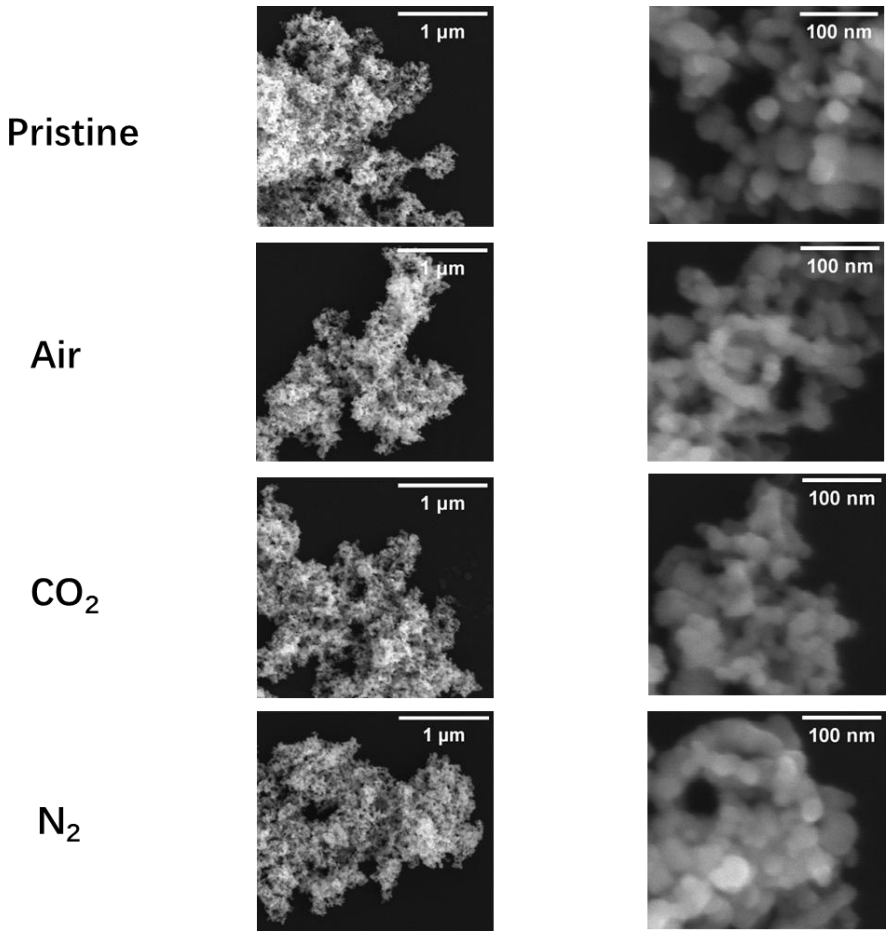

Figure 6-5 SEM images at low magnifications (1 μm) and high magnifications (100 nm) of the TiO_2 powders separated from PVA-TiO_2 mixture (2:1 molar ratio) before and after air, CO_2 and N_2 non-thermal plasma reaction at 25 ℃.

In Figure 6-6, a similar morphology was observed with different shapes of TiO_2 powder clusters (separated from PVA-TiO_2 4:1 molar ratio). When looking at the high-resolution images (100 nm), the size of individual TiO_2 powder is around 10-20 nm. However, due to the smaller amount of TiO_2 utilized (PVA-TiO_2 4:1 molar ratio), the size discrepancy and linkage were less observed than the powders separated from PVA-TiO_2 2:1 ratio. In summary, no coking or tar was observed on the surface and the retained morphology suggests the reactant diffusion pathways are not deteriorated in the plasma environment.

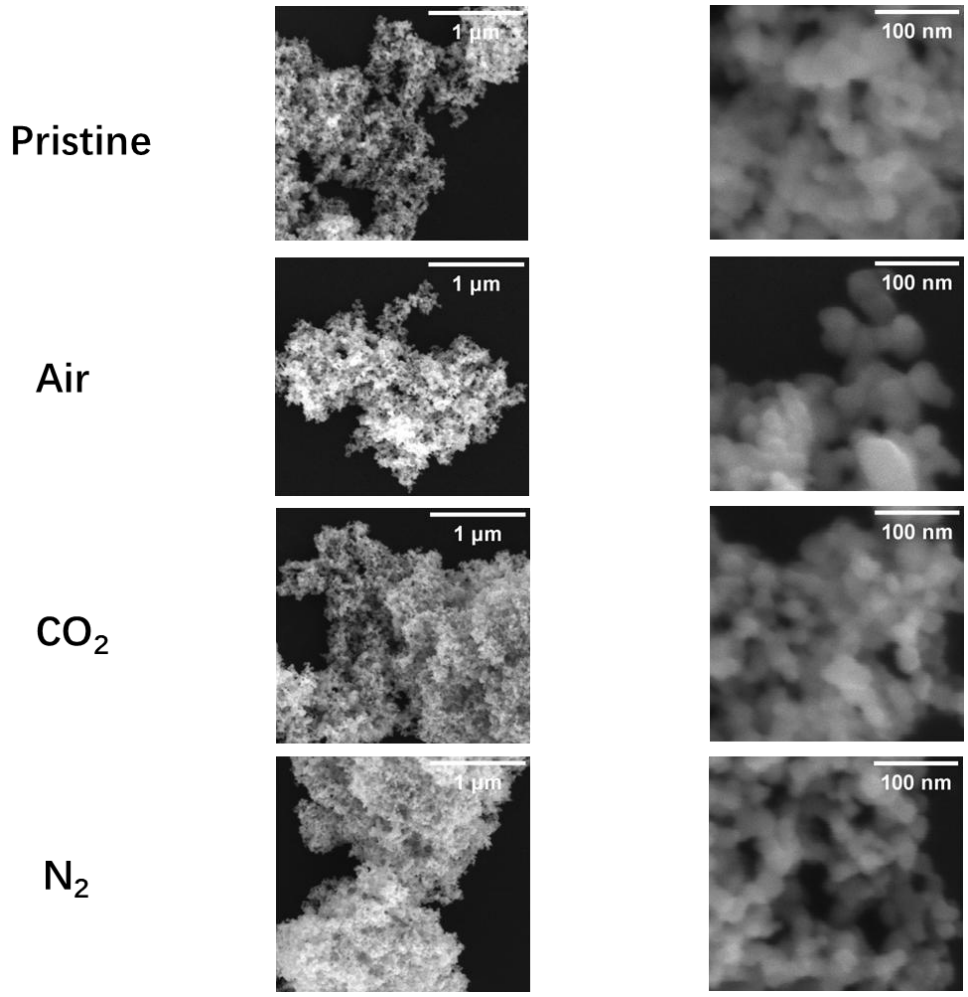

Figure 6-6 SEM images at high (100 nm) and low magnifications (1 µm) of the TiO_2 powders separated from the PVA-TiO_2 mixture (4:1 molar ratio) before and after air, CO_2 and N_2 non-thermal plasma treatments at 25 ℃.

TEM images for TiO_2 powders from PVA-TiO_2 2:1 and 4:1 molar ratios

Figure 6-7 shows the transmission electron microscopy (TEM) images of catalyst TiO_2 powders (separated from PVA-TiO_2 2:1 molar ratio) in pristine, air, CO_2 and N_2 plasma conditions. In the left and center columns of the images, The TiO_2 powders show random shapes without certain forms like triangles, tetragons, or

pentagons and they are in different orientations. In addition, from the TEM images, the average size of different powders is around 20 nm. After enlarging the images to a higher resolution with a 2 nm scale bar (right column images), we can observe the crystal lattice fringes and the interplanar distance is measured to be around 0.37 nm, calculated from the average of 10 interplanar distances, which is close to the reported value of 0.35 nm for the signature (101) plane of anatase.[28–30] However, there is a small difference in the distances, which could be due to subtle variations of the crystal lattice or the measurement. More bright dots observed from TiO_2 powders treated under air plasma suggest that more oxygen derived from the surface of the TiO_2 catalyst participates in the plasma reaction, especially in the production of CO_2, ketone groups and the subsequent reactions. These TEM images can conclude that the catalyst stays intact and retains the complete and unaltered crystal structure. We speculate that the catalyst TiO_2 treated in PVA-TiO_2 4:1 ratio presents the same phenomenon based on other spectroscopic measurement results. Through more refined morphology and structural study via TEM, the results of no significant morphology or shape changes are consistent with our SEM findings.

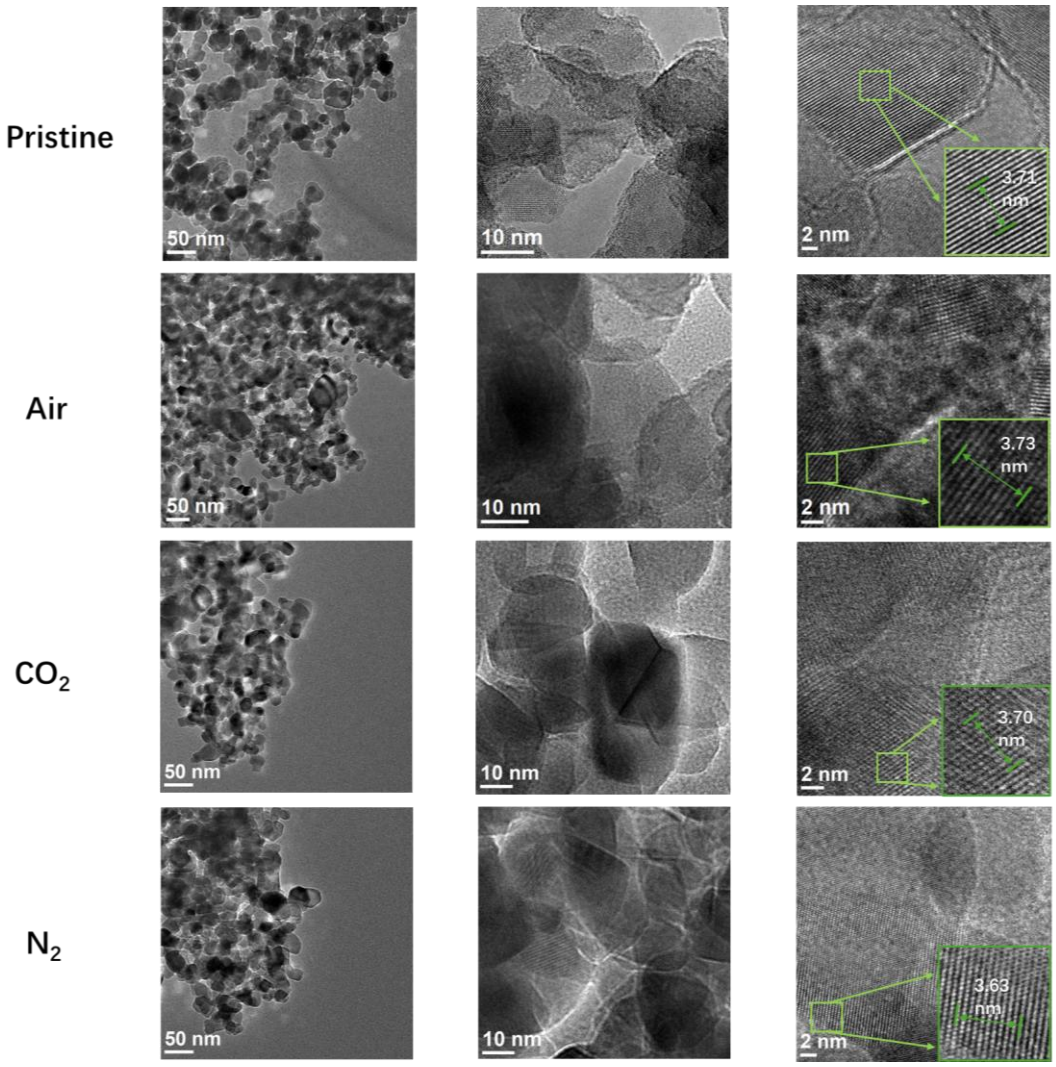

Figure 6-7 TEM and HR-TEM (high-resolution TEM) images of TiO_2 powders separated from the PVA-TiO_2 mixture (2:1 molar ratio) before and after air, CO_2 and N_2 non-thermal plasma treatments at 25 °C. From left to right, the scale bars are 50 nm (left column), 10 nm (center column) and 2 nm (right column).

Figure 6-8 shows more TEM images of catalyst TiO_2 powders (separated from PVA-TiO_2 2:1 molar ratio) in N_2 plasma condition. With closer observation, some lattice fringes disappeared after the plasma reaction. This is unique under N_2 plasma

only and this phenomenon is in line with the shortened lattice spacing in Figure 6-7, which provides a reason for the distorted crystal lattice structure. This result needs further confirmation with other characterizations.

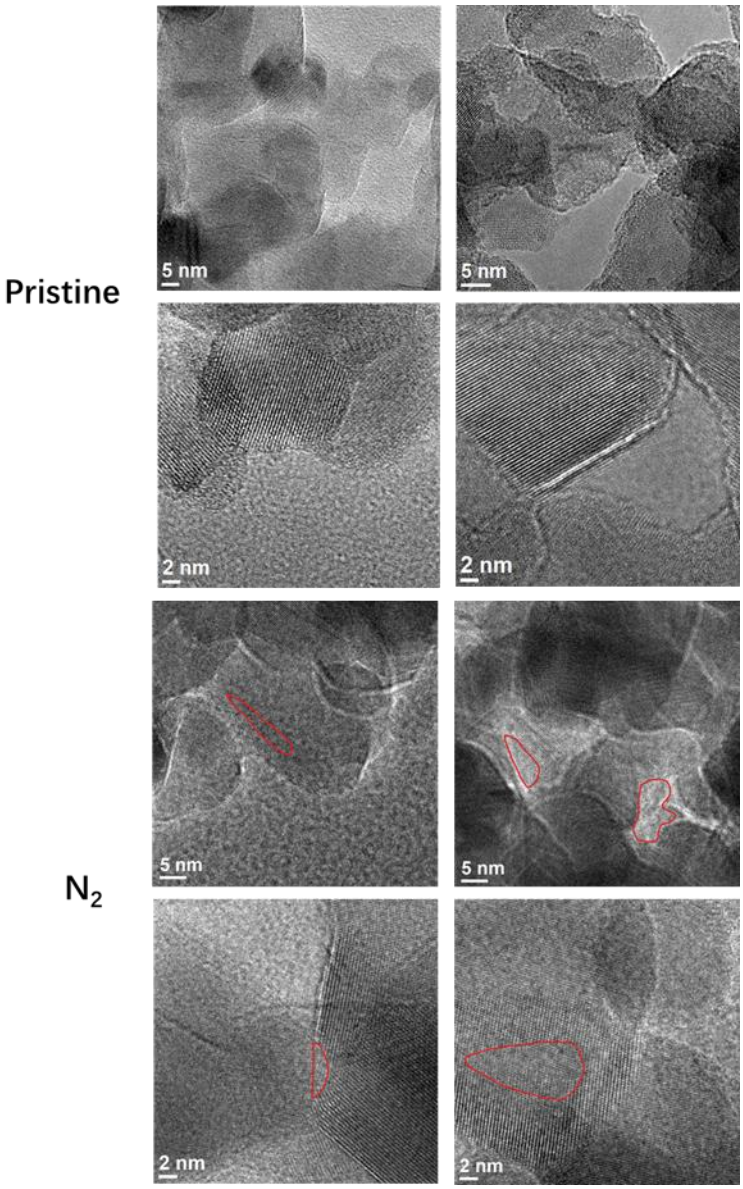

Figure 6-8 HR-TEM (high-resolution TEM) images of TiO_2 powders separated from the PVA-TiO_2 mixture (2:1 molar ratio) before and after N_2 non-thermal plasma treatments at 25 ℃. The red circles show the possible holes in the catalyst TiO_2 after

the N_2 plasma reaction.

To further evaluate the catalyst properties after the plasma reactions, Raman spectra were acquired to determine the chemical structure changes. Figure 6-9 presents the Raman peaks of TiO_2 in PVA-TiO_2 2:1 and 4:1 ratio before and after the gas plasma reactions. The four signature peaks at 142, 398, 513 and 640 cm^{-1} are associated with symmetric stretching vibration, symmetric bending vibration, anti-symmetric bending vibration and symmetric stretching vibration of Ti-O-Ti bond and agree well with the anatase phase.[31–34] The sharp peaks for the symmetric stretching vibration of the Ti-O-Ti bond stand out and retain high intensity after the reaction studies. The increased intensity of the 142 cm^{-1} peak after non-thermal N_2 reaction indicates changes in the surface structure of the TiO_2 catalyst, likely due to surface cleaning, nitrogen incorporation, defect passivation, or enhanced crystallinity.[35–38] Meanwhile, the intensity ratio among the three peaks in the 350 to 850 cm^{-1} region remains the same for all the samples, indicating the Ti-O-Ti bond remains stable and intact. Also, the increased background for the samples treated with plasma was noticed and it could be due to the degradation effect of PVA (-CH_2-CHOH-), and some solid residues are left on the surface of the catalyst indicated by the C-C stretch vibration at 865 cm^{-1}, in turn, implying the catalyst surface was involved in the plasma-assisted polymer degradation.[39,40] This chemical structure study demonstrates the high stability of the catalyst TiO_2 used in the plasma reaction, without the deactivation caused by the accumulation of carbonaceous residues,[41] providing an excellent example of intermediates for non-thermal polymer depolymerization.

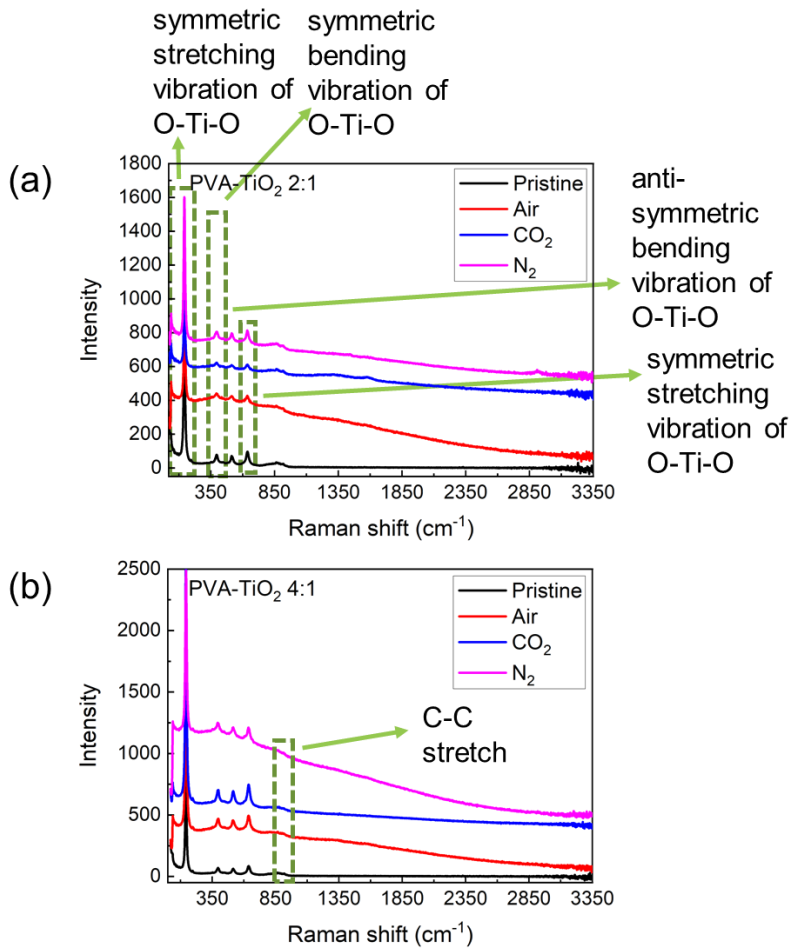

Figure 6-9 Raman spectra of TiO_2 powders separated from PVA-TiO_2 mixture in (a) 2:1 molar ratio and (b) 4:1 molar ratio before and after air, CO_2 and N_2 non-thermal plasma reaction at 25 ℃. The green boxes show the same peak position among different conditions.

Figure 6-10 shows the XRD pattern of the TiO_2 powders before and after the plasma reactions. All XRD patterns indicate the well-defined crystal structure of TiO_2 before and after the reactions. The diffraction peaks remain the same under different conditions and peaks at 25.2°, 37.8°, 48.0°, 54.0°, 55.1°, 62.7°, 69.0°, 70.3° and 75.1°

assigned to (101), (004), (200), (105), (211), (204), (116), (220) and (215) diffraction planes match well with the anatase phase of TiO_2.[42–44] We can conclude that the crystal structure of the catalyst TiO_2 stays intact and there are no O^{2-} holes induced local structure distortions under the plasma reactions.

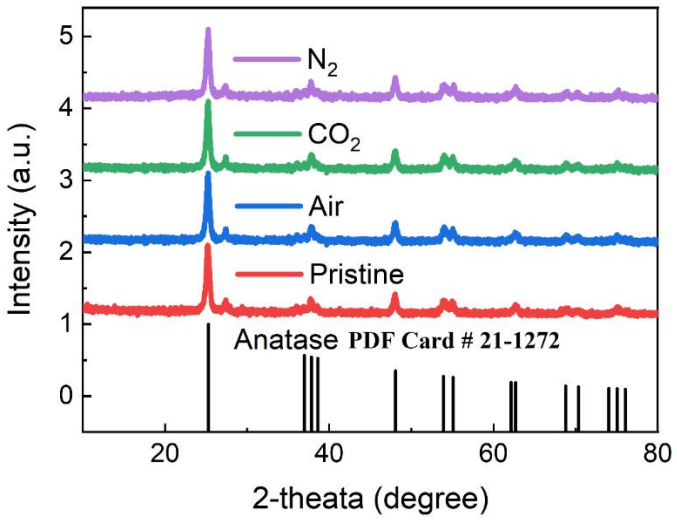

Figure 6-10 XRD pattern of TiO_2 powders at the pristine state and after air, CO_2 and N_2 plasma reactions. The TiO_2 anatase phase PDF card was put at the bottom of the figure for reference.[45]

6.3.3 Non-Thermal Plasma Effect on Solid PVA Residues

Figure 6-11 shows the Raman peaks of PVA, PVA separated from PVA-TiO_2 mixture in 2:1 and 4:1 molar ratio under air, CO_2 and N_2 non-thermal plasma reactions. In Figure 6-11 (a) for the pristine PVA samples, after the gas plasma reactions, the peak at 2910 cm^{-1} assigned to the CH_2 stretch increases the intensity, suggesting the production of the CH_2 bond and the breaking of the C-OH bond in the (-CH_2-CHOH-) backbone at the same time.[46] Under the air and N_2 plasma conditions,

a significantly increased background was observed, showing a high fluorescence intensity, which is due to the generated short fragments of depolymerized materials on the surface.[39,40] These results confirm that the depolymerization reaction happened on the surface. In the N_2 plasma-treated samples, the intensity of peaks attributed to the C-OH vibrations decreases dramatically while the CH_2 bond intensity increases largely compared to the pristine samples, demonstrating the scission of the C-OH bond and hydrogenated to CH_2 in the structure, which was discussed in the gaseous products.[9] In conclusion, these Raman spectra indicate the cleavage of the C-OH bond in the repeating units of the PVA and of all the reaction conditions, N_2 plasma demonstrates the highest efficiency in breaking the C-OH group and generation of a further related function group, in line with the result of higher selectivity to the aldehydes in N_2 plasma in the gaseous products.[9]

In Figure 6-11 (b) and (c), the TiO_2 was added as a catalyst to promote depolymerization efficiency. The PVA-TiO_2 samples were washed to separate PVA from the mixture before being characterized, although a small amount of the TiO_2 can still be found on the surface as indicated by the vibration of Ti-O-Ti bond peaks. Since we are focusing on the PVA depolymerization after the reaction, the TiO_2 signals are the catalyst residual on the surface and won't be discussed here. For the samples with a PVA-TiO_2 2:1 ratio (Figure 6-11 (b)), the intensity of peaks assigned to the C-C stretch, C-OH vibrations, CH_2 bend and the CH_2 stretch increases by the same degree, implying the similar degradation effect on the solid samples. For the samples separated from a PVA-TiO_2 4:1 ratio (Figure 6-11 (c)), the intensity of

different peaks shows a similar trend to those with a PVA-TiO_2 2:1 ratio. All the spectra from both PVA-TiO_2 2:1 and 4:1 ratios don't show the fluorescence background, which could be due to the washing on the PVA surface. Nonetheless, in the gaseous products study, the TiO_2 catalysts enhanced the total oxidation of PVA to CO_2 evidenced by that decreasing the amount of TiO_2 (PVA-TiO_2 4:1 molar ratio) led to the return of aldehyde products and CO.[9] The aid of degradation or selectivity effect was not observed in the solid products.

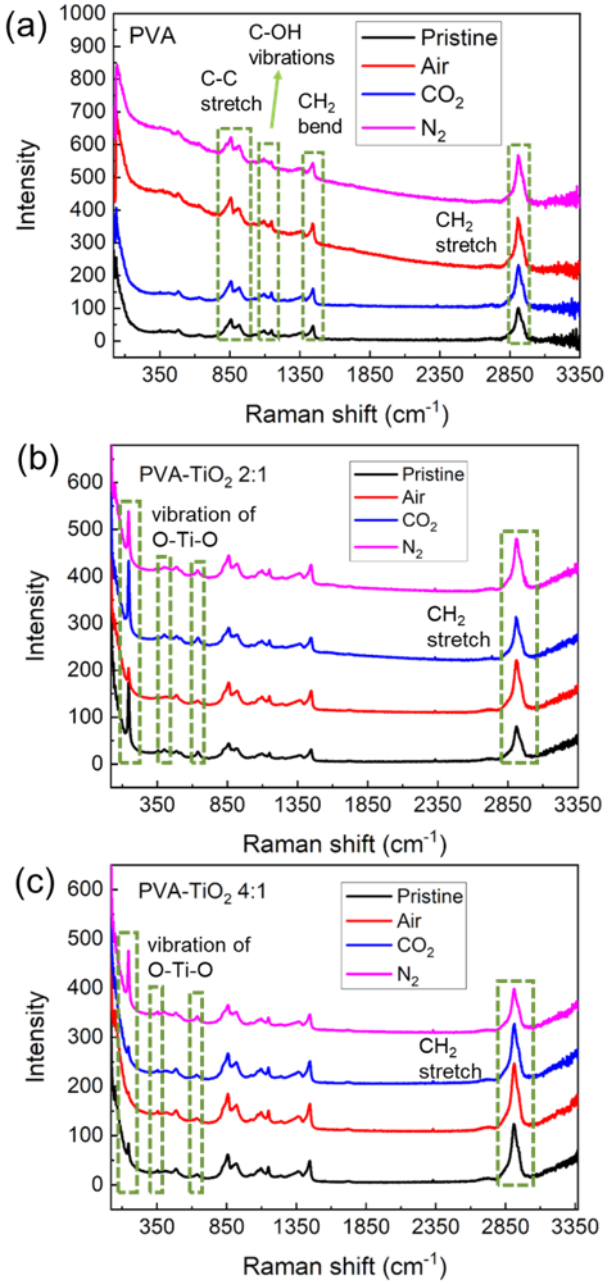

Figure 6-11 Raman spectra of PVA samples (a) without TiO_2 addition, (b) separated from PVA-TiO_2 2:1 molar ratio, (c) separated from PVA-TiO_2 4:1 molar ratio before and after air, CO_2 and N_2 non-thermal plasma at 25 °C. The green boxes show the same peak position among different conditions.

Figure 6-12 shows the FTIR spectra for PVA samples with and without TiO_2 in different plasma conditions to fully investigate the chemical structure. For the PVA samples in Figure 6-12 (a), we assigned the peaks at 3271 cm^{-1}, 2908 cm^{-1}, 1711 cm^{-1}, 1417 cm^{-1}, 1089 cm^{-1} and 844 cm^{-1} to O-H stretching, CH stretching, C=O stretching, CH_2 bending, C-O stretching in acetyl group, C-C stretching vibrations, in conformity with earlier studies.[27,47–49] The O-H stretching vibration decreases after the plasma reaction, indicating the cleavage of the O-H bond and the left H will be an active species for PVA decomposition reactions. Also, the decrease of the CH stretching intensity suggests the CH-OH bone breaks down with the reaction. In the meantime, the increase of the C=O stretching vibration implies that more carbonyl groups have formed due to the reaction on the OH group. The original C=O stretching is attributed to the residual acetate group after the preparation of PVA from hydrolysis of polyvinyl acetate or oxidation during synthesis and processing.[47,48] The C-C bond intensity decreases after the plasma reactions, indicative of the PVA backbone cleavage. These results inform the fracture of the main structure and O-H bond with the formation of the C=O bond, during which the N_2 plasma reaction exhibits the highest efficiency.

For the PVA samples treated with TiO_2 catalyst (PVA-TiO_2 2:1 and 4:1 ratio), we assigned the peaks 3272 cm^{-1}, 2909 cm^{-1}, 1714 cm^{-1}, 1417 cm^{-1}, 1089 cm^{-1} and 844 cm^{-1} to O-H stretching, CH stretching, C=O stretching, CH_2 bending, C-O stretching in acetyl group, C-C stretching vibrations. The O-H bond diminishes more with the aid of the catalyst TiO_2. A similar phenomenon that the decrease in the O-H

bond and CH bond and the increase in the C=O bond is observed in the catalyst-treated samples. The C-C bond intensity in PVA-TiO_2 4:1 ratio also decreases in the TiO_2-treated samples, implying the fracture of the PVA chains. And with a higher amount (PVA-TiO_2 2:1) of the catalyst, CO_2 plasma enables an increased generation of C=O bond. These results suggest the scission of the backbone and O-H bonds under plasma reactions and catalyst facilitates with CO_2 plasma reaction for carbonyl group generation but N_2 plasma helps with the OH bond cleavage. The specific molecules still need further study with techniques like NMR and will be used later to show the structural change and possible detailed compound.

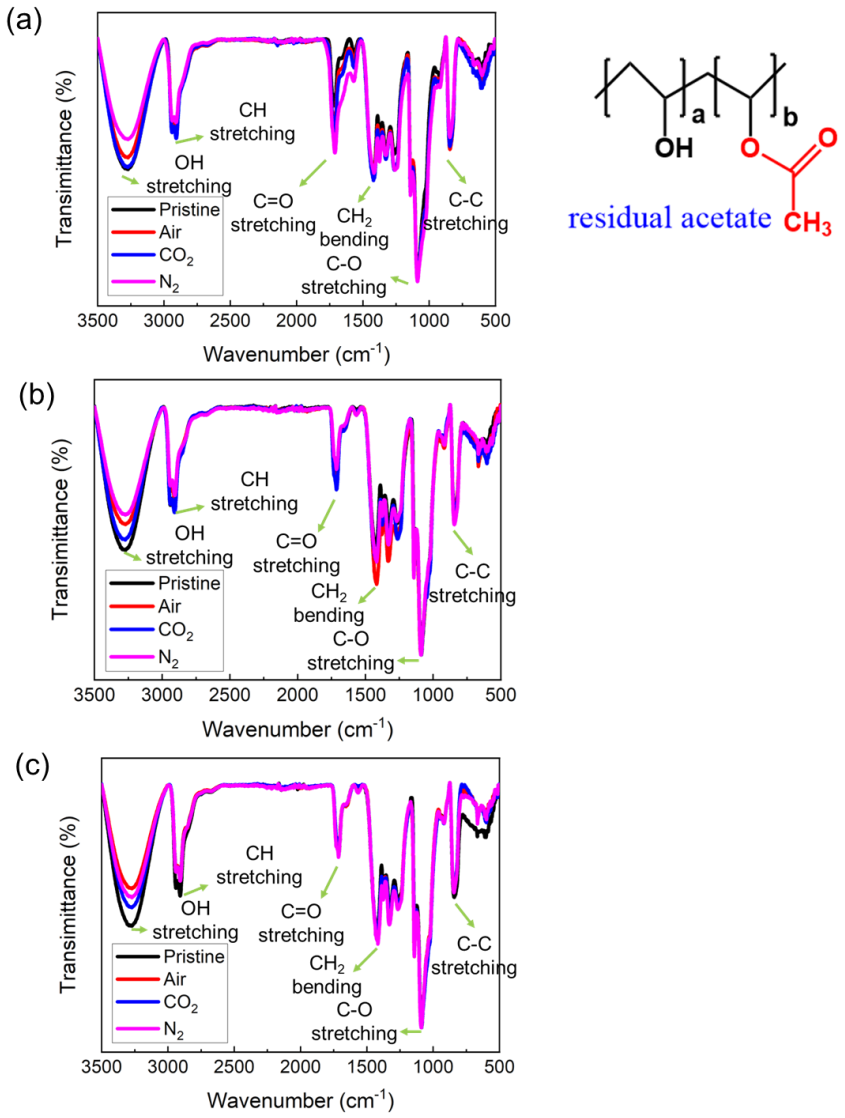

Figure 6-12 FTIR spectra of PVA samples (a) without TiO_2 addition, (b) separated from PVA-TiO_2 2:1 molar ratio, (c) separated from PVA-TiO_2 4:1 molar ratio before and after air, CO_2 and N_2 non-thermal plasma at 25 °C. The side images illustrate the hydrolyzation of PVA. The vinyl alcohol polymer and acetate are produced in a ratio of a and b in mol %, and b is significantly smaller than m due to the low concentration of residual acetate.

Figure 6-13 shows the C *K*-edge XAS spectra to determine the electronic state of the C element in PVA before and after the non-thermal plasma reactions. Across all conditions, the C *K*-edge XAS spectra exhibit a distinct splitting around 287 eV, with the peak at 287.3 eV assigned to σ* (C-O-H) and the peak at 288.2 eV associated with the σ* (C=O) bond.[50] Figure 6-13 (a) displays C K-edge XAS collected on pure PVA samples, where the feature at 285 eV is assigned to the C 1s to C π* transition in the C-C bond. Treatments under different conditions produce minimal changes in the backbone C-C structure. However, in the photon energy region near 287 eV, the intensity of the C*-O-H and C*=O bond peaks shows a dramatic change before and after treatment. The dominant contribution observed at 288.2 eV (Figure 6-13 (a)) corresponds to the C=O group, showing an increasing C*=O bond absorption signal in the sequence of air, CO_2 and N_2 plasma reactions, indicative of the reaction degree of the breaking of the C-OH bond and forming of the C=O bond and N_2 plasma reaction showing the highest efficiency.

Similar phenomena for C element-specific XAS spectra were observed in the PVA samples separated from the PVA-TiO_2 mixtures, where the C*=O bond absorption signal increased, while the C*-OH bond absorption signal decreased, indicating the scission of the CO-H bond from the polymer main structure. In the PVA samples separated from PVA-TiO_2 2:1 ratio, air plasma is most effective in breaking C-OH bond. In contrast, in PVA samples separated from the PVA-TiO_2 4:1 ratio, CO_2 exhibits the best condition for this bond scission. Overall, the XAS data

are consistent with the FTIR and Raman results, supporting the conclusion of C-OH to C=O conversion.

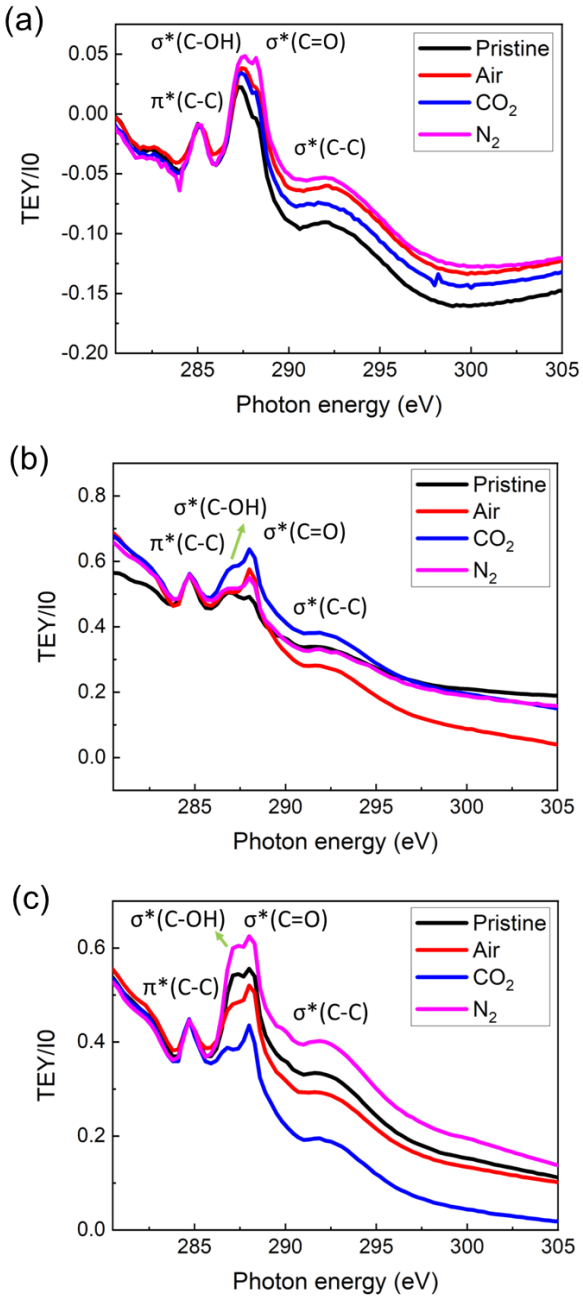

Figure 6-13 XAS spectra on C element of PVA samples (a) without TiO_2 addition, (b) separated from PVA- TiO_2 2:1 molar ratio, (c) separated from PVA- TiO_2 4:1 molar ratio before and after air, CO_2 and N_2 non-thermal plasma at 25 °C.

The comparative analysis of Raman, FTIR and XAS spectroscopy reveals

consistent findings regarding the effectiveness of PVA depolymerization in non-thermal plasma. N_2 plasma is particularly efficient in cleaving the C-OH bond and eliminating OH group from PVA in terms of solid products while when catalyst TiO_2 is present, air and CO_2 plasma is more active for CH_2 formation (alkylation) in Raman and FTIR and C=O generation (oxidization) by XAS spectra, probably due to the synergic effect of the O radicals arising from TiO_2 and air or CO_2 plasma. The catalytic role of TiO_2 in enhancing depolymerization efficiency is evidenced clearly in FTIR and XAS results based on the decrease degree of the OH group compared to the pristine PVA. These complementary spectroscopic analyses provide a comprehensive understanding of depolymerization of PVA by non-thermal plasma.

Figure 6-14 shows the ^{1}H and ^{13}C NMR spectra of PVA samples in pristine, treated in N_2 plasma, and treated in N_2 plasma and TiO_2 catalyst for detailed structure determination. The assignments of the solvent, deuterated DMSO-d_6, and PVA signature chemical group are based on the previous reports.[48,51] In ^{1}H NMR spectra, the peaks for all the signature chemical groups in PVA either decreased in TiO_2-assisted samples or changed shapes after the N_2 plasma reaction, showing the modification of the backbone to break down and generate new compounds. In the ^{13}C NMR spectra, the peak positions and intensities don't show significant changes after the N_2 plasma and catalyst (PVA-TiO_2 2:1) treatment, but there are decreased intensities for all the existing peaks and emerging new peaks in the PVA N_2 plasma condition. The TMS signal is from the DMSO-d_6, and the variance from different spectra is from the two bottle sources with different concentrations of TMS. The ^{1}H

NMR peaks at 1.4 and 3.6 ppm (middle spectra) are tentatively assigned to CH_2 and CH-O from PVAc (polyvinyl acetate). The ^{13}C NMR peaks at 19, 66 and 172 ppm in PVA treated in N_2 plasma match well with the reported data, showing the PVAc structure in the solid compounds.[52,53] The peak at 42.4 ppm is tentatively assigned to CH_2 from PVAc. The peak at 78.5 ppm is assigned to CH-O, the ether structure.[54,55] This result indicates the plasma reaction provides an oxidation environment and oxidizes the PVA back to PVAc compared to the hydrolysis of PVAc during preparation in the factory. In the acid environment created by alcohol oxidation products, the ethers are suggested to be produced. This result demonstrated that the sole N_2 plasma boosts the abundant reactions and creates the most products in the solid. The production of PVAc and ether is supported by our FTIR data with increased C=O bond and C-O bond intensity but without the peak position changes.

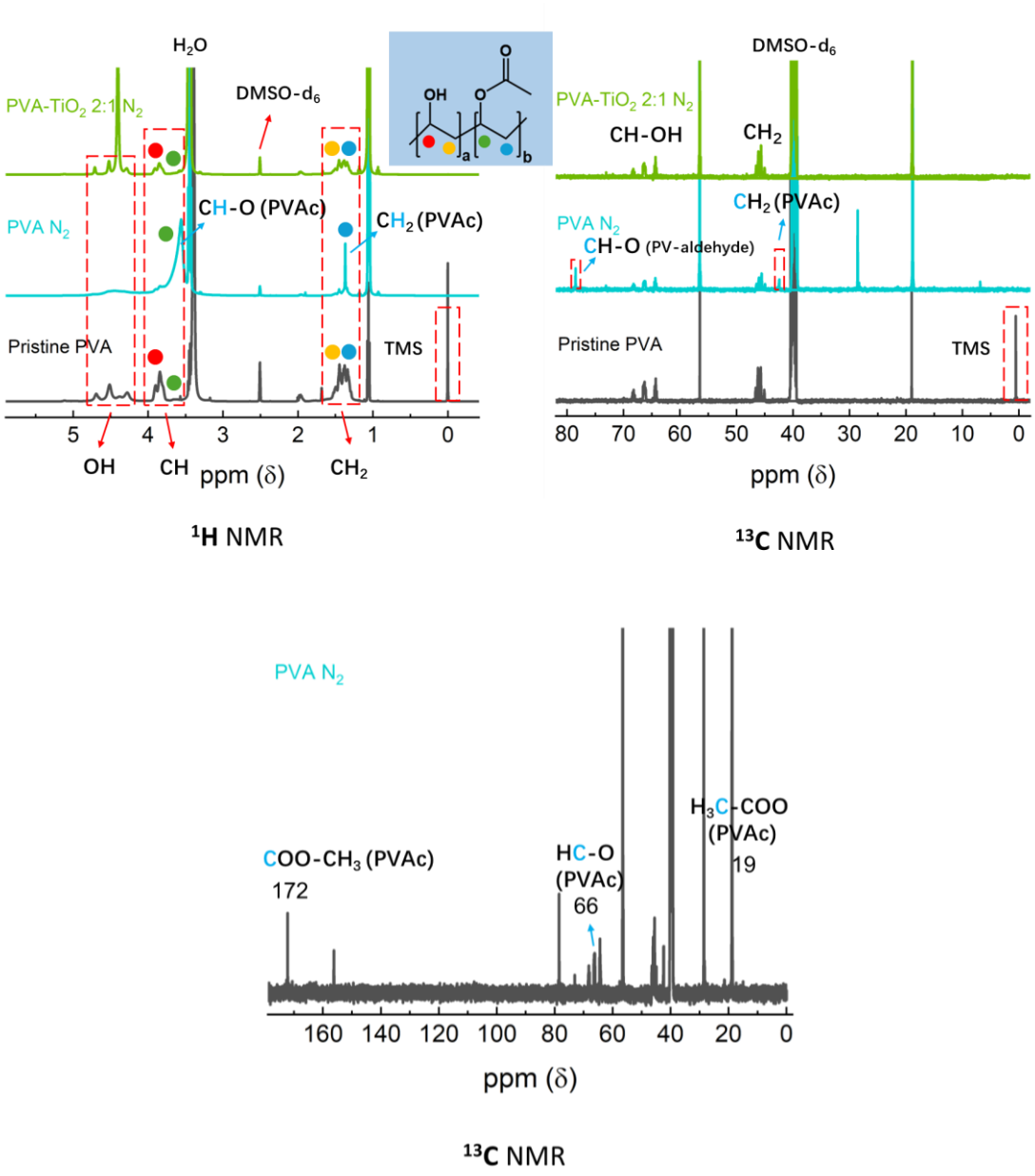

Figure 6-14 ^{1}H and ^{13}C NMR spectra of pristine PVA samples, PVA samples reacted under N_2 plasma, PVA samples separated from the PVA-TiO_2 mixture (2:1 molar ratio) reacted under N_2 plasma and PVA samples reacted under N_2 plasma at large range (0-180 ppm).

Figure 6-15 shows the mass spectra of PVA in pristine, treated in N_2 plasma, and

treated in N_2 plasma and TiO_2 catalyst to learn about the molecular weight of decomposed products. All the PVA samples show the fragmented polyvinyl alcohol in the low mass region, e.g., 200, 332, 372 m/z, which is interpreted as 4, 7, and 8 polyvinyl alcohol units. Similarly, PVA reacted in N_2 plasma shows the most solid products and two new peaks at 618 and 860, respectively. These two peaks are assigned to PVA-PVAc and PVA-PVAc-PVA-acetal (O-CH_3CH_2-O) or PVA-PVAc-PVA-propional (O-$CH_3CH_2CH_2$-O) as shown in insets in MS of PVA reacted in N_2 plasma, although PVAc, PVA-acetal or PVA-propional are in a small amount suggested from the mass spectrum. 887 m/z can be explained as the PVA-PVAc with 19 polyvinyl alcohol units and 1 polyvinyl acetate unit and longer than the structure with a molecular weight of 618 Da, indicating the catalyst TiO_2 can promote the PVAc production (618 Da) but with a larger molecular weight. This result aligns with the NMR results to support the production of PVAc and ether structures.

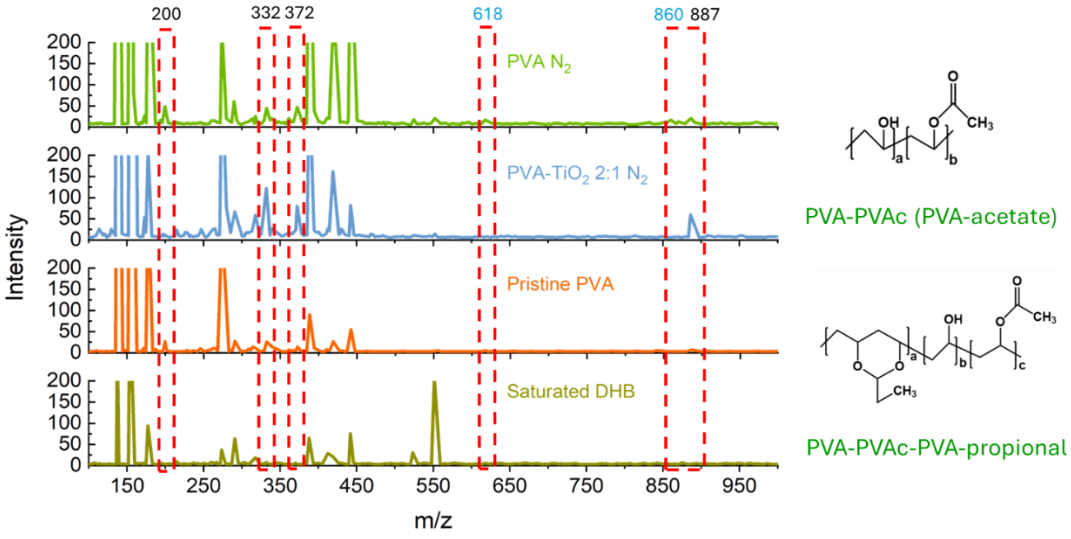

Figure 6-15 MALDI-Mass Spectra of matrix DHB (2,5-dihydroxybenzoic acid), pristine PVA samples, PVA samples reacted under N_2 plasma and PVA samples separated from the PVA-TiO_2 mixture (2:1 molar ratio) reacted under N_2 plasma. Insets in MS of PVA reacted under N_2 plasma show PVA-PVAc and PVA-PVAc-PVA-propional structure.

6.3.4 Depolymerization Mechanisms

The experimental results are summarized and discussed below to provide more insights into our study. Raman spectra exhibited that some C-OH groups are hydrogenated to CH_2 group solid products, implying the cracking of C-OH bond in the backbone. FTIR measurement confirmed the cleavage of the long chain to the short chain through the C-C bond breakage. The diminishing of the OH bond signal suggests its cleavage and the generation of free H species. Moreover, the decline of the C-OH group and the ascent of the C=O group in the spectra indicate the transformation of the alcohol group to the ketone group. When taking the charged species and radicals into account, the produced C, N and O plasma species play an important role in oxidatively dehydrogenating the C-OH group. All the measurements, including Raman, FTIR, XAS, NMR, and MS, confirmed the formation of the carbonyl group and the viability and efficiency of non-thermal plasma to depolymerize the PVA. Extracted from all the information with the gaseous products study included, we conclude that the major reaction in the non-thermal plasma-assisted PVA depolymerization is the evolution of alcohol group to the ketone group and the following esterification and acetal reactions in the plasma environment.

The gas plasma, including air, CO_2 and N_2 produces active species, such as radicals, ions and electrons, attack the bonds and break down the main structure into shortened solid fragments and valuable small gas molecules.

In a former PVA solution study treated with gamma irradiation, a similar result that OH to C=O transition was extracted from FTIR and the breaking of C-H and C-OH bonds, and therefore the formation of more carbonyl double bonds (C=O) and the chain structure breaking was concluded. The water solution under gamma radiation will generate electrons, ions, radicals and molecules, such as e^-, H^+, H_3O^-, $H\cdot$, $OH\cdot$, H_2 and H_2O_2, similar to our gas plasma system.[47] This result supports our observation of the conversion of the alcohol group to the ketone group by the scission of O-H and C-OH and the formation of a C=O bond in the PVA main structure.

And some researchers emphasized the electron impact effect to improve the polymer reforming in the non-thermal plasma reactions. Williams's group utilized the non-thermal plasma method to improve the biofuel quality during the treatment.[25,56] The improvement is attributed to high-energy electrons, excited radicals, ions, and intermediates that increase the interaction of the polystyrene and biomass pyrolysis volatiles. The chemical bonds in polymer and the gaseous products can be easily broken down by high-energy electrons or other excited species because these bonds have lower mean energies; for example, the C-H bond with a binding energy of 4.3 eV and the C-C bond of 3.4 eV in high-density polyethylene (HDPE) compared to the excited electrons (with high energy in the range of 0–10 eV) and N_2* (with an energy of 6.2 eV).[17,57] The covalent bond dissociation energies in the polyvinyl

polymers are between 300 and 500 kJ mol^{-1} which corresponds to 3-5 eV in electron volt unit, specifically C-C, 3.59 eV; C-O 3.71 eV; C-H 4.25 eV; H-O 4.75 eV.[55] Furthermore, according to Meng et al., the high-energy electrons produced in the non-thermal plasma process facilitate the tar removal in the final products, which is also shown in this study.[56]

From the previous plasma studies, different gases will have different reactions under high voltages, for example, air plasma: $O_2 + e \rightarrow 2O + e$, $N_2 + e \rightarrow 2N + e$; CO_2 plasma: $CO_2 + e \rightarrow CO + O + e$, $CO + e \rightarrow C + O + e$; N_2 plasma: $N_2 + e \rightarrow 2N + e$.[58–61] The electrons and C, N, O and CO radicals are reactive atomic species and will dissociate the OH bond and have the H radicals as the reactive species.[62] At air, CO_2 and N_2 conditions, the dominant reactive species are different and bond scission mechanisms vary slightly. The different reaction mechanisms are summarized below. Air plasma generates a mix of reactive oxygen species (ROS) such as atomic oxygen (O), ozone (O_3), hydroxyl radicals ($OH\cdot$), and superoxide (O_2^-).[62-64] These species are highly effective in initiating partial oxidation of polymers that incorporate oxygen atoms into the polymer structure, leading to functional groups like ketones, aldehydes, or carboxylic acids. In contrast, total oxidation to CO_2 is less favored due to the competition between reaction pathways and the limited availability of ROS under typical non-thermal plasma conditions. Air plasma facilitates a broad range of oxidative reactions, with partial oxidation being predominant and total oxidation being secondary and less efficient.

Non-thermal plasma in nitrogen primarily generates high-energy electrons,

which drive the reactions through electron impact ionization and excitation. High-energy electrons can excite N_2 molecules to metastable states (e.g., N_2*), which contribute to bond scission indirectly by transferring energy to polymer bonds.[65] Dissociation reactions such as $N_2 + e \rightarrow 2N + e$, provide reactive atomic nitrogen, but these species are less involved in oxidative pathways than oxygen-based plasmas. Overall, high-energy electrons are the dominant reactive species in N_2 plasma, facilitating bond cleavage, especially with the reactive atomic oxygen (O) in polymers through direct electron interactions rather than oxidative mechanisms.

Non-thermal plasma in CO_2 primarily produces CO and reactive oxygen species (O), with the dissociation reaction $CO_2 + e \rightarrow CO + O + e$, $CO + e \rightarrow C + O + e$. Reactive oxygen species from CO_2 plasma have lower oxidative potential than those derived from O_2 plasma due to the differences in dissociation energy and reactive pathways.[66,67] Atomic oxygen from CO_2 dissociation is less reactive toward initiating chain scission or oxidation compared to the ROS generated in air plasma. In all, CO_2 plasma is less effective for partial oxidation and predominantly generates CO and less-reactive oxygen species, limiting its impact on oxidative depolymerization compared to air plasma.

The high energy electrons from the C, N and O atoms play a key role in the plasma to scissor the chemical bonds (3-5 eV in PVA) compared with radicals and excited species.[68-70] Based on the experimental results, N_2 plasma dissipated the most OH groups from PVA chain. The OH· radicals have the strongest oxidation ability among the C, N, O, CO radicals via H abstraction from organic groups and oxidize

the alcohol group to ketone group and further acid group, probably some due to the reactive O atoms cracking from OH·.[69-71]

Overall, the PVA depolymerization mechanism is shown below in Figure 6-16. After the high-energy electrons and radicals synergically attack the PVA, the backbone dissociates into smaller fragments, some with the alcohol groups oxidatively dehydrogenating to ketone groups and then cleaving into gas-phase radicals or continuing to oxidize to carboxylic acid groups, while the rest was unoxidized into short-chain solid fragments. Then the unstable intermediate gas products will diffuse along the catalyst surface and be adsorbed to the surface, increasing the chance of chemical reactions. The subsequent desorption gas species will combine with O* (part of O radicals from TiO_2) and H* via the oxidation or hydrogenation reaction to form small gas molecules like CO_2 and aldehydes as detected by the in-situ FTIR and all three gas plasmas give off the same gaseous products from the previous study.[9] Part of the fragmented solid products will continue to be scissored and hydrogenated to the CH_2 group in the backbone afterward. The subsequent oxidation reaction of the alcohol group in the rest of PVA leads to carboxylic acid or ketone group. Carboxylic acid will react with PVA to produce PVAc via esterification reaction. And the gas products acetaldehyde and propionaldehyde will further react with the alcohol group in the acid environment to produce cyclic cross-linking structures like PVA-PVAc-PVA-acetal (O-CH_3CH_2-O) or PVA-PVAc-PVA-propional (O-$CH_3CH_2CH_2$-O). Given all the products we found in the gas and solid phases, the catalyst TiO_2 not only facilitates the decomposition of

the backbone but also promotes the reaction for alcohol group reduction, gas production, especially CO_2, and the PVAc formation in the solid products. This proposal unveils the complex chemical reactions in plasma chemistry, including dehydrative oxidation, alkylation, esterification, and acetal reactions, and are well validated by the experimental results in our plasma-assisted PVA depolymerization case.

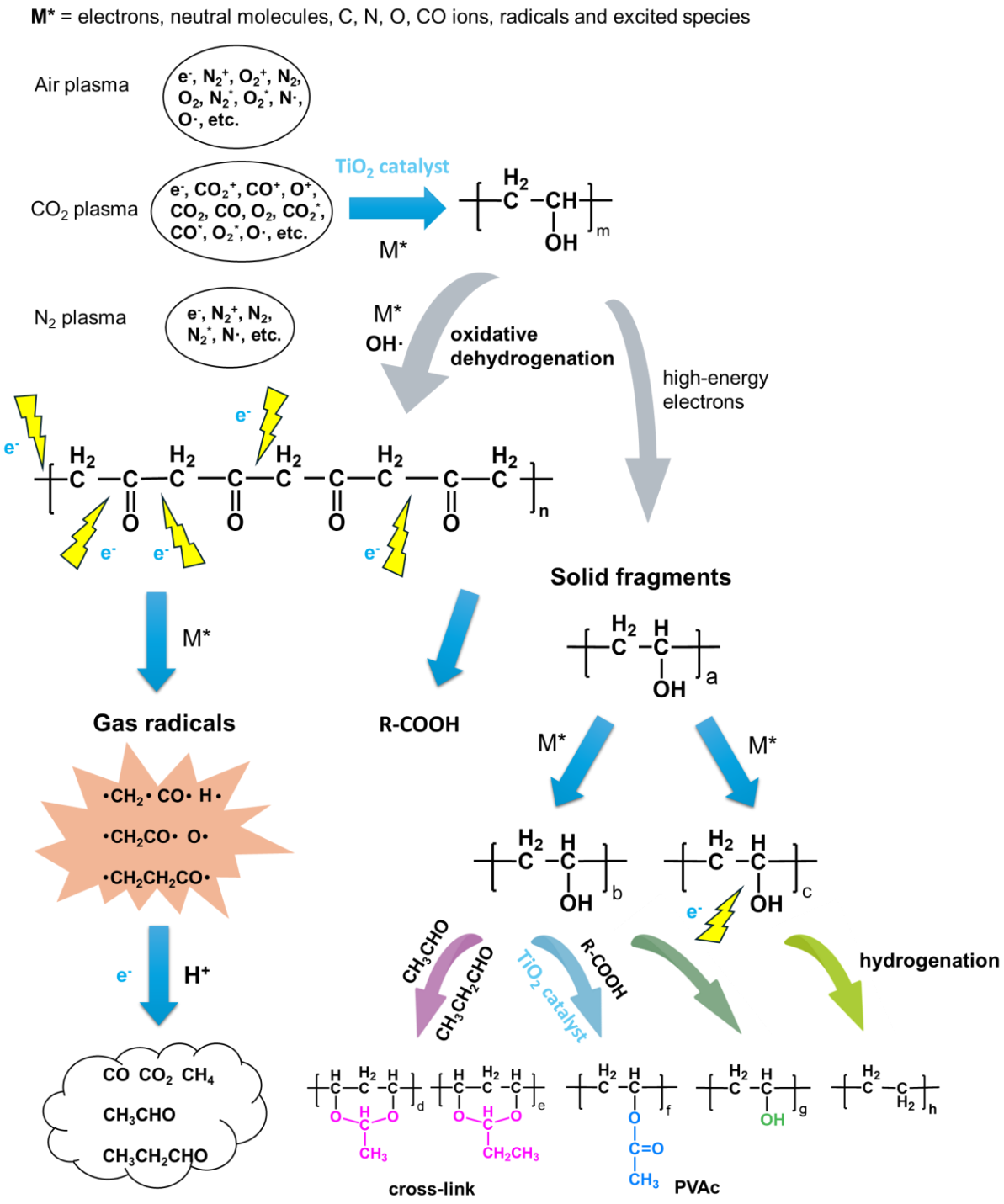

Figure 6-16 Proposed reaction pathways in the air, CO_2 and N_2 non-thermal plasma-assisted PVA degradation process.

6.4 Conclusion

In summary, PVA was effectively depolymerized using a non-thermal air, CO_2 and nitrogen plasma generated in a dielectric barrier discharge setup with TiO_2 serving as a catalyst. Raman, FTIR and XAS characterizations confirmed the scission of the C-C backbone and the conversion of the alcohol group to the ketone group in the fragmented polymers. The NMR and MS studies suggested PVAc and cross-linked structure PVA-aldehyde. TiO_2 as a catalyst with O radicals significantly enhanced the degradation process as evidenced by the evenly distributed plasma reaction on the PVA surface in SEM comparison between the PVA and PVA-TiO_2 mixture. Further XRD and TEM measurements on TiO_2 show no major surface and crystal structure changes, indicating its stability and effectiveness as a catalyst for non-thermal plasma-assisted reactions. This study also found that nitrogen plasma enhances the production of ketone (i.e., carbonyl) groups, while oxygen plasma improves the overall conversion efficiency. These findings align with previous reports on the composition of gas phase products, which showed high selectivity toward carbonyl-containing products, acetaldehyde and propionaldehyde, thereby providing complementary insights into the overall mechanism of non-thermal plasma-assisted polymer depolymerization. This technique serves as a low-energy cost and efficient method with the rational selection of catalysts and the design of plasma reactions under ambient conditions (25 ℃ and 1 atm).

6.5 Experimental Methods

1. Materials

Poly(vinyl alcohol) (PVA, M.W. = 95 000 g/mol, Acros Organics – average size 400 μm) and titanium (IV) oxide (Anatase, Sigma-Aldrich, <25 nm particle size) were used as received. CO_2 (99.999%) and N_2 (99.999%) gases were purchased from Praxair, Linde. The PVA-TiO_2 mixture in 2:1 and 4:1 molar ratio was mixed and shaken well before putting into the non-thermal plasma reactor.

2. Raman Spectroscopy

Raman analysis was performed using a Thermo Fisher DRX3 Raman Micro Spectrometer. The laser excitation source was a diode laser (λex = 785 nm). Spectra were recorded under the following conditions: stainless steel substrate, 50x objective, collect exposure time 30s for 5 accumulations, laser power 30 mW (in focus) and aperture 50 μm slit.

3. FTIR Spectroscopy

The FTIR spectra for solid products were collected via the PerkinElmer brand FTIR Spectrum Two Series spectrometer on a universal ATR sampling accessory (UATR). This solid FTIR uses a high refractive index diamond to apply pressure on the solid samples and guide the beam to the samples up to a few microns. To make the IR signal intensities consistent, the pressure applied to all the solid samples is around 100.

4. XAS Spectroscopy

Soft X-ray absorption spectroscopy (sXAS) experiments were conducted for the C K-edge at the beamlines 7.3.1 in Advanced Light Source (ALS) at Lawrence Berkeley National Laboratory. In this facility, the bending magnet beamline 7.3.1

provides a linearly polarized photon beam with an energy range from 250 eV to 1500 eV. The polymer samples were cut to 3 mm x 3 mm size and attached to the copper tape on a copper sample holder. A narrow copper tape was also attached to the surface of the samples to increase the conductivity of electrons from the sample's surface to the sample holder. All spectra for PVA were recorded using both total electron yield (TEY) and total fluorescence yield (TFY) modes, while the C spectra were shown exclusively in TEY mode due to a better signal-to-noise ratio. The energy positions of the C K-edge were calibrated using standard samples, HOPG.

5. SEM measurement

We used different methods to prepare the samples for SEM measurement. For PVA and PVA-TiO_2 mixture samples, they were sputtered with ~20 nm of gold before the measurement and imaged in an FEI Quanta 3D Dualbeam SEM operating at 5 kV and 6.7 pA.

For TiO_2 powders, 1mg of them was dispersed in 15 mL methanol under ultrasound for 15 minutes before the measurement. All the suspension solutions were further dropped onto a hexagonal, 400 mesh copper grid coated with carbon film of standard 3-4 nm thickness (Electron Microscopy Sciences, CF400H-Cu-UL) and allowed to dry in an ambient environment. The samples were imaged in an FEI Quanta 3D Dual Beam SEM operating at 5 kV and 6.7 pA later.

6. TEM measurement

We used the same prepared TiO_2 powder samples from the SEM measurement for the TEM characterization. TEM and HRTEM (high-resolution TEM) were

performed at the National Center for Electron Microscopy (NCEM) at the Lawrence Berkeley National Laboratory Molecular Foundry on an FEI UT Tecnai microscope operated at 200 kV acceleration voltage. The images were analyzed with Gatan Digital Microscope and ImageJ software.

7. XRD measurement

The TiO_2 powders were rubbed and shaken to be separated from the PVA mixture samples. XRD patterns were collected on a Bruker D8 Discover Diffractometer using Cu Ka radiation (40 kV and 40 mA) with degrees per step and time/step parameters of 0.02 degrees per step and 0.4 s/step, respectively, at 2θ angle from 10 to 80 °. X-ray diffraction patterns were plotted in Origin and the XRD diffraction pattern of PVA anatase phase was compared to JCPDS PDF no. 21-1272 extracted from Jade software.

8. NMR measurement

The PVA mixture samples were washed to remove the TiO_2 powder on the surface. 10 mg of separated PVA crystals were dissolved in 0.5 ml DMSO-d6 with an elevated temperature at 90 ℃ and the solution were filtered with cotton for the final characterization. The NMR data were collected on a Bruker Avance III HD 500 MHz NMR equipped with a BBFO broadband probe. Both the 1D proton and carbon experiments were collected using pulse programs from the Bruker Pulse Program library. The 1D Proton experiment was collected using a spectral width of 10000.0 Hz with acquisition time of 3.2768 second, 1 seconds recycle delay, 16 scans at 300K. The 1D Carbon experiment was collected using a spectral width of 29761.9 Hz with

acquisition time of 1.1010 second, 2 seconds recycle delay, 1024 scans at 300K. The data were processed using Mestrenova.

9. MALDI-MS (Matrix-assisted laser desorption/ionization mass spectrometry) measurement

MALDI-MS analyses were conducted with a Bruker Microflex MALDI-LT (linear time of flight) instrument. The matrix and sample were mixed together and deposited on the stainless steel, and the concentrations were as follows: matrix: saturated DHB (2,5-dihydroxybenzoic acid) solution dissolved in 78:22 MilliQ H_2O: ACN + 0.1% TFA with a concentration around 30 mg/ml; PVA sample: dissolved in H_2O at 10 mg/ml concentration. The analyses were performed in a linear mode. The measurement was calibrated with a standard reference, phosphorus red, used in protein. Detection ranges from 200 to 1100 and 2000 to 19000 Da. The data were originally processed and saved in XML format in FlexControl software and converted to mzXML format in the MSConvertGUI application program downloaded from ProteoWizard website. The mzXML files were opened, processed and exported as CSV files in the MALDIquant package running on the R platform comprising all steps from importing of raw data, preprocessing (e.g. baseline removal), peak detection and non-linear peak alignment to calibration of mass spectrograph. Some codes to run the functions in R with MALDI quant package were from ChatGPT with modifications. The CSV files were opened in Excel and replotted in Origin software.

Non-thermal plasma reactor setup

Experiments were conducted using a non-thermal Dielectric Barrier Discharge

(DBD) plasma reactor, which was reported previously and demonstrated in Figure 6-17. The setup design and experiment parameters are the same as those used in the gaseous phase study in the previous paper.[9] The applied voltages range from 4.5 kV to 10.5 kV and the frequencies are controlled at 40 and 70 kHz. Operating environments are in 1 atmospheric pressure with the ambient temperature at 25 ℃ as the initial reaction temperature. Air, nitrogen, or pure CO_2 gas were fed into the reactor at a flow rate of 33 cm^3/min. Notably, high AC voltage and frequency produce a high concentration of non-thermal plasma and the generation of dielectric discharge leads to heating of a quartz reactor. Thus, the applying time for electric power is limited to less than 6 sec to avoid raising the reactor temperature above 65 ℃. The solid samples including the PVA samples, TiO_2 catalyst and the PVA-TiO_2 mixture samples, were collected lastly after finishing the experiments at different conditions. The PVA samples treated with TiO_2 catalyst were washed to study the PVA underneath for the characterizations.

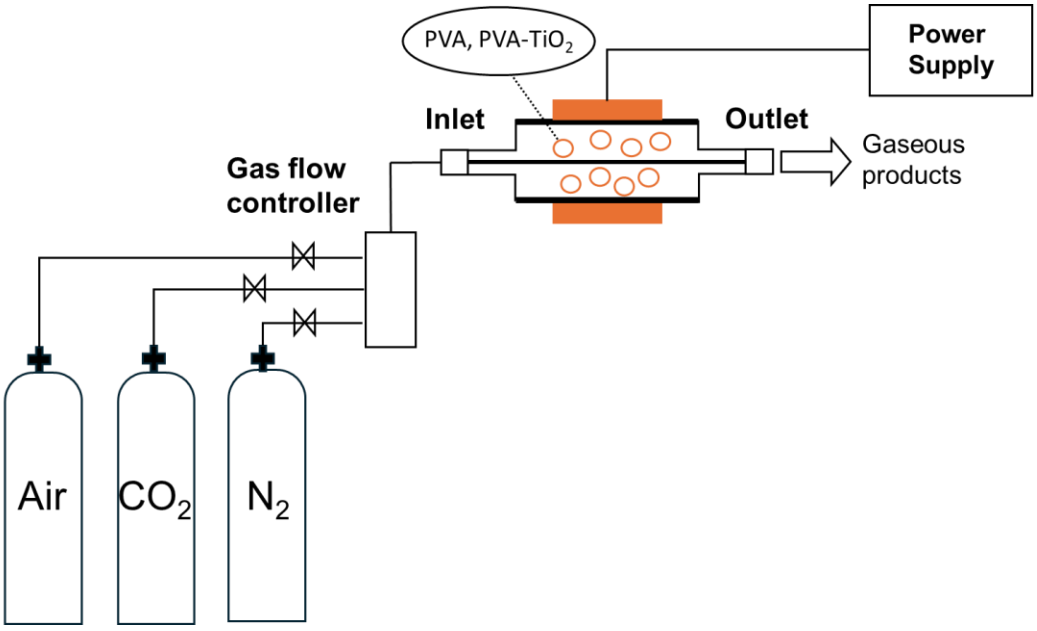

Figure 6-17 The scheme of the experimental setup for non-thermal plasma-assisted degradation on PVA polymers at 25 ℃ and 1 atm.

Table 6-1 summarizes the reports on thermal cracking and other non-thermal plasma methods for polymer depolymerization to compare with our work, showing the significance of non-tar or coke products in this work. In their work, the working temperature is over 100 ℃ or they do not limit the pulse time to avoid the rising temperature. Whereas, in our study, we specifically limited the working temperature below 65 ℃ by applying a pulse time of less than 6 s, to decrease the production of the tar or coke and the deactivation of the catalyst, thus reducing the energy use and catalyst refilling cost.

Table 6-1 Summary of the thermal cracking and other non-thermal plasma methods for polymer depolymerization.

Thermal cracking methods

Polymers	Reactor	Operating conditions	Products & Yields	Selectivity	Tar & Coking	Efficiency	Reference
PE (polyethylene)	Gray–King apparatus	600 ℃	Gas: ethene, propene, butene; Liquid: toluene, naphthalene, xylene; Tar and wax; Residue.	C_2 and C_3 alkene/alkane ratio of PE is quite high	Tar and wax	N/A	[63]
PE (polyethylene)	Tube reactor	520 ℃, ZSM-5 catalyst	Gases: 5.1%; Gasoline: 18.2 %; Light oil: 17.9%.	Catalyst aids with gas, gasoline and lighter oil	Paraffins& olefins	N/A	[21]
PE (polyethylene)	Fixed bed reactor	450 ℃, zeolite catalyst	gas products and gasoline-range hydrocarbons	95% of light alkanes (C_1-C_3) 5% of unsaturated hydrocarbons			[22]
PP (polypropylene)	Semi-batch reactor	400 ℃, FCC (fluid catalytic cracking) catalyst	Gas: Liquid: 85-90%.(paraffins, olefins and aromatics) Solid: 1%	paraffin, olefin, naphthene and aromatic products	Paraffin	N/A	[64]

PS (polystyrene)	Glass reactor	350-420 °C	Gas: high octane number. Gasoline and diesel fractions: styrene, ethylbenzene, toluene, and trimethylbenzene. Residue.	Pressure cracking gave higher yields of gas and gasoline and lower diesel oil and residue	Coke residue	95%	[65]
PS (polystyrene)	Batch autoclave reactor	300-500 °C, N_2 pressure of 0.3-1.6 MPa.	Gas: methane, ethane, ethene and propane. Oil: toluene, ethylbenzene, cumene and triphenylbenzene. . Char.	Higher temperature leads to char production	Char	97%	[66]
PVC (Polyvinyl Chloride)	Fixed-bed reactor	750 °C in N_2	Gas: HCl, CH_4. (59.2 %). Oil: bio-tar, oil, wax and water (30.3 %). Char: 10.3 %.	High gas yield and low oil yield	Char	N/A	[67]

PET (Polyethylene terephthalate)	conical spouted-bed reactor	500−600 °C	Gas: CO, CO_2, C_2H_4; Liquid: acetaldehyde, acetone, benzene; Solid: benzoic acid; Solid residue.	Higher temperature leads to less solid residue in reactor coating	Solid residue coated on sand base	N/A	[68]

Non-thermal plasma methods

Polymers	Plasma & reactor	Operating conditions	Products	Yields	Selectivity	Tar & Coking	Efficiency	Reference
LDPE (low-density polyethylene)*	Air, Air+CO_2 25 :1 DBD (dielectric barrier discharge)	27 kV, 29.6 kV, and 32 kV; Cycled 118 µs with 50 kHz; 30, 120, and 300 s.	C-O, C=O		C-O, C=O	N/A	N/A	[39]
LDPE (low-density polyethylene) $[-CH_2-CH_2-]_n$	O_2 (DC glow)	13.56 MHz RF, 300 W, 31-32 Pa, 1, 2, 5, 10, 15, 20, 25 and 30 min	C=O, COO^-, OH			N/A	N/A	[69]

HDPE (high-density polyethylene) [-CH_2-CH_2-]$_n$	H_2, DBD (dielectric barrier discharge)	20-100 ml/min flow rate, 0-101 kPa and 60-90 W. **25-150 ℃**	CH_4, C_2H_2, C_2H_4, C_3H_6 and C_3H_8 OH		95% of light alkanes (C_1-C_3) 5% of unsaturated hydrocarbons	N/A	N/A	[18]
HDPE (high-density polyethylene) [-CH_2-CH_2-]$_n$*	N_2, DBD (dielectric barrier discharge) with ZSM-5 catalyst.	10-60 W, 30 kV, 5-20 kHz. **250-500 ℃**	H_2, CH_4, C_2H_2, C_2H_4, C_2H_6.	Gas yield of 13.4 mmol g^{-1}	light products such as hydrogen and methane	Solid residue and sintering of catalyst.	N/A	[17]
PS (polystyrene) [-CH_2-CHC_6H_5-]$_n$	H_2, DBD (dielectric barrier discharge)	20-100 ml/min flow rate, 0-101 kPa, 90 W, 2-12 mins. **500 ℃**	CH_4, C_2H_2, C_2H_4, C_3H_6, and C_3H_8, C6–C9 paraffins and alkylbenzenes	40.99 % of gas, 50.98 % of liquid and 1.86% of solid	Gas yield >40% (C_1–C_3 hydrocarbons) and selectivity of ethylene >70%	N/A	90%	[70]
Rubrene*	Ar, CO_2 and H_2O, DBD (dielectric barrier discharge)	RT, 6-9 kV, 50-60 Hz, 0-5 min. **< 100 ℃**	CH_4, C_2H_4, C_2H_6, O_2, CO and CO_2.		CH_4	N/A	N/A	[16]

* indicates the high-energy electrons play a critical role in the plasma reaction process.

6.6 References

(1) Pathak, V. M.; Navneet. Review on the Current Status of Polymer Degradation: A Microbial Approach. *Bioresour. Bioprocess.* **2017**, *4* (1), 15. https://doi.org/10.1186/s40643-017-0145-9.

(2) Beaumont, C.; Turgeon, J.; Idir, M.; Neusser, D.; Lapointe, R.; Caron, S.; Dupont, W.; D'Astous, D.; Shamsuddin, S.; Hamza, S.; et al. Water-Processable Self-Doped Conducting Polymers via Direct (Hetero)Arylation Polymerization. *Macromolecules* **2021**, *54* (12), 5464–5472. https://doi.org/10.1021/acs.macromol.1c00847.

(3) Schneiderman, D. K.; Hillmyer, M. A. 50th Anniversary Perspective: There Is a Great Future in Sustainable Polymers. *Macromolecules* **2017**, *50* (10), 3733–3749. https://doi.org/10.1021/acs.macromol.7b00293.

(4) Mahmoodi Khah, H.; Soleimani, O. Properties and Applications of Polymers: A Mini Review. *J. Chem. Rev.* **2023**, *5* (2), 204–220. https://doi.org/10.22034/jcr.2023.383915.1213.

(5) Mayadunne, R. T. A.; Jeffery, J.; Moad, G.; Rizzardo, E. Living Free Radical Polymerization with Reversible Addition−Fragmentation Chain Transfer (RAFT Polymerization): Approaches to Star Polymers. *Macromolecules* **2003**, *36* (5), 1505–1513. https://doi.org/10.1021/ma021219w.

(6) Song, J. H.; Murphy, R. J.; Narayan, R.; Davies, G. B. H. Biodegradable and Compostable Alternatives to Conventional Plastics. *Philos. Trans. R. Soc. B* **2009**, *364* (1526), 2127–2139. https://doi.org/10.1098/rstb.2008.0289.

(7) Uekert, T.; Singh, A.; DesVeaux, J. S.; Ghosh, T.; Bhatt, A.; Yadav, G.; Afzal, S.; Walzberg, J.; Knauer, K. M.; Nicholson, S. R.; et al. Technical, Economic, and Environmental Comparison of Closed-Loop Recycling Technologies for Common Plastics. *ACS Sustain. Chem. Eng.* **2023**, *11* (3), 965–978. https://doi.org/10.1021/acssuschemeng.2c05497.

(8) Javed, S.; Vogt, D. Development of Eco-Friendly and Sustainable PET Glycolysis Using Sodium Alkoxides as Catalysts. *ACS Sustain. Chem. Eng.* **2023**, *11* (31), 11541–11547. https://doi.org/10.1021/acssuschemeng.3c01872.

(9) Oduntan, A.; Wei, J. F.; Ma, J.; Toskin, A.; Miyoshi, T.; Liu, T.; Chuang, S. S. C. Remarkable Selectivity of Polyvinyl Alcohol Oxidation: An Insight from Ambient Air Plasma in the Presence and Absence of TiO_2. *Applied Catalysis O: Open* **2024**, 206921. https://doi.org/10.1016/j.apcato.2024.206921.

(10) Dey, U.; Mondal, N. K.; Das, Kousik; Dutta, S. An Approach to Polymer Degradation through Microbes. *IOSR J. Pharm.* **2012**, *2* (3), 385–388. https://doi.org/10.9790/3013-0230385388.

(11) Bhatnagar, S.; Kumari, R. Bioremediation: A Sustainable Tool for Environmental Management-a Review. *Annu. Rev. Res. Biol.* **2013**, *3*, 974–993.

(12) Arutchelvi, J.; Muniyasamy, S.; Arkatkar, A.; Doble, M.; Bhaduri, S.; Uppara, P. Biodegradation of Polyethylene and Polypropylene. *Indian J. Biotechnol.* **2008**, *7*, 9–22.

(13) Lee, Y.; Cho, J.; Sohn, J.; Kim, C. Health Effects of Microplastic Exposures: Current Issues and Perspectives in South Korea. *Yonsei Med. J.* **2023**, *64* (5),

301–308. https://doi.org/10.3349/ymj.2023.0048.

(14) Ayer, M. A.; Simon, Y. C.; Weder, C. Azo-Containing Polymers with Degradation On-Demand Feature. *Macromolecules* **2016**, *49* (8), 2917–2927. https://doi.org/10.1021/acs.macromol.6b00418.

(15) Steinman, N. Y.; Starr, R. L.; Brucks, S. D.; Belay, C.; Meir, R.; Golenser, J.; Campos, L. M.; Domb, A. J. Cyclopropenium-Based Biodegradable Polymers. *Macromolecules* **2019**, *52* (9), 3543–3550. https://doi.org/10.1021/acs.macromol.9b00430.

(16) Chuang, S. S. C.; Huhe, F.; Oduntan, A.; Peng, Z. Transient Responses of Product Formation in Nonthermal Plasma-Assisted D_2O-CO_2-Rubber Reaction. *Catal. Commun.* **2023**, *180*, 106707. https://doi.org/10.1016/j.catcom.2023.106707.

(17) Nguyen, H. M.; Carreon, M. L. Non-Thermal Plasma-Assisted Deconstruction of High-Density Polyethylene to Hydrogen and Light Hydrocarbons over Hollow ZSM-5 Microspheres. *ACS Sustain. Chem. Eng.* **2022**, *10* (29), 9480–9491. https://doi.org/10.1021/acssuschemeng.2c01959.

(18) Yao, L.; King, J.; Wu, D.; Chuang, S. S. C.; Peng, Z. Non-Thermal Plasma-Assisted Hydrogenolysis of Polyethylene to Light Hydrocarbons. *Catal. Commun.* **2021**, *150*, 106274. https://doi.org/10.1016/j.catcom.2020.106274.

(19) Aminu, I.; Nahil, M. A.; Williams, P. T. Hydrogen Production by Pyrolysis–Nonthermal Plasma/Catalytic Reforming of Waste Plastic over Different Catalyst Support Materials. *Energy Fuels* **2022**, *36* (7), 3788–3801.

https://doi.org/10.1021/acs.energyfuels.1c04186.

(20) Pishva, P.; Li, J.; Xie, R.; Tang, J.; Nandy, P.; Farouk, T.; Guo, J.; Peng, Z. Nonthermal Hydrogen Plasma-Enabled Ambient, Fast Lignin Hydrogenolysis to Valuable Chemicals and Bio-Oils. *Chem. Eng. J.* **2024**, *501*, 157776. https://doi.org/10.1016/j.cej.2024.157776.

(21) Miskolczi, N.; Angyal, A.; Bartha, L.; Valkai, I. Fuels by Pyrolysis of Waste Plastics from Agricultural and Packaging Sectors in a Pilot Scale Reactor. *Fuel Process. Technol.* **2009**, *90* (7), 1032–1040. https://doi.org/10.1016/j.fuproc.2009.04.019.

(22) Lee, K.-H. Effects of the Types of Zeolites on Catalytic Upgrading of Pyrolysis Wax Oil. *J. Anal. Appl. Pyrolysis* **2012**, *94*, 209–214. https://doi.org/10.1016/j.jaap.2011.12.015.

(23) Xu, C.; Luo, J.-L. Understanding the Light-Induced Oxygen Vacancy in the Photochemical Conversion. *J. Phys. Energy* **2023**, *5* (1), 011001. https://doi.org/10.1088/2515-7655/acb28f.

(24) Bogaerts, A.; Tu, X.; Whitehead, J. C.; Centi, G.; Lefferts, L.; Guaitella, O.; Azzolina-Jury, F.; Kim, H.-H.; Murphy, A. B.; Schneider, W. F.; et al. The 2020 Plasma Catalysis Roadmap. *J. Phys. D: Appl. Phys.* **2020**, *53* (44), 443001. https://doi.org/10.1088/1361-6463/ab9048.

(25) Khatibi, M.; Nahil, M. A.; Williams, P. T. Interaction of Furfural and Hexadecane as Bio-Oil and Plastics Pyro-Oil Model Compounds with Non-Thermal Plasma Processing as a Route to *in-Situ* Hydrogen Donor Upgrading of

Bio-Oil. *Biomass Bioenergy* **2024**, *187*, 107301. https://doi.org/10.1016/j.biombioe.2024.107301.

(26) Ren, L.; Mao, M.; Li, Y.; Lan, L.; Zhang, Z.; Zhao, X. Novel Photothermocatalytic Synergetic Effect Leads to High Catalytic Activity and Excellent Durability of Anatase TiO_2 Nanosheets with Dominant {001} Facets for Benzene Abatement. *Appl. Catal. B Environ.* **2016**, *198*, 303–310. https://doi.org/10.1016/j.apcatb.2016.05.073.

(27) Bhat, N. V.; Nate, M. M.; Kurup, M. B.; Bambole, V. A.; Sabharwal, S. Effect of γ-Radiation on the Structure and Morphology of Polyvinyl Alcohol Films. *Nucl. Instrum. Methods Phys. Res., Sect. B* **2005**, *237* (3), 585–592. https://doi.org/10.1016/j.nimb.2005.04.058.

(28) Hong, W.; Zhou, Y.; Lv, C.; Han, Z.; Chen, G. NiO Quantum Dot Modified TiO_2 toward Robust Hydrogen Production Performance. *ACS Sustain. Chem. Eng.* **2018**, *6* (1), 889–896. https://doi.org/10.1021/acssuschemeng.7b03250.

(29) Deepak, T. G.; Subash, D.; Anjusree, G. S.; Pai, K. R. N.; Nair, S. V.; Nair, A. S. Photovoltaic Property of Anatase TiO_2 3-D Mesoflowers. *ACS Sustain. Chem. Eng.* **2014**, *2* (12), 2772–2780. https://doi.org/10.1021/sc500642c.

(30) Kim, H.; Bae, S.-R.; Lee, T. H.; Lee, H.; Kang, H.; Park, S.; Jang, H. W.; Kim, S. Y. Enhanced Optical Properties and Stability of $CsPbBr_3$ Nanocrystals Through Nickel Doping. *Adv. Funct. Mater.* **2021**, *31* (28), 2102770. https://doi.org/10.1002/adfm.202102770.

(31) Al-Taweel, S. S.; Saud, H. R. New Route for Synthesis of Pure Anatase TiO_2

Nanoparticles via Ultrasound-Assisted Sol-Gel Method. *J. Chem. Pharm. Res.* **2016**, *8* (2), 620–626.

(32) Taudul, B.; Tielens, F.; Calatayud, M. On the Origin of Raman Activity in Anatase TiO_2 (Nano)Materials: An Ab Initio Investigation of Surface and Size Effects. *Nanomaterials* **2023**, *13* (12), 1856. https://doi.org/10.3390/nano13121856.

(33) Appadurai; Subramaniyam, C.; Kuppusamy, R.; Karazhanov, S.; Subramanian. Electrochemical Performance of Nitrogen-Doped TiO_2 Nanotubes as Electrode Material for Supercapacitor and Li-Ion Battery. *Molecules* **2019**, *24*, 2952. https://doi.org/10.3390/molecules24162952.

(34) Challagulla, S.; Tarafder, K.; Ganesan, R.; Roy, S. Structure Sensitive Photocatalytic Reduction of Nitroarenes over TiO_2. *Sci. Rep.* **2017**, *7* (1), 8783. https://doi.org/10.1038/s41598-017-08599-2.

(35) Kamegawa, T.; Irikawa, K.; Yamashita, H. Multifunctional Surface Designed by Nanocomposite Coating of Polytetrafluoroethylene and TiO_2 Photocatalyst: Self-Cleaning and Superhydrophobicity. *Sci. Rep.* **2017**, *7* (1), 13628. https://doi.org/10.1038/s41598-017-14058-9.

(36) Bakar, S. A.; Ribeiro, C. Nitrogen-Doped Titanium Dioxide: An Overview of Material Design and Dimensionality Effect over Modern Applications. *J. Photochem. Photobiol. C: Photochem. Rev.* **2016**, *27*, 1–29. https://doi.org/10.1016/j.jphotochemrev.2016.05.001.

(37) Balog, Á.; Samu, G. F.; Pető, S.; Janáky, C. The Mystery of Black TiO_2:

Insights from Combined Surface Science and In Situ Electrochemical Methods. *ACS Mater. Au* **2021**, *1* (2), 157–168. https://doi.org/10.1021/acsmaterialsau.1c00020.

(38) Deng, H.; Yuan, L.; Li, Z.; Wang, D.; Wang, X.; Liang, P.; Wang, L.; Liu, Y.; Fu, Y.; Chang, Z.; et al. A Hybrid Amorphous/Crystalline TiO_2 Material with Enhanced Photocatalytic Performance. *Adv. Sustainable Syst.* **2022**, *6* (12), 2200316. https://doi.org/10.1002/adsu.202200316.

(39) Scally, L.; Gulan, M.; Weigang, L.; Cullen, P. J.; Milosavljevic, V. Significance of a Non-Thermal Plasma Treatment on LDPE Biodegradation with Pseudomonas Aeruginosa. *Materials* **2018**, *11* (10), 1925. https://doi.org/10.3390/ma11101925.

(40) Remiš, T.; Bělský, P.; Kovářík, T.; Kadlec, J.; Ghafouri Azar, M.; Medlín, R.; Vavruňková, V.; Deshmukh, K.; Sadasivuni, K. K. Study on Structure, Thermal Behavior, and Viscoelastic Properties of Nanodiamond-Reinforced Poly (Vinyl Alcohol) Nanocomposites. *Polymers* **2021**, *13* (9), 1426. https://doi.org/10.3390/polym13091426.

(41) Weon, S.; Choi, W. TiO_2 Nanotubes with Open Channels as Deactivation-Resistant Photocatalyst for the Degradation of Volatile Organic Compounds. *Environ. Sci. Technol.* **2016**, *50* (5), 2556–2563. https://doi.org/10.1021/acs.est.5b05418.

(42) Sofyan, N.; Ridhova, A.; Yuwono, A. H.; Udhiarto, A. Preparation of Anatase TiO_2 Nanoparticles Using Low Hydrothermal Temperature for Dye-Sensitized

Solar Cell. *IOP Conf. Ser.: Mater. Sci. Eng.* **2018**, *316*, 012055. https://doi.org/10.1088/1757-899X/316/1/012055.

(43) Sridevi, A.; Ramji, B. R.; Prasanna Venkatesan, G. K. D.; Sugumaran, V.; Selvakumar, P. A Facile Synthesis of TiO_2/BiOCl and TiO_2/BiOCl/La_2O_3 Heterostructure Photocatalyst for Enhanced Charge Separation Efficiency with Improved UV-Light Catalytic Activity towards Rhodamine B and Reactive Yellow 86. *Inorg. Chem. Commun.* **2021**, *130*, 108715. https://doi.org/10.1016/j.inoche.2021.108715.

(44) Zare, M. H.; Mehrabani-Zeinabad, A. Photocatalytic Activity of ZrO_2/TiO_2/Fe_3O_4 Ternary Nanocomposite for the Degradation of Naproxen: Characterization and Optimization Using Response Surface Methodology. *Sci. Rep.* **2022**, *12* (1), 10388. https://doi.org/10.1038/s41598-022-14676-y.

(45) Uddin, M. J.; Cesano, F.; Chowdhury, A. R.; Trad, T.; Cravanzola, S.; Martra, G.; Mino, L.; Zecchina, A.; Scarano, D. Surface Structure and Phase Composition of TiO_2 P25 Particles After Thermal Treatments and HF Etching. *Front. Mater.* **2020**, *7*, 192. https://doi.org/10.3389/fmats.2020.00192.

(46) Marka, S. K.; Sindam, B.; Raju, K. C. J.; Srikanth, V. V. S. S. Flexible Few-Layered Graphene/Poly Vinyl Alcohol Composite Sheets: Synthesis, Characterization and EMI Shielding in X-Band through the Absorption Mechanism. *RSC Adv.* **2015**, *5* (46), 36498–36506. https://doi.org/10.1039/C5RA04038H.

(47) Kharazmi, A.; Faraji, N.; Hussin, R. M.; Saion, E.; Yunus, W. M. M.; Behzad, K.

Structural, Optical, Opto-Thermal and Thermal Properties of ZnS–PVA Nanofluids Synthesized through a Radiolytic Approach. *Beilstein J. Nanotechnol.* **2015**, *6* (1), 529–536. https://doi.org/10.3762/bjnano.6.55.

(48) Korbag, I.; Mohamed, S. Studies on the Formation of Intermolecular Interactions and Structural Characterization of Polyvinyl Alcohol/Lignin Film. *Int. J. Environ. Stud.* **2016**, 1–10. https://doi.org/10.1080/00207233.2016.1143700.

(49) Deleanu, I.; Stoica, A.; Stroescu, M.; Dobre, L.; Dobre, T.; Jinga, S.; Tardei, C. Potassium Sorbate Release from Poly(Vinyl Alcohol)–Bacterial Cellulose Films. *Chem. Pap.* **2012**, *66*, 138–143. https://doi.org/10.2478/s11696-011-0068-4.

(50) Zárate, I. A.; Aguilar-Bolados, H.; Yazdani-Pedram, M.; Pizarro, G. del C.; Neira-Carrillo, A. In Vitro Hyperthermia Evaluation of Electrospun Polymer Composite Fibers Loaded with Reduced Graphene Oxide. *Polymers* **2020**, *12* (11), 2663. https://doi.org/10.3390/polym12112663.

(51) D'Amelia, R. P.; Kimura, M. W.; Mancuso, J. Synthesis and Characterization of Polyvinyl Alkyl Ester and Polyvinyl Alcohol Homopolymers and Blends of Polyvinyl Alkyl Esters. *J. Polym. Biopolym. Phys. Chem.* **2021**, *9* (1), 1–12. https://doi.org/10.12691/jpbpc-9-1-1.

(52) Cheung, M. K.; Wang, J.; Zheng, S.; Mi, Y. Miscibility of Poly(Epichlorohydrin)/Poly(Vinyl Acetate) Blends Investigated with High-Resolution Solid-State ^{13}C NMR. *Polymer* **2000**, *41* (4), 1469–1474. https://doi.org/10.1016/S0032-3861(99)00314-6.

(53) Geng, S.; Ullah Shah, F.; Liu, P.; Antzutkin, O. N.; Oksman, K. Plasticizing and Crosslinking Effects of Borate Additives on the Structure and Properties of Poly(Vinyl Acetate). *RSC Adv.* **2017**, *7* (13), 7483–7491. https://doi.org/10.1039/C6RA28574K.

(54) Caló, E.; de Barros, J. M. S.; Fernández-Gutiérrez, M.; Román, J. S.; Ballamy, L.; Khutoryanskiy, V. V. Antimicrobial Hydrogels Based on Autoclaved Poly(Vinyl Alcohol) and Poly(Methyl Vinyl Ether- Alt -Maleic Anhydride) Mixtures for Wound Care Applications. *RSC Adv.* **2016**, *6* (60), 55211–55219. https://doi.org/10.1039/C6RA08234C.

(55) Audette, Y.; Congreves, K.; Schneider, K.; Zaro, G.; Pit Nunes, A.; Zhang, H.; Voroney, P. The Effect of Agroecosystem Management on the Distribution of C Functional Groups in Soil Organic Matter: A Review. *Biol. Fertil. Soils* **2021**, *57*, 1–14. https://doi.org/10.1007/s00374-021-01580-2.

(56) Khatibi, M.; Nahil, M. A.; Williams, P. T. Improving the Quality of Bio-Oil Using the Interaction of Plastics and Biomass through Copyrolysis Coupled with Nonthermal Plasma Processing. *Energy Fuels* **2024**, *38* (2), 1240–1257. https://doi.org/10.1021/acs.energyfuels.3c04082.

(57) Gao, X.; Lin, Z.; Li, T.; Huang, L.; Zhang, J.; Askari, S.; Dewangan, N.; Jangam, A.; Kawi, S. Recent Developments in Dielectric Barrier Discharge Plasma-Assisted Catalytic Dry Reforming of Methane over Ni-Based Catalysts. *Catalysts* **2021**, *11* (4), 455. https://doi.org/10.3390/catal11040455.

(58) Bian, W.; Song, X.; Liu, D.; Zhang, J.; Chen, X. Actions of Nitrogen Plasma in

the 4-Chlorophenol Degradation by Pulsed High-Voltage Discharge with Bubbling Gas. *Chem. Eng. J.* **2013**, *219*, 385–394. https://doi.org/10.1016/j.cej.2012.12.074.

(59) Sharma, V.; Hosoi, K.; Mori, T.; Kuroda, S. Electrical and Optical Characterization of Cold Atmospheric Pressure Plasma Jet and the Effects of N_2 Gas on Argon Plasma Discharge. *Appl. Mech. Mater.* **2013**, *268–270*, 522–528. https://doi.org/10.4028/www.scientific.net/AMM.268-270.522.

(60) Li, M.; Xu, G.; Tian, Y.; Chen, L.; Fu, H. Carbon Dioxide Reforming of Methane Using DC Corona Discharge Plasma Reaction. *J. Phys. Chem. A* **2004**, *108* (10), 1687–1693. https://doi.org/10.1021/jp037008q.

(61) Hagstrum, H. D. Ionization by Electron Impact in CO, N_2, NO, and O_2. *Rev. Mod. Phys.* **1951**, *23* (3), 185–203. https://doi.org/10.1103/RevModPhys.23.185.

(62) Takamatsu, T.; Uehara, K.; Sasaki, Y.; Miyahara, H.; Matsumura, Y.; Iwasawa, A.; Ito, N.; Azuma, T.; Kohno, M.; Okino, A. Investigation of Reactive Species Using Various Gas Plasmas. *RSC Adv.* **2014**, *4* (75), 39901–39905. https://doi.org/10.1039/C4RA05936K.

(63) Kiran, N.; Ekinci, E.; Snape, C. E. Recycling of Plastic Wastes via Pyrolysis. *Resour. Conserv. Recycl.* **2000**, *29* (4), 273–283. https://doi.org/10.1016/S0921-3449(00)00052-5.

(64) Lee, K.-H.; Noh, N.-S.; Shin, D.-H.; Seo, Y. Comparison of Plastic Types for Catalytic Degradation of Waste Plastics into Liquid Product with Spent FCC Catalyst. *Polym. Degrad. Stab.* **2002**, *78* (3), 539–544.

https://doi.org/10.1016/S0141-3910(02)00227-6.

(65) Walendziewski, J. Engine Fuel Derived from Waste Plastics by Thermal Treatment. *Fuel* **2002**, *81* (4), 473–481. https://doi.org/10.1016/S0016-2361(01)00118-1.

(66) Onwudili, J. A.; Insura, N.; Williams, P. T. Composition of Products from the Pyrolysis of Polyethylene and Polystyrene in a Closed Batch Reactor: Effects of Temperature and Residence Time. *J. Anal. Appl. Pyrolysis* **2009**, *86* (2), 293–303. https://doi.org/10.1016/j.jaap.2009.07.008.

(67) Ephraim, A.; Pham Minh, D.; Lebonnois, D.; Peregrina, C.; Sharrock, P.; Nzihou, A. Co-Pyrolysis of Wood and Plastics: Influence of Plastic Type and Content on Product Yield, Gas Composition and Quality. *Fuel* **2018**, *231*, 110–117. https://doi.org/10.1016/j.fuel.2018.04.140.

(68) Artetxe, M.; Lopez, G.; Amutio, M.; Elordi, G.; Olazar, M.; Bilbao, J. Operating Conditions for the Pyrolysis of Poly-(Ethylene Terephthalate) in a Conical Spouted-Bed Reactor. *Ind. Eng. Chem. Res.* **2010**, *49* (5), 2064–2069. https://doi.org/10.1021/ie900557c.

(69) Sanchis, M. R.; Blanes, V.; Blanes, M.; Garcia, D.; Balart, R. Surface Modification of Low Density Polyethylene (LDPE) Film by Low Pressure O_2 Plasma Treatment. *Eur. Polym. J.* **2006**, *42* (7), 1558–1568. https://doi.org/10.1016/j.eurpolymj.2006.02.001.

(70) Yao, L.; King, J.; Wu, D.; Ma, J.; Li, J.; Xie, R.; Chuang, S. S. C.; Miyoshi, T.; Peng, Z. Non-Thermal Plasma-Assisted Rapid Hydrogenolysis of Polystyrene to

High Yield Ethylene. *Nat. Commun.* **2022**, *13* (1), 885. https://doi.org/10.1038/s41467-022-28563-7.

7 Conclusions and Future Perspectives

7.1 Overall Summary

This dissertation focuses on understanding the relationships between structure, lattice dynamics, charge-carrier dynamics, and spin properties in low-dimensional to three-dimensional metal halide materials through a combination of structural characterization, ultrafast spectroscopy, Raman spectroscopy, and X-ray techniques.

The work began with the synthesis and structural characterization of amino metal halide molecular clusters (MCs). Stable crystalline molecular clusters were successfully prepared and their atomic structures were determined, providing a model system for investigating quantum-confined metal halide materials at the molecular scale.

Building on this structural foundation, ultrafast transient absorption spectroscopy was employed to investigate the excited-state dynamics of these molecular clusters. Distinct relaxation pathways involving vibrational cooling, band-edge recombination, and trap-assisted decay were identified, revealing how structural confinement influences carrier relaxation processes.

The relationship between lattice structure and optical properties was further explored in two-dimensional lead-free metal halide double perovskites. Low-frequency Raman spectroscopy revealed characteristic lattice vibrational modes associated with octahedral distortions and metal–halide framework dynamics. Comparative studies showed that Cu incorporation introduces stronger lattice

distortion and enhanced electron–phonon coupling relative to Ag-based analogues, leading to modified emission properties.

To extend the understanding of functional excited-state behavior, spin-polarized transient absorption spectroscopy was applied to Ni-doped $CsPbBr_3$ quantum dots. The results demonstrated that transition-metal doping alters spin relaxation pathways through defect-mediated interactions and localized electronic states.

In addition, X-ray absorption spectroscopy was utilized to investigate plasma-assisted depolymerization of poly(vinyl alcohol) over TiO_2 catalysts, illustrating the application of advanced spectroscopic techniques to catalytic and environmental systems.

Overall, this dissertation establishes a systematic framework connecting atomic structure, lattice vibrations, excited-state dynamics, and spin behavior in low-dimensional metal halide materials.

7.2 Major Scientific Contributions

The major contributions of this dissertation can be summarized as follows:

1. Established stable amino metal halide molecular clusters as model low-dimensional metal halide systems through synthesis and crystal structure determination.
2. Revealed excited-state relaxation pathways in molecular clusters using ultrafast transient absorption spectroscopy, identifying vibrational cooling, band-edge recombination, and trap-assisted decay processes.

3. Elucidated low-frequency lattice vibrations in two-dimensional lead-free metal halide double perovskites and established correlations between structural distortion, electron–phonon coupling, and optical properties.
4. Demonstrated the influence of transition-metal doping on spin relaxation dynamics in $CsPbBr_3$ quantum dots, providing insights into spin manipulation in halide perovskites.
5. Applied advanced X-ray absorption spectroscopy to investigate catalytic reaction mechanisms in plasma-assisted polymer depolymerization systems.
6. Developed a unified understanding of how local structure and lattice dynamics govern charge and spin behaviors across different classes of metal halide materials.

7.3 Future Perspectives

The studies presented in this dissertation establish connections between local structure, lattice vibrations, charge-carrier dynamics, and spin properties in metal halide materials. While significant progress has been made, several important questions remain open and provide promising directions for future research.

Ultrafast X-ray Techniques for Structural Dynamics

In this dissertation, ultrafast optical spectroscopy was employed to investigate excited-state and spin dynamics in metal halide materials. While these measurements provide detailed information about electronic relaxation pathways, they do not directly capture the accompanying atomic structural motions. Future studies combining ultrafast optical spectroscopy with time-resolved X-ray scattering and X-

ray absorption techniques can provide direct visualization of structural evolution following photoexcitation. Such approaches would enable simultaneous investigation of electronic and atomic dynamics, offering a more complete understanding of photoinduced processes in metal halide materials. The integration of ultrafast optical and X-ray methods is expected to reveal transient structural distortions, lattice rearrangements, and excited-state structural pathways that are inaccessible using optical techniques alone.

Structure–Dynamics Correlations in Metal Halide Materials

The results presented in this dissertation demonstrate that local structure and lattice dynamics play critical roles in determining the optical and electronic properties of low-dimensional metal halide materials. Studies of molecular clusters and lead-free double perovskites revealed strong relationships between structural distortions, low-frequency vibrational modes, electron–phonon coupling, and excited-state behavior. However, the microscopic mechanisms connecting specific structural motifs to charge-carrier relaxation and energy dissipation remain incompletely understood. Future investigations combining advanced spectroscopy, temperature-dependent measurements, and theoretical modeling may further elucidate how atomic-scale structural fluctuations influence excited-state processes. Such knowledge will be essential for the rational design of materials with improved optical performance and enhanced stability.

Spin Dynamics and Quantum Information Applications

The spin-polarized transient absorption studies of Ni-doped $CsPbBr_3$ quantum

dots demonstrate that dopants and defects can significantly influence spin relaxation pathways in metal halide systems. Future efforts may focus on engineering spin coherence through defect control, isotope engineering, magnetic-ion doping, and dimensionality modulation. In particular, recent studies by Vivien in our group have shown that isotope enrichment can substantially extend spin lifetimes in halide perovskites, highlighting the importance of hyperfine interactions in spin relaxation processes. A deeper understanding of spin-dependent phenomena may enable the development of metal halide materials for spintronic devices, quantum sensing, and emerging quantum information technologies.

Materials Science for a Sustainable Future

Human activities since the industrial era have relied heavily on fossil fuels, leading to increasing greenhouse gas emissions and environmental challenges, including rising global temperatures, melting glaciers, extreme weather events, and frequent wildfires. At the same time, the accumulation of plastic waste has become a growing global concern. Addressing these issues requires the development of efficient energy-conversion materials, environmentally friendly chemical processes, and effective approaches for waste reduction and resource recovery. The plasma-assisted depolymerization study presented in this dissertation demonstrates how advanced spectroscopic techniques can be applied to investigate catalytic pathways relevant to polymer degradation and recycling. Future research may further integrate materials science, catalysis, and advanced characterization methods to develop sustainable strategies for plastic upcycling, carbon utilization, clean energy

production, and environmental remediation. Combining fundamental mechanistic understanding with innovative materials design will play an increasingly important role in addressing global energy and environmental challenges.

AI-Guided Materials Discovery

The growing availability of large datasets generated from spectroscopy, diffraction, microscopy, and computational studies provides new opportunities for artificial intelligence (AI) and machine learning (ML) in materials research. The multimodal characterization techniques utilized throughout this dissertation generate complex datasets that often contain hidden correlations between structure, vibrations, and electronic properties. Future research may integrate machine learning algorithms with advanced characterization methods to accelerate the discovery of structure–property relationships, automate spectral analysis, and predict material performance. More broadly, combining high-throughput experiments, first-principles calculations, and data-driven modeling may significantly accelerate the design of next-generation optoelectronic, spintronic, and energy-related materials.

Looking forward, the integration of advanced spectroscopy, X-ray science, artificial intelligence, and predictive materials design may provide unprecedented opportunities for understanding and controlling complex structure–property relationships in functional materials for optoelectronic, spintronic, and energy applications.